QED and X-ray Polarization from Neutron Stars and Black Holes

by

Ilaria Caiazzo

A THESIS SUBMITTED IN PARTIAL FULFILLMENT
OF THE REQUIREMENTS FOR THE DEGREE OF

Doctor of Philosophy

in

THE FACULTY OF GRADUATE AND POSTDOCTORAL STUDIES
(Physics)

The University of British Columbia
(Vancouver)

December 2019

The following individuals certify that they have read, and recommend to the Faculty of Graduate and Postdoctoral Studies for acceptance, the thesis entitled:

QED and X-ray Polarization from Neutron Stars and Black Holes

submitted by **Ilaria Caiazzo** in partial fulfillment of the requirements for the degree of **Doctor of Philosophy** in **Physics**.

Examining Committee:

Jeremy Heyl, Physics and Astronomy
Supervisor

Harvey Richer, Physics and Astronomy
Supervisory Committee Member

Ingrid Stairs, Physics and Astronomy
Supervisory Committee Member

Marcel Franz, Physics and Astronomy
Supervisory Committee Member

Gary Hinshaw, Physics and Astronomy
University Examiner

Stephen Gustafson, Mathematics
University Examiner

Andrew Melatos, University of Melbourne
External Examiner

Abstract

The emission from accreting black holes and neutron stars, as well as from the highly magnetized neutron stars called magnetars, is dominated by X-rays. For this reason, spectral and timing studies in the X-rays have been extremely successful in broadening our understanding of compact objects in the past few decades. Soon, a new observational window will open on compact objects: X-ray polarimetry. In this work, I explore how polarized light is generated in black-hole accretion disks, magnetar atmospheres and magnetospheres and in the accretion region of X-ray pulsars. In the different chapters, I show how the polarization signal is sensitive to several unknowns in our theoretical models: the geometry of accretion in X-ray pulsars, the strength and structure of the magnetic field threading accretion disks around black holes, the process of the non-thermal emission in magnetars. For this reason, the future X-ray polarimetry missions will be extremely helpful in constraining our theoretical models. Furthermore, the polarization emission will provide, for the first time, a test of one of the first theoretical predictions of quantum electrodynamics: vacuum birefringence. In this work, I show how this effect, previously considered only for neutron stars, plays a crucial role for black holes as well.

Lay Summary

Neutron stars and black holes share the same origin: they are born in the spectacular event that we call a supernova. Such a dramatic beginning results in extreme properties, that place them among the most fascinating objects in the Universe. In the 50 years since their discoveries, observations over the entire electromagnetic spectrum and in gravitational waves have brought us closer to understand these objects. Soon, a new type of X-ray telescope, able to detect the polarization of light, will be in space, opening a new window on neutron stars and black holes. In this work, I show how X-ray polarization can give us answers to the questions: what is the structure and strength of magnetic fields surrounding black holes? How can a neutron star steal matter from an orbiting companion star? What is causing the strange emission that we see in the ultra-magnetized neutron stars called magnetars?

Preface

All the work presented in this thesis is a result of a collaboration between the author, Ilaria Caiazzo (I.C.), and her advisor Jeremy Heyl (J.H.).

- Chapter 1. Some introductory text was adapted from the white papers [39] and [88], submitted to the Bulletin of the AAS, from [37], published in the journal *Galaxies* and from [40], the book chapter "Polarimetry of Magnetars and Isolated Neutron Stars," of the book *Astronomical Polarimetry from the Infrared to the Gamma-rays*, currently in press by Springer. The white papers [39] and [88] where written by the Colibrí collaboration, for which J.H. is PI and I.C. is project scientist; I.C. wrote the bulk of [39], and parts of [88], which J.H. wrote the bulk of. All the other authors wrote part of the text and gave useful feedback. I.C. and J.H. wrote the majority of [40], while Roberto Turolla edited and integrated the final draft. J.H. and I.C. conceived the calculations of [37], while I.C. performed the calculations and wrote the bulk of the text.

- Chapter 3 was adapted from [40] (see above).

- Chapter 4 was adapted from the paper [87], published by the journal *Galaxies*. J.H. wrote the bulk of [87], while I.C. wrote part of the text; the calculations were done in part by J.H. and in part by I.C.

- Chapter 5 is partly original, partly adapted from [87], published by the journal *Galaxies* and from [40] (see above).

- Chapter 6 was adapted from [38], published by the journal *Physical Review D* and from [37], published in *Galaxies*. J.H. and I.C. conceived the calculations of [38], while I.C. performed the calculations and wrote the bulk of the text.

- All the calculations in Chapters 7 and 8 where conceived by I.C. and J.H., and performed by I.C. A figure in Chapter 7 was previously published in [87], by the journal *Galaxies* (see above).

- A figure in Chapter 9 was previously published in [37], by the journal *Galaxies* (see above).

Table of Contents

List of Tables

List of Figures

Glossary

X-ray pulsar Accreting neutron star that shows a pulsating emission in the X-rays.

Magnetar Highly magnetized neutron star, with magnetic field exceeding 10^{14} Gauss.

ISCO Innermost Stable Circular Orbit, for a black hole accretion disk.

X-mode or $\perp$-mode, polarization mode in which the electric field of the photon is perpendicular to the local magnetic field.

O-mode or $\|$-mode, polarization mode in which the electric field of the photon is parallel to the local magnetic field.

Birefringent medium anisotropic medium in which the index of refraction depends on the polarization direction of light.

Acknowledgments

I would like to thank Jeremy Heyl, my advisor, for being the best advisor anyone could ask for. Thanks to you I have learned so much and we have embarked in so many projects together, but most importantly, doing research was always fun and exciting. Thank you for being such a good friend.

I would like to thank all the collaborators and friends with whom I had stimulating conversations and glasses of wine. In particular, I would like to thank all the people in our research group at UBC, headed by Jeremy Heyl and Harvey Richer. And thank you Harvey for all the good times and all the great projects that we have done together.

I would like to thank all the friends that supported me in these past years. Thank you for being there for me when I needed a place to stay or a beer or a hug. You have done more for me than you can ever imagine.

Finally, to Carlo. Thank you for everything.

Chapter 1

Introduction

When a massive star runs out of fuel in its core, at the end of its life, the source of energy that used to balance the star's self-gravitation, nuclear energy, is extinguished. The collapse that ensues gives birth to the spectacular and extremely energetic event called a supernova. A supernova, however, does not destroy the star completely; it leaves over what remains of the star's compact core: either a black hole or a newly born neutron star.

Being born in such a dramatic event, neutron stars and black holes (also called *compact objects*) present peculiar characteristics that place them among the most fascinating and puzzling objects in the Universe. They uniquely provide an environment to test the laws of physics at their extremes, as density in a neutron star reaches values several times higher than nuclear density, magnetic fields are billions of times higher than the Sun's, and gravity around black holes is so strong as to trap light itself. Compact objects, however, do not like to reveal their secrets all at once. Fifty years after their discovery, we still do not know what neutron stars are made of, and the question of how black holes modify space and time around them is still open.

As always in the history of astronomy, the opening of a new observational window on an astronomical object brings the promise of a much deeper understanding of the object itself, together with a wealth of unexpected discoveries. We are now at the door of such an exciting time, with a new window opening on compact objects: X-ray polarimetry. Several observatories with an X-ray polarimeter on board are now at different stages of development: in the 1–10 keV range, the NASA SMEX mission *IXPE* [241], scheduled to fly in 2021, and the Chinese–European *eXTP* [253]; in the medium range, 5-30 keV, the Indian *POLIX*, scheduled for launch in 2020 [175, 235]; in the hard-X-ray range, 15–150 keV, the balloon-borne *X-Calibur* [22] and *PoGO+* [43]; and, in the sub-keV range, the narrow band (250 eV) *LAMP* [208] and the broad band (0.2–0.8 keV) rocket-based *REDSox* [64].

Being able to measure the polarization of X-ray photons will provide two new observables, polarization degree and angle, which are extremely sensitive to the geometry of the emission regions and to the structure of magnetic fields. In particular, the focus of this work is on how X-ray polarization will help us probe the geometry of the emission from accreting neutron stars (X-ray pulsars), the structure and strength of magnetic fields surrounding accreting black holes and the emission processes in ultramagnetized neutron stars (magnetars). I will present models for the polarization of the X-ray emission from compact objects based on the most realistic assumptions and physical models to date, and show that the observation of polarization will provide a powerful tool to understand the physical processes in action. Specifically, I show the effects of vacuum birefringence on the polarization from accreting black holes, and how the polarization signal can be used to probe the magnetic field threading the accretion disk (Chapter 6); I find the polarization signal of X-ray pulsars by including QED in an old model and presenting a brand new model that fits the spectral data very well (Chapter 7); and I model the polarization in the soft X-rays from magnetars in the context of different emission models (Chapter 8).

1.1 Neutron stars

Neutron stars are the most compact stars in the Universe. The typical radius of a neutron star is about 10 km and the currently measured masses of neutron stars range between 1 and 2 solar masses. This extreme compactness leads to a very high density in their cores, that can reach a few times the saturation density for terrestrial atomic nuclei. Furthermore, neutron stars rotate with periods that can be as low as a few milliseconds and they possess very strong magnetic fields, that range from the 10^8 G of millisecond pulsars, to $10^{11} - 10^{12}$ G for radio and X-ray pulsars, up to $10^{14} - 10^{15}$ G for magnetars. These extreme conditions cannot be found anywhere else in the Universe and therefore, neutron stars represent unique laboratories where we can test our understanding in many fields of fundamental physics.

In the fifty years since their discovery, neutron stars have never stopped puzzling and amazing astronomers. First discovered as radio pulsars, neutron stars have revealed themselves in different fashions, over the entire electromagnetic spectrum and via gravitational waves (and neutrinos). From the almost 3,000 radio pulsars detected up to now, to the radio-quiet, thermally emitting isolated neutron stars (XDINs), from the young and active magnetars with extreme magnetic fields and slow rotation periods, to the old and rapidly rotating millisecond pulsars, from accreting to merging binaries; neutron-star phenomenology is rich and we have learned a lot from it. Yet, many puzzles remain, including the key question: What are neutron stars made of? This question has profound implications for the physics of dense matter. The density reached in a neutron star's core, several times higher than nuclear density, is not reached anywhere else in the universe at cold temperatures, let alone in our terrestrial physics labs, and therefore neutron stars represent the only laboratory available to look for the equation of state for cold, dense matter.

What is currently known about the neutron star internal structure is shown in Fig. 1.1. Neutron stars possess a very thin atmosphere, most likely made of light elements, either hydrogen or helium, with a thickness that can vary from some ten centimeters in a hot neutron star, to a few millimeters in a cold one [2]. Underneath, the envelope of the star that goes from the surface to a density of about 4×10^{11} g cm^{-3}, called the outer crust, is made of a mostly solid lattice of neutron rich nuclei and a gas of degenerate electrons. At a density of $\sim 4 \times 10^{11}$ g cm^{-3}, the *neutron drip* density, neutrons start to spill out of nuclei, and the inner crust is therefore made by a lattice of nuclei even richer in neutrons that coexist with a degenerate, superfluid gas of dripped, unbound neutrons and a gas of ultra-relativistic electrons. At the inner edge of the crust, at densities of the order of $10^{13} - 10^{14}$ g cm^{-3}, spherical shapes are no longer energetically favorable for nuclei. Competition between strong interactions at short distance and Coulomb repulsion at long distance, called *frustration*, leads to the formation of complex nuclear structures with different shapes, called *nuclear pasta*. In the core, at densities higher than

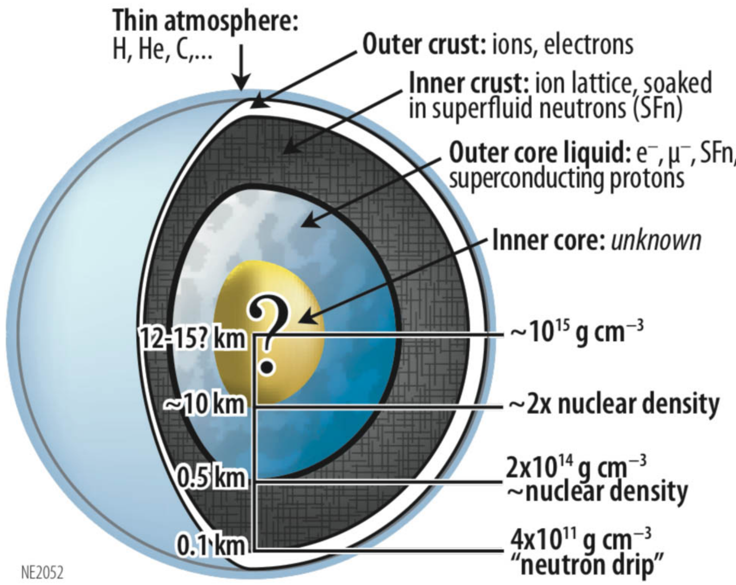

Figure 1.1: Diagram of the internal structure of a neutron star. Credit: NASA/NICER.

the nuclear density, the nuclei finally melt and create a uniform, beta-equilibrated nuclear plasma, consisting mainly of superfluid neutrons, with a mixture of superconducting protons, electrons and muons. At higher densities in the core, a phase transition is theoretically possible, with the appearance of hyperons, pion or kaon condensates, or even deconfined quark matter.

The holy grail of neutron star observations, the mass-radius relation, if measured for several neutron stars, could put stringent constraints on the equation of state [212]. Mass measurements of massive neutron stars exclude a number of equations of state that predict a relatively soft dependence of pressure on density. The record holder as of December 2019 is the millisecond pulsar J0740+6620, with a measured mass of 2.14 ± 0.10 $M_\odot$ [48]; the previous mass measurements around 2 solar masses, of the millisecond pulsar J0348+0432 at 2.01 ± 0.04 $M_\odot$ [6] and of the pulsar J1614-2230 at 1.97 ± 0.04 $M_\odot$ [53], already excluded many soft equations of state. Although a number of masses of neutron stars have been measured with high precision, especially for compact binaries, radius measurements are much harder to achieve with the precision of less than a kilometer required to put stringent constraints on the equation of state.

1.1.1 A bit of history

At the 1973 Solvay Conference, Léon Rosenfeld reminesced about a conversation between Niels Bohr, Lev Landau, and himself that took place in Copenhagen in February 1932, right after the discovery of the neutron, in which Landau improvised the conception of neutron stars [1]. This is often taken as the first time the idea of neutron stars was ever proposed. In reality, Landau submitted a paper to the Physikalische Zeitschrift der Sowjetunion before the discovery of the neutron, in January 1932, in which he mentioned the possible existence of dense stars that look like one giant nucleus [126, 247]. After this first theoretical prediction, a second, prescient hypothesis was advanced only two years later by Baade and Zwicky [7]: a neutron-rich compact object could be the remnant of the gravitational collapse of the core of a star after a supernova.

Neutron stars were expected to be cold and faint and hard to detect; nonetheless, some scientists kept studying the properties that such objects would have, if they existed. The first model of the neutron star structure in general relativity, now called the TOV model, was proposed in 1939 by Oppenheimer and Volkoff [171] and separately by Tolman [230]. In early 1967, Pacini suggested that supernova remnants such as the Crab could be powered by the radiation emitted by a rotating, strongly magnetized neutron star.

The serendipitous discovery took place the same year, in the summer of 1967, by a doctoral student at Cambridge, Jocelyn Bell. Bell and her advisor, Antony Hewish, were building the Interplanetary Scintillation Array, a radio telescope, to study quasars, when she noticed a regular pulsation in the radio signal. In November, they managed to record the regular pulses of the celestial object, presently known as PSR B1919+21, with a period of 1.337 seconds. In the discovery paper, published in February, 1968, they also proposed that the source of this rapid pulsation may be a compact object, such as a white dwarf or a neutron star [86].

In the first year following the discovery of the first pulsar, many theories were proposed. Many scientists leaned toward explaining the source of the radio signal as a binary system or a white dwarf, because both concepts where more familiar back then [133]. A few months later, however, pulsars showing much shorter periods were discovered, like the Vela pulsar (89 ms) [127] and the Crab pulsar (33 ms) [211]. Only an object as compact as a neutron star could rotate or vibrate at these newly observed frequencies. Moreover, these two pulsars were found inside supernova remnants, providing a confirmation of Baade-Zwicky's prediction. Thomas Gold, professor at Cornell University, in a paper in Nature, suggested that the source of the radio signal could be identified with a rotating neutron star. He proposed the *lighthouse mechanism*, for which the pulsating signal is caused by a beam of radiation swept across the observer [72].

For several years after the first pulsar discovery, it was widely accepted that neutron stars could only be observed as pulsars within radio wavelengths. However, in the last four decades, many different types of neutron stars, other than rotation powered pulsars (radio pulsars), have been discovered: isolated, thermally emitting neutron stars (XDINs), silent in radio; compact central objects (CCOs), found in supernova remnants; accreting X-ray and γ-ray emitters; magnetars, i.e. young pulsars with huge magnetic fields (up to 10^{15} Gauss), and rotating radio transients (RRATs), i.e. rapidly changing objects that act as pulsars but only for a few seconds per day.

1.1.2 Neutron stars in the X-rays: X-ray pulsars

Even though the first *identified* neutron star was a radio pulsar, the first *observation* of emission coming from a neutron star coincided with the first detection of X-rays from outside the solar system: the discovery of Scorpius X-1 by the Aerobee rocket, in 1962 [68]. The correct identification of Scorpius X-1 as a binary system containing an accreting neutron star came only after other systems were discovered in the 1970s by the satellite UHURU that contained a pulsating neutron star: Centaurus X-3 and Hercules X-1 [69, 218].

Accreting X-ray pulsars (to be concise I will use the term X-ray pulsars hereafter) are highly magnetized neutron stars that live in a binary and accrete material from a companion star. The material, mostly ionized hydrogen, gets unbound from the companion (either by exceeding the Roche lobe, or because of strong winds) and becomes gravitationally bound to the neutron star. As the material gets closer to the compact object, it forms an accretion disk, and when it reaches the surface of the compact object, the kinetic energy of the accretion flow is converted into X-ray emission. The accretion luminosity generated in this process is given by

$$L_X \sim \frac{GM_* \dot{M}}{R_*} \tag{1.1}$$

where G is the gravitational constant, M_* and R_* are the mass and radius of the neutron star, respectively, and $\dot{M}$ is the mass accretion rate. The presence of a strong magnetic field on the neutron star (B$\sim 10^{12} - 10^{13}$ G) disrupts the plasma flow in the accretion disk at the magnetospheric radius, and the ionized gas is funneled along the magnetic field lines to the magnetic poles of the neutron star, possibly forming accretion columns above the poles. The polar caps are heated by the infalling material, and the kinetic energy is converted into X-ray emission, which appears to be pulsating due to the rotation of the neutron star. The position of the magnetospheric radius can be estimated as the distance from the neutron star where the magnetic pressure becomes equal to the ram pressure, and it is usually quite far from the star, $r_m \sim 10^9$ cm $\sim 1,000 R_*$ [125, 185]. The observational appearance of X-ray pulsars can vary because of several factors, including the nature of the donor star and the parameters of the binary system, but also the geometry and physical conditions of the emission region.

The spectra of accretion-powered X-ray pulsars are usually well fitted by a power law component in the 5-20 keV range, plus a blackbody component at a temperature of about $10^6 - 10^7$ K and a quasi-exponential cut-off at about $20 - 30$ keV [e.g. 46, 242]. Also, close to the cyclotron region, resonant scattering of photons off electrons can generate absorption-like features, like cyclotron resonance scattering features or simply cyclotron lines. The cyclotron absorption features and the pulse shape in the X-rays are both dramatically affected by the geometrical configuration of the emission region, which in turn can depend on the accretion rate. A major change can happen close to the Eddington luminosity:

$$L_{\mathrm{Edd}} = \frac{4\pi GM_* c}{\kappa} = 1.26 \times 10^{28} \left(\frac{\kappa_{\mathrm{T}}}{\kappa}\right) \left(\frac{M_*}{M_\odot}\right) \mathrm{erg\,s^{-1}} \tag{1.2}$$

where c is the speed of light, κ is the opacity and κ_T is the opacity due to Thomson scattering. If the accretion rate is high, so is the X-ray luminosity (see eq.1.1), and when the luminosity approaches the Eddington luminosity, the pressure from the outgoing radiation becomes important in stopping the infalling gas. As first proposed by [15], at low luminosity, the gas can freefall all the way to the neutron star surface, and the kinetic energy of the accretion flow is only released upon the impact with the neutron star surface, where the ionized gas is stopped mainly by nucleon-nucleon collisions. The heat is released deeply in the atmosphere. generating hot-spots at the magnetic poles. The opacity of a strongly magnetized plasma is lower along the field lines, and therefore the Comptonized X-rays escape predominantly upwards, and form a so-called "pencil-beam" pattern. As the luminosity increases, the stopping power of radiation becomes more important and if the luminosity is higher than the critical luminosity $L_c \sim 4 \times 10^{36}$ erg s^{-1} $\sim 0.03\,L_{\rm Edd}$ [16, 21, 161], a radiation dominated shock rises above the neutron star surface, forming an extended accretion column [16, 20, 34]. In this case, photons can only escape through the walls of the column, and a "fan" emission pattern is expected. The higher the accretion rate, the higher the luminosity, and consequently the accretion column, until an asymptotic luminosity is reached, that depends strongly on the accretion geometry [16]. For a solid axisymmetric column it corresponds to a quarter of the Eddington luminosity, but it can exceed the Eddington luminosity by several times in the case of a hollow accretion column in which the material is confined to a narrow wall of magnetic funnel.

The emission from X-ray pulsars is hard to model, because the picture is complicated by the presence of a strong magnetic field, by the importance of radiation pressure in the description of the accretion flow and by the fact that the emitting gas is flowing with a high bulk velocity, up to half of the speed of light. Several attempts have been made to calculate the spectral formation based on theoretical models [112, 149, 150, 162, 246] but the results do not agree very well with the observed profiles. On the other hand, the procedure of fitting the spectra with multicomponent functions of energy as power laws, blackbodies and exponential cut-offs is not easy to relate to physical properties of the source.

The situation improved with the development by Becker and Wolff of a new model for the spectral formation that includes the effect of "thermal" and "bulk"

Comptonization of the photons by the converging flow of electrons [18–20, 244]. This new model, which I will introduce in detail in Chapter 7, predicts a spectrum that fits very well the observed profiles and returns estimates of the properties of the accretion flow, as for example the optical thickness of the column, the temperature of the electrons and the size of the column itself. Even though several simplifying assumptions are made to make the treatment analytic, the Becker and Wolff model is the current theoretical model that best fits observations, and it is the basis of my treatment of the polarized emission from X-ray pulsars (Chapter 7).

1.1.3 Neutron stars in the X-rays: Magnetars

The history of magnetars is more recent, as the first detection of "Unusual γ-ray bursts [...] from a flaring X-ray pulsar in the constellation Dorado" dates to 1979, by the space probes Venera 11 and 12 [137, 138]. These bursts were initially thought to be of the same origin as gamma-ray bursts [139], but their spectra were softer and, contrary to gamma-ray bursts, they were observed to repeat. The identification with a neutron star was immediate thanks to the 8-second pulsation seen in the tail of the burst [138] and to the association with the supernova remnant N49 [45]. The period of 8 seconds, however, was much longer compared to previously detected neutron stars as the Crab pulsar (33 ms), and the object was interpreted initially as an accreting neutron star. It was only when a total of three objects showing the same behaviour was found that these neutron stars started to be considered as a separate class, and they were called *Soft Gamma-ray Repeaters*, or SGRs [116, 128].

The first magnetar models were proposed by Duncan and Thompson [56] in 1992, and at about the same time by Paczynski [173]: a strong magnetic field is the cause of both the SGR activity and of the very long periods observed. Given the location of the 8-second period SGR 0526-66 in the center of the supernova remnant N49, a magnetic field of the order of $10^{14} - 10^{15}$ G is required to brake the pulsar from a birth period of milliseconds in the typical lifetime of a supernova remnant (about 10,000 years). Moreover, the high magnetic field, especially if it is even higher in the interior of the star, can function as a reservoir for the energy needed to explain the SGR activity. Thompson and Duncan [226, 227] also demonstrated that the gamma ray bursts can be explained by large-scale reconnection events, and that the decay of the strong magnetic field can power the quiescent emission (see also [92]).

In the meantime, a new class of pulsars was discovered that had persistent soft X-ray emission and long pulsation periods but no sign of a binary companion [58, 78, 84, 101, 204]. These sources, called *Anomalous X-ray Pulsars* or AXPs, were interpreted as very-low-mass X-ray binaries [146, 234]. The first identification of AXPs as SGRs in quiescence was advanced by Thompson and Duncan [227], and it was confirmed less than ten years later when two AXPs exhibited SGR-like bursts [66, 109].

Nowadays, SGRs and AXPs are considered to be the same class of sources: magnetars. Confirmation on the strength of the magnetic field has come from the measurement of the spin down rates of a few magnetars [117, 118], of which both magnitude and sign showed a very good agreement with the predictions from the models. Even if the origin is still debated, absorption features have been detected in magnetar spectra that have been mostly interpreted as proton cyclotron features from a magnetar-strength magnetic field, confirming in many cases the high magnetic field value inferred from spin-down measurements (e.g., 5 keV absorption line from SGR1806-20 [100]; 8.1 keV absorption line from 1RXS J170849-4009104 [187]; 4 keV and 8 keV emission lines from 4U 0142+62 [67]).

I will not present a detailed review of the phenomenology of magnetars, the reader is invited to read the exhaustive review by Kaspi and Beloborodov [107]. However, the main observational characteristics of magnetars can be summarized as [232]:

- long pulsation periods, in the range 2-12 s;
- large spin-down rates: $\dot{P} \sim 10^{-13} - 10^{-11}$ s s^{-1}, which convert to magnetic fields of the order $10^{14} - 10^{15}$ G if interpreted as due to magnetic braking;
- a persistent X-ray luminosity of the order $10^{33} - 10^{36}$ erg s^{-1} in the soft (0.5-10) and in the hard (20-100 keV) X-ray range;
- many exhibit bursting activities, comprising of short bursts of about 0.1-1 s, the most common, with peak luminosity of $\sim 10^{39} - 10^{41}$ erg s^{-1} and thermal

spectra; intermediate bursts of $\sim$ 1-40 s, with peak luminosity of $\sim 10^{41} - 10^{43}$ and also thermal spectra; and the exceptionally rare giant flares, with an energy output of $\sim 10^{44} - 10^{47}$ erg s^{-1}. Giant flares were only detected three times, and all three events started with an initial spike of $\sim 0.1 - 0.2$ s, followed by a long pulsating tail (lasting a few hundred seconds) modulated at the neutron star spin period.

In Chapter 8, I will model the polarized persistent emission of magnetars in quiescence. Spectra of magnetars are best studied in the soft X-rays ($0.3 - 10$ keV), thanks to decades of observations from instruments such as *XMM-Newton, Chandra* and *Swift* [169]. In this range, spectra are well parametrized by an absorbed blackbody component ($kT \sim 0.3 - 0.5$) and a steep power law, with photon index between -2 and -4 (see Fig 8.1). In some sources, good fits of the observed spectra are obtained with a double blackbody as well [79]. These are only phenomenological parametrizations; however, the thermal component is thought to come from the hot surface of the neutron star, while the steep power law is thought to be caused by a combination of atmospheric and magnetospheric effects.

Hard X-ray observations with *INTEGRAL* and *RXTE*, later confirmed by *NuSTAR*, have shown an inversion in the spectrum at about 20 keV in a few persistent sources: a "hard tail" was detected, with a positive slope, that extends to hundreds of keV. This means that a non-thermal process is causing the bulk of the magnetar's emission. The origin of this hard emission is still debated, and proposed mechanisms range from thermal bremsstrahlung in the surface layers of the star, heated by a downward beam of charges, to synchrotron emission from pairs created in the magnetosphere [224], to resonant Compton scattering (RCS) of seed photons on a population of highly relativistic electrons [13].

1.2 Black holes

The definition of a black hole is quite simple: a black hole is an object so compact that not even light can escape from it. The fact that light is trapped in a black hole, causally separates the region where the black hole lives from the rest of the universe: there is no possible communication between the two regions of spacetime. The boundary of the isolated region of spacetime is called event horizon.

Shortly after the Newtonian theory of gravity was developed, in the 17th century, John Michell and Pierre-Simon Laplace discussed the possibility of an object so compact that not even light, that at that time was thought to be particle-like and with a characteristic velocity, could escape from it [11]. The first formal solution for a black hole in full general relativity was developed only a year after Einstein proposed the theory in 1915, by Karl Schwarzschild in 1916 [57, 201]. The first rigorous calculation for the formation of a black hole from gravitational collapse was performed by Oppenheimer and Snyder [170] in 1939, but the full understanding of the crucial properties of a black hole did not come until later. For example, the first to realize the existence of an event horizon was David Finkelstein [63] in 1958.

The first suggestion of a connection between black holes and astrophysical objects was advanced by Zeldovich and by Salpeter in 1964 [196, 252], who separately proposed the idea that supermassive black holes are the engines of quasars. The first strong observational evidence for the existence of black holes only came in the next decade, thanks to X-ray and optical observations of the X-ray binary Cygnus X-1 in 1972, [32, 238]. Today, more than 20 binary systems containing a stellar-mass black hole have been found [141, 190], together with tens of supermassive black holes at the center of galaxies [114]. In addition, starting from September 2015, the date of the first detection of merging black holes by LIGO [3], the gravitational waves emitted from the coalescence of two black holes have been detected from many systems [164, 222].

Black holes are divided in two main categories: stellar-mass black holes, formed by the collapse of massive stars, that can have masses in the range of $3-100\ \mathrm{M}_{\odot}$, and supermassive black holes, found at the center of galaxies, with a wide range of masses, between 10^5 and 10^{10} solar masses. The existence of a third class with masses in between, called intermediate-mass black holes, is still debated. The focus of my work is on accreting stellar-mass black holes in X-ray binaries, but most of my results can be extended to supermassive black holes in active galactic nuclei (or AGNs), as they are independent of the black hole mass (see Chapter 6).

1.2.1 The Kerr black hole

One of the most subtle consequences of general relativity is the *no-hair* theorem, for which black holes can be fully characterized by a small number of parameters (they have no "hair") [159]. In known black-hole solutions of the Einstein equations, such parameters are mass, angular momentum and charge. Since we expect no charge on astrophysical black holes, the spacetime that surrounds a black hole can be nearly exactly described just by two parameters: mass (M) and angular momentum (J), and the solution to the Einstein's equation is called the Kerr metric, found in 1963 by Roy Kerr [110]. The Schwarzschild metric is the special case with $J = 0$.

The specific angular momentum or spin of the black hole is identified by the parameter $a = J/cM$, where c is the speed of light. It is often convenient to express the spin value in terms of a dimensionless spin parameter, $a_\star = a/R_g$, where $R_g = GM/c^2$ is the gravitational radius. The value of $a_\star$ lies between 0 for a Schwarzschild hole and 1 for a Kerr hole rotating at critical velocity. While the mass gives the scale of the system, the spin parameters modify the geometry of the spacetime. In general relativity, the choice of the coordinate system is arbitrary. In the case of a Kerr black hole, the Boyer-Lindquist coordinate system is a convenient choice. In natural units ($G = c = 1$), the spacetime interval in the Kerr metric is expressed in the form:

$$\begin{aligned} ds^2 &= g_{tt}\mathrm{d}t^2 + 2g_{t\phi}\mathrm{d}t\mathrm{d}\phi + g_{rr}\mathrm{d}r^2 + g_{\theta\theta}\mathrm{d}\theta^2 + g_{\phi\phi}\mathrm{d}\phi^2 \\ &= -\left(1 - \frac{2Mr}{\Sigma}\right)\mathrm{d}t^2 - \frac{4aMr\sin^2\theta}{\Sigma}\mathrm{d}t\mathrm{d}\phi + \frac{\Sigma}{\Delta}\mathrm{d}r^2 + \Sigma\mathrm{d}\theta^2 \\ &\quad + \left(r^2 + a^2 + \frac{2Mra^2\sin^2\theta}{\Sigma}\right)\sin^2\theta\mathrm{d}\phi^2 \end{aligned} \tag{1.3}$$

where

$$\Sigma \equiv r^2 + a^2\cos^2\theta \tag{1.4}$$

$$\Delta \equiv r^2 + a^2 - 2Mr \tag{1.5}$$

The metric is stationary (independent of t) and axi-symmetric about the polar axis (independent of ϕ). In this coordinate system, the radial coordinate of the event horizon is given by $\Delta = 0$

$$R_H = R_g \left(1 + \sqrt{1 - a_\star^2}\right) \tag{1.6}$$

and it ranges from $2R_g$ for a Schwarzschild hole, to R_g for a hole rotating at critical velocity ($a_\star = \pm 1$).

It is useful to consider a stationary observer, which is an observer at fixed coordinates r and θ, but that is rotating at a constant angular velocity

$$\Omega = \frac{\mathrm{d}\phi}{\mathrm{d}t} = \frac{u^\phi}{u^t} \tag{1.7}$$

where u is the four-velocity of the observer. Since the observer has to follow a time-like worldline, the following condition applies

$$-1 = g_{\mu\nu} u^\mu u^\nu = (u^t)^2 [g_{tt} + 2\Omega g_{t\phi} + \Omega^2 g_{\phi\phi}]\,. \tag{1.8}$$

Imposing the quantity in the square brackets to be negative returns the condition

$$\Omega_- < \Omega < \Omega_+ \tag{1.9}$$

where

$$\Omega_\pm = \frac{-g_{t\phi} \pm \sqrt{g_{t\phi}^2 - g_{tt} g_{\phi\phi}}}{g_{\phi\phi}}\,. \tag{1.10}$$

Ω_- vanishes when $g_{tt} = 0$; this occurs at

$$R_0 = R_g \left(1 + \sqrt{1 - a_\star^2 \cos^2\theta}\right)\,. \tag{1.11}$$

This means that observers between R_H and R_0 cannot be static, and they must orbit the black hole with $\Omega > 0$. The surface $r = R_0(\theta)$ is called the boundary of the *ergosphere*.

It is insightful to look at the geodesics in the equatorial plane. By symmetry, a geodesic that starts tangent to the equatorial plane will remain in the equatorial plane. At $\theta = \pi/2$, the Lagrangian is given by [206]

$$2\mathscr{L} = -\left(1 - \frac{2M}{r}\right)\dot{t}^2 - \frac{4aM}{r}\dot{t}\dot{\phi} + \frac{r^2}{\Delta}\dot{r}^2 + \left(r^2 + a^2 + \frac{2Mra^2}{r}\right)\dot{\phi}^2. \qquad (1.12)$$

From it, we can obtain two integrals of motion

$$p_t \equiv \frac{\partial \mathscr{L}}{\partial \dot{t}} = -E \qquad (1.13)$$

$$p_\phi \equiv \frac{\partial \mathscr{L}}{\partial \dot{\phi}} = L. \qquad (1.14)$$

A third integral of motion can be obtained by setting $g_{\mu\nu}p^\mu p^\nu = -m^2$, which is the same as imposing $\mathscr{L} = -m^2/2$. After some algebra, one can obtain

$$\begin{aligned} r^3\dot{r}^2 &= V(E,L,r) \\ &= E^2(r^3 + a^2 r + 2Ma^2) - 4aMEL - (e - 2M)L^2 - m^2 r \end{aligned} \qquad (1.15)$$

where V can be regarded as the effective potential for radial motion in the equatorial plane. Circular orbits correspond to geodesics with $\dot{r} = 0$; which requires $V = 0$ and $\partial V/\partial r = 0$. This yields

$$E_{\rm circ} = \frac{r^2 - 2Mr \pm a\sqrt{Mr}}{r(r^2 - 3Mr \pm 2a\sqrt{Mr})^{1/2}} \qquad (1.16)$$

$$L_{\rm circ} = \frac{\sqrt{Mr}(r^2 \mp 2a\sqrt{Mr} + a^2)}{r(r^2 - 3Mr \pm 2a\sqrt{Mr})^{1/2}} \qquad (1.17)$$

where the upper sign refers to corotating or prograde orbits, i.e. orbits with angular momentum parallel to the black hole spin, while the lower sign corresponds to counterrotating or retrograde orbits. Circular orbits exist for all radii greater than the limiting orbit, when the denominator is equal to zero, which is the photon circular orbit:

$$R_{\rm ph} = 2R_g\left\{1 + \cos\left[\frac{2}{3}\cos^{-1}(\mp a_\star)\right]\right\}. \qquad (1.18)$$

At this radii, photons with zero angular momentum orbit the black hole in a circular orbit. For a Schwarzschild black hole, $a_\star = 0$, the photons can orbit the hole in either direction and the circular orbit is at $R_{\rm ph} = 3R_g$, while for a Kerr black hole the prograde and retrograde orbits are at different radii: for $a_\star = 1$, $r_{\rm ph} = R_g$ for prograde and $R_{\rm ph} = 4R_g$ for retrograde orbits.

If we consider the motion of a test-particle around a massive body in Newtonian gravity, equatorial circular orbits are always stable. In the case of the Kerr metric, for $r > R_{\rm ph}$, circular orbits exist, but not all orbits are stable. Orbits with $E/m > 1$ are unbound, which means that, given an infinitesimal outward perturbation, a particle in such an orbit would escape. Moreover, even if a circular orbit is bound, it can still be unstable. Stability requires $\partial^2 V/\partial^2 r \leq 0$. The limiting case ($\partial^2 V/\partial^2 r = 0$), yields the radius for the *Innermost Stable Circular Orbit* or ISCO:

$$\begin{aligned} r_I &= R_g\{3 + Z_2 - [(3 - Z_1)(3 + Z_1 + 2Z_2)]^{1/2}\} \qquad (1.19) \\ Z_1 &\equiv 1 + (1 - a_\star^2)^{1/3}[(1 + a_\star)^{1/3} + (1 - a_\star)^{1/3}] \\ Z_2 &\equiv (3a_\star^2 + Z_1^2)^{1/2} \end{aligned}$$

For $a_\star = 0$, $r_I = 6R_g$, while for $a_\star = 1$, $r_I = R_g$ for prograde orbits and $R_I = 9R_g$ for retrograde orbits.

1.2.2 The accretion disk

As light cannot escape from a black hole, when a black hole is detected in the X-rays the observed light is usually coming from an accretion disk. Accretion disks in black-hole binaries are formed because the gas transferred from the stellar companion has to lose its angular momentum before it can accrete onto the black hole. In the case of supermassive black holes, the accretion disk material comes from the surrounding interstellar medium. Depending on their origin, accretion disks can have different characteristic and properties. An accretion disk is considered *geometrically thin (thick)* if its semi-thickness h at a distance r from the black hole is much less than r (is about r). The disk is considered *optically thin (thick)* if $h \ll \lambda$ ($h \gg \lambda$), where λ is the photon mean free path in the disk.

In Chapter 6 I will employ the accretion disk model of Novikov and Thorne [168, N&T]. The N&T accretion disk model is the general relativistic generalization of the Shakura-Sunyaev model [205], set in the Kerr spacetime. It assumes a geometrically thin, optically thick disk, radiation dominated, where the motion of the gas is determined by the gravitational field of the black hole (the impact of the gas pressure is ignored). Also, the direction of the angular momentum of the disk is assumed to be aligned with the spin of the hole.

1.2.3 Black holes in the X-rays

X-ray binaries are grouped in two classes depending on the mass of the companion star: low-mass X-ray binaries (LMXB), where the donor star has a mass $\lesssim 3$ $M_\odot$, and high-mass X-ray binaries, with companion masses $\gtrsim 10$ $M_\odot$. In HMXB containing a black hole, like Cygnus X-1, accretion is typically due to the strong winds from the companion star, which is a continuous process, and the sources are usually persistent in the X-rays. LMXB, on the other hand, are usually transient sources, with the notable exception of GRS 1915+105, which has been continuously bright since 1992. The peculiarity of GRS 1915+105 is in the very large accretion disk, which does not easily get depleted.

In black-hole X-ray binaries and AGNs, accretion to the central black hole takes place via a geometrically thin, optically thick accretion disk. The spectral shape of the disk emission can be well fitted by a multi-temperature blackbody, where the temperature at each radius depends on the accretion rate and the black hole mass. The peak temperature is reached close to the ISCO and it is in the soft X-rays (0.1–1 kev) for black hole binaries and in the optical and UV bands (1–10 eV) for AGNs [168, 205]. The photons emitted by the disk are thought to be Compton up-scattered in an optically thin corona, which produces a power-law spectrum in the hard X-rays [217, 229]. The geometry of the corona is still unknown, but it is believed to be a quite compact cloud of optically thin plasma laying above and below the central object. Some of the up-scattered photons in the corona are reflected back into the line of sight by the disk. This reflection emission presents particular features, that include an iron Kα fluorescence line at 6.4 keV and a reflection hump that peaks at $\sim$30 keV, formed via inelastic scattering from free electrons [65, 193].

The same black-hole binary can be found in different spectral states, which are thought to be related to different accretion rates. For a detailed description the reader is directed to the reviews by McClintock and Remillard [141], Remillard and McClintock [190]. The different spectral components become more or less predominant depending on the state of the source. In the soft state, the X-ray luminosity is high and the thermal component from the disk is the predominant emission. In Chapter 6, I will estimate the polarization degree of the emission from the disk, and therefore I will focus on the soft state.

1.2.4 The role of the magnetic field

Accretion disks have to transfer angular momentum outward in order for matter to radially fall inward toward the central object. Black-hole accretion disks, as most astrophysical accretion disks, are rarefied, and angular momentum transfer due to molecular viscosity is inefficient and cannot lead to accretion [184]. Conventional accretion disk models invoke viscous and magnetic torques to transport angular momentum outwards in the disc [8, 9, 83, 205]. In § 6.2 I will calculate the minimum magnetic field strength needed for accretion to occur in the α-model [168, 205], which assumes the magnetic field and the turbulence in the flow to be the source of shear stresses. Another possible mechanism for angular momentum transfer is given by winds: angular momentum flows along open magnetic field lines that leave from the accretion disk surface, and it is eventually expelled in a outgoing wind [30].

Information on the strength and structure of magnetic fields around black holes is hard to obtain by direct observations. From the analysis of the spectra of two Galactic stellar-mass black holes, Miller et al. [154, 155, 157] showed that a wind is generated from the disk as close as 850 GM/c^2 to the hole. In the paper, Miller and his collaborators obtained an estimate of the strength of the magnetic field when different magnetic process are assumed to be driving the wind [157]. The only indication that we have on the magnetic field structure closer to the central engine comes from interferometry observations of the radio polarization from Sagittarius A*, the supermassive black hole at the center of the Milky Way, which shows evidence for a partially ordered magnetic field on scales of 12 GM/c^2 [105]. In Chapter 6, I describe how X-ray polarization measurements from black-hole accretion disks could provide a way to probe, for the first time, the strength and structure of the magnetic field close to the event horizon.

1.3 This Thesis

The main goal of this thesis is to study the polarization of light in the X-rays for accreting black holes, X-ray pulsars and magnetars, starting from realistic physical models and including the effects of vacuum birefringence and general relativity. In Chapter 2, I introduce the concept of polarization, how it is described in the Stokes parameters formalism, and how it can change because of scattering or when light propagates in a birefringent medium. In Chapter 3, I focus on neutron stars and black holes and describe how polarized radiation is generated in black-hole accretion disks and neutron star atmospheres. In Chapter 4, I start from the Lagrangian of quantum electrodynamics to derive from first principles the prediction of vacuum birefringence. In Chapter 5, I describe how birefringence, both in plasma and in the vacuum, can affect the polarization of neutron stars. In Chapter 6, I derive the polarization signal of black-hole accretion disks in Kerr metric and including the QED effect of vacuum birefringence. In Chapter 7, I calculate the polarization signal of bright X-ray pulsars, including general relativity and QED, for existing models and I present my new model, based on a physically realistic accretion scheme. In Chapter 8, I employ realistic atmosphere models for the thermal emission of magnetars and different models for the non-thermal emission and I calculate the polarization signal in the context of the different models. Finally, Chapter 9 summarizes my results and reinterprets them in the context of upcoming polarimetry missions.

Chapter 2

Polarized Radiation and Its Propagation

The polarization of light indicates the direction in which a photon's electric field oscillates. The direction may remain constant, as in the case of linear polarization, or change with time, as for circular or elliptical polarization. In this latter case, the direction of the oscillating field draws a circle (or an ellipse) in the plane perpendicular to the propagation direction of the photon.

In order for radiation to be polarized at emission, the emitting medium has to have some sort of anisotropy: the electric field of the photons must have a preferred axis of oscillation. In Chapter 3 I will show that the presence of a strong magnetic field in neutron stars has the role of breaking the symmetry of the atmosphere and determining the preferred axis, and it is at the origin of the polarized emission from the compact objects. But even when radiation is unpolarized at emission, polarization can be built through the scattering of photons off charged particles, as I will show in the following sections. This effect is enhanced if in the scattering medium a strong magnetic field is present, as I will show in § 2.2.1.

Usually, as light travels without being scattered or absorbed, its polarization parameters remain unchanged. However, if light travels through a birefringent medium, in which the index of refraction depends on the polarization direction (and I will show in Chapter 4 that even vacuum can be birefringent), the anisotropy of the medium will affect the polarization of light and change its direction. In § 2.3

I will introduce a formalism to describe the change in polarization as light traverses a birefringent medium.

2.1 Polarization of light and the Stokes parameters

By superposing two plane waves with orthogonal polarization directions, one can describe the most general state of polarization of a wave. We can focus on the electric field only, as the magnetic field will follow at 90°. The generic expression for a monochromatic, linearly polarized wave can be written as

$$\boldsymbol{E} = \boldsymbol{E_0} e^{i(\boldsymbol{k}\cdot\boldsymbol{r} - \omega t)} \tag{2.1}$$

where $\boldsymbol{E_0}$ is a real vector and its direction determines the direction of polarization. I now take $\boldsymbol{k}$ to be in the $\hat{z}$ direction and focus on an arbitrary point in space, let us say $\boldsymbol{r} = 0$. A wave with a generic polarization state can be written as (see Chapter 15 of [42] or Chapter 2 of [195])

$$\boldsymbol{E} = \boldsymbol{E_0} e^{-i\omega t} = (E_1 \hat{\boldsymbol{x}} + E_2 \hat{\boldsymbol{y}}) e^{-i\omega t} \tag{2.2}$$

where now $\boldsymbol{E_0}$ is a complex vector with components

$$E_1 = \mathscr{E}_1 e^{i\phi_1}, \quad E_2 = \mathscr{E}_2 e^{i\phi_2} \tag{2.3}$$

For fully polarized light, the Jones calculus can be used to describe the polarization state of the wave. In theJones calculus, the polarization state is described by a two-component vector, the Jones vector, and, in the case of Cartesian coordinates, the two components correspond to E_1 and E_2, the x and y complex amplitudes of the electric field, while the effects of an optically active material on the polarization state are expressed by 2×2 matrices. The advantage of Jones calculus is that it includes a description of the absolute phase of the wave. However, it assumes the light to be fully polarized, and therefore cannot be used to represent scattering or partially polarized beams. I will now introduce the Stokes parameter formalism and the Mueller calculus, which is the formalism I will employ in this work. The Mueller calculus does not keep track of the phase of the wave as it considers only the time-averaged intensity of light, and it can describe partially-polarized radiation.

Taking the real part of eq. 2.2, I can write the physical components of the electric field:

$$E_x = \mathscr{E}_1 \cos(\omega t - \phi_1), \quad E_y = \mathscr{E}_2 \cos(\omega t - \phi_2) \tag{2.4}$$

These equations describe the movement of the tip of the electric field in the $x-y$ plane and they trace an ellipse: a generic polarization state is an elliptical polarization state. If the ellipse's axes are parallel to the coordinate axes, the x and y components can be written as

$$E_x = \mathscr{E}_0 \cos\beta \cos\omega t, \quad E_y = -\mathscr{E}_0 \sin\beta \sin\omega t \tag{2.5}$$

where $-\pi/2 < \beta < \pi/2$. For $\beta > 0$ the ellipse is traced clockwise and the polarization state is called right-handed, while for $\beta < 0$ the ellipse is traced in a counterclockwise sense and the polarization state is called left-handed. For $\beta = \pm\pi/4$ we find the special case of circular polarization, while for $\beta = 0$ or $\beta = \pm\pi/2$ the wave is linearly polarized.

In the general case in which the ellipse's axes are rotated with respect to the coordinate axes of an arbitrary angle χ, eq. 2.5 becomes:

$$E_x = \mathscr{E}_0(\cos\beta \cos\chi \cos\omega t + \sin\beta \sin\chi \sin\omega t) \tag{2.6a}$$

$$E_y = \mathscr{E}_0(\cos\beta \sin\chi \cos\omega t - \sin\beta \cos\chi \sin\omega t) \tag{2.6b}$$

This generic expression is equal to the expression in eq. 2.4 if we take

$$\mathscr{E}_1 \cos\phi_1 = \mathscr{E}_0 \cos\beta \cos\chi, \tag{2.7a}$$

$$\mathscr{E}_1 \sin\phi_1 = \mathscr{E}_0 \sin\beta \sin\chi, \tag{2.7b}$$

$$\mathscr{E}_2 \cos\phi_2 = \mathscr{E}_0 \cos\beta \sin\chi, \tag{2.7c}$$

$$\mathscr{E}_2 \sin\phi_2 = -\mathscr{E}_0 \sin\beta \cos\chi, \tag{2.7d}$$

The state of polarization can always be described by the quantities $\mathscr{E}_0$, β and χ. An alternative set of parameters that is often used to describe the polarization state is given by the Stokes parameters:

$$I = \mathscr{E}_1^2 + \mathscr{E}_2^2 = \mathscr{E}_0^2 \tag{2.8a}$$

$$Q = \mathscr{E}_1^2 - \mathscr{E}_2^2 = \mathscr{E}_0^2 \cos 2\beta \cos 2\chi \tag{2.8b}$$

$$U = 2\mathscr{E}_1\mathscr{E}_2 \cos(\phi_1 - \phi_2) = \mathscr{E}_0^2 \cos 2\beta \sin 2\chi \tag{2.8c}$$

$$V = 2\mathscr{E}_1\mathscr{E}_2 \sin(\phi_1 - \phi_2) = \mathscr{E}_0^2 \sin 2\beta \tag{2.8d}$$

Since the polarization state can be derived from three parameters, the Stokes parameters are not independent and they are bound by the relation

$$I^2 = Q^2 + U^2 + V^2. \tag{2.9}$$

The Stokes parameters are useful because they relate to physical properties of radiation: I is proportional to the intensity of the ray, and the constant of proportionality is usually set equal to 1, as done in eq.s 2.8; V measures the ratio of the principal axes of the polarization ellipse and therefore gives a measure of the "circularity" of the wave ($V = 0$ means linearly polarized light); Q or U is the remaining independent parameter and it measures the orientation of the ellipse relative to the x-axis ($Q = I$ means vertical linear polarization and $Q = -I$ means horizontal linear polarization, while $U = I$ means polarized light at 45° with respect to the vertical).

Until now, I have treated light that is 100% polarized, which means that the polarization state of all photons in the beam adds up to a certain polarization state. However, the polarization state of a beam can be varying stochastically with time, or the polarization states of the photons can cancel each other when summing over the beam, and in this case light is said to be unpolarized. For unpolarized light $Q = U = V = 0$. In general, a light beam can be partially polarized, and it can be regarded as the superposition of a beam of polarized light and a beam of unpolarized light (see § 15.2 and § 15.3 of [42]). In this case:

$$I^2 \geq Q^2 + U^2 + V^2 \tag{2.10}$$

and the total degree of polarization is given by

$$\Pi = \frac{\sqrt{Q^2+U^2+V^2}}{I} \leq 1. \tag{2.11}$$

Other useful quantities are the linear degree of polarization or linear polarization fraction

$$\Pi_l = \frac{\sqrt{Q^2+U^2}}{I} \tag{2.12}$$

and the circular degree of polarization or circular polarization fraction

$$\Pi_c = \frac{|V|}{I}. \tag{2.13}$$

In Mueller calculus, the polarization state of a beam is described by a 4-dimensional vector, $\boldsymbol{S} = (I, Q, U, V)$, where the 4 components are the 4 Stokes parameters, and the effect of the element of an optical system on the polarization state of a beam is described by the Mueller matrix:

$$\boldsymbol{S}' = \boldsymbol{M}\boldsymbol{S} \tag{2.14}$$

where $\boldsymbol{M}$, the Mueller matrix, is a 4×4 matrix.

2.1.1 The Poincaré sphere

The Poincaré sphere is a useful graphical tool to depict the polarization state of a beam of light. The radius of the sphere is usually set equal to 1 or to the intensity of the polarized fraction ($\sqrt{Q^2+U^2+V^2}$). If we consider the case of the unit sphere, the polarization vector is defined as

$$\boldsymbol{s} = \frac{1}{S_0}\begin{pmatrix} S_1 \\ S_2 \\ S_3 \end{pmatrix}, \quad \text{where} \quad (\mathrm{S_0, S_1, S_2, S_3}) = (\mathrm{I, Q, U, V}) \tag{2.15}$$

The polarization states of fully polarized radiation are mapped onto the surface of the sphere. Linearly polarized states are positioned on the equator of the sphere, while purely circularly polarized states correspond to the north (right-handed) and

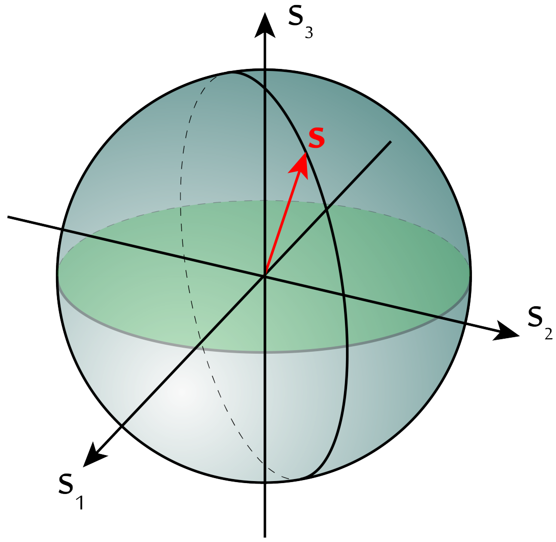

Figure 2.1: The Poincaré sphere. Polarization states are mapped onto the surface of the sphere, identified by the vector $\boldsymbol{s}$. Linearly polarized states are positioned on the equator of the sphere (in green). Circularly polarized states correspond to the north (right-handed) and south (left-handed) poles of the sphere.

south (left-handed) poles of the sphere. On the equatorial plane, the s_1 axis spans the states from vertically to horizontally polarized light, while s_2 represents $\pm 45°$ polarized light. Any point between the equatorial plane and the poles represents an elliptical polarization state.

Only fully polarized light is represented at the surface of the sphere, while partially polarized light will be located at a radius equal to its polarization degree (eq. 2.11), with completely unpolarized light being mapped to the origin of the sphere.

2.2 Thomson Scattering

Thomson scattering is the process of photons scattering off free electrons. The electron oscillates in response to the incoming electromagnetic wave and re-emits a photon in a new direction. I will first address the case of linearly polarized incoming radiation in a non-magnetized medium and I will extend the results to unpolarized light. I will describe the case of scattering in a strongly magnetized medium in § 2.2.1.

If the charge oscillates at velocities that are not relativistic, the magnetic field of the photon can be ignored and the force acting on the electron is just the Lorentz force

$$\boldsymbol{F} = m_e \ddot{\boldsymbol{r}} = e\boldsymbol{\varepsilon} E \sin \omega t \tag{2.16}$$

where $\boldsymbol{\varepsilon}$ is the polarization vector and ω is the frequency of the incoming radiation. If I indicate with $\boldsymbol{d} = e\boldsymbol{r}$ the dipole moment of the electron, I can write

$$\ddot{\boldsymbol{d}} = \frac{e^2 E}{m_e} \boldsymbol{\varepsilon} \sin \omega t \tag{2.17}$$

Using the Larmor's Formula, I can obtain the time-averaged power of the emitted radiation as [195]

$$\frac{\mathrm{d}P}{\mathrm{d}\Omega} = \frac{\sin^2 \Theta}{4\pi c^3} \langle \ddot{d} \rangle^2 = \frac{e^4 E^2}{8\pi m_e^2 c^3} \sin^2 \Theta \tag{2.18}$$

$$P = \frac{e^4 E^2}{3 m_e^2 c^3} \tag{2.19}$$

where Θ is the angle between the incident polarization vector $\boldsymbol{\varepsilon}$ and the propagation direction of scattering. I can find the cross section by dividing the power emitted by the incident flux (which is simply $cE^2/8\pi$)

$$\left(\frac{\mathrm{d}\sigma}{\mathrm{d}\Omega}\right)_{\text{polarized}} = \frac{e^4}{m_e^2 c^4} \sin^2 \Theta = r_e^2 \sin^2 \Theta \tag{2.20}$$

$$\sigma_T = \frac{8\pi e^4}{3 m_e^2 c^4} = \frac{8\pi}{3} r_0^2 \tag{2.21}$$

where r_e is the classical radius of the electron, and σ_T is the Thomson cross section. The scattered radiation remains linearly polarized in the plane of the incident polarization $\boldsymbol{\varepsilon}$ and the direction of the outgoing radiation.

I will now consider the incoming radiation as unpolarized. Unpolarized radiation can be described as the independent superposition of two beams of light linearly polarized in orthogonal directions. Without loss of generality, I can choose one beam to be polarized in the same plane as the outgoing radiation direction $\boldsymbol{n}$, with polarization vector $\boldsymbol{\varepsilon}_1$. The angle Θ now indicates the angle between $\boldsymbol{\varepsilon}_1$ and $\boldsymbol{n}$, while the angle between $\boldsymbol{\varepsilon}_2$ (the orthogonal beam's polarization vector) and $\boldsymbol{n}$ is $\pi/2$. The differential cross section for the unpolarized radiation will be the average of the cross sections for scattering of the two beams

$$\begin{aligned}\left(\frac{\mathrm{d}\sigma}{\mathrm{d}\Omega}\right)_{\text{unpol}} &= \frac{1}{2}\left[\left(\frac{\mathrm{d}\sigma}{\mathrm{d}\Omega}(\Theta)\right)_{\text{pol}} + \left(\frac{\mathrm{d}\sigma}{\mathrm{d}\Omega}(\pi/2)\right)_{\text{pol}}\right] \\ &= \frac{1}{2}r_0^2(1+\sin^2\Theta) \\ &= \frac{1}{2}r_0^2(1+\cos^2\theta) \qquad (2.22)\end{aligned}$$

where $\theta = \pi/2 - \Theta$ is the angle between the incident radiation and the scattered one. I can easily derive the degree of polarization of the scattered radiation as the two polarized intensities in the plane and perpendicular to the plane of scattering are in the ratio $\cos^2\theta$:

$$\Pi = \Pi_l = \frac{1-\cos^2\theta}{1+\cos^2\theta} \qquad (2.23)$$

Even when the incident radiation is totally unpolarized, some fraction of the scattered light is linearly polarized in the plane of scattering, and the polarization fraction increases with θ: if we look in the direction of the incident radiation, at $\theta = 0$, as we expect we see no net polarization since, by symmetry, all directions in the plane are equivalent. On the other hand, since the electron motion is confined in the plane perpendicular to the incident wave, if we look in the direction perpendicular to the incident wave we see 100% polarized light.

2.2.1 Thomson scattering in a strong magnetic field

Strong magnetic fields affect the motion of electrons by forcing them to move mainly along the field lines. This tendency strongly alters the interaction between photons and electrons: in Chapter 3 I will show how strong magnetic fields alter opacities in neutron star atmospheres and in Chapter 4 I will describe how plasma and vacuum can become birefringent in the presence of a strong magnetic field.

Thomson scattering is no exception. Following the calculations performed by Chou [44], I will develop a formalism to analyze the change in the Stokes parameters after Thomson scattering in the presence of a strong magnetic field.

In contrast with the previous section, now the presence of a strong magnetic field alters the equation of motion of the electrons

$$m_e \dot{\boldsymbol{v}} = -e\boldsymbol{E}(t) - \frac{e}{c}\boldsymbol{v} \times \boldsymbol{B} \tag{2.24}$$

where

$$\boldsymbol{E}(t) = (E_x \hat{\boldsymbol{x}} + E_y \hat{\boldsymbol{y}} + E_z \hat{\boldsymbol{z}})e^{i\omega t} = (E_\parallel \cos\alpha \hat{\boldsymbol{x}} + E_\perp \hat{\boldsymbol{y}} - E_\parallel \sin\alpha \hat{\boldsymbol{z}})e^{i\omega t} \tag{2.25}$$

is the photon's electric field and $\boldsymbol{B} = B\hat{\boldsymbol{z}}$ is the uniform, static magnetic field. Also, I indicate with α the angle between the incident radiation and the magnetic field, and with $E_\parallel$ the component of $\boldsymbol{E}(t)$ in the plane of $\boldsymbol{B}$ and $\boldsymbol{k}$, the wavevector of the incident wave, and with $E_\perp$ the component perpendicular to the plane.

If I write the induced electron acceleration as $\dot{\boldsymbol{v}}(t) = (\dot{v}_x \hat{\boldsymbol{x}} + \dot{v}_y \hat{\boldsymbol{y}} + \dot{v}_z \hat{\boldsymbol{z}})e^{i\omega t}$, then eq. 2.24 yields

$$\dot{v}_x = \frac{e}{m_e} \frac{\omega^2 E_\parallel \cos\alpha + i\omega\omega_c E_\perp}{\omega_c^2 - \omega^2} \tag{2.26}$$

$$\dot{v}_y = \frac{e}{m_e} \frac{\omega^2 E_\perp - i\omega\omega_c E_\parallel \cos\alpha}{\omega_c^2 - \omega^2} \tag{2.27}$$

$$\dot{v}_z = \frac{e}{m_e} E_\parallel \sin\alpha \tag{2.28}$$

The dipole radiation field emitted by the electron is given by [103]

$$\boldsymbol{E}_e(\boldsymbol{x}, t) = \frac{-e}{Dc^2}[\hat{\boldsymbol{r}} \times (\hat{\boldsymbol{r}} \times \dot{\boldsymbol{v}})] \tag{2.29}$$

where $\hat{\boldsymbol{r}} = \boldsymbol{D}/D$ is the unit vector directed from the position of the electron to the observer, and D is the distance between the emission region and the observer.

It is now convenient to transition to spherical coordinates, where (r, θ, ϕ) indicates the direction of the scattered radiation. The velocity of the electron in this system is given by

$$\dot{v}_r = \dot{v}_x \sin\theta\cos\phi + \dot{v}_y \sin\theta\sin\phi + \dot{v}_z \cos\theta \tag{2.30}$$

$$\dot{v}_\theta = \dot{v}_x \cos\theta\cos\phi + \dot{v}_y \cos\theta\sin\phi - \dot{v}_z \sin\theta \tag{2.31}$$

$$\dot{v}_\phi = -\dot{v}_x \sin\phi + \dot{v}_y \cos\phi \tag{2.32}$$

where $\dot{v}_x$, $\dot{v}_y$ and $\dot{v}_z$ are given in eq. 2.28. Eq. 2.29 therefore yields

$$\begin{aligned}\boldsymbol{E}_e &= E^e_\theta \hat{\boldsymbol{\theta}} + E^e_\phi \hat{\boldsymbol{\phi}} \\ &= \frac{r_e}{D}\{[\zeta\cos\theta(u_1 + ixu_2) - u_3]\hat{\boldsymbol{\theta}} + \zeta(u_2 - ixu_1)\hat{\boldsymbol{\phi}}\}\end{aligned} \tag{2.33}$$

where $r_e = e^2/m_e c^2$ is the classical radius of the electron and

$$x = \frac{\omega_c}{\omega}, \quad \zeta = \frac{1}{x^2 - 1} \tag{2.34}$$

$$u_1 = E_\parallel \cos\alpha\cos\phi + E_\perp \sin\phi\,, \tag{2.35}$$

$$u_2 = -E_\parallel \cos\alpha\sin\phi + E_\perp \cos\phi\,, \tag{2.36}$$

$$u_3 = E_\parallel \sin\alpha\sin\theta \tag{2.37}$$

The Stokes parameters for the incident radiation can be written in terms of the parallel and perpendicular components of the electric field

$$\begin{aligned} I &= S_0 = E_\parallel E^*_\parallel + E_\perp E^*_\perp \\ Q &= S_1 = E_\parallel E^*_\parallel - E_\perp E^*_\perp \\ U &= S_2 = E_\parallel E^*_\perp + E_\perp E^*_\parallel \\ V &= S_3 = i(E_\parallel E^*_\perp - E_\perp E^*_\parallel) \end{aligned} \tag{2.38}$$

while the Stokes parameters of the scattered radiation can be expressed in terms of the emitted electric field components derived in eq. 2.33

$$
\begin{aligned}
I' = S'_0 &= E^e_\theta E^{e*}_\theta + E^e_\phi E^{e*}_\phi \\
Q' = S'_1 &= E^e_\theta E^{e*}_\theta - E^e_\phi E^{e*}_\phi \\
U' = S'_2 &= E^e_\theta E^{e*}_\phi + E^e_\phi E^{e*}_\theta \\
V' = S'_3 &= i(E^e_\theta E^{e*}_\phi - E^e_\phi E^{e*}_\theta)
\end{aligned} \tag{2.39}
$$

From eq.s 2.33, 2.38 and 2.39 we can express (I', Q', U', V') as a function of the incident Stokes parameters (I, Q, U, V), of the direction of the incident radiation with respect to the magnetic field, expressed by the angle α, of the direction of the outgoing radiation, expressed through the polar and azimuthal angles θ and ϕ, of the energy of the photon, encoded in ω, and of the strength of the magnetic field, in ω_c, or more precisely by the ratio of the two, encoded in x. In Mueller calculus, the relations can be written in a matrix form

$$
\begin{pmatrix} I' \\ Q' \\ U' \\ V' \end{pmatrix} = \frac{r_e^2}{2D^2} \begin{pmatrix} M_{11} & M_{12} & 0 & M_{14} \\ M_{21} & M_{22} & 0 & M_{24} \\ 0 & 0 & M_{33} & M_{34} \\ M_{41} & M_{42} & 0 & M_{44} \end{pmatrix} \begin{pmatrix} I \\ Q \\ U \\ V \end{pmatrix} \tag{2.40}
$$

For the full expressions of the matrix elements M_{ij} see [44]. In the cases that I will consider in this work, azimuthal symmetry is always present, and therefore I can average over ϕ, which yields

$$M_{11} = \frac{\zeta^2}{2}(1+x^2)(\cos^2\alpha+1)(\cos^2\theta+1)+\sin^2\alpha\sin^2\theta \tag{2.41a}$$

$$M_{12} = \frac{\zeta^2}{2}(1+x^2)(\cos^2\alpha-1)(\cos^2\theta+1)+\sin^2\alpha\sin^2\theta \tag{2.41b}$$

$$M_{14} = -2\zeta^2 x\cos\alpha(1+\cos^2\theta) \tag{2.41c}$$

$$M_{21} = \frac{\zeta^2}{2}(1+x^2)(\cos^2\alpha+1)(\cos^2\theta-1)+\sin^2\alpha\sin^2\theta \tag{2.41d}$$

$$M_{22} = \frac{\zeta^2}{2}(1+x^2)(\cos^2\alpha-1)(\cos^2\theta-1)+\sin^2\alpha\sin^2\theta \tag{2.41e}$$

$$M_{24} = 2\zeta^2 x\cos\alpha\sin^2\theta \tag{2.41f}$$

$$M_{33} = 0 \tag{2.41g}$$

$$M_{41} = -2\zeta^2 x(1+\cos^2\alpha)\cos\theta \tag{2.41h}$$

$$M_{42} = 2\zeta^2 x\sin^2\alpha\cos\theta \tag{2.41i}$$

$$M_{44} = 2\zeta^2(1+x^2)\cos\alpha\cos\theta \tag{2.41j}$$

After taking the average over ϕ, I find that all the matrix elements that involve U are equal to zero. I can therefore reduce the matrix to a 3×3 matrix where the third element correspond to the circular polarization parameter V:

$$\begin{pmatrix} I' \\ Q' \\ V' \end{pmatrix} = \frac{r_e^2}{2D^2} \begin{pmatrix} M_{11} & M_{12} & M_{13} \\ M_{21} & M_{22} & M_{23} \\ M_{31} & M_{32} & M_{33} \end{pmatrix} \begin{pmatrix} I \\ Q \\ V \end{pmatrix} \tag{2.42}$$

and where $M_{13} = M_{14}$ of eq. 2.41c and so forth.

The angular dependence of the incoming and outgoing radiation can be expanded in a series of orthonormal functions in α and θ. Since the matrix elements are only functions of $\cos\alpha$, $\cos^2\alpha$, $\sin^2\alpha$ and the same for θ, the only important functions for the expansion are given by

$$f_1(\alpha) = \frac{\sqrt{15}}{4} \sin^2 \alpha; \tag{2.43}$$

$$f_2(\alpha) = \frac{\sqrt{6}}{2} \cos \alpha; \tag{2.44}$$

$$f_3(\alpha) = \frac{5\sqrt{3}}{4} \left(\cos^2 \alpha - \frac{1}{5} \right) \tag{2.45}$$

and the same for θ. I can write the Stokes parameter in this new basis:

$$\begin{aligned}
I &= l_1 \times f_1(\alpha) + l_2 \times f_2(\alpha) + l_3 \times f_3(\alpha) \\
Q &= l_4 \times f_1(\alpha) + l_5 \times f_2(\alpha) + l_6 \times f_3(\alpha) \\
V &= l_7 \times f_1(\alpha) + l_8 \times f_2(\alpha) + l_9 \times f_3(\alpha) \\
I' &= l'_1 \times f_1(\theta) + l'_2 \times f_2(\theta) + l'_3 \times f_3(\theta) \\
&\vdots
\end{aligned}$$

and so forth, where l_i do not depend on angles. In this way, I can rewrite the scattering matrix in eq. 2.42 as a 9x9 matrix in this new basis

$$\begin{pmatrix} l'_1 \\ l'_2 \\ \vdots \\ l'_9 \end{pmatrix} = \frac{r_e}{2D^2} \begin{pmatrix} a_{1,1} & a_{1,2} & \cdots & a_{1,9} \\ a_{2,1} & a_{2,2} & \cdots & a_{2,9} \\ \vdots & \vdots & \ddots & \vdots \\ a_{9,1} & a_{9,2} & \cdots & a_{9,9} \end{pmatrix} \begin{pmatrix} l_1 \\ l_2 \\ \vdots \\ l_9 \end{pmatrix} \tag{2.46}$$

where the matrix elements are just functions of x and ζ, and the angle dependence is conveyed by the f functions. In this way, I can efficiently compute the effects of the external magnetic field on the scattered radiation.

I will employ this formalism in Chapter 7 and in Chapter 8 to analyze the effect on the X-ray polarization of Compton scattering in strong magnetic fields. The relation expressed in eq. 2.46 is valid in the instantaneous rest frame of the electrons; if the motion of the electrons is relativistic, I will have to consider beaming effects. Also, I have not considered any energy transfer between the electron and the photon, which I will have to include in the case of Compton scattering.

2.3 Propagation of light through an inhomogeneous and anisotropic medium

In this section I will follow the work of Kubo and Nagata [119], who analyzed the change in the polarization state as light travels through an inhomogeneous and anisotropic medium employing the Stokes parameters formalism. Maxwell's equations in an inhomogeneous medium can be written as

$$\nabla \times \boldsymbol{H} = \frac{1}{c}\frac{\partial \boldsymbol{D}}{\partial t}\,, \qquad \nabla \times \boldsymbol{E} = -\frac{1}{c}\frac{\partial \boldsymbol{H}}{\partial t} \tag{2.47}$$

$$\nabla \cdot \boldsymbol{D} = 0\,, \qquad \nabla \cdot \boldsymbol{B} = 0 \tag{2.48}$$

$$\boldsymbol{D} = [\varepsilon]\boldsymbol{E}\,, \qquad \boldsymbol{B} = \boldsymbol{H} \tag{2.49}$$

where $\boldsymbol{E}$, $\boldsymbol{D}$, $\boldsymbol{B}$, and $\boldsymbol{H}$ are the electric vector, the electric induction, the magnetic induction, and the magnetic vector, respectively. The tensor $[\varepsilon]$ is a non-Hermitian and asymmetrical dielectric tensor with general complex elements, which represents the various types of birefringence and absorption in the medium.

I take the coordinate system to be (x_1, x_2, x_3) and light to be propagating along the x_3 direction. Without loss of generality, the tensor $[\varepsilon]$ can be written as $[\varepsilon] = [\varepsilon']_s + i[\varepsilon']_a + i[\varepsilon'']_s - [\varepsilon'']_a$, where $[\varepsilon']_s$ and $[\varepsilon'']_s$ are symmetric real tensors and $[\varepsilon']_a$ and $[\varepsilon'']_a$ are antisymmetric real tensors. The tensor $[\varepsilon]$ with respect to propagation in the direction of the x_3 axis can be written as the two-dimensional tensor

$$[\bar{\varepsilon}] = \begin{bmatrix} \varepsilon_{11} & \varepsilon_{12} \\ \varepsilon_{21} & \varepsilon_{22} \end{bmatrix} \tag{2.50}$$

$$= \begin{bmatrix} \varepsilon_{11}^{\prime s} + i\varepsilon_{11}^{\prime\prime s} & \varepsilon_{12}^{\prime s} + i\varepsilon_{12}^{\prime a} + i\varepsilon_{12}^{\prime\prime s} - \varepsilon_{12}^{\prime\prime a} \\ \varepsilon_{21}^{\prime s} + i\varepsilon_{21}^{\prime a} + i\varepsilon_{21}^{\prime\prime s} - \varepsilon_{21}^{\prime\prime a} & \varepsilon_{22}^{\prime s} + i\varepsilon_{22}^{\prime\prime s} \end{bmatrix} \tag{2.51}$$

I can obtain the $\boldsymbol{E}$ vector equation from eq.s 2.47 and 2.49:

$$\frac{1}{c^2}\frac{\partial^2[\varepsilon]\boldsymbol{E}}{\partial^2 t} = -\nabla \times \nabla \times \boldsymbol{E}\,, \tag{2.52}$$

and I can express the waves propagating in the x_3 direction as

$$E_j = G_j \exp[i(k_0\Phi - \omega t)], \tag{2.53}$$

$$\Phi = \int \left[\frac{1}{2}(\varepsilon'^{s}_{11} + \varepsilon'^{s}_{22})\right]^{1/2} \mathrm{d}x_3 \tag{2.54}$$

where E_j are the components of the electric field, G_j are the complex electric field amplitudes of E_j (without the rapidly varying phase), ω is the frequency of light in vacuum, and $k_0 = \omega/c$.

For a weakly inhomogeneous, anisotropic and optically active medium, eq. 2.52 yields

$$\frac{\partial}{\partial x_3}\begin{bmatrix} G_1 \\ G_2 \end{bmatrix} = \frac{i}{2}\begin{bmatrix} \Omega_1 + iT_0 + iT_1 & \Omega_2 + i\Omega_3 + iT_2 - T_3 \\ \Omega_2 - i\Omega_3 + iT_2 + T_3 & -\Omega_1 + iT_0 - iT_1 \end{bmatrix}\begin{bmatrix} G_1 \\ G_2 \end{bmatrix} \tag{2.55}$$

where $\Omega_1 = C(\varepsilon'^{s}_{11} - \varepsilon'^{s}_{22})$, $\Omega_2 = 2C\varepsilon'^{s}_{12}$, $\Omega_3 = 2C\varepsilon'^{a}_{12}$, $T_0 = C(\varepsilon''^{s}_{11} + \varepsilon''^{s}_{22})$, $T_2 = 2C\varepsilon''^{s}_{12}$, $T_3 = 2C\varepsilon''^{a}_{12}$ and $C = k_0/(\varepsilon'^{s}_{11} + \varepsilon'^{s}_{22})^{1/2}$.

The expression in eq. 2.55 represents the evolution of the polarization state as described by the Jones formalism, in terms of the complex amplitudes of the electric field. I want now to rewrite the expression in eq. 2.55 in terms of the Stokes parameters and the Mueller calculus. This translation can be performed with the help of Wolf's coherency matrix, $\boldsymbol{J}$. Wolf's matrix is a 2×2 matrix whose components are given by $J_{ij} = E_i^* E_j$, where the E_i are the complex amplitudes of the electric field. The relation between the coherency matrix and the Stokes parameters $(S_0, S_1, S_2, S_3) = (I, Q, U, V)$ is given by [74]

$$\boldsymbol{J} = \frac{1}{2}\sum_{i=0}^{3} \boldsymbol{\sigma}\boldsymbol{S} \tag{2.56}$$

where $\boldsymbol{S} = [S_0, S_1, S_2, S_3]$, $\boldsymbol{\sigma}^t = \{\hat{\sigma}_0, \hat{\sigma}_1, \hat{\sigma}_2, \hat{\sigma}_3\}$, $\boldsymbol{\sigma}^t$ is the transpose of $\boldsymbol{\sigma}$ and

$$\hat{\sigma}_0 = \begin{bmatrix} 1 & 0 \\ 0 & 1 \end{bmatrix},\ \hat{\sigma}_1 = \begin{bmatrix} 1 & 0 \\ 0 & -1 \end{bmatrix},\ \hat{\sigma}_2 = \begin{bmatrix} 0 & 1 \\ 1 & 0 \end{bmatrix},\ \hat{\sigma}_3 = \begin{bmatrix} 0 & i \\ -i & 0 \end{bmatrix} \tag{2.57}$$

In other words, the Stokes parameters are the components of the coherency matrix of the radiation when expanded in the basis of $\{\hat{\sigma}_0, \hat{\sigma}_1, \hat{\sigma}_2, \hat{\sigma}_3\}$, where $\hat{\sigma}_0$ is the unit matrix and $\hat{\sigma}_i$ are the Pauli matrices. Therefore we can write

$$\boldsymbol{S} = \boldsymbol{E}^{\dagger}\boldsymbol{\sigma}\boldsymbol{E} = \boldsymbol{G}^{\dagger}\boldsymbol{\sigma}\boldsymbol{G} \tag{2.58}$$

where $\boldsymbol{E}^{\dagger}$ is the adjoint of $\boldsymbol{E}$. The representation of eq. 2.55 with the matrix $\boldsymbol{\sigma}$ becomes

$$\begin{aligned}\frac{\partial \boldsymbol{G}}{\partial x_3} &= \frac{i}{2}[iT_0\hat{\sigma}_0 + (\Omega_1 + iT_1)\hat{\sigma}_1 + (\Omega_2 + iT_2)\hat{\sigma}_2 + (\Omega_3 + iT_3)\hat{\sigma}_3]\boldsymbol{G} \\ &= \frac{i}{2}(\boldsymbol{\Omega} + i\boldsymbol{T})\boldsymbol{G}\end{aligned} \tag{2.59}$$

where $\boldsymbol{\Omega} = \Omega_1\hat{\sigma}_1 + \Omega_2\hat{\sigma}_2 + \Omega_3\hat{\sigma}_3 = \{0, \Omega_1, \Omega_2, \Omega_3\}$ and $\boldsymbol{T} = T_0\hat{\sigma}_0 T_1\hat{\sigma}_1 + T_2\hat{\sigma}_2 + T_3\hat{\sigma}_3 = \{T_0, T_1, T_2, T_3\}$. From the derivatives of $\boldsymbol{S}$ with respect to x_3 and eq. 2.59, I can derive the change in the Stokes parameters as light travels in the x_3 direction

$$\frac{\partial \boldsymbol{S}}{\partial x_3} = \frac{i}{2}\boldsymbol{G}^{\dagger}[(\boldsymbol{\Omega} + i\boldsymbol{T})^{\dagger}\boldsymbol{\sigma} - \boldsymbol{\sigma}(\boldsymbol{\Omega} + i\boldsymbol{T})]\boldsymbol{G} \tag{2.60}$$

Using the commutation relations $\hat{\sigma}_j\hat{\sigma}_k = \hat{\sigma}_0\delta_{jk} - i\varepsilon_{jkm}\hat{\sigma}_m$ $(j,k = 1,2,3)$ in eq. 2.60, I can derive

$$\frac{\partial \boldsymbol{S}}{\partial x_3} = [\omega]\boldsymbol{S} = \{[\omega]_s + [\omega]_a\}\boldsymbol{S} \tag{2.61}$$

where

$$[\omega]_s = \begin{bmatrix} T_0 & T_1 & T_2 & T_3 \\ T_1 & T_0 & 0 & 0 \\ T_2 & 0 & T_0 & 0 \\ T_3 & 0 & 0 & T_0 \end{bmatrix}, \quad [\omega]_a = \begin{bmatrix} 0 & 0 & 0 & 0 \\ 0 & 0 & -\Omega_3 & \Omega_2 \\ 0 & \Omega_3 & 0 & -\Omega_1 \\ 0 & -\Omega_2 & \Omega_1 & 0 \end{bmatrix} \tag{2.62}$$

and $[\omega]_s$ and $[\omega]_a$ are the symmetric and antisymmetric parts of $[\omega]$ respectively.

Eq. 2.61 can be rewritten in a simple vectorial manner if the normalized Stokes vector is considered $\boldsymbol{s} = (S_1/S_0, S_2/S_0, S_3/S_0)$

$$\frac{\partial \boldsymbol{s}}{\partial x_3} = \hat{\boldsymbol{\Omega}} \times \boldsymbol{s} + (\hat{\boldsymbol{T}} \times \boldsymbol{s}) \times \boldsymbol{s} \tag{2.63}$$

where $\hat{\mathbf{\Omega}} = (\Omega_1, \Omega_2, \Omega_3)$ is the birefringence vector and $\hat{\boldsymbol{T}} = (T_1, T_2, T_3)$ is the dichroic vector. The component T_0 drops out since only the relation among the components S_1, S_2 and S_3 is considered.

In the following chapters, I will not consider any dichroic effect (for the photon energies that I am interested in, in the X-rays, there is no pair production), and therefore $\hat{\boldsymbol{T}} = 0$.

2.3.1 Propagation of light in a birefringent medium

A birefringent medium is an anisotropic medium in which the index of refraction depends on the polarization direction of light. The simplest birefringence is called uniaxial, which means that the optical anisotropy is driven by a single axis, and the medium is still symmetric for rotation around this special axis. The birefringence that I will consider in the following chapters is given by the presence of a strong magnetic field, and the direction of the magnetic field sets the special axis.

As shown in § 2.1, light can always be considered as a superposition of waves linearly polarized in orthogonal directions. In the case of uniaxial birefringence, as light travels through the birefringent medium, the component polarized parallel to the special axis can propagate faster (or slower) than the orthogonal component, and the difference in velocity is given by $\Delta v = c \left| \frac{1}{n_\parallel} - \frac{1}{n_\perp} \right|$, where $n_{\parallel,\perp}$ are the indices of refraction in the parallel and the perpendicular mode. In this case, the birefringent vector amplitude is given by $|\hat{\Omega}| = |k_0 \Delta n|$ where $\Delta n = n_\parallel - n_\perp$ and k_0 is the wavenumber of the radiation in the vacuum. Therefore the change in the Stokes parameters is given by (eq. 2.63)

$$\frac{\mathrm{d}\boldsymbol{s}}{\mathrm{d}\lambda} = \hat{\mathbf{\Omega}} \times \boldsymbol{s} \tag{2.64}$$

where λ measures the length of the photon path in the medium. The direction of $\hat{\mathbf{\Omega}}$ points toward the polarization of the faster mode on the Poincaré sphere of polarization states.

This equation may seem more familiar if one considers the Faraday rotation of polarized light passing through a weakly magnetized plasma. In this case, $\hat{\mathbf{\Omega}}$ points toward the S_3-direction, corresponding to the circular polarization, so the polarization direction of linearly polarized light will rotate. In general, if the direction of $\hat{\mathbf{\Omega}}$

is constant, the vector $\boldsymbol{s}$ will circle the direction of $\hat{\boldsymbol{\Omega}}$. If $|\hat{\Omega}|$ is sufficiently large, the vector $\boldsymbol{s}$ will circle the direction of $\hat{\boldsymbol{\Omega}}$ even in the case in which $\hat{\boldsymbol{\Omega}}$ changes direction and magnitude, if it does so sufficiently gradually. In particular, if the polarization state is initially parallel (or perpendicular) to $\hat{\boldsymbol{\Omega}}$, that is, the initial polarization is parallel (or perpendicular) to the special axis, the polarization state will remain nearly parallel (or perpendicular) to $\hat{\boldsymbol{\Omega}}$ as long as [93]

$$\left| \hat{\Omega} \left(\frac{\mathrm{d} \ln |\hat{\Omega}|}{\mathrm{d}\lambda} \right)^{-1} \right| \geq 0.5. \tag{2.65}$$

If this condition holds, the polarization states evolve adiabatically, and the polarization direction will follow the direction of the birefringence.

Chapter 3

The Origin of Polarized Radiation in Black Holes and Neutron Stars

In the previous chapter I showed how polarization is described in the Stokes formalism and how it can change when propagating toward the observer. In this chapter, I focus on compact objects and describe how polarized radiation is generated in the atmospheres of neutron stars and in black-hole accretion disks.

3.1 Black holes

The simplest and best understood spectral state of accreting black holes is the thermal state, which is characterized by the predominance of the thermal emission by the disk and thus is well fitted by a multi-temperature blackbody peaking in the soft X-rays (see § 1.2.3). In this section, I will only consider the thermal polarized emission from the accretion disk itself; for polarized emission from the corona see [199] and references therein. The physical model usually employed is that of a geometrically thin, optically thick disk [168, 205], and the polarized radiation from the inner disk can be well described by an electron-scattering dominated atmosphere.

3.1.1 Polarization of an electron-scattering atmosphere

The polarization degree of a plane-parallel, electron-scattering atmosphere, was derived by Chandrasekhar [42] in 1960. In his book, instead of using the usual Stokes vector $\boldsymbol{S} = (I, Q, U, V)$, Chandrasekhar uses the polarization vector $\boldsymbol{I} = (I_l, I_r, U, V)$, where

$$I_l = \frac{1}{2}(I+Q) \quad \text{and} \quad \mathrm{I_r} = \frac{1}{2}(\mathrm{I}-\mathrm{Q}) \tag{3.1}$$

are the intensities in two directions at right angles to each other, and U and V are the same Stokes parameters as in the original set. In the case of Thomson scattering, we can take $I_l = I_{\parallel}$ as the intensity in the plane of scattering and $I_r = I_{\perp}$ as the intensity in the perpendicular direction. In this basis, if we indicate with Θ the angle between incident and scattered light, from eq. 2.22 the scattered intensity in the direction Θ can be written as

$$\left(\sigma_T \frac{\mathrm{d}\Omega'}{4\pi}\right) \boldsymbol{RI} \mathrm{d}\Omega \tag{3.2}$$

where $\boldsymbol{I}$ and $\mathrm{d}\Omega$ are the polarization vector and solid angle of the incident beam of light, $\mathrm{d}\Omega'$ is the solid angle of the scattered light in the Θ direction and

$$\boldsymbol{R} = \frac{3}{2} \begin{pmatrix} \cos^2\Theta & 0 & 0 & 0 \\ 0 & 1 & 0 & 0 \\ 0 & 0 & \cos\Theta & 0 \\ 0 & 0 & 0 & \cos\Theta \end{pmatrix}. \tag{3.3}$$

I now characterize the radiation field at each point by the intensity vector

$$\boldsymbol{I}(\theta,\phi) = [I_l(\theta,\phi), I_r(\theta,\phi), U(\theta,\phi), V(\theta,\phi)] \tag{3.4}$$

where θ and ϕ are the polar angles of an appropriate coordinate system. If I write the scattering opacity as

$$\kappa = \frac{\sigma_T}{\rho} n = \frac{\sigma_T}{m_p} \frac{1+X}{2} \tag{3.5}$$

where n is the number of scattering centers per unit volume, ρ is the mass density, m_p is the proton mass and X is the hydrogen mass fraction, I can write the equation of radiative transfer as

$$-\frac{\mathrm{d}\boldsymbol{I}(\theta,\phi)}{\kappa\rho\mathrm{d}s}=\boldsymbol{I}(\theta,\phi)-\boldsymbol{\mathcal{S}}(\theta,\phi) \tag{3.6}$$

where $\boldsymbol{\mathcal{S}}(\theta,\phi)$ is the vector source function for $\boldsymbol{I}(\theta,\phi)$.

The contribution $\mathrm{d}\boldsymbol{\mathcal{S}}(\theta,\phi;\theta',\phi')$ to the source function arising from the scattering of a beam of radiation of solid angle $\mathrm{d}\Omega'$ in the direction (θ',ϕ') is given by

$$\boldsymbol{RI}\frac{\mathrm{d}\Omega'}{4\pi} \tag{3.7}$$

if $\boldsymbol{I}(\theta',\phi')$ is referred to the directions parallel and perpendicular to the plane of scattering.

After a considerable gymnastics with angles, one can integrate the contributions of $\mathrm{d}\boldsymbol{\mathcal{S}}(\theta,\phi;\theta',\phi')$ and find the total source function as

$$\boldsymbol{\mathcal{S}}(\theta,\phi)=\frac{1}{4\pi}\int_0^{\pi}\int_0^{2\pi}\boldsymbol{P}(\theta,\phi;\theta',\phi')\boldsymbol{I}(\theta',\phi')\sin\theta'\mathrm{d}\theta'\mathrm{d}\phi' \tag{3.8}$$

where the matrix $\boldsymbol{P}(\theta,\phi;\theta',\phi')$ is a mixture of $\boldsymbol{R}$ and rotation matrices and its full expression is given in § 17.1 of [42]. If I now define $\mu=\cos\theta$ and $\mu'=\cos\theta'$, I can write the transfer equation in the plane-parallel atmosphere as

$$\mu\frac{\mathrm{d}\boldsymbol{I}(\theta,\phi)}{\mathrm{d}\tau}=\boldsymbol{I}(\tau,\mu,\phi)-\frac{1}{4\pi}\int_{-1}^{+1}\int_0^{2\pi}\boldsymbol{P}(\mu,\phi;\mu',\phi')\boldsymbol{I}(\tau,\mu',\phi')\mathrm{d}\mu'\mathrm{d}\phi' \tag{3.9}$$

In the case of black hole accretion disks, the axial symmetry requires the polarization vector of the emitted photon to be in the direction parallel or perpendicular to the plane of the disk and perpendicular to the propagation direction of the photon. For this reason, $U=V=0$ and I can rewrite eq. 3.9 as

$$\begin{aligned}\mu\frac{\mathrm{d}}{\mathrm{d}\tau}&\begin{pmatrix}I_l(\tau,\mu)\\ I_r(\tau,\mu)\end{pmatrix}\\ &=\begin{pmatrix}I_l(\tau,\mu)\\ I_r(\tau,\mu)\end{pmatrix}-\frac{3}{8}\int_{-1}^{+1}\begin{pmatrix}2(1-\mu^2)(1-\mu'^2)+\mu^2\mu'^2 & \mu^2\\ \mu'^2 & 1\end{pmatrix}\begin{pmatrix}I_l(\tau,\mu)\\ I_r(\tau,\mu)\end{pmatrix}\mathrm{d}\mu'.\end{aligned} \tag{3.10}$$

Because I am not considering any illumination of the disk, the boundary conditions

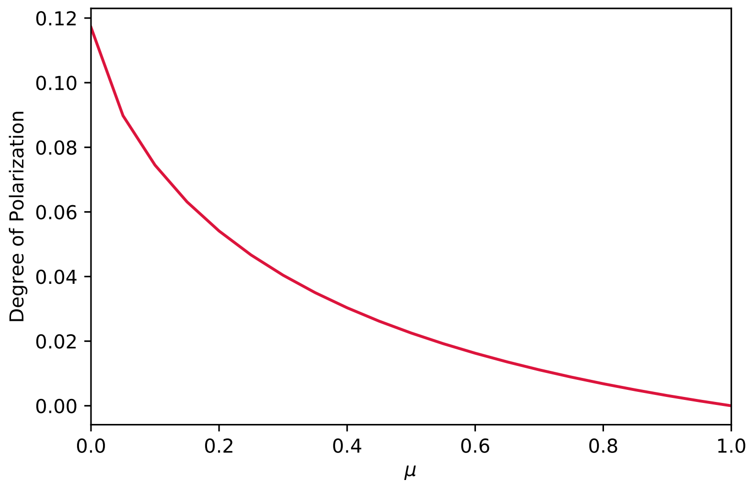

Figure 3.1: Degree of polarization of an electron scattering, plane-parallel atmosphere as a function of μ as tabulated in Table XXIV of [42].

to find a solution are

$$I_l(0,-\mu) = I_r(0,-\mu) = 0 \tag{3.11}$$

and

$$I_l(\tau,\mu) < e^{\tau} \quad \text{and} \quad \mathrm{I_r}(0,-\mu) < \mathrm{e}^{\tau} \quad \text{for} \quad \tau \to \infty \tag{3.12}$$

for convergence.

The exact solutions of eq. 3.10 that satisfy the boundary conditions were calculated in § 68 of [42]. The intensity at the surface for a direction parallel ($I_l(0,\mu)$) and perpendicular ($I_r(0,\mu)$) to the disk plane are tabulated in Table XXIV of [42] together with the degree of polarization. For light traveling in the vertical direction ($\mu = 1$) the two intensities are equal and therefore the degree of polarization is zero, while at the limb ($\mu = 0$), the ratio between the two is about 25 percent and therefore the mean polarization fraction is about 11.7 percent (see also Fig. 3.1).

3.1.2 The relativistic effects

The Chandrasekhar [42] result represents the seed radiation emitted at the surface of the accretion disk, in the fluid frame. The observed radiation will be much distorted by relativistic effects. Since these effects are stronger closer to the black hole, and since the temperature of the disk is higher closer to the hole, the changes in the polarization due to relativity are stronger for higher energy photons, which are emitted on average closer to the black hole.

Another effect is caused by returning radiation: photons emitted very close to the black hole are strongly deflected by gravitational lensing, and can bend over the black hole and intersect the accretion disk a second time. The disk is expected to be highly ionized ($T \sim 1$ keV), and therefore the returning radiation can scatter off the disk at large angles and reach te observer, which naturally leads to high polarization.

Schnittman and Krolik [198] calculated the polarization of the emission from the disk including all these effects. For the direct radiation, they found that the greatest changes in polarization are due to gravitational lensing and relativistic beaming. The former causes the far side of the disk to appear warped up toward the observer and thus that part of the disk has a smaller effective inclination, reducing the polarization seen by the observer. The latter, relativistic beaming, reduces the effective inclination and thus the degree of polarization of photons emitted along the direction of orbital motion (blue-shifted photons), while it increases effective inclination and degree of polarization for photons emitted against the direction of orbital motion (redshifted photons). Additionally, light bending rotates the polarization direction, decreasing the polarization degree of the spatially integrated emission. These effects are most important close to the black hole, where the gas is hottest and photons are emitted with higher energies. They find that for lower energies, the direct radiation follows the Chandrasekhar result, and depends only on the inclination angle. Higher energies probe the inner disk regions and the relativistic effects reduce the polarization degree, to a factor that depends on the spin of the black hole.

The direct radiation is polarized in a direction parallel to the plane, with a polarization degree of a few percent, while the scattered returning radiation is highly polarized in a direction perpendicular to the plane, especially for observers at high inclination angles. Therefore, when Schnittman and Krolik [198] take into account the returning radiation as well, they find that at low energies, where photons are coming mainly from the outer parts of the disk, the emission is dominated by direct radiation and the polarization is of the order of a few degrees parallel to the disk. At intermediate energies (above 1 keV), the returning radiation starts to dominate and the polarization degree reaches a minimum as the two contributions cancel each other. At high energies, the polarization degree goes up again, but this time the direction is perpendicular to the disk. The energy range at which the transition happens decreases with higher black hole spins (the polarization minimum is reached above 10 keV for $a_\star = 0$ and at around 2 keV for $a_\star = 0.9$).

An additional effect that can change the polarization of photons as they travel in the magnetosphere of the disk is the QED effect of vacuum birefringence. None of the previous calculations of the polarization of accreting black holes in the X-rays has taken into account this effect. In Chapter 4, I explain in detail the origin of the birefringence, and in Chapter 6 I calculate the effect of QED for photons traveling parallel to the disk plane, showing that QED has to be taken into account if we want to understand future polarimetric observations.

3.2 Neutron Stars

The polarized emission of isolated neutron stars comes from their surface, either from an atmosphere (§ 3.2.1) or from a condensed surface (§ 3.2.2), and thus I will focus on this region first. Afterwards (§ 3.2.3), I will describe how scattering in the magnetosphere can diminish the extent of polarization.

3.2.1 Neutron-Star Atmospheres

The emission processes in a neutron star's atmosphere are strongly influenced by the magnetic field. Isolated neutron stars have magnetic fields that range from 10^{11} to 10^{15} Gauss; such strong magnetic fields can constrain the motion of particles in the atmosphere and the geometry of emission.

In the atmosphere of a typical neutron star, the temperature is much less than the electron cyclotron energy,

$$kT = 0.086\ \mathrm{keV}\frac{T}{10^6\ \mathrm{K}} \ll \hbar\omega_c = \hbar\frac{eB}{m_e c} = 11.6\ \mathrm{keV}\frac{B}{10^{12}\ \mathrm{G}}\,, \tag{3.13}$$

and much higher than the proton cyclotron energy (~ 6 eV at 10^{12} G). This means that the typical photon energy is not sufficient to excite motion across the magnetic field lines and the scattering and absorption cross-sections depend strongly on the polarization state of the photon and its direction of motion [41]. Furthermore, as the typical electron energy is also much smaller than the cyclotron energy, the electrons are found in the ground Landau level and are restricted to move along the field lines.

The cyclotron energy is also much larger than the typical energy of electrons in atoms and the strong magnetic field squeezes the electron clouds around the nuclei, increasing the binding energies; therefore, the structure and binding energies of atoms, if atoms indeed exist at the surfaces of neutron stars, are expected to be dramatically different [194, 223], so even small atoms such as hydrogen may have a significant neutral fraction in the high temperatures of the neutron star atmosphere. The composition of the surface of isolated neutron stars is uncertain, and therefore current atmospheres models span a wide range of compositions: hydrogen [214], helium [145], carbon [216], mid-Z elements [160] and iron [186]. For simplicity, I will consider fully ionized hydrogen atmospheres in the discussion that follows, but the general polarization properties of emerging radiation depend on the geometry of the polarization states and on how they interact with free and bound electrons, so the results for hydrogen are illustrative of other compositions.

In the atmosphere, if a photon propagates in a direction that is perpendicular to the field, and its energy is far from the cyclotron energies, its polarization modes will remain nearly linear within the atmosphere, so that the transverse component of the electric field of the wave is either within the plane containing the magnetic field direction and the wave vector (parallel or ordinary mode) or perpendicular to that plane (perpendicular or extraordinary mode). Also, if the radiation is in the extraordinary mode, a small longitudinal component (E_L) is present along the direction of propagation: the ratio to the transverse field (E_T) is given by [148]:

$$\left|\frac{E_L}{E_T}\right| = \left|\frac{\omega_p^2\omega_c}{\omega\left(\omega^2-\omega_c^2-\omega_p^2\right)}\right| \approx \frac{\omega_p^2}{\omega\omega_c} \text{ for } \omega \ll \omega_c \tag{3.14}$$

where $\omega_p = (4\pi n_e e^2/m_e)^{1/2}$ is the plasma frequency, and n_e is the number density of electrons. This longitudinal electric field is typically smaller by a large factor relative to the transverse field. On the other hand, if the photon is propagating along the field, there is no longitudinal component of the photon's the electric field, and the transverse electric field in both modes is perpendicular to the magnetic field, and cannot accelerate the electrons unless the energy is close to the cyclotron energy.

If we focus on photons traveling nearly perpendicular to the magnetic field direction (the angle between the direction of propagation of the photon and the magnetic field θ is about $\pi/2$), the non-relativistic scattering cross sections for the two polarization modes, ordinary (1) and extraordinary (2), become [41, 80–82, 85, 106, 115, 213]:

$$\sigma_1 \approx \sigma_T \sin^2\theta \tag{3.15}$$

$$\sigma_2 \approx \sigma_T \left(\frac{\omega^2}{(\omega_c-\omega)^2} + \cos^2\theta\right). \tag{3.16}$$

where in the ordinary mode, the cross section tends to the Thomson cross section (σ_T), while in the extraordinary mode the transverse electric field can only excite the electrons close to the cyclotron resonance. For radiation that propagates approximately along the magnetic field (θ about zero), the cross section for both modes is reduced dramatically, as in both cases the electric field is mostly perpendicular to the magnetic field:

$$\sigma_1 \approx \sigma_T \left(\frac{\omega^2}{(\omega_c+\omega)^2} + \frac{1}{2}\sin^2\theta\right) \tag{3.17}$$

$$\sigma_2 \approx \sigma_T \left(\frac{\omega^2}{(\omega_c-\omega)^2} + \frac{1}{2}\sin^2\theta\right). \tag{3.18}$$

A similar result holds for intermediate angles. As ω gets closer to ω_c, the extraordinary mode's cross section increases, until it becomes larger than the ordinary mode's. Very close to ω_c however, the energy transfer from photons heats up the electrons and equations 3.15, 3.16, 3.17 and 3.18 are no longer valid, as damping effects become important [148].

Because the reduction in the cross section results from the restriction of the electron motion along the field lines and the geometry of the polarization modes, the cross sections for other processes such as free-free, bound-free and atomic transitions also depend on the polarization state and the direction of propagation [36, 50, 129, 163, 177, 182]. The properties of the emission from the atmosphere of neutron stars will depend sensitively on the strength of the magnetic field and its direction relative to the vertical.

To illustrate the various effects on the generation of polarization, I will consider a simple plane-parallel atmosphere consisting of magnetized, fully ionized hydrogen from Lloyd [130]. The neutron star atmosphere is incredibly thin compared to the radius of the star (centimeters vs. kilometers), so the plane-parallel approximation is appropriate; however, across the surface of the star, the magnetic field will vary in magnitude and direction, so the flux emergent through the surface will also depend on the location. Potekhin [181] present a comprehensive review of neutron-star atmospheres in general. To calculate the emission from the entire surface, a set of neutron-star atmosphere models must be computed accounting also for the surface temperature distribution. I will employ the same atmosphere models in Chapter 8 and I will present a prescription on how to add the contribution from different latitudes of the neutron star surface.

I will now focus on the situation where the magnetic field is perpendicular to the surface. Fig. 3.2 illustrates the various processes at play for a magnetic field strength of $B = 10^{12}$ and three values for the surface temperature, from top to bottom $T = 0.4,\ 1.0,\ 2.5 \times 10^6$ K. I will discuss the trends in Fig. 3.2 in conjunction with the polarization fraction depicted in Fig. 3.3, because the polarization of the emergent radiation clearly reflects the relative location of the two photospheres. In both these figures, the photospheres and the polarization fractions where calculated from the radiative transfer code developed by Lloyd [130]. The photosphere here is intended as the layer in the atmosphere where the total optical depth from the surface is unity. The ordinary mode (indicated as $\|$, in orange) is less strongly affected by the magnetic field, and therefore I will start by addressing its behaviour. For small photon energies, the opacity is dominated by free-free absorption, which decreases with photon energy as E^{-2}, so higher energy photons decouple deeper within the atmosphere, as long as their energy is still below the limit at which electron-scattering opacity starts to dominate over free-free opacity. Above this limit (at about $10^{0.5}$ keV in Fig. 3.2), the constant electron scattering opacity dom-

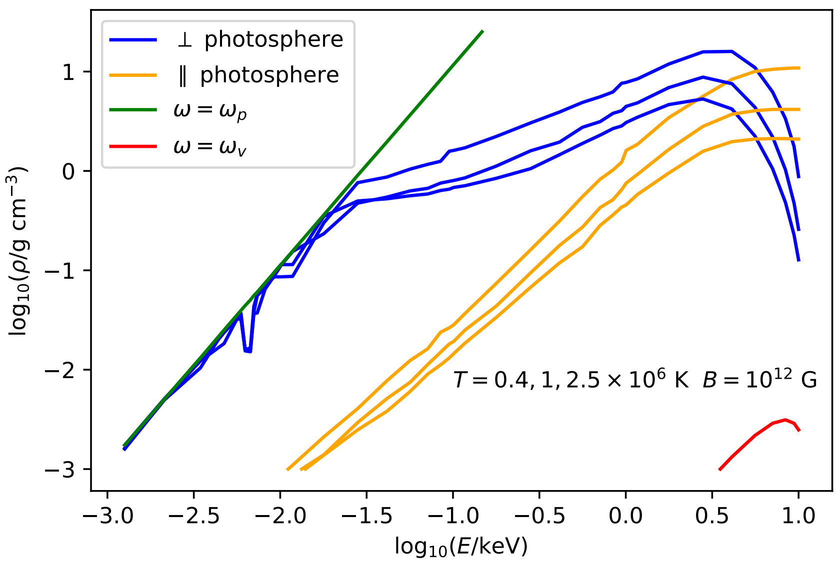

Figure 3.2: An illustration of the locations of the parallel and perpendicular model photospheres for $B = 10^{12}$ G and $T = 0.4,\ 1,\ 2.5 \times 10^6$ K using the models of Lloyd [130]. The radiation in higher temperature models decouples deeper within the star at larger densities.

inates, and the density of decoupling approaches a constant value.

For the extraordinary mode ($\perp$, in blue) the trends are somewhat more complicated. For energies below the proton cyclotron resonance, the opacity is so small that the photosphere lies at the plasma frequency, quite deep in the star compared to the ordinary mode's photospere, as the collective oscillations of the plasma dominate the generation of the extraordinary photons. The polarization fraction at these energies is quite high in the X direction. At the proton cyclotron resonance, the cross-sections for scattering and absorption increase, drawing the photosphere to shallower depths and we can see it both in Fig. 3.2 and in Fig. 3.3 as a dip at about 6 eV. The ordinary mode does not interact with the cyclotron resonances, so it is not affected at this energy. Above the proton cyclotron resonance, the photosphere follows the plasma frequency until free-free absorption takes over. Because the electric-field geometry of the extraordinary mode depends on the photon energy,

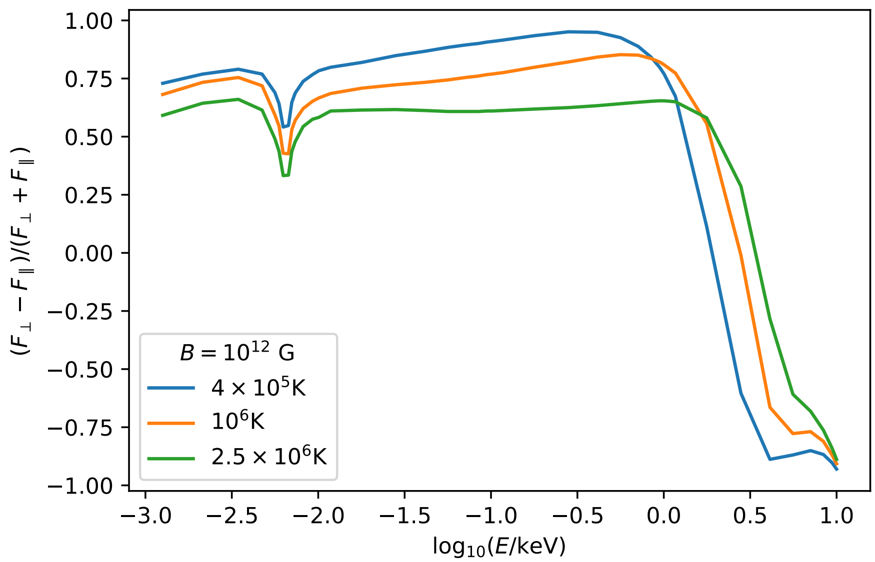

Figure 3.3: The polarization fraction as a function of energy for $B = 10^{12}$ G and $T = 0.5, 1, 2.5, \times 10^6$ K using the models of Lloyd [130]. The dip at 6 eV corresponds to the proton cyclotron line (see text).

the dependence of the free-free opacity with energy is shallower in this mode, so the depth of the photosphere does not increase as quickly as for the ordinary mode. The two photospheres approach each other. This reduces the extent of polarization in the total emission. Finally, as the photon energy approaches the electron cyclotron resonance at 11.6 keV, the opacity for the extraordinary mode increases dramatically because of the resonant cross section, and the photosphere of the extraordinary mode lies above that of the ordinary mode and the direction of the net polarization switches to the ordinary mode (the fraction becomes negative in Fig. 3.3).

I will now consider the general case, where the direction of the magnetic field can vary. We can see from the angular dependence of the scattering cross sections in Eq. 3.15 through 3.18 that the cross section is dramatically decreased when the photon is traveling along the direction of the magnetic field. If we examine radiation traveling along the magnetic field direction it should decouple at a larger depth and at a higher density than radiation traveling in other directions. Furthermore, away from the cyclotron line, the contribution by the two polarization states of photons traveling along the magnetic field should be nearly equal as their cross sections are also nearly equal. Fig. 3.4 depicts the specific intensity for radiation near the peak of the spectrum as a function of the angle between the propagation direction and the vertical for the case in which a magnetic field of 10^{12} G is directed at 30 degrees away from the vertical. The radiation is nearly fully polarized in the extraordinary mode direction and approximately isotropic except for very shallow angles where the intensity is diminished (limb-darkening) and within about ten degrees of the direction of the magnetic field, where the intensity is much larger and the radiation is not polarized. In this general case, the intensity depends not only on the zenith angle but also on the azimuthal angle relative to the local magnetic field direction. This dramatically increases the numerical effort in calculating a spectral model both relative to the unmagnetized case and to the situation where the magnetic field points in the vertical direction. It is this latter, more restrictive situation that is most often treated in the literature [76, 99, 214, 215], even if many works, including the model employed in this section, consider a varying inclination of B [75, 130, 179, 248].

3.2.2 Condensed Neutron-Star Surfaces

The properties of matter that form the surface regions of neutron stars are strongly affected by the strong magnetic fields [194]. Neutron stars may have a solid surface [33, 35, 122, 124, 143, 144, 181, 231, 233]; in this case, the emission will essentially depend on the reflectivity (R_ν) of the metallic surface. If one focuses on the interface between the vacuum outside and the condensed surface, one can argue by detailed balance that the intensity emerging from the surface is given by

$$I_{\nu,\mathrm{X/O}}(\theta_k) = \left(1 - R_{\nu,\mathrm{X/O}}(\theta_k)\right) B_\nu(T) \tag{3.19}$$

where $B_\nu(T)$ is the intensity of blackbody radiation at the temperature of the surface and θ_k is the angle with respect to the surface normal. The typical density of the condensed surface is $\approx 10^2$–10^3 g/cm^3, significantly larger than terrestrial metals, and the plasma frequency within the surface is about 1 keV, so even at X-

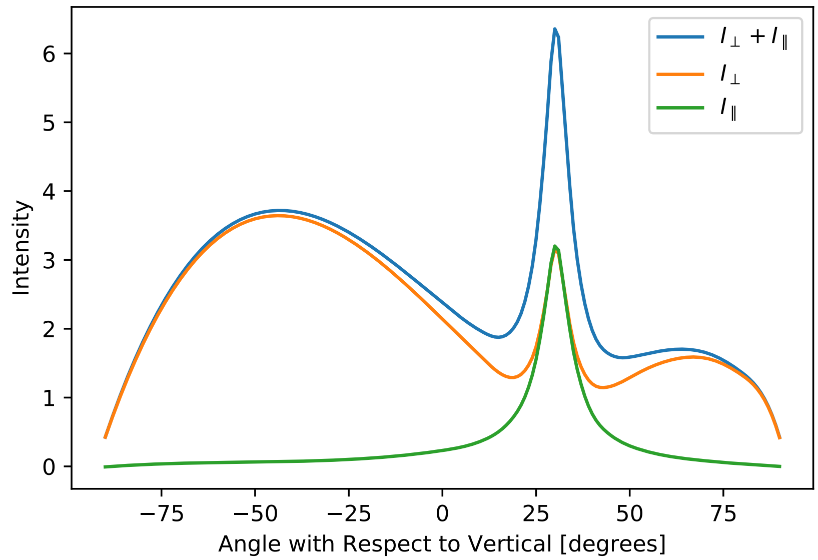

Figure 3.4: The polarized intensity at $E = 0.32$ keV, near the spectral peak, along a slice through sky containing the magnetic field direction. The magnetic field is directed at thirty degrees from the vertical. The atmosphere is calculated for $B = 10^{12}$ G and $T = 10^6$ K using the models of Lloyd [130]. The units of intensity are 10^{19} erg/cm^2/s/sr/keV.

ray energies we would expect the surface to be highly reflective and the emissivity $(1-R)$ to be small. However, there are some additional complications as the metal is highly magnetized and the ions can damp the radiation within the metal.

To address these complications we can relate the reflectivity to the electromagnetic modes within the condensed surface which is essentially a magnetized plasma (see § 5.2). Using the Fresnel equations, which establish the boundary conditions across the surface, we find the reflectance of the p-polarization (with the electric field along the plane of incidence) to be

$$R_{\rm p} = \left| \frac{\cos\theta_t - n\cos\theta_k}{\cos\theta_t + n\cos\theta_k} \right|^2, \tag{3.20}$$

and for the s-polarization (with the electric field normal to the plane of incidence)

$$R_{\mathrm{s}} = \left| \frac{\cos\theta_k - n\cos\theta_t}{\cos\theta_k + n\cos\theta_t} \right|^2, \tag{3.21}$$

where $n\sin\theta_t = \sin\theta$ (Snell's Law) and n is the index of refraction within the condensed material that forms the surface. We have neglected the index of refraction above the surface, the magnetic permeability of the material and the small longitudinal component of the X-mode. The Fresnel equations are defined in terms of the polarization states relative to the interface. The labels s and p refer to whether the radiation is polarized with its electric field in the plane containing the incoming ray and the normal to the surface (p) or perpendicular to it (s). The s-polarization is parallel to the interface itself. Both above the surface and within the condensed material, the propagation modes are determined relative to the magnetic field direction. Both regions are birefringent, so at the interface there are two reflected waves and two transmitted waves; thus, the complete picture is composed of a reflection coefficient for the X-mode to reflect into the X-mode, for the X-mode to reflect into the O and the other possibilities as well as the corresponding transmission coefficients that can be obtained by expanding the propagation modes in terms of the modes defined at the surface.

The left panel of Fig. 3.5 depicts the reflectivities and the emissivity for a condensed iron surface with a thin hydrogen atmosphere above it from Potekhin et al. [183]. The feature in the reflectivities at 0.25 keV results from the proton-cyclotron line that affects the polarization states in the region above the condensed surface. The increase in the reflectivities at about 0.125 keV corresponds to the ion-cyclotron frequency within the surface. The feature at 0.4 keV is given by

$$E_C = E_{c,i} + \frac{E_{p,e}^2}{E_{c,e}} \tag{3.22}$$

within the condensed surface (where $E_{c,i}$ is the ion-cyclotron energy, $E_{p,e}$ is the electron-plasma energy and $E_{c,e}$ is the electron-cyclotron energy). These two energies (0.25 and 0.4 keV) feature strongly in the observed polarization signature from the surface as local extrema in the polarization fraction. The right panel depicts the results also from Potekhin et al. [183] for a condensed iron surface without

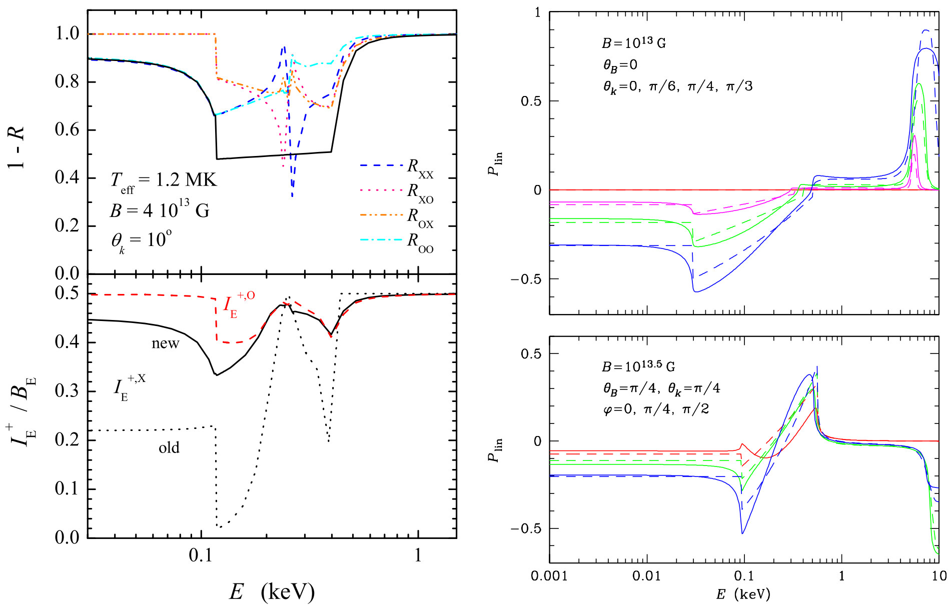

Figure 3.5: Left (Fig. 9 of [183]): The upper panel shows the four emissivities for coefficients of reflection as a function of energy R_{XX} (dashed curve), R_{XO} (dotted curve), R_{OX} (dash-dot-dotted curve), and R_{OO} (dash-dotted curve), together with the total dimensionless emissivity (solid curve). The lower panel shows the resulting dimensionless outward specific intensities for the X-mode (solid curve) and O-mode (dashed curve). Right: Degree of linear polarization as a function of photon energy E for condensed Fe surface from Fig. 7 of [183]. The upper panel depicts the case where the magnetic field is normal to the surface $\theta_B = 0$ and several directions of the photon relative to the normal direction θ_k: 0° (red), 30° (magenta), 45° (green) and 60° (blue). The lower panel holds the magnetic field and photon direction at 45° relative to the normal and examines the emission as a function of the azimuthal direction: 0° (red), 45° (green) and 90° (blue). The solid lines depict the numerical results, and the dashed lines show a fit.

an atmosphere above it. We see that the extent of polarization is typically much smaller than for an atmosphere. Furthermore the direction of the polarization depends on the energy of the photon, and the photon energy where the polarization switches from the ordinary to the extraordinary mode depends on the strength of the magnetic field through the electron and ion cyclotron frequencies and on the density of the surface layers through the plasma frequency [233]. Although the total polarization is somewhat lower than for the case of the neutron-star atmosphere, the condensed surface leaves many exciting signatures on the polarization, most importantly that the surface is indeed condensed.

3.2.3 Neutron-Star Magnetospheres

Although the typical density of the plasma in the magnetosphere is too low for many photons to be produced there, the cross section for scattering of photons from the surface may be large within the cyclotron resonance. The observed spectra of isolated neutron stars are characterized by one or two thermal components (below about one keV) [35, 197] and possibly a power-law component declining toward higher energies (above one keV) especially in magnetars [108, 136] (see Fig. 8.1). The spectra of magnetars often have an additional power-law component that becomes important from 10 keV to 100 keV [28, 77, 121, 147]. The source of the low-energy power-law component is often interpreted to be resonant inverse Compton scattering (RCS) onto mildly relativistic electrons/positrons flowing in the twisted magnetosphere [134, 228]. The origin of the harder power-law component is less clear, although it might still be related to RCS, possibly onto a different charge population(s) [12, 14, 26, 62, 188, 189, 236].

RCS in Magnetars

In magnetars the expected particle density due to charges flowing along the magnetic field lines, required to sustain the non-potential field, might be too low to build a sizable Thomson scattering depth [228]. On the other hand, this could be easily achieved in the cyclotron resonance [12, 14, 26, 62, 165, 166, 188, 189, 228, 236, 250, 251]. Given the typical energy of the photons from the surface, the cyclotron energy at scattering should be about 1 keV, much less than the rest-mass energy of the electron, so the scattering region must lie at several stellar radii, where the magnetic field is about $10^{11} - 10^{12}$ G.

The resonant scattering occurs when the photon frequency in the rest frame of the electron equals the cyclotron frequency; for an electron moving with velocity

$v = \beta c$ and Lorentz factor γ

$$\omega = \frac{\omega_c}{\gamma(1-\beta\mu)} \equiv \omega_D \tag{3.23}$$

where ω is the photon frequency in the stellar frame and

$$\mu = \hat{k} \cdot \hat{B} \tag{3.24}$$

is the cosine of the angle between the propagation of the photon and the magnetic field, also in the stellar frame. In the frame of the electron, the scattering is non-relativistic so we can use the cross sections from Eq. 3.17 and 3.18 to understand how the Compton scattering affects the two polarization states. In particular, for photons traveling along and across the field we see that only the extraordinary or perpendicular mode is resonantly scattered. Therefore, the incoming radiation from the atmosphere, which is mostly polarized perpendicular to the magnetic field direction, remains polarized perpendicular to the field direction after the resonant scattering, and then we expect the high-energy power-law component to be strongly polarized perpendicular to the local magnetic field direction as well. From a more detailed treatment [219], which includes geometric considerations, one finds that the resonant scattering can switch the polarization states. In fact, the cross sections are related in the following way [85, 166]:

$$\sigma_{1-1} = \frac{1}{3}\sigma_{1-2} = \frac{\pi^2 r_e c}{2}\delta(\omega - \omega_D)\cos^2\alpha, \tag{3.25}$$

$$\sigma_{2-2} = 3\sigma_{2-1} = \frac{3\pi^2 r_e c}{2}\delta(\omega - \omega_D) \tag{3.26}$$

where r_e is the classical radius of the electron and α is the angle between the incident photon direction and the magnetic field as measured in the rest frame of the electron ($\cos\alpha = (\mu - \beta)/(1 - \beta\mu)$). Again I use the convention that (1) indicates the ordinary or parallel mode and (2) indicates the extraordinary or perpendicular mode,. The resulting emission is polarized but less than fully polarized. If one assumes that the initial photons are completely in the extraordinary mode, after a single scattering the polarization fraction is reduced by 50% and it decreases with subsequent scatterings [62]. One can conclude that the resonant scattering process typically destroys the polarization.

3.2.4 X-ray Pulsars

The studies of polarization are more mature for magnetars and thermally emitting neutron stars, and much less developed for X-ray pulsars. The models developed by Mészáros and Nagel in the 1980s [M&N, 149–151], are still the most used in the field. Their calculations assumed a static, homogeneous atmosphere (with constant density, temperature and magnetic field) and two possible geometries: a slab, with the magnetic field perpendicular to the surface, and a column, with the field parallel to the walls. In order to calculate the spectrum of the outgoing polarization, they solved the approximate radiative transfer equations separately for the two polarization modes, following the so-called Feautrier method [153], including vacuum, thermal and incoherent scattering effects. In their model, photons are mainly produced by thermal bremsstrahlung, and the polarization of the X-ray signal is driven by the difference in opacities between the two polarization modes. An alternative model, which however ignores the effect of vacuum birefringence and the contribution from Comptonization, was calculated by Kii [111].

M&N predict the smallest linear polarization degree being coincident with the maximum flux for the "pencil beam", i.e. when photons propagate along the field (see § 1.1.2), and viceversa, a peak in polarization degree when the flux is at maximum for the "fan beam". Therefore, phase resolved measurements of the linear polarization could help distinguishing between the two scenarios.

However, the M&N models do not include relativistic effects and are based on quite crude assumptions on the physics of the emission region; for example, they assume a static atmosphere even if the ionized plasma is expected to reach the surface of the neutron star at a considerable fraction (up to ~ 0.5) of the speed of light. Moreover, the spectral shape obtained in [149] fails to describe the more recent observations of luminous X-ray pulsars [e.g. 244], expecially the flattening at low energies. For this reason, also in view of the upcoming polarimeters, a new, upgraded model is needed to predict the polarization parameters that we will observe from X-ray pulsars in the near future. In Chapter 7, I calculate the polarization degree of X-ray pulsars in the context of the M&N model, including relativistic effects and the QED effect of vacuum birefringence (see Chapter 4). In addition, I present a new model for the polarization parameters of X-ray pulsars based on the accretion model by Becker and Wolff [20]. As already mentioned in Chapter 1, Becker and Wolff analytically modeled the channeled steady-state accretion flow at the surface of the neutron star as a radiating plasma heated by a radiation-dominated shock above the neutron star surface and obtained a good spectral fit for luminous X-ray pulsars as Her X-1.

Chapter 4

The QED Effect of Vacuum Birefringence

Quantum electrodynamics or QED is the relativistic quantum field theory of electrodynamics. It is usually thought to apply only to the realm of the very small. However, its effects can be important on macroscopic scales in extreme environments, like the ones attained inside and around astrophysical compact objects, such as neutron stars and black holes.

In classical electrodynamics, photons do not interact with other electromagnetic fields as Maxwell equations are linear in the fields. In QED, the presence of a Dirac current in the vacuum results in an addition to the usual action integral of the electromagnetic field that is more than quadratic in the fields. This implies that the interaction between the fields is not linear as photons can interact with virtual electron-positron pairs as they travel through a magnetized vacuum. As a result, the speed at which light travels through the vacuum depends on its polarization and on the strength of the field. In other words, in the presence of a magnetic field the vacuum becomes birefringent, i.e., it acquires an index of refraction that is different depending on the angle between the direction of the photon's polarization and the magnetic field.

In § 4.1, I derive the effective Lagrangian of QED from the classical Lagrangian of the electromagnetic field coupled to a Dirac field using modern functional techniques. In § 4.3, I calculate the index of refraction in the case of a uniform magnetic field. In § 4.4 I use the formalism introduced in § 2.3 to describe how birefringence affects the propagation of polarization radiation.

4.1 Effective Action: Formal Derivation

The Lagrangian of QED is

$$\mathscr{L} = \bar{\psi}(i\gamma^{\mu}\frac{\partial}{\partial x^{\mu}} + e\gamma^{\mu}A_{\mu} - m)\psi - \frac{1}{4}F_{\mu\nu}F^{\mu\nu} \tag{4.1}$$

where the interaction between the fermionic fields and the external field is given by the Feynman rule

$$-ie\gamma^{\mu}\tilde{A}^{0}_{\mu}(\mathbf{q}) \, . \tag{4.2}$$

This rule must be taken into account in all fermion propagators, including internal lines such as in the vacuum polarization and in photon splitting processes. The symbols γ^{μ} are the Dirac matrices that span the spinorial components of the fermion fields.

If the external field is sufficiently weak, the interactions with the field may be treated as perturbations, as a series of discrete interactions. On the other hand, at a field strength of $B_{\rm QED} = m^2c^3/(e\hbar) = 4.4 \times 10^{13}$ G, the gyration energy of an electron or, equivalently, the potential energy drop across its Compton wavelength, is equal to its rest mass. For this reason, when the field exceeds a critical value of approximately $B_{\rm QED}/2$, this series fails to converge. Essentially, each term in the sum of diagrams is equally large in this limit.

In the following sections, I derive the effective action of a general field configuration to one-loop order from the QED Lagrangian (Eq. 4.1) using the method of functional integration. The key results for X-ray polarization are the index of refraction (Section 4.3) and how polarization changes as radiation propagates through an inhomogeneous birefringent medium (§ 4.4).

4.1.1 The functional method

The connections between the theory of quantum and statistical fields are manifold. The following derivation of the effective action and Lagrangian will exploit these connections. The final results that I present here are well known in the specialized literature for quantum field theory in strong fields (e.g., [54, 55]) and older introductory texts (e.g., [29, 102]), but they are typically absent from recent introductory texts (e.g., [135, 180]). I present a derivation of the effective action using functional techniques familiar from modern treatments of quantum field theory (e.g., [180]) and statistical mechanics. The analysis in this section draws on § 11.3 and § 11.4 of [180].

In the functional method of quantum field theory, correlation functions can be derived from the functional derivative of a *generating functional*. For example, for a field theory governed by the lagrangian $\mathscr{L}$, the generating functional is given by:

$$Z[J] = \int \mathscr{D}\phi \exp\left[i \int d^4x(\mathscr{L} + J\phi)\right], \tag{4.3}$$

where J is an external current and ϕ is the field. The integral $\int \mathscr{D}\phi$ indicates an integration over all field configurations. In this case, correlation functions can be derived as:

$$\langle 0|T\phi(x_1)\phi(x_2)|0\rangle = Z[J]^{-1}\left(-i\frac{\delta}{\delta J(x_1)}\right)\left(-i\frac{\delta}{\delta J(x_2)}\right)Z[J]\bigg|_{J=0}. \tag{4.4}$$

where T is the time-ordering operator. The generating functional has many similarities with the partition function of statistical mechanics. In particular, it consists of an integral over the quantum phases (or statistical weights) of each possible state of the system, and the source $J(x)$ plays the role of an external field. In the case of QED, the generating functional takes the following form:

$$\begin{aligned} Z[J^\mu, \bar{\eta}, \eta] &= \exp\left(-\frac{i}{\hbar}E[J^\mu, \bar{\eta}, \eta]\right) \\ &= \int \mathscr{D}A_\mu \mathscr{D}\psi \mathscr{D}\bar{\psi} \exp\frac{i}{\hbar}\int \mathrm{d}^4x \left(\mathscr{L} + J^\mu A_\mu + \bar{\eta}\psi + \bar{\psi}\eta\right). \end{aligned} \tag{4.5}$$

where J^μ and A_μ are the electromagnetic current and vector potential respectively, η and $\bar{\eta}$ are the fermionic currents and ψ and $\bar{\psi}$ are the fermionic fields. $E[J^\mu, \bar{\eta}, \eta]$ is an energy functional that corresponds to the vacuum energy. Brackets are used to denote functionals (integrals of the fields over the entire spacetime) while parentheses indicate functions. The variables $\eta, \bar{\eta}, \psi$ and $\bar{\psi}$ are Grassmann numbers. Grassmann numbers are introduced to implement the anti-commuting nature of the fermion wave function: they anti-commute, which means that $\eta\psi = -\psi\eta$ and $\eta^2 = 0$. Grassmann numbers behave differently from commuting numbers under integration and differentiation as well. For a more complete introduction to the properties of Grassmann numbers, I redirect the reader to § 9.5 of [180].

Following the example of [180], it is useful to compare the generating functional to the partition function of a specific system, in their case a magnetic system:

$$Z(B) = e^{-\beta F(B)} = \int \mathscr{D}s \exp\left[-\beta \int dx(\mathscr{H}[s] - Bs(x))\right], \tag{4.6}$$

where $\beta = 1/kT$, B is the external magnetic field, $s(x)$ is the local spin field, $\mathscr{H}[s]$ is the spin energy density and again $\int \mathscr{D}s$ is the integral over all spin configurations. In eq. (4.5), each field configuration receives a phase proportional to the integral of the Lagrangian over spacetime, i.e., the action. The constant of proportionality is $i/\hbar$; in statistical physics, the constant of proportionality is $-\beta = -1/kT$, and the states are weighted by energy and not action. Drawing the analogy further, the functional $E[J^\mu, \bar{\eta}, \eta]$, would correspond to the Helmholtz free energy $F(T,V,N)$ in statistical mechanics; it is the vacuum energy as a function of the external sources $J^\mu, \bar{\eta}$ and η. In the case of a magnetic system, I can find the magnetization at a certain temperature by differentiating $F(B)$:

$$\begin{aligned} -\frac{\mathrm{d}F}{\mathrm{d}B}\bigg|_{\beta\,\text{fixed}} &= \frac{1}{\beta}\frac{\mathrm{d}}{\mathrm{d}B}\log Z \\ &= \frac{1}{Z}\int dx \int \mathscr{D}s\, s(x) \exp\left[-\beta \int dx(\mathscr{H}[s] - Bs(x))\right] \\ &= \int dx \langle s(x)\rangle \equiv M\,. \end{aligned} \tag{4.7}$$

At zero temperature, the ground state is the state of lowest energy, while at $T \neq 0$ the preferred state is the state that minimize the Gibbs free energy:

$$G = F + MB\,. \tag{4.8}$$

Therefore:

$$\begin{aligned}\left.\frac{\mathrm{d}G}{\mathrm{d}M}\right|_{\beta\,\text{fixed}} &= \left.\frac{\mathrm{d}F}{\mathrm{d}M}\right|_{\beta\,\text{fixed}} + M\left.\frac{\mathrm{d}B}{\mathrm{d}M}\right|_{\beta\,\text{fixed}} + B \\ &= \left.\frac{\mathrm{d}B}{\mathrm{d}M}\frac{\mathrm{d}F}{\mathrm{d}B}\right|_{\beta\,\text{fixed}} + M\left.\frac{\mathrm{d}B}{\mathrm{d}M}\right|_{\beta\,\text{fixed}} + B = B\,. \end{aligned} \tag{4.9}$$

G is extremal at $B = 0$ and the corresponding value of M. In general, the most stable state corresponds to the minimum of $G(M)$: $G(M)$ represent the preferred state at a temperature greater than zero that includes all the thermal fluctuations.

For the quantum field, the result proceeds similarly: the functional derivative of $E[\,]$ with respect to one of the currents yields the classical field, i.e., the vacuum expectation value of the corresponding field, which I denote as $A^0_\mu(x)$

$$\begin{aligned}\frac{\delta E[J^\mu,\bar{\eta},\eta]}{\delta J^\mu(x)} &= i\hbar\frac{\delta}{\delta J^\mu(x)}\ln Z \\ &= -\frac{\int \mathscr{D}A_\mu \mathscr{D}\psi \mathscr{D}\bar{\psi} A_\mu(x) \exp\frac{i}{\hbar}\int \mathrm{d}^4x\left(\mathscr{L} + J^\mu A_\mu + \bar{\eta}\psi + \bar{\psi}\eta\right)}{\int \mathscr{D}A_\mu \mathscr{D}\psi \mathscr{D}\bar{\psi} \exp\frac{i}{\hbar}\int \mathrm{d}^4x\left(\mathscr{L} + J^\mu A_\mu + \bar{\eta}\psi + \bar{\psi}\eta\right)} \\ &= -\left\langle \Omega|A_\mu(x)|\Omega\right\rangle \equiv -A^0_\mu(x). \end{aligned} \tag{4.10}$$

where I use the symbol δ to denote a functional derivative and where $|\Omega\rangle$ denotes the vacuum state. This correspond to a weighted average over all possible quantum fluctuations.

Generally, when one considers the properties of the magnetized vacuum, it is the fields that are specified, not the currents. The effective action is related to $E[\,]$ through a Legendre transformation, just as the Gibbs free energy G is related to F:

$$\Gamma[A^0_\mu,\bar{\psi}^0,\psi^0] = -E[J^\mu,\bar{\eta},\eta] - \int \mathrm{d}^4y\left(J^\mu(y)A^0_\mu(y) + \bar{\eta}(y)\psi^0(y) + \bar{\psi}^0(y)\eta(y)\right). \tag{4.11}$$

The functional derivative of the effective action, $\Gamma[\,]$, with respect to one of the classical fields yields the distribution of the corresponding current. Using the analogy with thermodynamics, the effective action is the vacuum energy with the distribution of the fields fixed.

4.1.2 Functional Integration

Computing the effective action begins with the expression for $Z[\,]$, the partition function, specifically by expanding the classical action with currents about the values of the classical fields,

$$\begin{aligned}
\int \mathrm{d}^4x \left(\mathscr{L} + J^\mu A_\mu + \bar{\eta}\psi + \bar{\psi}\eta\right) = \int \mathrm{d}^4x \left(\mathscr{L}[A^0_\mu, \bar{\psi}^0, \psi^0] + J^\mu A^0_\mu + \bar{\eta}\psi^0 + \bar{\psi}^0\eta\right) + \\
\int \mathrm{d}^4x \left[\Delta A_\mu(x)\left(\frac{\delta\mathscr{L}}{\delta A_\mu} - J^\mu\right) + \Delta\bar{\psi}(x)\left(\frac{\delta\mathscr{L}}{\delta\bar{\psi}} - \bar{\eta}\right) + \left(\frac{\delta\mathscr{L}}{\delta\psi} - \eta\right)\Delta\psi(x)\right] + \\
\frac{1}{2}\int \mathrm{d}^4x\mathrm{d}^4y \Bigg[(\Delta A_\mu(x))(\Delta A_\nu(y))\frac{\delta^2\mathscr{L}}{\delta A_\mu(x)\delta A_\nu(y)} + \\
(\Delta\bar{\psi}(x))\frac{\delta^2\mathscr{L}}{\delta\bar{\psi}(x)\delta\psi(y)}(\Delta\psi(y)) + \\
(\Delta A_\mu(x))\frac{\delta^2\mathscr{L}}{\delta A_\mu(x)\delta\psi(y)}(\Delta\psi(y)) + \\
(\Delta\bar{\psi}(x))\frac{\delta^2\mathscr{L}}{\delta\bar{\psi}(x)\delta A_\mu(y)}(\Delta A_\mu(y))\Bigg] + \text{Higher Order Terms}
\end{aligned} \tag{4.12}$$

where $\Delta A_\mu(x) = A_\mu(x) - A^0_\mu(x)$, the difference between the electromagnetic field including the quantum fluctuations and the classical electromagnetic field, and similarly for the other fields. Since the functional derivatives will be evaluated at $\psi^0(y) = \bar{\psi}^0(y) = 0$, the last two terms vanish. Furthermore, second derivatives with respect to the same Grassmann field also vanish because of the anti-commutative nature of the fields. Let us now evaluate for an example the term

$$\begin{aligned}
\frac{\delta\mathscr{L}}{\delta A_\mu} - J^\mu &= \frac{\delta}{\delta A_\mu}\left(\bar{\psi}(i\gamma^\mu\frac{\partial}{\partial x^\mu} + e\gamma^\mu A_\mu - m)\psi - \frac{1}{4}F_{\mu\nu}F^{\mu\nu}\right) - J^\mu \\
&= \bar{\psi}e\gamma^\mu\psi - J^\mu - \frac{1}{4}\frac{\delta}{\delta A_\mu}\left(A_{\mu,\nu}A^{\mu,\nu} - A_{\nu,\mu}A^{\mu,\nu} - A_{\mu,\nu}A^{\nu,\mu} + A_{\nu,\mu}A^{\nu,\mu}\right) \\
&= \bar{\psi}e\gamma^\mu\psi - J^\mu - \frac{1}{4}\frac{\delta}{\delta A_\mu}\left(2A_{\mu,\nu}A^{\mu,\nu} - 2A_{\mu,\nu}A^{\nu,\mu}\right) \\
&= \bar{\psi}e\gamma^\mu\psi - J^\mu - \frac{\overleftarrow{\partial}}{\partial x^\nu}A^{\mu,\nu} + \frac{\overleftarrow{\partial}}{\partial x^\nu}A^{\nu,\mu}\,.
\end{aligned} \tag{4.13}$$

The $\overleftarrow{\partial}$ notation indicates that the resulting derivative is an operator that differentiates something to the left. As the derivative lives within a integral over all of spacetime, one can use integration by parts to simplify the result further if one assumes that the boundary terms vanish:

$$\frac{\delta \mathscr{L}}{\delta A_\mu} - J^\mu = \bar{\psi} e \gamma^\mu \psi - J^\mu + \frac{\partial}{\partial x^\nu}\left(A^{\mu,\nu} - A^{\nu,\mu}\right) = \bar{\psi} e \gamma^\mu \psi - J^\mu + \frac{\partial}{\partial x^\nu} F^{\mu\nu} \quad (4.14)$$

The first-order derivatives vanish when the fields satisfy the field equations.

Although there is not an explicit relationship that connects the currents to the classical fields that they generate, I will impose that the currents J^μ, $\bar{\eta}$ and η along with the classical fields A^0_μ, $\bar{\psi}^0$ and ψ^0 satisfy the field equations and evaluate all of the functional derivatives at the values of the classical fields. Thereby, I focus on the quantum fluctuations about a classical field configuration. In this case the first order terms in the expansion vanish and the vacuum energy $E[\,]$ to lowest order is a Gaussian functional integral,

$$\begin{aligned}
E[J^\mu, \bar{\eta}, \eta] = & -\int \mathrm{d}^4x \left(-\frac{1}{4} F^0_{\mu\nu} F^{0,\mu\nu} + J^\mu A^0_\mu\right) + \\
& i\hbar \ln \int \mathscr{D}A_\mu \mathscr{D}\bar{\psi} \mathscr{D}\psi \exp \frac{i}{2\hbar} \int \mathrm{d}^4x \mathrm{d}^4y \Bigg[(\Delta A_\mu(x))(\Delta A_\nu(y)) \frac{\delta^2 \mathscr{L}}{\delta A_\mu(x) \delta A_\nu(y)} \\
& \qquad + (\Delta \bar{\psi}(x)) \frac{\delta^2 \mathscr{L}}{\delta \bar{\psi}(x) \delta \psi(y)} (\Delta \psi(y)) \Bigg] \\
= & -\int \mathrm{d}^4x \left(-\frac{1}{4} F^0_{\mu\nu} F^{0,\mu\nu} + J^\mu A^0_\mu\right) - \\
& \frac{i\hbar}{2} \ln \mathrm{Det} \left[\frac{\delta^2 \mathscr{L}}{\delta A_\mu(x) \delta A_\nu(y)}\right] + i\hbar \ln \mathrm{Det} \left[\frac{\delta^2 \mathscr{L}}{\delta \bar{\psi}(x) \delta \psi(y)}\right] \\
& + \text{Constant Terms}
\end{aligned} \quad (4.15)$$

I integrated over all of the possible field configurations by assuming that a particular field configuration is a point in an infinite dimensional space and by looking at the functional derivatives as infinite dimensional matrices. Let us look at the following term in detail to see how this works:

$$
\begin{aligned}
E_{A_\mu} &= i\hbar \ln \int \mathscr{D}A_\mu \exp \frac{i}{2\hbar} \int \mathrm{d}^4x\mathrm{d}^4y \left[(\Delta A_\mu(x))(\Delta A_\nu(y)) \frac{\delta^2 \mathscr{L}}{\delta A_\mu(x)\delta A_\nu(y)} \right] \\
&= i\hbar \ln \int \prod \left(\mathrm{d}A_\mu(x_i)\right) \exp \frac{i}{2\hbar} \sum_{i,j} (\Delta A_\mu(x_i))(\Delta A_\nu(y_j)) \left[\frac{\delta^2 \mathscr{L}}{\delta A_\mu(x_i)\delta A_\nu(y_j)} \right] \\
&= i\hbar \ln \int \prod \left(\mathrm{d}A_\mu(x_i)\right) \exp \left[-\sum_i (\Delta A_\mu(x_i))^2 \left(-\frac{i}{2\hbar}\lambda_i \right) \right]
\end{aligned} \tag{4.16}
$$

where λ_i are the eigenvalues of the matrix $\left[\delta^2\mathscr{L}/(\delta A_\mu(x_i)\delta A_\nu(y_j))\right]$, and I have chosen the eigenvectors as a basis for performing the integral over the field configurations, $\int \prod \left(\mathrm{d}A_\mu(x_i)\right)$. Now I will perform the integration over each of the $\mathrm{d}A_\mu(x_i)$ to yield

$$
\begin{aligned}
E_{A_\mu} &= i\hbar \ln \prod_i \left(-\frac{i}{2\hbar}\lambda_i \right)^{-1/2} = -\frac{i\hbar}{2} \ln \prod_i (\lambda_i) - \frac{i\hbar}{2} \prod_i \left(-\frac{i}{2\hbar} \right) \\
&= -\frac{i\hbar}{2} \ln \mathrm{Det} \left[\frac{\delta^2 \mathscr{L}}{\delta A_\mu(x)\delta A_\nu(y)} \right] + \text{Constant Terms.}
\end{aligned} \tag{4.17}
$$

The constant terms absorb the constant prefactor in front of the integral, $-i/(2\hbar)$, as well as some divergent terms. The symbol Det denotes the functional determinant over both the spacetime and the spin space in the case of the Dirac fields. One subtlety is the plus sign in front of the functional derivative involving the Grassmann fields $\bar{\psi}(x)$ and $\psi(y)$. Simply, the integral of

$$
\begin{aligned}
\int d\bar{\psi} d\psi \exp(-\bar{\psi} a \psi) &= \int d\bar{\psi} d\psi (1 - \bar{\psi} a \psi) \\
&= \int d\bar{\psi} d\psi (1 + a\bar{\psi}\psi) \\
&= \int d\bar{\psi} (a\bar{\psi}) = a \text{ and not } \frac{2\pi}{a},
\end{aligned} \tag{4.18}
$$

where the first equality is not an approximation because the higher terms of the expansion vanish. This unexpected result comes from the anti-commuting nature of the fields. Performing the Legendre transformation yields an expression for the effective action to lowest order (one loop),

$$\Gamma[A_\mu^0] = \int \mathrm{d}^4x \left(-\frac{1}{4} F_{\mu\nu}^0 F^{0,\mu\nu} \right) + \frac{i\hbar}{2} \ln \mathrm{Det} \left[\frac{\delta^2 \mathscr{L}}{\delta A_\mu(x) \delta A_\nu(y)} \right] - i\hbar \ln \mathrm{Det} \left[\frac{\delta^2 \mathscr{L}}{\delta \bar{\psi}(x) \delta \psi(y)} \right] \tag{4.19}$$

where I have dropped the constant terms from the expression. So far, I have not been concerned with renormalizing the effective action, but the functional determinants are probably divergent. The effective action vanishes as the classical field vanishes, so I have to subtract two terms corresponding to the functional determinants in the absence of an external field. This renormalizes the zero-point energy and yields,

$$\begin{aligned}\Gamma[A_\mu^0] &= \int \mathrm{d}^4x \left(-\frac{1}{4} F_{\mu\nu}^0 F^{0,\mu\nu} \right) \\ &\quad - i\hbar \ln \mathrm{Det} \left[\frac{\delta^2 \mathscr{L}}{\delta \bar{\psi}(x) \delta \psi(y)} \right] \Bigg|_{A_\mu = A_\mu^0} + i\hbar \ln \mathrm{Det} \left[\frac{\delta^2 \mathscr{L}}{\delta \bar{\psi}(x) \delta \psi(y)} \right] \Bigg|_{A_\mu = 0} \\ &= \int \mathrm{d}^4x \left(-\frac{1}{4} F_{\mu\nu}^0 F^{0,\mu\nu} \right) - i\hbar \ln \mathrm{Det} \left[\frac{\not{\Pi} - m}{\not{p} - m} \right] \end{aligned} \tag{4.20}$$

where

$$\not{\Pi} = \gamma^\mu \Pi_\mu = i\gamma^\mu \frac{\partial}{\partial x^\mu} + e\gamma^\mu A_\mu^0 = \gamma^\mu p_\mu + e\gamma^\mu A_\mu^0. \tag{4.21}$$

The functional derivative of the Lagrangian with respect to the vector potential is same for all values of the classical vector potential as along as the fermionic classical field vanishes. The effective action contains the classical Maxwell action of electrodynamics and an additional term that quantifies the effects of the vacuum fluctuations of the Dirac (here electron-positron) fields.

I will use the linear algebra result, $\ln \mathrm{Det} A = \mathrm{Tr} \ln A$, to simplify the expression for the effective action further. I use the convention that Det and Tr span both coordinate and spin space, while tr and det just cover the spinorial components (the analysis in this subsection builds upon § 4.3.3 and § 4.3.4 of [102]),

$$\Gamma[A^0_\mu] = \int \mathrm{d}^4x \mathscr{L}_{\mathrm{eff}} = \int \mathrm{d}^4x \left(-\frac{1}{4}F^0_{\mu\nu}F^{0,\mu\nu}\right) - i\hbar \mathrm{Tr}\ln\left[\frac{\not{\Pi} - m}{\not{p} - m}\right] \tag{4.22}$$

I would like to put the logarithm in a more manageable form.

$$\mathrm{Tr}\ln\left[\frac{\not{\Pi} - m}{\not{p} - m}\right] = \mathrm{Tr}\ln\left[\frac{\not{\Pi} + m}{\not{p} + m}\right] = \frac{1}{2}\mathrm{Tr}\ln\left[\frac{\not{\Pi}^2 - m^2}{\not{p}^2 - m^2}\right]. \tag{4.23}$$

The first equality holds since the charge conjugation matrix C satisfies $C\gamma_\mu C^{-1} = -\gamma_\mu^T$, so $C\not{\Pi}C^{-1} = -\not{\Pi}^T$ (similarly for $\not{p}$), and the trace of an operator is invariant under transposition. The second equality results from summing the first two expressions.

4.1.3 Effective Action : Proper-time Integration

I use the identity

$$\ln\frac{a}{b} = \lim_{\varepsilon\to 0}\int_0^\infty \frac{\mathrm{d}s}{s}\left(\exp is(b+i\varepsilon) - \exp is(a+i\varepsilon)\right) \tag{4.24}$$

to expand the logarithm

$$\mathrm{Tr}\ln\left[\frac{\not{\Pi} - m}{\not{p} - m}\right] = \tag{4.25}$$
$$-\frac{1}{2}\int \mathrm{d}^4x \int_0^\infty \frac{\mathrm{d}s}{s} e^{-ism^2} e^{-\varepsilon s}\mathrm{tr}\Big(\langle x|\exp(is\not{\Pi}^2)|x\rangle - \langle x|\exp(is\not{p}^2)|x\rangle\Big)$$

and obtain the proper-time expression for the effective Lagrangian density [203],

$$\mathscr{L}_{\mathrm{eff}} = -\frac{1}{4}F^0_{\mu\nu}F^{0,\mu\nu} + \frac{i\hbar}{2}\int_0^\infty \frac{\mathrm{d}s}{s} e^{-ism^2} e^{-\varepsilon s}\mathrm{tr}\left(\langle x|U(s)|x\rangle - \langle x|U_0(s)|x\rangle\right) \tag{4.26}$$

where $U(s)$ is the time-evolution operator governed by the Hamiltonian,

$$\mathscr{H} = -\not{\Pi}^2 = \Pi^\mu\Pi_\mu - \frac{1}{2}e\sigma^{\mu\nu}F^0_{\mu\nu}. \tag{4.27}$$

where $\sigma^{\mu\nu} = \frac{i}{2}[\gamma^\mu, \gamma^\nu]$. $U_0(s)$ is the analogous operator for vanishing external fields. Please notice that, for convenience, I dropped the limit for $\varepsilon \to 0$ in eq. 4.25, but we have to keep in mind that I will have to take $\varepsilon \to 0$ at the end of the calculation. Equation 4.26 forms the basis of the worldline numerics technique that facilitates the calculation of the effective action for arbitrary field configurations [70, 140].

4.2 Results for a Uniform Field

I will select a particular frame and gauge to calculate the trace and obtain an expression for the effective Lagrangian from a uniform electromagnetic field. I begin with

$$\mathrm{tr}\left(\left\langle x\right|\exp(is\not{\Pi}^2)\left|x\right\rangle\right) = \mathrm{tr}\left(\left\langle x\right|\exp(is\Pi^\mu\Pi_\mu)\left|x\right\rangle\right)\mathrm{tr}\left(\langle x|\exp\left(\frac{i}{2}es\sigma^{\mu\nu}F^0_{\mu\nu}\right)|x\rangle\right) \tag{4.28}$$

since $\sigma^{\mu\nu}F^0_{\mu\nu}$ commutes with $\Pi^\mu\Pi_\mu$ for constant fields.

In a general frame, the eigenvalues of $\frac{i}{2}es\sigma^{\mu\nu}F^0_{\mu\nu}$ are $\pm es(a \pm ib)$, where

$$(a+ib)^2 = (\mathbf{E}+i\mathbf{B})^2 = |\mathbf{E}|^2 - |\mathbf{B}|^2 + 2i\mathbf{E}\cdot\mathbf{B}\,, \tag{4.29}$$

$\mathbf{E}$ and $\mathbf{B}$ are the classical electric and magnetic fields respectively, and a and b are Lorentz invariants of the field (see [202]). I can therefore rewrite the second trace as

$$\mathrm{tr}\left(\langle x|\exp\left(\frac{i}{2}es\sigma^{\mu\nu}F^0_{\mu\nu}\right)|x\rangle\right) = 4\cosh(eas)\cos(ebs)\,. \tag{4.30}$$

The evaluation of the first trace is more complicated. I now choose a frame such that $\mathbf{E}\|\mathbf{B}$, and $a \equiv |\mathbf{E}|$ and $b \equiv |\mathbf{B}|$. With no loss of generality, I can assume that the magnetic and electric fields point in the z-direction and select a gauge with $A^3 = -at$ and $A^1 = -by$; this yields,

$$\Pi^\mu\Pi_\mu = (P^0)^2 - (P^2)^2 - (P^1 + ebX^2)^2 - (P^3 + eaX^0)^2 \tag{4.31}$$

Using the commutation relation $[x, p_x] = -i$, I can define the shift operator

$$e^{-ip_x c} f(x) e^{ip_x c} = f(x+c) \tag{4.32}$$

which allows me to write

$$\Pi^\mu \Pi_\mu = \exp\left(-i\frac{P^2 P^1}{eb} - i\frac{P^0 P^3}{ea}\right) \left[(P^0)^2 - (P^2)^2 - (ebX^2)^2 - (eaX^0)^2\right] \times \\ \exp\left(i\frac{P^2 P^1}{eb} + i\frac{P^0 P^3}{ea}\right) \tag{4.33}$$

To evaluate the trace itself I use the momentum representation

$$\begin{aligned} \mathrm{tr}\left(\langle x|\exp(is\Pi^\mu\Pi_\mu)|x\rangle\right) = &\int \frac{\mathrm{d}p_3 \mathrm{d}p_1}{(2\pi)^4} \mathrm{d}p_0 \mathrm{d}p_0' \mathrm{d}p_2 \mathrm{d}p_2' \exp\left[i(p_0' - p_0)\left(t + \frac{p_3}{ea}\right)\right] \times \\ &\exp\left[i(p_2' - p_2)\left(y + \frac{p_1}{eb}\right)\right] \langle p_0|\exp[is(P_0^2 - e^2a^2(X^0)^2)]|p_0'\rangle \times \\ &\langle p_2|\exp[-is(P_2^2 + e^2b^2(X^2)^2)]|p_2'\rangle \\ = &\frac{e^2 ab}{(2\pi)^2} \int_{-\infty}^{\infty} \mathrm{d}p_0 \langle p_0|\exp[is(P_0^2 - e^2a^2(X^0)^2)]|p_0\rangle \times \\ &\int_{-\infty}^{\infty} \mathrm{d}p_2 \langle p_2|\exp[-is(P_2^2 + e^2b^2(X^2)^2)]|p_2\rangle \end{aligned} \tag{4.34}$$

Let us examine the last of the two integrals in detail.

$$\begin{aligned} \int_{-\infty}^{\infty} \mathrm{d}p_2 \langle p_2|\exp[-is(P_2^2 + e^2b^2(X^2)^2)]|p_2\rangle &= \mathrm{Tr}\exp[-is(p^2 + e^2b^2x^2)] \\ &= \mathrm{Tr}\exp[-2is\mathscr{H}] \end{aligned} \tag{4.35}$$

where $\mathscr{H}$ is the Hamiltonian of a harmonic oscillator with unit mass and spring constant $k = e^2b^2$. Using the known eigenvalues of the system yields an expression for the integral,

$$\mathrm{Tr}\exp[-2i\mathscr{H}s] = \sum_{n=0}^{\infty} \exp\left[-2iebs\left(n + \frac{1}{2}\right)\right] = \frac{1}{2i\sin(ebs)}\,. \tag{4.36}$$

The result for the first integral is similar except here $k = -e^2a^2$. Therefore, the complete expression for eq. 4.28 is

$$\operatorname{tr}\left(\langle x|\exp(is\not{\Pi}^2)|x\rangle\right) = -i\frac{e^2ab}{(2\pi)^2}\coth(eas)\cot(ebs). \tag{4.37}$$

Taking the limit of this expression as a and b vanish yields

$$\operatorname{tr}\left(\langle x|\exp(is\not{p}^2)|x\rangle\right) = -\frac{i}{(2\pi)^2}\frac{1}{s^2}. \tag{4.38}$$

4.2.1 Effective Lagrangian in a Constant Field

Substituting this result into 4.26 yields an expression for the effective Lagrangian,

$$\mathscr{L}_{\text{eff}} = -\frac{1}{4}F^0_{\mu\nu}F^{0,\mu\nu} + \frac{\hbar}{2(2\pi)^2}\int_0^\infty \frac{\mathrm{d}s}{s}e^{-ism^2}e^{-\varepsilon s}\left[e^2ab\coth(eas)\cot(ebs) - \frac{1}{s^2}\right] \tag{4.39}$$

For small values of s, the integrand diverges as $e^2(a^2-b^2)/(3s)$. Since this is proportional to the classical Lagrangian, it can be absorbed through a renormalization, or a scale change, of all fields and a corresponding scale change of charge. I identify the quantities thus far employed with a zero subscript, and introduce new units of field strength and charge according to [202]

$$(a+ib)^2 = (1+Ce_0^2)(a_0+ib_0)^2 \tag{4.40a}$$

$$e^2 = \frac{e_0^2}{1+Ce_0^2} \tag{4.40b}$$

$$C = \frac{1}{12\pi^2}\int_0^\infty \frac{\mathrm{d}s}{s}\exp\left(-m^2s\right) \tag{4.40c}$$

This yields the renormalized expression for the effective Lagrangian,

$$\begin{aligned}\mathscr{L}_{\text{eff}} = &-\frac{1}{4}F^0_{\mu\nu}F^{0,\mu\nu} \\ &+\frac{\hbar}{8\pi^2}\int_0^\infty \frac{\mathrm{d}s}{s}e^{-ism^2}e^{-\varepsilon s}\left[e^2ab\coth(eas)\cot(ebs) - \frac{1}{s^2} - \frac{1}{3}e^2(a^2-b^2)\right]\end{aligned} \tag{4.41}$$

Performing a Wick rotation and substituting $\zeta = sm^2$ yields

$$\begin{aligned}\mathscr{L}_{\text{eff}} =& \frac{a^2-b^2}{2} \\ &+ \frac{\alpha}{8\pi^2} B_{\text{QED}}^2 \int_0^\infty \frac{d\zeta}{\zeta} e^{-\zeta} \left[\frac{ab}{B_{\text{QED}}^2} \cot\left(\zeta \frac{a}{B_{\text{QED}}}\right) \coth\left(\zeta \frac{b}{B_{\text{QED}}}\right) \right. \\ &\left. + \frac{1}{\zeta^2} - \frac{1}{3} \frac{a^2-b^2}{B_{\text{QED}}^2} \right] \end{aligned} \tag{4.42}$$

where $\alpha = e^2/(\hbar c)$ and I have taken $\varepsilon \to 0$.

4.3 Index of refraction

From the effective Lagrangian, I can derive the index of refraction for low-energy photons by defining the macroscopic fields as the generalized momenta conjugate to the fields [29],

$$\mathbf{D} = \frac{\partial \mathscr{L}}{\partial \mathbf{E}} = \mathbf{E} + \mathbf{P}, \quad \mathbf{H} = -\frac{\partial \mathscr{L}}{\partial \mathbf{B}} = \mathbf{B} - \mathbf{M}, \tag{4.43}$$

and linearizing these relations about the background field [4]. For an external magnetic field this yields [89]

$$n_\parallel = 1 - \frac{\alpha}{4\pi} X_1\left(\frac{1}{\xi}\right) \sin^2\theta + \mathscr{O}\left[\left(\frac{\alpha}{2\pi}\right)^2\right] \tag{4.44}$$

$$n_\perp = 1 + \frac{\alpha}{4\pi}\left[X_0^{(2)}\left(\frac{1}{\xi}\right)\xi^{-2} - X_0^{(1)}\left(\frac{1}{\xi}\right)\xi^{-1}\right]\sin^2\theta + \mathscr{O}\left[\left(\frac{\alpha}{2\pi}\right)^2\right] \tag{4.45}$$

where $\xi = B/B_{\text{QED}}$, $n_\perp$ and $n_\parallel$ are the index if refraction for the perpendicular and parallel modes respectively (see below),

$$\begin{aligned} X_1\left(\frac{1}{\xi}\right) =& \frac{2}{3}\xi - \frac{1}{3} + 8\left[\ln A - \int_1^{1/(2\xi)+1} \ln\Gamma(v)\mathrm{d}v\right] + \frac{2}{3}\Psi\left(\frac{1}{2\xi}\right) \\ &+ \frac{1}{\xi}\left[2\ln\Gamma\left(\frac{1}{2\xi}\right) - 3\ln\xi + \ln\left(\frac{\pi}{4}\right) - 2\right] - \frac{1}{2\xi^2}, \end{aligned} \tag{4.46}$$

$$X_0^{(2)}\left(\frac{1}{\xi}\right)\xi^{-2} - X_0^{(1)}\left(\frac{1}{\xi}\right)\xi^{-1} = \frac{2}{3} + \frac{1}{\xi}\left[-2\ln\Gamma\left(\frac{1}{2\xi}\right) + \ln\xi + \ln 4\pi + 1\right] + \frac{1}{\xi^2}\left[\Psi\left(\frac{1}{2\xi}\right) - 1\right] \tag{4.47}$$

and $\ln A = \frac{1}{12} - \zeta^{(1)}(-1) \approx 0.248754477$. The functions $X_0(1/\xi)$ and $X_1(1/\xi)$ are related to the effective action and its derivative with respect to a in the limit of $a \to 0$ [90].

My naming convention is the following: if $\varepsilon^{\mu\nu\alpha\beta}F_{\mu\nu}F_{\alpha\beta} = 0$ or $\vec{E}\cdot\vec{B} = 0$, the photon is in the perpendicular mode, otherwise it is in the parallel mode, where $F_{\mu\nu}$ is the sum of field tensors of the wave and external field. In the weak field limit, $n - 1 \propto \xi^2$; while in the strong field limit $n_\parallel - 1 \propto \xi$ and $n_\perp$ approaches a constant [89]. In particular, in the weak field I get

$$n_\parallel = 1 + \frac{\alpha}{4\pi}\frac{14}{45}\xi^2\sin^2\theta \quad n_\perp = 1 + \frac{\alpha}{4\pi}\frac{8}{45}\xi^2\sin^2\theta \tag{4.48}$$

and a birefringence of

$$n_\parallel - n_\perp = \frac{\alpha}{4\pi}\frac{2}{15}\xi^2\sin^2\theta. \tag{4.49}$$

4.4 Propagation through the Birefringent Vacuum

As polarized radiation propagates through a birefringent medium, the direction of polarization changes. In particular, the evolution of the normalized Stokes vector $\boldsymbol{s} = (S_1, S_2, S_3)/S_0$ is given by (eq. 2.64, in § 2.3)

$$\frac{\mathrm{d}\boldsymbol{s}}{\mathrm{d}\lambda} = \hat{\boldsymbol{\Omega}} \times \boldsymbol{s}$$

In the case of the magnetized vacuum, the birefringence vector is given by

$$|\hat{\Omega}| = |k_0\Delta n| = \frac{\alpha}{15}\frac{\nu}{c}\left(\frac{B_\perp}{B_{\mathrm{QED}}}\right)^2 \tag{4.50}$$

where ν is the frequency of the radiation. The value of Δn is the difference in the index of refraction for the two polarization states (eq. 4.49), and the equality holds in the weak-field limit of QED. The direction of $\hat{\Omega}$ points toward the polarization of the perpendicular mode on the Poincaré sphere of polarization states.

If the magnitude of $\hat{\Omega}$ is high, the polarization modes decouple, the evolution is adiabatic and the polarization direction follows the direction of the birefringence. The condition for adiabatic evolution is given in eq. 2.65:

$$\left| \hat{\Omega} \left(\frac{\mathrm{d} \ln |\hat{\Omega}|}{\mathrm{d}\lambda} \right)^{-1} \right| \geq 0.5.$$

In Chapter 5 I will show how this effect can dramatically change the polarization of neutron stars, while in Chapter 6 I will analyze how the effect of vacuum birefringence changes the polarization of X-ray photons as they travel in the magnetosphere of accreting black holes.

Chapter 5

The Effect of Birefringence on Neutron-Star Emission

In Chapter 3, I describe how polarized radiation is generated in the atmospheres of neutron stars and in black hole accretion disks. However, as light travels through the magnetosphere of these objects, its polarization state can still change because of the effect of birefringence, and I need to account for it to understand the observed polarization. In Chapter 6, I will analyze the effect of vacuum birefringence on the polarization from black-hole accretion disks. Here, I will focus on neutron stars instead.

As described in § 2.3, the presence of a strong magnetic field can make a medium birefringent: the index of refraction in the medium depends on the angle between the polarization of the photon and the magnetic field. In the case of the magnetized vacuum, the birefringence is caused by the interaction of photons with virtual electron-positron pairs: it is easier to excite virtual electrons along the direction parallel to the magnetic field than perpendicular to it, and thus photons in the ordinary mode travel slower than photons in the extraordinary mode (see Chapter 4). If real electrons and positrons are present, they can also interact with photons and the presence of a strong magnetic field causes the plasma to be birefringent. In this chapter, I analyze the effect on polarization of vacuum birefringence (§ 5.1), of plasma birefringence (§ 5.2), and the interplay between the two effects (§ 5.2.1).

5.1 Vacuum Birefringence

In § 2.3 I showed that in a birefringent medium, in which the anisotropy is set by the magnetic field, the two polarization modes, parallel and perpendicular to the magnetic field, are decoupled if (eq. 2.65)

$$\left| \hat{\Omega} \left(\frac{\mathrm{d} \ln |\hat{\Omega}|}{\mathrm{d}\lambda} \right)^{-1} \right| \geq 0.5 \,.$$

where λ measures the length of the photon path in the medium and $\hat{\Omega}$ is the birefringence vector, given by (eq. 4.50)

$$|\hat{\Omega}| = |k_0 \Delta n| = \frac{\alpha}{15} \frac{\nu}{c} \left(\frac{B_\perp}{B_{\rm QED}} \right)^2 .$$

In this case, the evolution is called adiabatic, and the photon polarization follows the direction of the local field lines.

In the case of neutron stars, for which the magnetic field is dipolar ($B \approx \mu r^{-3}$, where μ is the magnetic dipole moment of the star and r is the distance from the center of the star) the adiabatic condition of eq. 2.65 translates into

$$\left| \frac{\alpha}{15} \frac{\nu}{c} \frac{\mu^2 \sin^2 \beta}{r^6 B_{\rm QED}^2} \frac{r}{6} \right| \geq 0.5 \tag{5.1}$$

where β is the angle between the dipole axis and the line of sight. If I define the polarization-limiting radius ($r_{\rm PL}$) to be the distance at which the equality holds, I find that the polarization will follow the direction of magnetic field out to

$$\begin{aligned} r_{\rm PL} &= \left(\frac{\alpha}{45} \frac{\nu}{c} \right)^{1/5} \left(\frac{\mu}{B_{\rm QED}} \sin \beta \right)^{2/5} \\ &\approx 1.2 \times 10^7 \left(\frac{\mu}{10^{30}\ \mathrm{G\ cm^3}} \right)^{2/5} \left(\frac{\nu}{10^{17}\ \mathrm{Hz}} \right)^{1/5} (\sin \beta)^{2/5}\, \mathrm{cm}. \end{aligned} \tag{5.2}$$

Figure 5.1 illustrates the propagation of radiation away from the surface of the neutron star toward a distant observer. For X-ray photons coming from near the surface of a neutron star with a surface field of 10^{12} G, the polarization-limiting radius is much larger than the star, according to eq. 5.2, so the observed polarization of the photons will reflect the direction of the magnetic field at a large distance from the star and not at the surface. For a much more weakly magnetized star, the polarization-limiting radius will be comparable to the radius of the star, so the observed polarization will reflect the field structure close to the star.

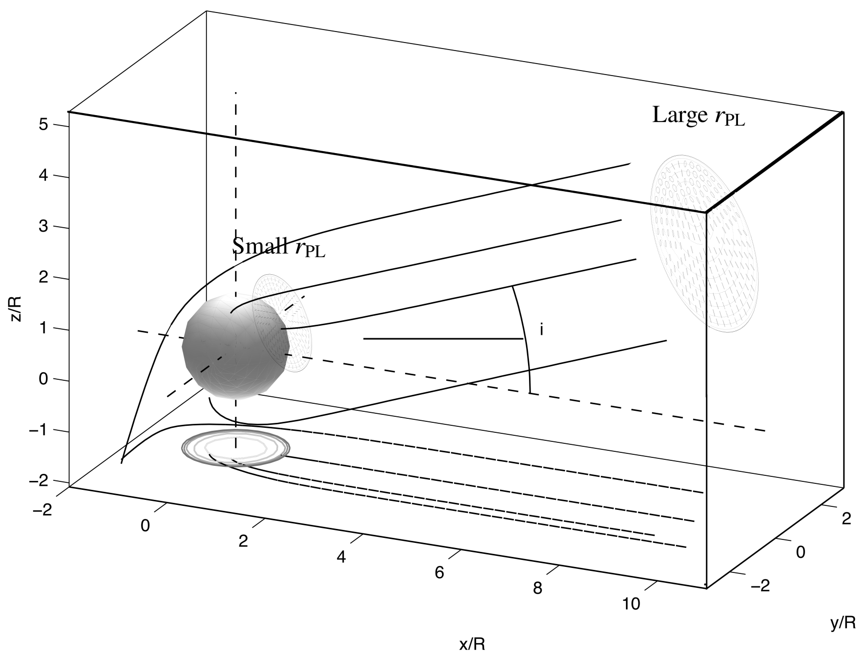

Figure 5.1: Radiation leaving the surface of a neutron star follows geodesics so that the bundle of rays that reaches the distant observer is approximately cylindrical. The three-dimensional coordinates (x, y, z) are given in terms of the radius of the neutron star (R). If the polarization-limiting radius is small, the final polarization will reflect the magnetic field structure near to the star where the bundle covers a large fraction of hemisphere so the field structure varies a lot over the bundle at this point, and the final polarization will also vary a lot over the image. On the other hand, if the polarization-limiting radius is large, the field structure over the ray bundle is simpler, and the polarization direction will not vary much over the image. Since the magnetic field is assumed to be that of a dipole (aligned with the z-axis), it has axial symmetry and different images will be distinguishable by the observer's magnetic inclination angle i. Adapted from [207].

Fig. 5.2 depicts the broadband polarization from the entire visible surface of a neutron star with a mass of 1.4 $M_\odot$, and temperature and field strength at the magnetic pole of $10^{6.5}$ K and 2×10^{12} G respectively, using the fully ionized hydrogen atmospheres discussed in § 3.2.1. The proton cyclotron line can be seen as a dip at about 10 eV, and the electron cyclotron line is at the right end, at about 22 keV. The thermal structure of neutron stars is affected by the presence of the strong magnetic field, and the thermal flux through the surface varies as $B^{0.4} \cos^2 \psi$, where ψ is the angle of the local magnetic field with respect to the normal [91, see also § 8.1.1]. The polarized fraction is plotted in terms of the total flux polarized perpendicular and parallel to the projection of the magnetic moment of the star onto the sky. A value of 1 indicates radiation fully polarized perpendicular to the moment, and -1 indicates radiation fully polarized parallel to the moment. In the upper panel, the magnetic moment makes an angle of 30 degrees with respect to the line of sight, and in the lower panel the angle is 60 degrees. In each panel, the upper set of curves traces the result including vacuum birefringence in the magnetosphere and the lower curves neglect it. Vacuum birefringence dramatically increases the expected polarization fraction after integrating over the stellar surface. With vacuum birefringence, the expected polarized fraction is larger for smaller neutron stars and larger at higher energies until one approaches the cyclotron resonance. The trend with stellar radius is simply due to the fact that the bundle of rays for smaller stars is smaller so it subtends a smaller fraction of the magnetosphere at the polarization-limiting radius; furthermore, as the energy of the photons increases, the polarization-limiting radius also increases, increasing the expected polarized fraction. Without vacuum birefringence, both of these trends are reversed. Furthermore, the polarized fraction is larger when the magnetic field makes a larger angle with the line of sight. If one assumes that the flux is largest when the magnetic field is closest to the line of sight, one would expect the polarized fraction and the flux to be somewhat anti-correlated. In particular, the off-pulse radiation is more polarized than on pulse, so polarized emission off-pulse may come from the neutron star itself rather than the background.

Table 5.1 lists several classes of possible sources and their polarization limiting radii. For the magnetars and XDINS, the polarization-limiting radius is much larger than the radius of the star. As the emission in these sources is expected

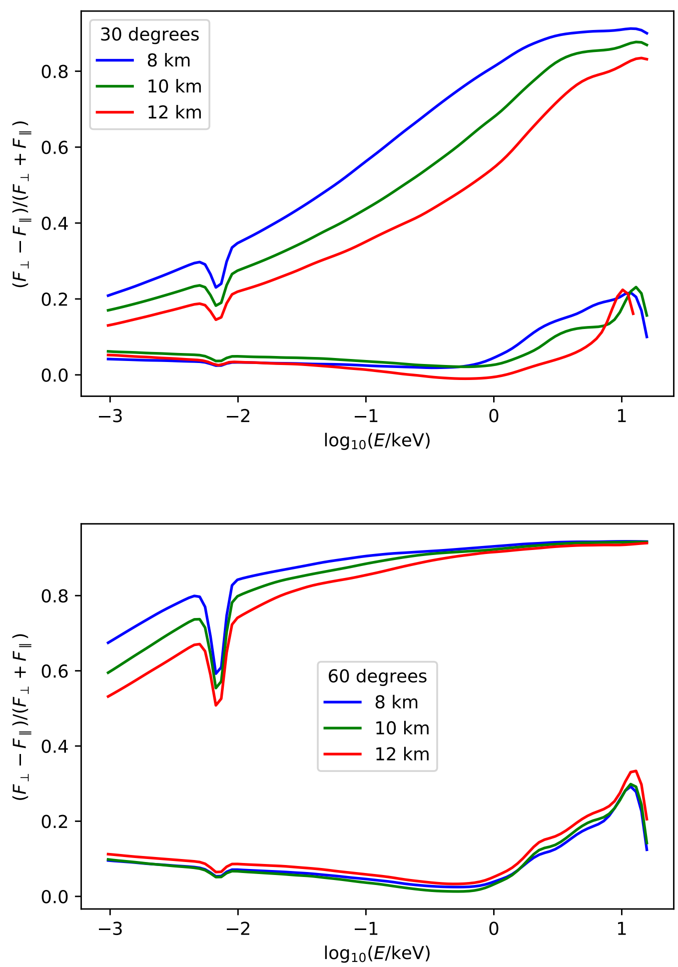

Figure 5.2: The extent of the polarization averaged over the stellar surface as a function of energy, angle and stellar radius using the fully ionized hydrogen atmospheres discussed in § 3.2.1. Here, the perpendicular direction is defined to be perpendicular to the projection of the magnetic moment of the star into the sky. In the upper panel, the magnetic pole makes an angle of 30° with the line of sight. In the lower panel, the angle is 60°. The lower set of curves trace the results without vacuum polarization, and the results for the upper curves include it.

to come from a larger region of the stellar surface or magnetosphere (in the case of the non-thermal emission from magnetars [219]), a large increase in the observed polarization fraction due to QED is also expected. Although the ratio of the polarization-limiting radius to the stellar radius is also large for the X-ray pulsars (XRP), as we shall see in Chapter 7, the effect for these objects is more subtle. The QED effects for more weakly magnetized stars such as millisecond XRPs (ms XRPs) and strongly magnetized white dwarfs have not yet been explored. Chapter 6 focuses on the effect of QED on accreting black holes [see also 37, 38].

Table 5.1: The expected polarization-limiting radii for various sources; the typical observing times are for eXTP at 2–8 keV for the magnetars (4U 0142+61) and XRPs (Her X-1) from the text and for RedSOX [64] at 0.2–0.8 keV for RX J1856.5-3754 to make a four-sigma detection.

	R [cm]	**B [G]**	$\boldsymbol{\mu}$ **[G cm^{-3}]**	$\boldsymbol{r}_{\rm pl}$ **at 4 keV [cm]**	$\boldsymbol{r}_{\rm pl}/\boldsymbol{R}$	$\boldsymbol{t}_{\rm obs}$
Magnetar	10^6	10^{15}	10^{33}	3.0×10^8	300	10 ks
XDINS	10^6	10^{13}	10^{31}	4.7×10^7	50 *	1 ks
XRP	10^6	10^{12}	10^{30}	1.9×10^7	20	100 ks
ms XRP	10^6	10^9	10^{27}	1.2×10^6	1.2	
AM Her	10^9	10^8	10^{35}	1.9×10^9	1.9	
Black Hole	10^{6+}	?	N/A	See Chapter 6		

* XDINS have little emission at 4 keV, and therefore will be difficult to observe with eXTP and IXPE. The value of $r_{\rm pl}/R$ at 0.4 keV is 32, so vacuum birefringence is important for observations with soft-X-ray polarimeters.

5.1.1 The Quasi-tangential effect

Figure 5.3 depicts the final polarization states across the image of the neutron star surface assuming that the radiation is initially in the extraordinary mode, that is, the electric field is perpendicular to the local magnetic field. The left panel shows the case where the vacuum birefringence is neglected, and the right panel show the case where the surface field is about 10^{12} G and the frequency is 10^{17} Hz or an energy of about 0.4 keV. This is appropriate for a thermally emitting neutron star such as one of the X-ray dim neutron stars (XDINS). The effect of the vacuum polarization is to comb the polarization direction to be aligned with the direction of the magnetic

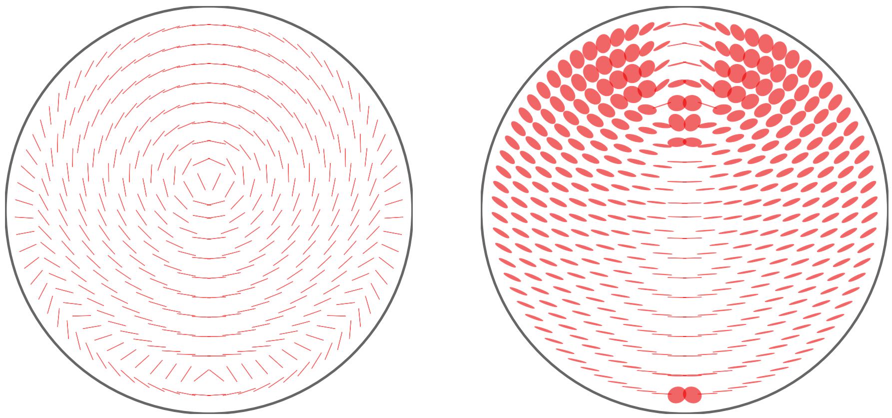

Figure 5.3: The polarized emission map of a neutron star overlaid on the apparent image of the NS. The left panel depicts the observed map of polarization directions if one assumes that the surface emits only in the extraordinary mode (perpendicular to the local field direction) and neglects the vacuum birefringence induced by QED. The right panel shows the polarization map including birefringence for a frequency of $\nu = (\mu/(10^{30}\mathrm{G\,cm}^3))^{-2}10^{17}$ Hz. The ellipses and short lines describe the polarization of a light ray originating from the surface element beneath them. The lines and the major axes of the ellipses point towards the direction of the linear component of the polarization direction. The minor to major axis ratio provides the amount of circular polarization (s_3). The observer's line of sight makes an angle of 30° with the dipole axis. For comparison, if one assumes that the entire surface is emitting fully polarized radiation, the net linear polarization on the left sums up to about 13%, while it is 70% on the right.

axis of the star and dramatically increase the observed total polarization from about 13% to about 70%. For more strongly magnetized neutron stars the effect is more dramatic. Linearly polarized radiation can also be converted to circularly polarized radiation, if the radiation happens to pass through the polarization-limiting radius when it is propagating approximately tangential to the field (in Fig. 5.3 this effect is shown by the ellipses near the polar cap in the right panel). This is called the Quasi-Tangential effect.

In their 2009 paper, Wang and Lai [237] showed that the polarization of X-ray photons can change significantly when they cross the quasi-tangential (QT) point, where the photon momentum is nearly aligned with the magnetic field, and that the net effect, when averaged over a finite emission area, is to decrease the fraction of linear polarization.

Not all light rays go through a real tangential point, where the photon wavevector $\boldsymbol{k}$ is perfectly aligned with the local magnetic field direction; however, there is always a point in the photon path, called QT point, where the angle between $\boldsymbol{k}$ and $\boldsymbol{B}$, θ_B, reaches a minimum. The magnetic field around the QT point can be expressed, without loss of generality, as

$$B_X = \frac{B}{\mathscr{R}} s, \quad B_Y = \varepsilon B \tag{5.3}$$

in the fixed XYZ frame where $\hat{\boldsymbol{Z}} \parallel \hat{\boldsymbol{k}}$. Here $\mathscr{R}$ is the curvature radius of the projected magnetic field line in the $X-Z$ plane and s measures the distance from the QT point along the $Z-$ axis. At the QT point, $s = 0$ and $\varepsilon = \sin\theta_B$. Depending on the strength of the vacuum birefringence at the QT point, the outcome for the polarization of the photon crossing the point can be different.

In § 2.3 I have shown that whenever the vacuum birefringence dominates the photon polarization modes are decoupled and evolve independently following the local magnetic field lines (eq. 2.65). Wang and Lai [237] introduced an equivalent condition to eq. 2.65, which states that the photon modes are decoupled if $\Gamma_{\rm ad} \gg 1$ (eq. 2.12 in [237]), where they call $\Gamma_{\rm ad}$ the adiabaticity parameter. The value of $\Gamma_{\rm ad}$ at the QT point is given by (eq. 3.22 in [237])

$$\Gamma_t \simeq 1.0 \times 10^8 E_1 B_{13}^2 \varepsilon^3 \mathscr{R}_1 \tag{5.4}$$

where $E_1 = E_p/(1 \text{ keV})$, $B_{13} = B/(10^{13} \text{ G})$ and $\mathscr{R}_1 = \mathscr{R}/(10 \text{ km})$. Wang and Lai [237] show that in both limiting cases of adiabatic ($\Gamma_t \gg 1$) and non-adiabatic ($\Gamma_t \ll 1$) propagation, the polarization direction is unchanged when the photon traverses the QT point. The only interesting effect is for the intermediate case, $\Gamma_t \sim 1$. In this latter case, even if a photon is in a pure mode prior to QT crossing, it will come out of the QT region in a mixture of the two modes.

In the same paper, Wang and Lai [237] give a prescription to account for the

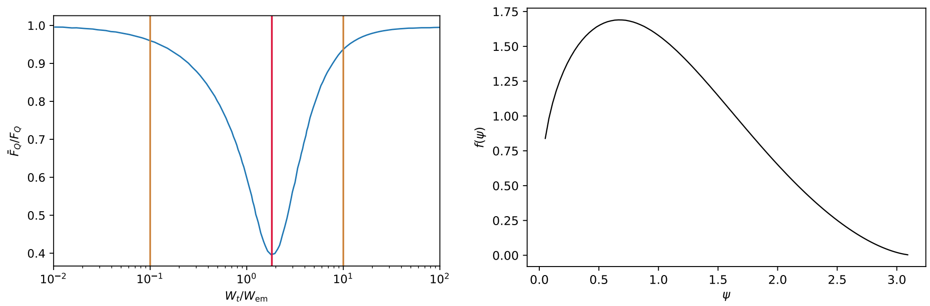

Figure 5.4: Left panel: the depolarization effect of QT propagation on linear polarization; W_t is the width of the QT effective region, W_{em} is the width of the emission region and F_Q ($\bar{F}_Q$) is the polarized radiation flux before (after) traversing the QT region. Same as Figure 11 in [237]. The vertical beige lines highlight the region where the effect is stronger, and the red vertical line pinpoints the peak of the effect, at $W_t/W_{\text{em}} \sim 1.82$. Right panel: the function $f(\psi)$, which in [237] is called $f(\theta_{\mu_i})$.

QT effect in case of a dipolar field. In particular, they calculate the effect on the emission coming from the polar cap. They find that the region in which the QT effect is important is the region where $\Gamma_t \lesssim 3$ and the width of this region can be expressed as (eq. 4.32 in [237])

$$W_t \simeq 2.7 \times 10^{-2} (B_{*13}^2 E_1)^{-1/3} f(\psi) R_* \tag{5.5}$$

where B_* is the magnetic field at the pole and $f(\psi)$ is a dimensionless function of the angle between the magnetic axis and the line of sight, which they call θ_{μ_i} and which I will be calling ψ in Chapter 7. Once the width of the QT effective region has been calculated, the linearly polarized radiation flux ($\bar{F}_Q$) can be obtained from the ratio between the width of the QT effective region (W_t) and the emission region (W_{em}); the numerical result, taken from Figure 11 of [237], is shown in the left panel of Figure 5.4, where F_Q is the flux of linearly polarized radiation prior to passing the QT region.

In [237], the authors are only interested in $\psi < 90°$, while in the cases of interest of this work, ψ can be higher than that. For this reason, I have calculated $f(\psi)$ for all angles. First, I define r_{qt} as the distance from the center of the star to the QT point. I indicate with δ the angle between the magnetic axis and $r_{\rm qt}$, and since the magnetic field is dipolar, the relation between δ and ψ is given by

$$\cos^2(\psi - \delta) = \frac{4\cos^2\delta}{3\cos^2\delta + 1} \tag{5.6}$$

The relation between the impact parameter b and $r_{\rm qt}$ is

$$r_{\rm qt}\sin(\psi - \delta) = b = (R_* + z)\sin\psi \tag{5.7}$$

where z is the height above the star of the part of the column that we are considering. This yields

$$r_{\rm qt} = \frac{(R_* + z)\sin\psi}{\sin(\psi - \delta)} \tag{5.8}$$

I can write the dipolar field as (eq. 4.28 of [237])

$$\boldsymbol{B} = -\frac{\boldsymbol{\mu}}{r_{\rm qt}^3} + \frac{3\boldsymbol{r}_{\rm qt}}{r_{\rm qt}^5}(\boldsymbol{\mu}\cdot\boldsymbol{r}_{\rm qt}) \tag{5.9}$$

where r is the distance from the center of the star, and since at the QT point $\mu_y = 0$

$$B_y = \frac{3y_{\rm qt}}{r_{\rm qt}^5}\mu r_{\rm qt}\cos\delta \tag{5.10}$$

The field strength at the QT point is related to the field strength at the pole by

$$B = B_*\left(\frac{R_*}{r_{\rm qt}}\right)^3\left(\frac{3\cos^2\delta + 1}{4}\right)^{1/2}, \quad \text{and} \quad B_* = \frac{2\mu}{r_{\rm qt}^3} \tag{5.11}$$

This yields

$$\varepsilon = \frac{B_y}{B} = \frac{3y_{\rm qt}}{r_{\rm qt}}\frac{\cos\delta}{(3\cos^2\delta + 1)^{1/2}} \tag{5.12}$$

From ε, I can find the width of the QT region

$$\frac{W_t}{R_*} = \frac{2y_{\rm qt}}{R_*} = \varepsilon\frac{2r_{\rm qt}}{3R_*}\frac{(3\cos^2\delta + 1)^{1/2}}{\cos\delta} \tag{5.13}$$

From eq. 5.4, I can determine the value of ε for which $\Gamma_t \lesssim 3$

$$\varepsilon(\Gamma_t = 3) = (3 \times 10^{-8})^{1/3} * (E_1 B_{13}^2 \mathscr{R}_1)^{-1/3} \tag{5.14}$$

I still need the radius of curvature $\mathscr{R}$, which for a dipolar magnetic field reads

$$\mathscr{R} = \frac{r_{\rm qt}}{3} \frac{(3\cos^2\delta + 1)^{3/2}}{|\sin\delta|(\cos^2\delta + 1)} \tag{5.15}$$

I finally have all the ingredients to find $f(\psi)$ of eq. 5.5

$$f(\psi) = 7.7 \times 10^{-2} \left(\frac{r_{\rm qt}}{R_*}\right)^{8/3} \left(\frac{10\,\mathrm{km}}{R_*}\right)^{1/3} \left(\frac{12|\sin\delta|(\cos^2\delta + 1)}{\cos^3\delta(3\cos^2\delta + 1)}\right)^{1/3} \tag{5.16}$$

where the relation between ψ and δ is given in eq. 5.6. This result is shown in the right panel of Figure 5.4 and it reproduces the function $f(\theta_{\mu_i})$ shown in Figure 10 of [237] for $\psi = \theta_{\mu_i} < 90°$.

If one integrates eq. 2.64 along the photon path, the QT effect will come naturally from the integration, as can be seen in Fig. 5.3. However, the numerical result obtained in this section will be useful in § 7.2, where the only effect of the vacuum birefringence is due to the QT effect and there is no need to integrate eq. 2.64 for each photon path.

5.2 Plasma Birefringence

At low photon energies or high plasma densities, the plasma may play an important role in the propagation of polarized radiation through the atmospheres and magnetospheres of neutron stars and black holes. The typical energy where plasma and vacuum trade off, if one assumes that the density of the plasma is approximately the Goldreich and Julian [73] density, is in the infrared, but it will increase with the density of the plasma. If the magnetosphere carries substantial currents as in magnetars [e.g. 228], the effect of the plasma will be more important. The combination of plasma and vacuum birefringence results in an eigenvalue equation for the complex amplitudes of the electric field [148],

$$\begin{bmatrix} \eta_{xx} - n^2 & \eta_{xy} \\ \eta_{yx} & \eta_{yy} - n^2\rho \end{bmatrix} \begin{bmatrix} E_x \\ E_y \end{bmatrix} = 0 \tag{5.17}$$

where η_{ij} are components of the dielectric tensor and I have assumed that the photon propagates along the $z-$axis and that the magnetic field lies in the $x-z-$plane. The parameter ρ,

$$\rho = 1 - \frac{4\alpha_{\rm QED}}{45\pi}\left(\frac{B}{B_{\rm QED}}\right)^2 \sin^2\theta, \tag{5.18}$$

accounts for the magnetization of the vacuum and the tensor η characterizes the dielectric response of the plasma and vacuum. Since I am considering photon frequencies well above the plasma frequency ($\omega \gg \omega_p = \sqrt{4\pi e^2 n/m}$) and below the cyclotron resonance ($\omega < \omega_c = eB/(mc)$), the eigenvalues of the matrix, n_1^2 and n_2^2, are of the order unity. These conditions hold in the neutron star magnetosphere for the photon energies from the visual to the X-rays but do not necessarily hold in the atmosphere.

I can employ the formalism of Kubo and Nagata [120] (§ 2.3) by noting that the magnitude of $\hat{\Omega}$ is related to the two eigenvalues of the matrix ($n_{1,2}^2$), in particular $|\hat{\Omega}| = k_0\left|\Delta n_{\parallel\perp}\right|$ where

$$\begin{aligned} \Delta n_{\parallel\perp} &= n_\parallel - n_\perp = \frac{n_\parallel^2 - n_\perp^2}{n_\parallel + n_\perp} \approx \frac{n_\parallel^2 - n_\perp^2}{2} & (5.19)\\ &\approx \frac{1}{2}\left[\left(\eta_{xx} - \rho^{-1}\eta_{yy}\right)^2 + 4\rho^{-1}|\eta_{xy}|^2\right]^{1/2} & (5.20)\\ &\approx \sin^2\theta\left[\frac{\alpha_{\rm QED}}{30\pi}\left(\frac{B}{B_{\rm QED}}\right)^2 - \frac{1}{2}\frac{\omega_p^2}{\omega^2}\frac{\omega_c^2}{\omega_c^2-\omega^2}\right] & (5.21)\\ &\approx \sin^2\theta\frac{\alpha_{\rm QED}}{30\pi}\left(\frac{B}{B_{\rm QED}}\right)^2\left[1 - \frac{\omega_p^2}{\omega^2}\frac{1}{v_r}\right] & (5.22) \end{aligned}$$

where

$$v_r = \frac{\alpha_{\rm QED}}{15\pi}\left(\frac{B}{B_{\rm QED}}\right)^2\frac{\omega_c^2-\omega^2}{\omega_c^2} \tag{5.23}$$

and where I have assumed $n_1, n_2 \approx 1$.

If $\omega^2 v_r \approx \omega_p^2$, the value of $\Delta n_{\parallel\perp}$ vanishes; in this regime (close to the vacuum resonance), the modes of the plasma plus vacuum are approximately circular and in the resonance, the difference in index of refraction between the two helicities is given by

$$\Delta n_{\pm,\mathrm{res}} = [n_+ - n_-]_{\mathrm{res}} = -\cos\theta \frac{\omega\omega_p^2}{\omega_c\left(\omega^2 - \omega_{c,i}^2\right)}. \tag{5.24}$$

where $\omega_{c,i} = Z_i eB/(m_i c)$ is the ion cyclotron frequency. In general, the helicity of the photon is an adiabatic invariant for the polarization states and

$$(\Delta n_\pm)^2 = (\Delta n_{\pm,\mathrm{res}})^2 + \left(\Delta n_{\parallel\perp}\right)^2 \tag{5.25}$$

The direction of $\hat{\Omega}$ is given by the direction of the eigenvector with the larger eigenvalue on the Poincaré sphere. The eigenvectors of eq. 5.17 yield the polarization vectors

$$\vec{e}_+ = [i\cos\theta_m, \sin\theta_m, 0]\,,\ \vec{e}_- = [-i\sin\theta_m, \cos\theta_m, 0]\,. \tag{5.26}$$

where I have labelled the states by their helicity rather than parallel and perpendicular. The angle θ_m lies between 0 and $\pi/2$ and characterizes the mixing between the parallel and perpendicular polarization states. For $\theta_m = 0$, the electric field in the $+$ state is parallel to the $x-$axis and for $\theta_m = \pi/2$, it is parallel to the $y-$axis. I can determine the value of θ_m from the ratio of the linear to the circular portion of the birefringence

$$\tan 2\theta_m = \frac{\Delta n_{\pm,\mathrm{res}}}{\Delta n_{\parallel\perp}}. \tag{5.27}$$

I map $\vec{e}_1$ onto the Poincaré sphere using the definitions

$$I = S_0 = |\vec{e}_1 \cdot \hat{x}|^2 + |\vec{e}_1 \cdot \hat{y}|^2 = 1 \tag{5.28}$$

$$Q = S_1 = |\vec{e}_1 \cdot \hat{x}|^2 - |\vec{e}_1 \cdot \hat{y}|^2 = \cos 2\theta_m \tag{5.29}$$

$$U = S_2 = \left|\vec{e}_1 \cdot \frac{1}{\sqrt{2}}(\hat{x}+\hat{y})\right|^2 - \left|\vec{e}_1 \cdot \frac{1}{\sqrt{2}}(\hat{x}-\hat{y})\right|^2 = 0 \tag{5.30}$$

$$V = S_3 = \left|\vec{e}_1 \cdot \frac{1}{\sqrt{2}}(\hat{x}+i\hat{y})\right|^2 - \left|\vec{e}_1 \cdot \frac{1}{\sqrt{2}}(\hat{x}-i\hat{y})\right|^2 = \sin 2\theta_m, \tag{5.31}$$

yielding the direction of $\hat{\mathbf{\Omega}}$ on the Poincaré sphere. Finally this yields

$$\hat{\mathbf{\Omega}} = |\Delta n_\pm| \frac{\omega}{c} \begin{bmatrix} \cos 2\theta_m \\ 0 \\ \sin 2\theta_m \end{bmatrix}. \tag{5.32}$$

I find that $|\Delta n_{\|\perp}| \gg \Delta n_{\pm,\mathrm{res}}$ is large so the modes of the plasma and vacuum are linear except in the vicinity of the cyclotron resonance and of the two vacuum resonance frequencies, where $\Delta n_{\|\perp} \approx 0$.

In the neutron star magnetosphere, we expect the net charge density of the plasma to be at least the Goldreich and Julian [73] density $\rho = -\vec{\Omega} \cdot \vec{B}/(2\pi c)$. The total charge density could be some multiple ζ (the multiplicity) of this, yielding an estimate of the local plasma frequency of

$$\omega_p = (2\zeta\Omega\omega_c|\cos\beta|)^{1/2} = 14.88 \text{ GHz}(\zeta\cos\beta)^{1/2}\left(\frac{P}{1 \text{ s}}\right)^{-1/2}\left(\frac{B}{10^{12} \text{ G}}\right)^{1/2} \tag{5.33}$$

where β is the angle between the spin axis and the magnetic field direction locally. The first vacuum resonance energy in the magnetosphere is typically at

$$\hbar\omega_{v,1} = 0.068 \text{ eV}(\zeta\cos\beta)^{1/2}\left(\frac{P}{1 \text{ s}}\right)^{-1/2}\left(\frac{B}{10^{12} \text{ G}}\right)^{-1/2}. \tag{5.34}$$

The vacuum resonance energy increases as $r^{3/2}$ further into the magnetosphere if the density follows the Goldreich-Julian expresion and the magnetic field is dipolar.

Although the plasma density may be sufficiently large for this energy to reach into the visual range ($\zeta \sim 10^3$), I do not expect the magnetospheric density to be large enough ($\zeta \sim 10^8$) for this energy to reach the X-ray regime; in this case the magnetosphere would become somewhat opaque even outside of the resonant energies (see § 5.2.1 for the role of plasma birefringence in the atmosphere).

Below the vacuum resonance energy, the plasma dominates the birefringence and I can calculate the magnitude of the birefringent vector

$$|\hat{\mathbf{\Omega}}| = \zeta |\cos\beta| \frac{\Omega\omega_c}{\omega c} \sin^2\theta. \tag{5.35}$$

The polarization-limiting radius for low photon energies will be determined by the plasma birefringence. On the other hand, for radiation in the visual and blueward for pair multiplicities less than 10^3, the vacuum birefringence dominates the evolution of the polarization in the magnetosphere, and the magnitude of the birefringence vector can be calculated from eq. 2.64.

This section considered just the weak-field limit. The strong-field limit is somewhat more complicated. For a detailed treatment of the propagation of radiation through the combined plasma and vacuum for arbitrary fields consult [98, 123].

5.2.1 The vacuum resonance in the neutron-star atmosphere

As the density of plasma in the atmosphere is much larger than in the magnetosphere, the energy of the vacuum resonance is also much larger and typically in the range of X-ray energies. Therefore, it may be important for the propagation of X-ray radiation above the photosphere. At the resonance

$$\hbar\omega_v = \hbar\omega_p v_r^{-1/2} = 2.0 \left(\frac{n}{10^{22}\mathrm{cm}^{-3}}\right)^{1/2} \frac{10^{12}\ \mathrm{G}}{B}\ \mathrm{keV}. \tag{5.36}$$

Deep within the atmosphere, the density is large and the birefringence is dominated by the plasma: $\Delta n_{\|\perp} < 0$, $|\Delta n_{\|\perp}| \gg \Delta n_\pm$ and $2\theta_m \approx \pi$. We can see from eq. 5.28 to 5.31 that, in this regime, the polarization modes are linear: $S_1 = -1$ and $S_3 = 0$; also, the $+$ mode is polarized along the y-axis (perpendicular to the magnetic field). As the radiation in the $+$ mode propagates upward and through the vacuum resonance, it will remain in the $+$ mode if the condition of eq. 2.65 holds (the adiabatic criterion). At low densities the vacuum dominates so $\Delta n_{\parallel\perp} > 0$, $2\theta_m \approx 0$ and therefore, for the $+$ mode, $S_1 = 1$ and $S_3 = 0$. As the photon crosses the resonance, the polarization is transformed from perpendicular to parallel.

I can calculate whether the adiabatic criterion holds as the radiation passes through the vacuum resonance. The index of refraction difference reaches a minimum value of $\Delta n_{\pm,\mathrm{res}}$ at the resonance precisely. In the resonance, the change in the value of $\hat{\boldsymbol{\Omega}}$ is entirely in its direction at a rate of $2\theta_m' = (\Delta n_{\parallel\perp})'/\Delta n_{\pm}$ so we have

$$\begin{aligned}
\left|\hat{\boldsymbol{\Omega}}\left(\frac{1}{|\hat{\boldsymbol{\Omega}}|}\left|\frac{\partial\hat{\boldsymbol{\Omega}}}{\partial x_3}\right|\right)^{-1}\right| &= \left|\frac{\omega}{c}\frac{(\Delta n_{\pm,\mathrm{res}})^2}{\left(\Delta n_{\parallel\perp}\right)'}\right| \qquad (5.37)\\
&= \frac{\omega}{c}H_\rho\left[\cos\theta\frac{\omega\omega_p^2}{\omega_c\left(\omega^2-\omega_{c_i}^2\right)}\right]^2\left[\sin^2\theta\frac{\alpha_{\mathrm{QED}}}{30\pi}\left(\frac{B}{B_{\mathrm{QED}}}\right)^2\right]^{-1}\\
&= \frac{\omega^3}{c}H_\rho\left[\frac{\cot\theta}{\omega_c\left(1-\frac{\omega_{c,i}^2}{\omega^2}\right)}\right]^2\frac{2\alpha_{\mathrm{QED}}}{15\pi}\left(\frac{B}{B_{\mathrm{QED}}}\right)^2 = \left(\frac{E_\gamma}{E_{\mathrm{ad}}}\right)^3.
\end{aligned}$$

This yields the abiabatic energy [98, 123]

$$E_{\mathrm{ad}}^3 = \frac{15\pi}{2\alpha_{\mathrm{QED}}}\left(1-\frac{\omega_{c,i}^2}{\omega^2}\right)^2\tan^2\theta\frac{\hbar c}{H_\rho}\left(mc^2\right)^2 \approx (2.6\ \mathrm{keV})^3\left(1-\frac{\omega_{c,i}^2}{\omega^2}\right)^2\tan^2\theta\frac{1\ \mathrm{cm}}{H_\rho} \qquad (5.38)$$

where H_ρ is the density scale height along the ray (in the $\hat{k}$ direction), typically $kT/(Am_u\hat{k}\cdot\vec{g}) \approx 8$ mm for a temperature $T = 10^6$K, surface gravity $\hat{k}\cdot\vec{g} = 10^{14}$ cm s^{-2} and for hydrogen atmosphere, $A = 0.5$.

If one considers blackbody emission, for effective temperatures greater than about 5×10^6 K, the energy of the typical photon is greater than the adiabatic energy, so much of the radiation will pass through the resonance adiabatically. Typically, light element atmospheres peak at higher photon energies than $3kT_{\mathrm{eff}}$, so the effect would be even more pronounced. If the vacuum resonance occurs in the neutron star above both the photosphere for parallel polarization and the photosphere for perpendicular polarization (which I found in § 3.2.1), the main effect is to switch the polarization coming from the surface from mostly perpendicular to the magnetic field to mostly parallel, if the energy of the photon is greater than $E_{\rm ad}$. Below this energy, the polarization would remain perpendicular.

For sufficiently strongly magnetized neutron stars (magnetars), the vacuum resonance lies above the photosphere for radiation polarized perpendicular to the magnetic field and below the photosphere for parallel photons. In this case, the effective photosphere for perpendicularly polarized photons with energies greater than the adiabatic energy will lie at the vacuum resonance itself which is at a lower temperature than the photosphere for low-energy perpendicularly polarized radiation. Even in this case, the bulk of the radiation will emerge in the perpendicular polarization, and the emission of parallel photons will be diminished for photon energies above the vacuum resonance energy at the photosphere. I can estimate the number density of electrons at the photosphere for the parallel polarization to be $n \approx (\sigma_T H_\rho)^{-1}$ so

$$\hbar\omega_{v,\|} \approx 4 \text{ keV} \left(\frac{B}{B_{\rm QED}}\right)^{-1} \left(\frac{g}{10^{14}\text{cm s}^{-2}}\right)^{1/2} \left(\frac{T}{10^6 \text{ K}}\right)^{-1/2}. \qquad (5.39)$$

Although this equation is not accurate for magnetic fields approaching or exceeding $B_{\rm QED}$, one can see that the role of the vacuum resonance in the formation of the spectrum will be crucial for the magnetars where the magnetic field exceeds $B_{\rm QED}$ and the temperatures exceed several million degrees. The number density at the photosphere for the perpendicular polarization is larger by a factor of ω^2/ω_c^2, giving the energy of photons in the vacuum resonance at this surface of

$$\hbar\omega_{v,\perp} \approx 45 \text{ keV} \left(\frac{g}{10^{14}\text{cm s}^{-2}}\right)^{1/4} \left(\frac{T}{10^6 \text{ K}}\right)^{-1/4} \qquad (5.40)$$

or approximately the electron cyclotron energy, whichever is smaller.

Fig. 5.5 illustrates how the vacuum resonance affects the location of the photosphere for the perpendicular mode photons. At low energies, the photosphere lies at a density where the plasma frequency equals the frequency of the photon, then it runs at nearly constant density punctuated by a dramatic drop in the density at the proton cyclotron line and then above the adiabatic energy it follows the density at which photon frequency equals the vacuum resonance energy (this is a

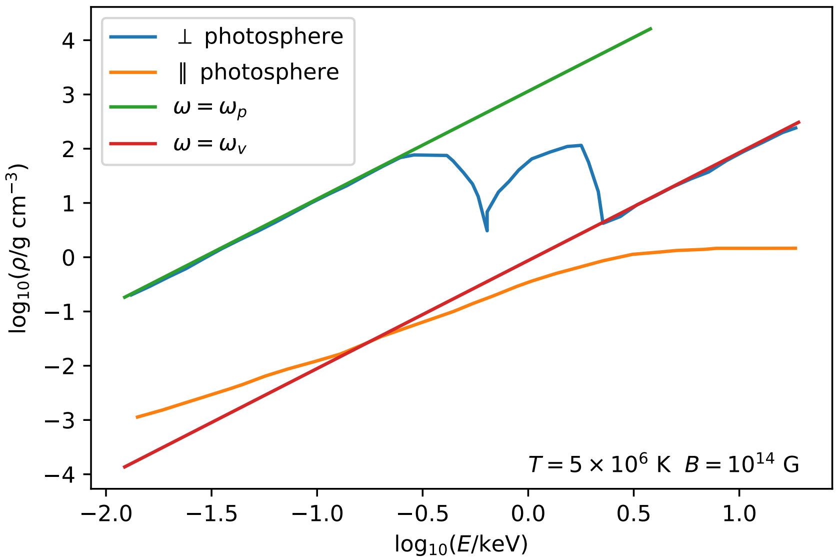

Figure 5.5: An illustration of the locations of the parallel and perpendicular model photospheres for $B = 10^{14}$ G and $T = 5 \times 10^6$ K using the models of Lloyd [130]. This is similar to Fig. 3.2, but for the strong field case. The proton cyclotron line has moved into the X-rays; the key new thing is that the $\perp$-mode photosphere lies along the vacuum resonance line at high energies, because the $\perp$-mode photons have a significant parallel component at the vacuum resonance so the opacity for them is really high there. The vacuum resonance is effectively their photosphere. In fact a significant amount of energy is deposited in this layer so it forms a local maximum in the temperature of the atmosphere.

constant multiple of the plasma frequency that depends on the strength of the magnetic field). For photons above the adiabatic energy, the structure of the atmosphere is rather complicated. At high densities, where the birefringence is plasma dominated, but not so high that the the plasma is opaque to photons in the perpendicular mode, the bulk of the energy flux is carried by photons in the perpendicular mode, while those in the parallel mode are trapped. As the radiation approaches the density of the vacuum resonance, both the photons in the parallel mode and those in the perpendicular mode become circularly polarized and both couple strongly to the plasma. At the resonance density, the flux carried in the perpendicular mode is dumped back into the plasma. Just below the resonance density the modes become mainly linear again, so the perpendicular mode is no longer well coupled to the plasma and again travels freely, and the photosphere for the perpendicular mode follows the vacuum resonance density above the adiabatic energy. For stronger magnetic fields, the proton cyclotron line can lie above the adiabatic energy, so the structure of the line, even without polarization information, will be affected by the resonance [98].

This picture, in which above the adiabatic energy the radiation behaves adiabatically and below this energy it does not, is a gross approximation. In detail, the behaviour near the vacuum resonance will also depend on the imaginary portion of the index of refraction [148, 178], and the entire mode description may collapse. How to treat photons passing through the vacuum resonance within the atmosphere is still uncertain, and it is often treated as such in the calculations [76, 98, 123, 249]. However, it is clear that when the radiation passes through the vacuum resonance outside the atmosphere, as in more weakly magnetized stars (see Fig. 3.3), the resonance can switch the final polarization state of the radiation depending on whether the energy lies above or below the adiabatic energy, leaving an imprint of the local density scale height on the outgoing radiation, which could be a powerful diagnostic of the surface gravity in the polarization of the outgoing radiation.

Chapter 6

QED and Polarization from Accreting Black holes

6.1 Introduction

In the theory of accretion disks around black holes and astrophysical accretion in general, magnetic fields play a crucial role. They are expected to be the main source of shear stresses, without which accretion cannot occur [8, 205]. Moreover, magnetic fields in the inner regions of black-hole accretion disks are thought to lead to the formation of relativistic jets through the Penrose–Blandford–Znajek mechanism [31, 220]. As I already mentioned in § 1.2.4, however, direct measurements of the magnetic field strength and structure in the accretion disk of a black hole are hard, and the only estimates to date come from the spectral analysis of the winds from two Galactic stellar-mass black holes [154, 155, 157], and they probe only the field quite far from the horizon.

The first estimate of the structure of the magnetic field close to the event horizon of a black hole comes from polarimetric studies of the radio emission from Sagittarius A*, the supermassive black hole at the center of the Milky Way [105]. In this Chapter, I show that X-ray polarimetry could provide an additional tool to probe the strength and structure of the magnetic field close to the event horizon of accreting black holes if the effect of vacuum birefringence is properly accounted for in the modeling of the polarization.

If only classical electrodynamics is considered, at energies higher than 1–2 keV, the polarization of a photon emitted by the accretion disk is not affected by the presence of a magnetic field. The linear polarization of X-ray photons stays the same as they travel through the magnetosphere of the hole all the way to the observer. At lower photon energies, the presence of a magnetized corona could destroy the linear polarization of X-ray photons due to the effect of plasma birefringence [52, 149] (see § 6.3.1). In quantum electrodynamics (QED), the vacuum is also expected to be birefringent in presence of a magnetic field. This effect, which was one of the first predictions of QED, has never been proven. Recent observations of the visible polarization from a radio-quiet neutron star [152] have strongly hinted that vacuum birefringence is indeed affecting the photons' polarization. If the vacuum is indeed birefringent, after photons are emitted from the disk, their polarization will change as they travel through the magnetized vacuum. A detailed derivation of the vacuum birefringence in QED is described in Chapter 4.

In this Chapter, I assume the strength of the magnetic field in the accretion disk to be the minimum needed for accretion to occur if an α-model structure of the disk is considered. I find that the effect of vacuum birefringence on the photon polarization becomes important, depending on the angular momentum of the black hole and that of the photon, around 10 keV, for both stellar-mass and supermassive black holes. A stronger (weaker) field would shift this range to lower (higher) energies. Observation of the X-ray polarization from accretion disks in the 1–30 keV range, if properly modeled with QED, would both probe the strength of the magnetic field and test the currently accepted models of astrophysical accretion.

6.2 Accretion disk model

Black-hole accretion disks are rarefied; thus, angular momentum transfer due to molecular viscosity is inefficient and cannot lead to accretion [184]. In current theories of astrophysical accretion disks, magnetic fields and turbulence are expected to be the source of shear stresses. In this section, I will calculate the minimum magnetic field strength needed for accretion to occur in a α-model disk [205]. The relation between the tangential stresses between layers in the disks and the magnetic field is given by [205]

$$t_{\hat{\phi}\hat{r}} = \rho c_s v_t + \frac{B^2}{4\pi} = \alpha P \tag{6.1}$$

where ρ is the mass density, c_s is the speed of sound, v_t is the turbulence velocity, P is pressure and $t_{\hat{\phi}\hat{r}}$ is the shear stress as measured in a frame of reference moving with the gas. The last equality is the simplifying assumption of the α-model: the efficiency of the angular momentum transfer is expressed with one parameter, α. Since turbulence in the disk is generated by shear instability caused by the same magnetic field [8], I expect the viscosity term and the magnetic field term to be of the same order. The minimum strength for the magnetic field to generate the shear stresses needed for accretion is then of the order $B \sim (4\pi\alpha P)^{1/2}$.

In this work, I will model the accretion disk physics using the Novikov and Thorne (N&T) model [168] for a geometrically thin, optically thick disk (see also § 1.2.2). For simplicity, in order to split expressions into Newtonian limits times relativistic corrections, N&T introduced the following functions (from now on I will use $c = G = 1$), which are equal to one in the non-relativistic limit:

$$\mathscr{A} = 1 + a_\star^2/r_\star^2 + 2a_\star^2/r_\star^3 \tag{6.2a}$$
$$\mathscr{B} = 1 + a_\star/r_\star^{3/2} \tag{6.2b}$$
$$\mathscr{C} = 1 - 3/r_\star + 2a_\star/r_\star^{3/2} \tag{6.2c}$$
$$\mathscr{D} = 1 - 2/r_\star + a_\star^2/r_\star^2 \tag{6.2d}$$
$$\mathscr{E} = 1 + 4a_\star^2/r_\star^2 - 4a_\star^2/r_\star^3 + 3a_\star^4/r_\star^4 \tag{6.2e}$$
$$\mathscr{F} = 1 - 2a_\star/r_\star^{3/2} + a_\star^2/r_\star^2 \tag{6.2f}$$
$$\mathscr{G} = 1 - 2/r_\star + a_\star/r_\star^{3/2} \tag{6.2g}$$
$$\mathscr{N} = 1 - 4a_\star/r_\star^{3/2} + 3a_\star^2/r_\star^2 \tag{6.2h}$$

where $r_\star = r/M$ and $a_\star = a/M$. The last expression, $\mathscr{N}$, is not from Novikov and Thorne [168] and corresponds to the quantity called C in Riffert and Herold [191]. In the N&T accretion disk model, the disk lies in the equatorial plane ($\theta = \pi/2$), matter rotates in quasi-circular orbits with angular velocity

$$\omega = \frac{d\phi}{dt} = \sqrt{\frac{M}{r^3}}\frac{1}{\mathscr{B}}. \tag{6.3}$$

and the inner edge of the disk is assumed to be coincident with the innermost stable circular orbit of the Kerr metric (or ISCO, see eq. 1.19). Also, the angular momentum of the disk is assumed to be aligned with the spin of the hole.

In order to calculate the pressure in the disk, I have to analyze the local vertical structure of the disk near the equatorial plane. The easiest way is to perform the calculations in the local orbiting frame at the center of the disk ($z = 0$). In this inertial frame of reference, all that is needed are the following equations, in which the Newtonian value is multiplied by the relativistic corrections defined in eqs. (6.2). I will need, of course, the equation for hydrostatic equilibrium in general relativity. I use the correction to the N&T equilibrium found by Riffert and Herold [191]:

$$\frac{dP}{d\Sigma} = -\omega^2 z \frac{\mathscr{B}^2\mathscr{N}}{\mathscr{C}} \tag{6.4}$$

where $d\Sigma = \rho dz$. Since I am interested in the mid-plane, where by symmetry I expect the vertical density profile to reach a local maximum, I consider ρ to be approximately constant near the mid-plane.

Next, I will need an expression for how the energy is generated inside the disk. The viscous heating generated by friction between adjacent layers is given by [168]

$$\frac{dF}{dz} = \frac{3}{2}\omega t_{\hat{\phi}\hat{r}}\mathscr{C}^{-1}\mathscr{B}\mathscr{D} \tag{6.5}$$

where F is the energy flux. I assume the energy transport to be radiative:

$$F = -\frac{1}{\kappa_{\rm R}}\frac{dP_{\rm rad}}{d\Sigma} \tag{6.6}$$

where $\kappa_{\rm R}$ is the Rosseland mean opacity.

For the equation of state, in order to calculate the vertical structure, I assume that in the central part of the disk pressure is dominated by radiation. However, I still leave the possibility of a z dependence in the equation of state:

$$P = \frac{1}{\chi(\Sigma)} P_{\text{rad}} \,. \tag{6.7}$$

From eqs. (6.4), (6.6), and (6.7) I get:

$$\begin{aligned} -\kappa_R F &= \frac{d(\chi(\Sigma)P)}{d\Sigma} = \frac{d\chi}{d\Sigma}P + \chi\frac{dP}{d\Sigma} \\ &= \frac{d\chi}{d\Sigma}P + \chi(-\omega^2 z)\frac{\mathscr{B}^2\mathscr{N}}{\mathscr{C}} \end{aligned} \tag{6.8}$$

Thus, from eqs. (6.5) and (6.7):

$$\alpha P = \chi\frac{2\omega}{3\kappa_R}\frac{\mathscr{B}\mathscr{N}}{\mathscr{D}} - \frac{2F}{3\omega}\frac{d\ln\kappa_R}{dz}\frac{\mathscr{C}}{\mathscr{B}\mathscr{D}} + \frac{2\omega z}{3\kappa_R}\frac{d\chi}{dz}\frac{\mathscr{B}\mathscr{N}}{\mathscr{D}} - \frac{2}{3\kappa_R\omega}\frac{d}{dz}\left(\frac{d\chi}{d\Sigma}P\right)\frac{\mathscr{C}}{\mathscr{B}\mathscr{D}} \tag{6.9}$$

In the mid-plane this becomes:

$$\begin{aligned} \alpha P_c &= \chi_c\frac{2\omega}{3\kappa_R}\frac{\mathscr{B}\mathscr{N}}{\mathscr{D}} - P_c\frac{2}{3\kappa_R\omega}\frac{d}{dz}\left(\frac{d\chi}{d\Sigma}\right)\bigg|_{z=0}\frac{\mathscr{C}}{\mathscr{B}\mathscr{D}} \\ &\sim \chi_c\frac{2\omega}{3\kappa_R}\frac{\mathscr{B}\mathscr{N}}{\mathscr{D}} - P_c\frac{2}{3\kappa_R\omega}\frac{\chi_c}{\rho_c h^2}\bigg|_{z=0}\frac{\mathscr{C}}{\mathscr{B}\mathscr{D}} \end{aligned} \tag{6.10}$$

where h is the typical scale height of the disk. The second term is negative because χ decreases with z and Σ and it reaches its maximum at $z = 0$, so its derivative at $z = 0$ is less than 0.

Rewriting $\kappa_R\rho_c = 1/\lambda$ (mean free path), I obtain:

$$P_c\frac{2}{3\kappa_R\omega}\frac{\chi_c}{\rho_c h^2} = \chi_c P_c\frac{2\lambda^2}{\omega\lambda h^2} \tag{6.11}$$

In this expression, h^2/λ^2 corresponds to the number of mean free paths that a photon needs to perform a random walk out of the disk, while λ/c is the time for one mean free path. I can then rewrite this expression in terms of the diffusion time:

$$\chi_c P_c\frac{2\lambda^2}{\omega\lambda h^2} = \chi_c P_c\frac{2}{\omega t_{\text{diff}}} = \chi_c P_c\frac{t_{\text{rot}}}{\pi t_{\text{diff}}} \tag{6.12}$$

where $t_{\rm rot}$ is the time needed by the disk to undergo a complete rotation and $t_{\rm diff}$ is the diffusion time. Since $t_{\rm rot} \ll t_{\rm diff}$, this term is much smaller than the first one. The relativistic corrections do not affect this result because the value of $\mathscr{C}/(\mathscr{B}\mathscr{D})$ is less than one from the ISCO to infinity and it goes to one at infinity. I can then write the strength of the magnetic field in the mid-plane as:

$$B^2 \sim 4\pi\alpha P_c \sim \chi_c \frac{2\omega}{3\kappa_R}\frac{\mathscr{B}\mathscr{N}}{\mathscr{D}} = \chi_c \frac{8\pi}{3\kappa_R}\sqrt{\frac{M}{r^3}}\frac{\mathscr{N}}{\mathscr{D}} \; . \tag{6.13}$$

Since radiation dominates the pressure in the mid-plane of the disk, I can take $\chi_c \sim 1$. Moreover, it is safe to assume that in the innermost part of the disk the opacity is dominated by electron scattering:

$$\kappa_R = \kappa_{es} = \frac{8\pi}{3m_p}\left(\frac{e^2}{m_e c^2}\right)^2 \frac{(1+X)}{2} \tag{6.14}$$

where m_p and m_e are the proton mass and the electron mass respectively and X is the hydrogen mass fraction. For a 10 $M_\odot$ black hole at the ISCO, $r = r_I$, I obtain

$$B^2 = (0.36 - 1.22 \times 10^8\,{\rm G})^2 \left(\frac{M}{10\,M_\odot}\right)^{-1}\left(\frac{1+X}{2}\right)^{-1} \tag{6.15}$$

where the first value is for $a_\star = 0$ and the second is for $a_\star = 0.999$ (the value diverges for $a_\star = 1$). This is a crude estimate of the minimum magnetic field strength needed to generate enough shear stresses for accretion to occur. Both global magneto-hydrodynamic (MHD) simulations [200] and shearing box simulations [97] show that, when moving away from the mid-plane, the magnetic pressure decreases toward the photosphere. However, the expression in eq. (6.15), with the radial scaling of eq. (6.13), reproduces the strength of the magnetic field at the photosphere obtained with shearing box simulations by Hirose et al. [97] for a 6.62 $M_\odot$ black hole at a radius of 30 GM/c^2. Likewise, the expressions in eqs. (6.13) and (6.15) reproduce both the strength and the radial decrease of the magnetic field along the photosphere in Fig. 3 of Schnittman et al. [200], who performed a global MHD simulation for a 10 $M_\odot$ black hole. Regarding the estimates obtained by Miller et al. [157] for GRS 1915+105 at 850, 1,200, 3,000 and 30,000

GM/c^2, eqs. (6.13) and (6.15) reproduce their minimum estimate at every radius, the one obtained by assuming MHD pressure, while it is two orders of magnitude less than their estimates obtained by assuming a magnetocentrifugal driven wind or an α-model pressure. For the purposes of this work, I will then use the analytical expression found in eq. (6.13) for the minimum magnetic field strength at the photosphere.

6.3 Vacuum birefringence

From eq. 4.50 in Chapter 4 and eq. 6.13, I can estimate the amplitude of the birefringent vector in the vacuum just above the accretion disk. Reintroducing all the constants yields the magnitude of the birefringent vector

$$\hat{\Omega} = k_0 \Delta n = \frac{\alpha_{\rm QED}}{15} k_0 \left(\frac{B}{B_{\rm QED}}\right)^2 \sin^2\theta = k_0 \frac{\hbar m_p}{15\pi m_e^2 c^2} \frac{1}{(1+X)} \sqrt{\frac{GM}{r^3}} \frac{\mathscr{N}}{\mathscr{D}} \sin^2\theta \tag{6.16}$$

And the left term of eq. 2.65 (the adiabaticity condition) becomes

$$\begin{aligned} \left| \hat{\boldsymbol{\Omega}} \left(\frac{1}{|\hat{\boldsymbol{\Omega}}|} \frac{\partial |\hat{\boldsymbol{\Omega}}|}{\partial x_3} \right)^{-1} \right| &\simeq \hat{\Omega}(r) r \\ &\simeq k_0 \frac{\hbar m_p}{15\pi m_e^2 c^2} \frac{1}{(1+X)} \sqrt{\frac{GM}{r}} \frac{\mathscr{N}(r)}{\mathscr{D}(r)} \ . \end{aligned} \tag{6.17}$$

Equating this expression to $1/2$, I can calculate the polarization limiting radius, i.e. the distance from the hole at which the adiabaticiy condition breaks down, to be

$$\frac{r_p c^2}{GM} = \left(\frac{2 k_0 \hbar m_p}{15\pi m_e^2 c (1+X)} \frac{\mathscr{N}(r_p)}{\mathscr{D}(r_p)} \right)^2 \ . \tag{6.18}$$

The polarization-limiting radius is a rough indication of the distance from the source at which the polarization of light is not affected by the birefringence anymore. In Fig. 6.1, the energy of the photon at which r_p is equal to r_I is plotted against the spin of the black hole (solid red line). The dotted line represents the ISCO (right $y-$axis). This means that, for rapidly spinning black holes, the effect of QED will be important around a photon energy of 10 keV or lower, while

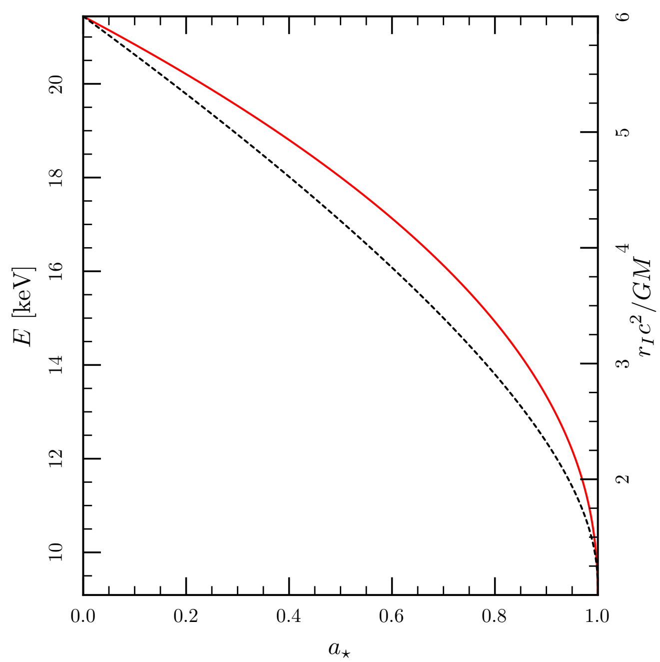

Figure 6.1: The plot shows, on the left, y axis, the energy at which $r_p = r_I$ (solid red line). On the right, y axis, the ISCO for a black hole as function of the spin parameter a (dashed black line).

for slowly spinning black holes, QED will affect the polarization only above 10-20 keV. However, if the magnetic field strength is higher (or lower), the energy at which QED becomes important decreases (or increases) as the inverse square of the magnetic field strength. The effect of vacuum birefringence, if properly modeled, can therefore provide an indication on the strength of the magnetic field that threads the accretion disk. It is worth noticing that this result depends on the spin of the black hole but not on the mass, so it stands for both stellar-mass and supermassive black holes. The polarization-limiting radius estimate does not account for light bending, which causes the photon's path in the strong magnetic field region to be longer due to the gravitational pull of the hole. For this reason, photons at energies lower than the one plotted in Fig. 6.1 could still be affected by the vacuum birefringence, depending on their angular momentum (see Sec. 6.4).

6.3.1 Competition with the plasma birefringence

The inferred presence of a corona above the inner regions of the disk introduces the possibility of a competing Faraday rotation due to the plasma birefringence. The effects of plasma birefringence for black hole accretion disks were studied in detail in a paper by Davis et al. [52] and comprise of a reduction of the photons linear polarization in a range of energies that depends on the strength of the magnetic field, on the energy of the photons and on the distance to the black hole of the emission region. In this section, I estimate the photon energy above which the vacuum birefringence dominates over the plasma. If I write the two photon polarization modes as

$$|e_1\rangle = \cos\psi|a\rangle + i\sin\psi|b\rangle \tag{6.19a}$$

$$|e_2\rangle = \sin\psi|a\rangle - i\cos\psi|b\rangle \tag{6.19b}$$

where

$$|a\rangle = \begin{pmatrix} -\sin\theta \\ 0 \\ \cos\theta \end{pmatrix}, \quad |b\rangle = \begin{pmatrix} 0 \\ 1 \\ 0 \end{pmatrix}, \tag{6.20}$$

in the cold plasma limit I obtain

$$b = \frac{1}{\tan 2\psi} \simeq \frac{\omega_B}{\omega}\left[1 + V\frac{\omega^2 - \omega_B^2}{\omega_B^2}\right]\frac{\sin^2\theta}{2\cos\theta} \tag{6.21}$$

where $\omega_B = eB/m_e c^2$ is the cyclotron frequency,

$$V = \frac{\alpha_{\text{QED}}}{15\pi}\left(\frac{B}{B_{\text{QED}}}\right)^2\left(\frac{\omega}{\omega_p}\right)^2 \tag{6.22}$$

measures the influence of the virtual $e^+ \, e^-$ pairs in the strong magnetic field relative to the real electrons of the plasma and ω_p is the plasma frequency [149].

For an accretion disk in the keV range, we are in the limit for which $\omega \gg \omega_B$. If b goes to zero, the polarization becomes circular, and without the presence of QED, the Faraday rotation induced by the plasma would destroy the linear polarization, as in that case $b \simeq \omega_B/\omega \ll 1$. The limit for which the QED and the plasma effects are similar is for $b \sim 1$. Since $\omega_B/\omega \ll 1$, in order for b to be about 1, $V\omega^2/\omega_B^2$ needs to be much greater than 1, so I can neglect the first term in the brackets of eq. (6.21) and then obtain

$$b \simeq \frac{\alpha_{\rm QED}}{15\pi}\left(\frac{B}{B_{\rm QED}}\right)^2 \frac{\omega^3}{\omega_p^2\omega_B} = \frac{eBE^3}{60\pi^2 n_e m_e^2 \hbar^2 c^6} \tag{6.23}$$

where E is the energy of the photon and n_e is the number density of electrons.

If I assume the optical depth over a distance comparable to the ISCO to be low:

$$\tau = n_e \sigma_T r_I \simeq 0.2 \tag{6.24}$$

where σ_T is the Thomson cross section, I obtain that $b \sim 1$ for

$$E = 2.11 - 2.43\,\mathrm{keV}\left(\frac{M}{10\mathrm{M}_\odot}\right)^{-\frac{1}{6}}\left(\frac{\tau}{0.2}\right)^{\frac{1}{3}}\left(\frac{1+X}{2}\right)^{\frac{1}{6}} \tag{6.25}$$

where the first value is for $a_\star = 0$ and the second value is for $a_\star = 1$. Because b scales as E^3, at higher energies the plasma birefringence does not destroy the linear polarization of the photons thanks to the predominance of QED, which renders the propagation modes approximately linear. The energy at which QED begins to dominate scales slowly with the assumed magnetic field strength, in fact as $B^{-1/3}$.

6.4 Depolarization in the disk plane

To better understand how vacuum birefringence affects the polarization of photons traveling through the black hole magnetosphere, in this section I will assume a simple structure for the magnetic field threading the accretion disk, and I will study how the polarization changes for photons traveling parallel to the disk plane. Recent observations of the radio polarization coming from the region close to the event horizon of Sagittarius A* suggest the presence of a partially organized field [105]. It is reasonable to assume the magnetic field to be organized on some length-scale that reflects the competition between the magnetic field itself, which would tend to be organized, and the shear of the disk, which prevents big structures from forming. I therefore assume the disk to be divided into regions of constant magnetic-field direction, which is also the structure often assumed for the magnetic field in the plane of the disk by magnetohydrodynamics (MHD) simulations [174]. I pick two different length-scales to test how my assumption on the size of the magnetic loops affects the results. Since I expect the length scale to be related to both the distance to the hole and to the size of the hole itself, I first divide the disk into five regions, each twice as large as the previous one: from the ISCO to twice the ISCO, to 4 times the ISCO, to 8 times the ISCO, to 16 times the ISCO, and to infinity. For simplicity, I call this configuration the *2-fold configuration*. In the second configuration, the regions of constant magnetic-field direction are each 1.5 times as large as the previous one: from the ISCO to 1.5 times the ISCO, to 2.3 times the ISCO, to 5.1 times the ISCO, to 7.6 times the ISCO, to 11 times the ISCO, to 17 times the ISCO, and to infinity. For simplicity, I call this configuration the *1.5-fold configuration*.

As a photon travels through a magnetized birefringent vacuum with difference in index of refraction Δn, the polarization direction rotates around the birefringent vector $\hat{\mathbf{\Omega}}$ as

$$\frac{d\Theta}{d\tau} = \Delta n \frac{p \cdot u}{\hbar c} \tag{6.26}$$

where p is the four-momentum of the photon, u is the four-velocity of the disk that anchors the field and τ is the proper time elapsed in the frame of the disk. I want to calculate the final depolarization of the photon, so I integrate along the geodesic

$$\Delta\Theta = \int \Delta n \frac{p \cdot u}{\hbar c} \left(\frac{dx^\mu}{dr} \right) u_\mu dr \tag{6.27}$$

to determine the total rotation of the polarization of a photon across the Poincaré sphere. The polarization of an individual photon will perform a random walk across the Poincaré sphere, and the total rotation of the polarization along the path is given by eq. 6.27, where the extremes of the integral are the ISCO and infinity. The direction of the individual step, is given by eq. 2.64.

For simplicity, I only consider photons traveling near the plane of the disk. In the equatorial plane, the spacetime interval in the Kerr metric (eq. 1.3) becomes

$$ds^2 = g_{\rm tt}dt^2 + 2g_{\rm t\phi}drd\phi + g_{\phi\phi}d\phi^2 + g_{\rm rr}dr^2 \tag{6.28a}$$

$$g_{\rm tt} = -1 + 2M/r \tag{6.28b}$$

$$g_{\rm t\phi} = -2Ma/r \tag{6.28c}$$

$$g_{\phi\phi} = r^2(1 + a^2/r^2 + 2Ma^2/r^3) = r^2\mathscr{A} \tag{6.28d}$$

$$g_{\rm rr} = (1 - 2M/r + a^2/r^2)^{-1} = \mathscr{D}^{-1} \tag{6.28e}$$

The four-velocity of an observer rotating with the disk can be easily obtained remembering that

$$u^\phi = \frac{d\phi}{d\tau} = \omega u^{\rm t} \tag{6.29}$$

From its definition, $g_{\mu\nu}u^\mu u^\nu = -1$, I obtain

$$u^{\rm r} = 0 \tag{6.30a}$$

$$u^{\rm t} = \sqrt{\frac{-1}{g_{\rm tt} + 2g_{\rm t\phi}\omega + g_{\phi\phi}\omega^2}} = \mathscr{B}\mathscr{C}^{-\frac{1}{2}} \tag{6.30b}$$

$$u^\phi = \frac{d\phi}{d\tau} = \omega u^{\rm t} = \omega\mathscr{B}\mathscr{C}^{-\frac{1}{2}} \tag{6.30c}$$

($u^{\rm r} = 0$ because we are in the local orbiting frame), and

$$u_{\rm t} = (g_{\rm tt} + g_{\rm t\phi}\omega)u^{\rm t} = -\mathscr{G}\mathscr{C}^{-\frac{1}{2}} \tag{6.31a}$$

$$u_\phi = (g_{\phi\phi}\omega + g_{\rm t\phi})u^\phi = \sqrt{Mr}\mathscr{F}\mathscr{C}^{-\frac{1}{2}} \tag{6.31b}$$

In order to study the path of the photon along its geodesic, it is useful to calculate quantities that do not change along the path. From the dot-product of the four-momentum of the photon and two of the Killing vectors of the metric, I find two quantities that remain constant along the geodesics: the energy and angular momentum of the photon

$$E = -\xi_{\rm t} \cdot p = -(g_{\rm tt}p^{\rm t} + g_{\rm t\phi}p^\phi) \tag{6.32a}$$

$$L = \xi_\phi \cdot p = g_{\phi\phi}p^\phi + g_{\rm t\phi}p^{\rm t} \tag{6.32b}$$

I call the specific angular momentum $L/E = l$. I analyze three cases: a photon coming from the ISCO with zero angular momentum ($l = 0$), a photon initially rotating with the disk (maximum prograde l_+) and a photon initially going against the rotation of the disk (maximum retrograde l_-).

6.4.1 Zero angular momentum photons

If $l = 0$, from eqs. (6.32a) and (6.32b), I obtain, for the photon,

$$\frac{d\phi}{dt} = -\frac{g_{\mathrm{t}\phi}}{g_{\phi\phi}} = 2\frac{Ma}{r^3}\mathscr{A}^{-1} \tag{6.33}$$

From the null-geodesic condition $ds^2 = 0$, I find:

$$\frac{dt}{dr} = \sqrt{\frac{g_{\mathrm{rr}}}{\frac{g_{\mathrm{t}\phi}^2}{g_{\phi\phi}} - g_{\mathrm{tt}}}} = \mathscr{A}^{\frac{1}{2}}\mathscr{D}^{-1} \tag{6.34}$$

I can then write the second part of eq. (6.27) as

$$\left(\frac{dx^\mu}{dr}\right)u_\mu = \frac{d\phi}{dr}u_\phi + \frac{dt}{dr}u_{\mathrm{t}} = -(\mathscr{A}\mathscr{C})^{-\frac{1}{2}}\mathscr{B}. \tag{6.35}$$

The first part becomes:

$$p \cdot u = E(-u^{\mathrm{t}} + bu^\phi) = -Eu^{\mathrm{t}} \tag{6.36}$$

Using Δn from eq. (6.16), and changing the integration variable to a dimensionless one ($r_\star = r/M$), eq. (6.27) becomes

$$\Delta\Theta = EK\int \sin^2\theta\, r_\star^{-\frac{3}{2}}\mathscr{A}^{-\frac{1}{2}}\mathscr{B}^2\mathscr{N}(\mathscr{D}\mathscr{C})^{-1}dr_\star \tag{6.37}$$

where $K = m_p/[15\pi m_e^2 c^2(1+X)]$.

6.4.2 Maximum prograde and retrograde angular momentum photons

From eqs. (6.32a) and (6.32b), I obtain, for the photon,

$$\frac{d\phi}{dt} = -\frac{l g_{\mathrm{tt}} + g_{\mathrm{t}\phi}}{g_{\phi\phi} + l g_{\mathrm{t}\phi}} \tag{6.38}$$

By imposing $dr^2 = 0$, at the point of emission (the ISCO), I obtain the values for the maximum prograde specific angular momentum (l_+) of a photon rotating with the disk and the maximum retrograde specific angular momentum (l_-) for a photon in retrograde motion:

$$l_\pm = \frac{g_{\mathrm{t}\phi} \pm \sqrt{g_{\mathrm{t}\phi}^2 - g_{\phi\phi} g_{\mathrm{tt}}}}{-g_{\mathrm{tt}}} = r\left(\frac{-2a_\star/r_\star^2 \pm \mathscr{D}^{1/2}}{1-2/r_\star}\right) \tag{6.39}$$

Since l is a constant along the geodesic, I calculate $l_\pm$ at the ISCO. Depending on the spin of the black hole, however, the ISCO can be inside the retrograde photon orbit (the prograde photon orbit is always inside the ISCO). In this case, I calculate l_- at the retrograde photon orbit (no photons can escape in retrograde motion from a smaller orbit than the retrograde photon orbit).

Employing eq. (6.38) in the null-geodesic condition, I find the path of the photon:

$$\frac{dt}{dr} = \frac{g_{\phi\phi} + l g_{\mathrm{t}\phi}}{r\mathscr{D}(l^2 g_{\mathrm{tt}} + 2l g_{\mathrm{t}\phi} + g_{\phi\phi})^{1/2}} \tag{6.40a}$$

$$\frac{d\phi}{dr} = \frac{-(l g_{\mathrm{tt}} + g_{\mathrm{t}\phi})}{r\mathscr{D}(l^2 g_{\mathrm{tt}} + 2l g_{\mathrm{t}\phi} + g_{\phi\phi})^{1/2}} \tag{6.40b}$$

Defining a dimensionless angular momentum as $l_\star = l/M$, I can then write the second part of eq. (6.27) as

$$\begin{aligned}\left(\frac{dx^{\mu}}{dr}\right)u_{\mu} &= \frac{d\phi}{dr}u_{\phi} + \frac{dt}{dr}u_{\mathrm{t}} \\ &= \frac{l\sqrt{Mr} - r^2\mathscr{B}}{r\mathscr{C}^{1/2}(l^2 g_{\mathrm{tt}} + 2l g_{\mathrm{t}\phi} + g_{\phi\phi})^{1/2}} \\ &= \frac{l_\star/r_\star^{3/2} - \mathscr{B}}{\mathscr{C}^{1/2}(l_\star^2 g_{\mathrm{tt}}/r_\star^2 - 4l_\star a_\star/r_\star^3 + \mathscr{A})^{1/2}} \end{aligned} \tag{6.41}$$

The first part becomes

$$p \cdot u = E(-u^{\mathrm{t}} + l u^{\phi}) = E\mathscr{C}^{-1/2}(l_\star/r_\star^{3/2} - \mathscr{B}) \tag{6.42}$$

I can then rewrite eq. (6.27) as

$$\Delta\Theta = EK \int \sin^2\theta r_\star^{-\frac{3}{2}} \frac{\mathscr{N}}{\mathscr{D}\mathscr{C}} \frac{(l_\star/r_\star^{3/2} - \mathscr{B})^2}{(l_\star^2 g_{\mathrm{tt}}/r_\star^2 - 4l_\star a_\star/r_\star^3 + \mathscr{A})^{1/2}} dr_\star \tag{6.43}$$

where $K = m_p/[15\pi m_e^2 c^2(1+X)]$ is the same as in the previous section.

6.4.3 Results

Equations (6.37) and (6.43) allow us to calculate the path that the polarization of a photon takes across the Poincaré sphere in each region. To calculate the direction of the step, I rotate $\mathbf{s}$ around $\hat{\mathbf{\Omega}}$ [eq. (2.64)]. In each region, I take the angle between the magnetic field and the photon, θ, and the angle between $\mathbf{s}$ and $\hat{\mathbf{\Omega}}$ as random.

In order to visualize the depolarization effect of the partially ordered field on the single photon, I first perform a Monte Carlo simulation for 60 photons for the *2-fold configuration*, calculating the evolution of their polarization from the ISCO to infinity. Each photon is emitted with the same angular momentum and the same energy at infinity from the ISCO of a black hole rotating with $a_\star = 0.84$ (as the AGN NGC 1365 [192]). I repeat the same calculation for photons traveling with zero, 90% of the maximum prograde and 90% of the maximum retrograde specific angular momentums and for three different energies: 3, 5 and 7 keV (at infinity). The results are shown in Fig. 6.2. Figure 6.2 depicts a solid Poincaré sphere, in which the dots represent the end-point of the polarization vectors. The

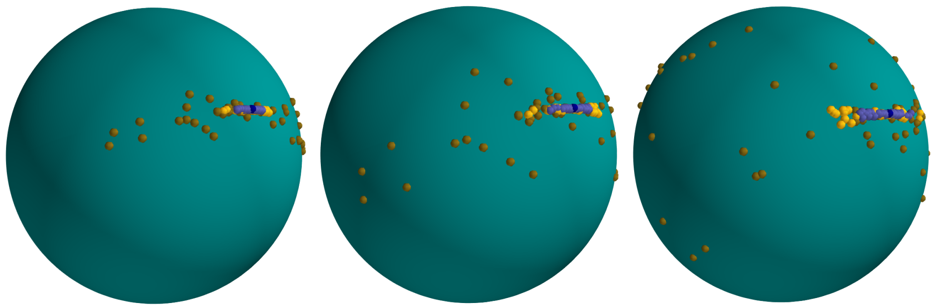

Figure 6.2: Monte-Carlo simulation of the depolarization of radiation from a black hole with $a = 0.84$ (as NGC 1365) for three photon energies (as measure by a distant observer): 3 keV (left), 5 keV (middle) and 7 keV (left). Polarization is represented on the Poincaré sphere: the dots represent the end-point of the polarization vector. The initial polarization vector is indicated by a dark blue dot. The violet dots are photons that receive a large blue shift (90% of l_+) , the yellow dots are zero-angular-momentum photons and the copper receive a large red shift (90% of l_-) on their way from the ISCO to us.

dark blue dot indicates the initial polarization, which is the same for every photon. Without the QED effect, the polarization would be frozen at the emission and the final polarization at infinity would be the same for all photons: still the dark blue dot. The other dots indicate the final polarization of the photons, calculated within QED. The yellow dots indicate the end-point of the polarization vector for the zero angular momentum photons; the violet dots correspond to the photons that receive a large blue shift (l_+ photons) and the copper dots represent the photons that receive a large red shift (l_- photons). We can immediately see that the final polarization is different from the initial one for all the photons, with a much bigger effect for red-shifted photons and for high-energy photons.

The same Monte-Carlo simulation, this time with 6,000 photons, for both the *2-fold configuration* and the *1.5-fold configuration*, for different energies from 1 to 80 keV (at the observer), and for four values of $a_\star$: 0.5, 0.7, 0.9 and 0.99, is shown in Fig. 6.3. Both plots show the polarization fraction obtained as an average of the final linear polarization of all the 6,000 photons against the photon energy. Results are shown for both the *2-fold configuration* (solid lines) and the *1.5-fold* *configuration* (dashed lines). The left plot shows the final polarization fraction of the zero angular momentum photons (black lines), the blue-shifted photons (blue lines) and the red-shifted photons (red lines) for a black hole rotating with $a_\star = 0.9$. The right plot shows the polarization fraction of red-shifted photons for four different $a_\star$: 0.5 (green lines), 0.7 (light blue lines), 0.9 (red lines) and 0.99 (purple lines).

In Figure 6.3, the dashed lines show the results for the *1.5-fold configuration* and the solid lines show the results for the *2-fold configuration*. I find that, if the magnetic loops are smaller, the depolarization effect is reduced linearly with the size of the loops: in this example, the dashed lines fall on top of the solid lines if I re-scale them by 2/1.5. However, the solid lines show peaks that are not present in the dashed lines. For example, for a hole rotating with spin $a_\star = 0.99$ in the *2-fold configuration* (purple solid line, right panel) the polarization fraction peaks at 7 keV and then again at 14 keV, at 21 keV and so on. These peaks are due to the fact that at those energies the integral in Equation (6.43) reaches, in the first zone of the disk, an average value of π, and therefore, the polarization vector remains closer to the $S_1 - S_2$ plane. In the *1.5-fold configuration*, this does not happen because the first region is smaller and the second region has a bigger effect on the final polarization, washing out the peaks. Ideally, the presence of features in the polarization spectrum such as the peaks shown for the *2-fold configuration* could provide hints on the structure of the magnetic field in the disk.

All of the aforementioned results are independent of the black hole mass.

6.4.4 A Simulation for GRS 1915+105

As an example, I simulated the observed polarization of the black-hole binary GRS 1915+105. GRS 1915+105 is a bright microquasar that hosts a rapidly spinning black hole. Measurements of its spin, which rely on observations in both X-rays and optical, seem to indicate a spin parameter $a_\star \gtrsim 0.98$ [142, 156]. I assumed an inclination angle of 75° [60, 158], and I used the polarization spectra from Figure 7 of Schnittman and Krolik (2009) [198]. To calculate the effects of the vacuum birefringence, I assumed that the bulk of the radiation comes from near the ISCO and has zero angular momentum.

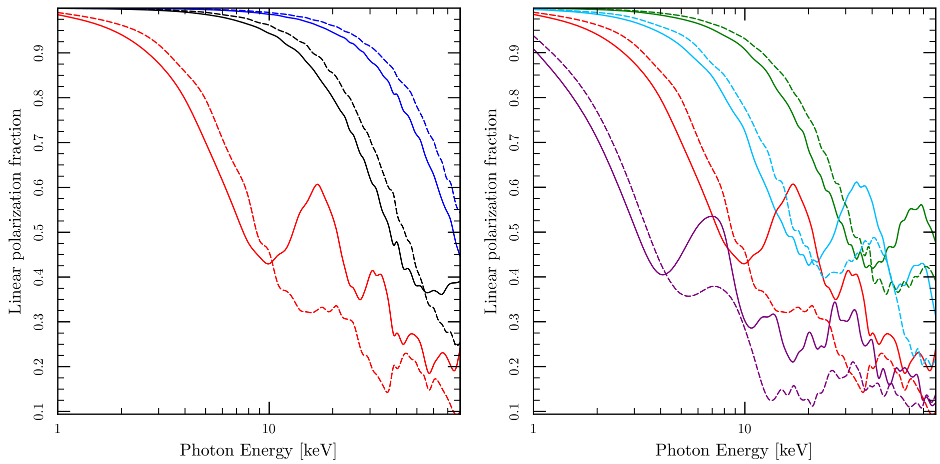

Figure 6.3: Final polarization fraction vs. photon energy calculated in the 2-fold configuration (solid lines) and in the 1.5-fold configuration (dashed lines). Left plot, left to right: maximum retrograde (90% l_-) angular momentum photons (red), zero angular momentum photons (black) and maximum prograde (90% l_+) angular momentum photons (blue), coming from the ISCO of a black hole with $a_\star = 0.9$. Right plot: 90% l_- photons for, left to right, $a_\star = 0.99$ (purple), 0.9 (red), 0.7 (light blue) and 0.5 (green).

Figure 6.4a shows the observed polarization degree for two spin parameters, $a_\star = 0.95$ and $a_\star = 0.99$, both with and without including QED. If QED were not included in the model, it would be easy to mistake a black hole actually spinning at $a_\star = 0.99$ (blue line) with one spinning at $a_\star = 0.95$ (green line). In the left panel of Figure 6.4, all the models were calculated assuming the minimum magnetic field needed for accretion to occur in an $\alpha-$model (Equation (6.13)). In Figure 6.4b, I show the effect of a stronger magnetic field. The red and the blue lines are the same as in Figure 6.4a: $a_\star = 0.99$ and the minimum magnetic field, with and without QED, while the black line represents a model with the same parameters but a magnetic field 2.5 times stronger. We can see that the curves are very different, with the QED effect being much stronger for the stronger magnetic field, and that the peaks have shifted into the 2–8 keV range. Of course, the magnetic field structure that I used in this work is just a toy model, but the peaks show that the QED effect can be sensitive to the magnetic field structure, and the upcoming polarime-

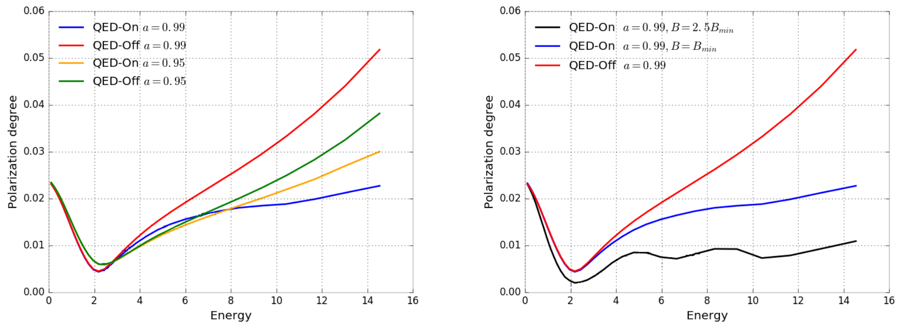

Figure 6.4: Observed polarization degree for the black-hole binary GRS 1915+105. (**a**) Model with $a_\star = 0.99$ with QED (blue line) and without QED (red line); model with $a_\star = 0.95$ with QED (yellow line) and without QED (green line). (**b**) Model with $a_\star = 0.99$ with QED and the minimum magnetic field (blue line) and without QED (red line); model with $a_\star = 0.99$ with QED and 2.5 times the minimum magnetic field (black line).

ters would be sensitive enough to detect them.

I want to stress that these figures show preliminary calculations, and further work is required to model the expected polarization degree. Indeed, our model assumes the flux to be dominated by photons coming from close to the ISCO and with nearly zero angular momentum, which could be a good assumption for high-energy photons but the contribution of photons coming from more distant regions has to be properly included in the calculations for low-energy photons. Moreover, the structure of the magnetic field that I employed is just a simple toy model, and better calculations are needed to make a prediction on whether features like the peaks in the polarization degree would be detectable and at which energies they would be present.

6.5 Conclusions

In Figure 6.3, all photons were emitted with the same polarization. If the vacuum were not birefringent, their final polarization would still be the same, and the final linear polarization fraction would still average at one. I can therefore conclude that vacuum birefringence has a big impact on the polarization of X-ray photons, especially for fast-spinning black holes and for red-shifted (retrograde) photons. The reason the effect is stronger for higher spinning parameters is because the ISCO is closer to the event horizon and, therefore, the magnetic field is stronger, but also because photons perform more orbits around fast-spinning holes, staying longer in the strong magnetic field region. Retrograde photons are more affected for two reasons: they perform more orbits around the black hole with respect to zero angular momentum and prograde photons, and they receive a red-shift, which means that their energy at emission was higher.

The results shown in Figure 6.3 were obtained for the minimum magnetic field needed to generate enough shear stresses for accretion to occur in an α-model for the accretion disk. The actual magnetic field threading the accretion disk could be higher, leading to a stronger effect of the vacuum birefringence on the polarization. In general, a stronger (or weaker) magnetic field would shift the $x-$axis of Figure 6.3 to a lower (higher) energy range, and the shifting would scale with the square of the magnetic field, as shown in Figure 6.4.

The simulations presented for GRS 1915+105 are not intended to be predictive as more detailed models are required for the structure of the magnetic field close to the disk plane and for the contribution to the total emission from photons emitted at different distances to the central engine. However, they show that vacuum birefringence has an effect on the observed polarization of fast-spinning black holes that can be detected.

My analysis was restricted to edge-on photons, traveling close to the disk plane, where the magnetic field is expected to be partially organized on small scales. Further studies are needed to calculate the effect of vacuum birefringence for photons coming out of the disk plane, where we expect the magnetic field to be organized on large scales. In this case, the effect of QED could be the opposite of what happens for edge-on photons: the organized magnetic field could align the polarization of photons traveling through the magnetosphere, resulting in a larger net observed polarization.

Chapter 7

The Polarization of X-ray Pulsars

X-ray pulsars are highly magnetized neutron stars that live in a binary and accrete ionized gas from a stellar companion. The pulsating nature of their X-ray emission was interpreted quickly after their discovery as resulting from the channeling along magnetic field lines of accretion gas onto their magnetic poles [5, 185]. However, it was immediately clear that the high pulse fraction detected was impossible to explain merely by the presence of isotropically emitting hot spots on the surface of the rotating neutron star, and that a strong beaming of the radiation was required [71]. A possible beaming mechanism is naturally given by the strong magnetic field: the cross-sections of the elementary processes of interaction between radiation and matter have a strong dependence on the angle between the magnetic field and the propagation direction of the photons, and at small angles with respect to the direction of the magnetic moment one can see deeper in the atmosphere. If the kinetic energy of the infalling material is deposited deep in the atmosphere, then the emission from the hot spots will have a characteristic "pencil" beam pattern [15, 49, 71]. As described in § 1.1.2, an alternative model invokes a radiative shock above the surface of the neutron star, in which the infalling gas is slowed down considerably by radiation before reaching the surface and an accretion column is formed above the magnetic pole in which the ionized gas is slowly sinking. In this second scenario, the photons escape from the walls of the column and the emission has a "fan" beam pattern [16, 20, 34, 51]. Due to the low resistivity, the depth to which the plasma penetrates into the dipole field is small compared to the

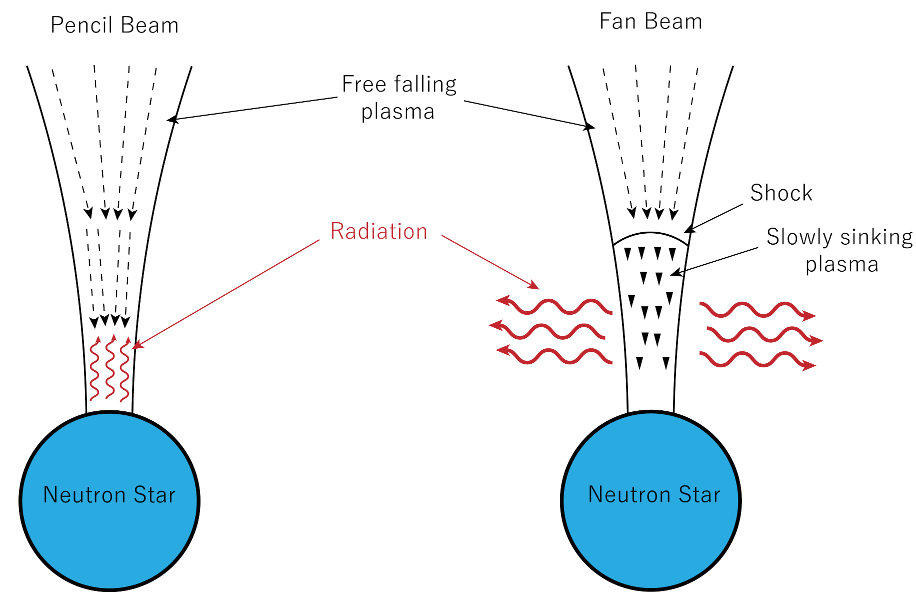

Figure 7.1: The two emission models for X-ray Pulsars: on the left, the gas can freefall all the way to the neutron star surface, and the kinetic energy of the accretion flow is only released upon the impact with the neutron star surface; the Comptonized X-rays escape predominantly upwards, and form a so-called “pencil-beam” pattern. If the luminosity is higher than the critical luminosity, a radiation dominated shock rises above the neutron star surface, forming an extended accretion column (right). In this case, photons can only escape through the walls of the column, and a “fan” emission pattern is expected.

magnetospheric radius, and the accretion channel is more likely to look like a thin wall of funnel more than a solid, axisymmetic column.

The continuum X-ray emission of accreting X-ray pulsars is often described by phenomenological models, including an absorbed power law extending up to ~ 100 keV with a roll-over at $\sim 30-50$ keV or a broken power law [59, 172]. Several attempts have been made to develop spectral models that link the X-ray emission to the accretion physics [51, 111, 112, 149, 150, 162, 246] but the modelling is complicated by the fact that the accretion regions are radiation-dominated, which means that the radiation transfer is coupled with the hydrodynamics of the flow; by the presence of a relativistic bulk motion in the infalling gas, which in turns makes the modeling of Compton upscattering more difficult; and by the strong magnetic field, which changes all the cross sections for scattering and absorption. All these complications should be addressed self-consistently and the study of the polarization parameters should be tailored to the spectral formation model. Of these attempts, only Mészáros and Nagel [150] and Kii [111] have addressed the problem of polarization (see § 3.2.4).

In the next section, I calculate the polarization signal of X-ray pulsars in the context of the currently available models for polarization by Mészáros and Nagel [150] and by Kii [111]. In these models, the emission is coming from a hot slab at the magnetic pole of the neutron star, and therefore we are considering the "pencil beam" case. Both models solve the problem of radiative transfer separately for the two polarization modes (parallel and perpendicular to the magnetic field) and therefore calculate at the same time the flux and the polarization degree of the emitted radiation. In § 7.1, I take the emission at surface provided by the models and I add the effects of gravitational lensing and of vacuum birefringence (see Chapter 4) to find the polarization at the observer.

In § 7.2, I will consider a different model of spectral formation, the Becker and Wolff [20] model (see also § 1.1.2). In this model, which analyzes the emission from an accretion column, in the "fan beam" context, the directional dependence of electron scattering is treated in terms of mode-averaged cross sections, and therefore the problems of polarization and of radiative transfer are considered separately, and no information is given on the polarization of light. The model, however, predicts a spectrum that fits very well the observed profiles and provides insights on the properties of the accretion flow. In § 7.2 I show that the polarization parameters can be calculated independently of the radiative transfer solution, and that a robust prediction can be made in the context of the model.

7.1 Previous models: Mészáros and Nagel and Kii

In this section, I calculate the polarization degree in the context of the models by Mészáros and Nagel [150] and by Kii [111], in the slab geometry. I use the results of [150] to estimate the total flux from the region. However, [150] do not report the polarization fraction as function of inclination angle, and therefore I employ the results of [111] to estimate the polarized fraction and the intensity as a function of direction from the slab. Both Mészáros and Nagel and Kii solve the Feautrier equations for the radiative transfer [153] in the assumption of complete Faraday depolarization, i.e. they assume that the two polarization modes stay distinct as the photons propagate through the slab and they track the 2 modes instead of the full Stokes vector. In their model, photons are mainly produced by thermal bremsstrahlung, and the polarization of the X-ray signal is driven by the difference in opacities between the two polarization modes.

In order to pick the temperature and magnetic field strength, I take as an example Her X-1, a bright X-ray pulsar with $kT \sim 8$ keV [151] and cyclotron energy $\varepsilon_c \sim 38$ keV [244]. As the emission in Her X-1 is strongly pulsed, I choose a geometry that results in a large pulsed fraction (an orthogonal rotator).

7.1.1 Description of the method

In the slab geometry, the X-ray emission comes from a slab of uniform temperature at the polar caps of the neutron star, heated by the infalling gas; in my calculations, I assume the region of emission to comprise about 6 degrees of the stellar surface.

Each element on the neutron star surface emits highly polarized radiation, and the value of polarization at the surface is given by [150] and [111]. In particular, the total intensity from the slab as function of inclination angle with respect to the surface and of energy is shown in Fig. 1b of [150], while Fig. 1a of the same paper only shows the flux in the two polarization modes integrated over angles. In order to get the differential flux for each mode, I use the polarization degree at surface shown in Fig. 4b of [111] as function of energy and inclination angle. In this way, I have the flux in the two polarization modes and the value of Q/I at the surface of the neutron star.

At emission, the direction of polarization is correlated with the direction of the magnetic field. However, the magnetic field orientation varies over the surface of the neutron star. Summing the polarized intensities of the 6° polar cap slightly reduces the net polarization. In order to calculate the polarization degree at the observer, I use a ray-tracing code, initially ignoring the effect of vacuum birefringence, and simply parallel-transporting the polarization vector along the geodesics. In this way, I obtain the "QED-off" polarization degree, which is shown in the left panel of Fig. 7.2.

When I include QED, I have to calculate the rotation induced by vacuum birefringence, and for that I solve the equations of the polarization evolution (eq. 2.64) through the neutron-star magnetosphere using an adaptive Runge-Kutta method as outlined in [94]. Additionally, I have to consider the fact that all of the photons coming through the atmosphere pass through the vacuum resonance region, in which the linear contribution to the birefringence from QED cancels that of the plasma [98] (see § 5.2.1). In this region, the value of $\hat{\Omega}$ swings from pointing along a particular direction in the $s_1 - s_2-$plane up toward s_3 and back onto the $s_1 - s_2-$plane in the opposite direction. As we know from eq. 2.65, if this happens slowly enough, the photon polarization will follow the direction of $\hat{\Omega}$, and this is in fact what happens for photons with energies greater than about 350 eV. The polarization state is switched from perpendicular to parallel.

7.1.2 Results

The effect of vacuum birefringence was already shown in Fig. 5.3, in § 5.1.1, which depicts the final polarization states across the image of the neutron star surface, assuming that the radiation is initially in the extraordinary mode, with and without QED. In this section, the effect is similar, but the initial intensities in the two polarization modes are taken to be the ones from [150] and [111] instead of being 100% in X. From Fig. 5.3, one can see that, when the emission is restricted to the region near the magnetic pole, the effect of QED is subtle: the projected magnetic field direction is well aligned near the pole even without vacuum birefringence in the left panel and the final polarization in the right panel is also well aligned in general but substantial circular polarization can be generated near the pole, due to the quasi-tangential effect [237] (see § 5.1.1). Because X-ray polarimeters only detect linear polarization, the circularly polarized radiation does not contribute to the observed polarization fraction, and the net effect of the vacuum birefringence is to reduce the polarization fraction integrated over the emission region and the

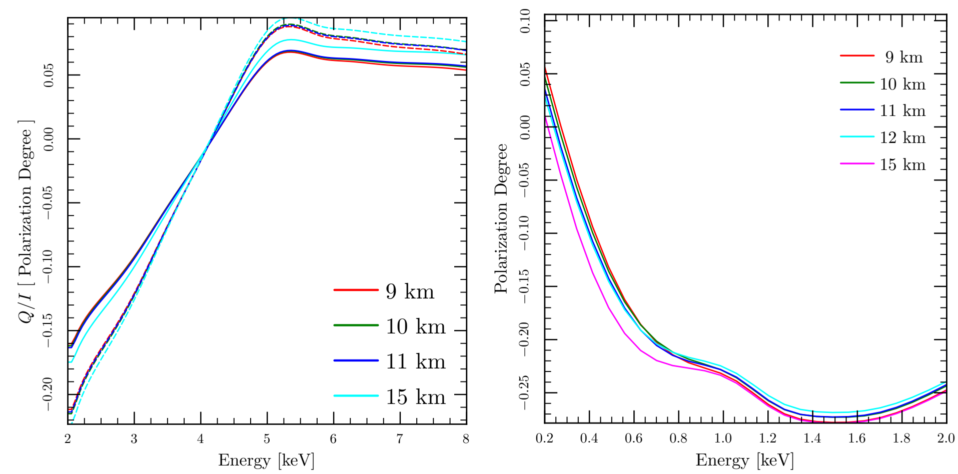

Figure 7.2: The polarization of Her X-1 as function of photon energy using the emission models of Kii [111] and Mészáros and Nagel [150], averaged over the rotation of the pulsar. A positive value of the polarization degree indicates that the polarization direction is perpendicular to the projection of the rotation axis onto the plane of the sky. The different colors represent different stellar radii, as indicated in the legend. The left panel shows the energy interval between 2 and 8 keV while the right panel shows the energy interval between 0.2 and 2 keV. In the left panel, the dashed lines give the result without vacuum birefringence (we have reversed the polarization direction in this case for ease of comparison, see the text) and the solid lines include the QED effect. A positive value of Q/I indicates that the net polarization is perpendicular to the projected spin axis of the stars in the QED-on case, and parallel in the QED-off case.

rotational phase as shown by the left panel of Fig. 7.2.

The results are shown in Fig. 7.2 for a range of stellar radii from 9 to 15 km. The solid lines trace the extent of linear polarization including QED, and the dashed lines neglect it. Across the 2–8-keV energy range, the trend in Q/I can be explained by looking at the opacities in the atmosphere. At low energies, the opacity for photons in the parallel polarization is larger than for the perpendicular polarization, so the bulk of the radiation emerges in the perpendicular mode. However, as the photon energy approaches the cyclotron energy (here taken to be ~ 38 keV), the opacity for the perpendicular mode increases and one gets more emission in the parallel mode.

Because the vacuum resonance reverses the polarization direction for all of the photons above about 350 eV, I have switched the sign of the value of Q/I for QED-off case for ease of comparison. Without an independent measurement of the projection of the spin axis of the star into the plane of the sky, measurements just in the 2-8-keV band cannot measure this polarization flip. The key effect of the QED birefringence in this harder band is to slightly reduce the polarization fraction.

I can apply Eq. 2.65 to determine how the conditions in the atmosphere, in particular the density scale height, determine the critical energy above which the polarization switches as the radiation passes through the vacuum resonance [98]. In the case of Her X-1, I have taken the temperature of the atmosphere to be 8 keV [151]; with the temperature fixed, the density scale height only depends on the composition of the atmosphere which is that of the donor star and the surface gravity; therefore, the photon energy at which the polarization direction flips depends on the surface gravity and can be used to measure the radius of the star. For the curves in Fig. 7.2 I have assumed a mass of 1.4 $M_\odot$ for the neutron star.

7.2 Polarization in the Becker and Wolff model

In this section, I will present a new model for the polarization parameters in the X-rays, based on the accretion model developed by Becker and Wolff [20].

7.2.1 The spectral formation model

In their 2007 paper [20, B&W07], Becker and Wolff propose a new model for spectral formation in luminous X-ray pulsars that quite successfully reproduces the phase-averaged spectrum of bright X-ray pulsars as Hercules X-1 (Her X-1). In their model, the ionized gas accreted from the companion star is funneled inside a column at the polar caps of the neutron star. The strong magnetic field keeps the gas confined inside the column as in a “pipe”, which is however transparent for radiation. Fig. 7.3 shows the geometry of the accretion column: the ionized gas free falls from the accretion disk along the field lines to the top of the column, where the speed of the flow is supersonic; inside the column, radiation pressure slows down the gas until it comes to rest at the bottom of the column. Seed photons in the column are produced by a combination of bremsstrahlung, cyclotron and blackbody radiation, and are scattered by electrons through Compton scattering. Blackbody photons are emitted by a thermal mound at the bottom of the column, so that the mound's surface represent the photosphere for creation and absorption of photons and the opacity in the rest of the column is given by electron scattering only. Bremsstrahlung and cyclotron photons are emitted throughout the column. The observed radiation comes from the walls of the column, in a "fan beam".

In their 2005 papers, Becker and Wolff [18, 19] considered only the effect of *bulk* Comptonization, for which photons are upscattered in energy through a first-order Fermi energization, ignoring the effects of thermal Comptonization. The difference between "bulk" and "thermal" Comptonization is mainly in the motion of the scattering centers: in the first case, photons gain energy interacting with electrons that are part of a converging flow, as opposed to the stochastic motion of scattering centers in the case of thermal scattering. Depending on the temperature of the electrons in the column and their infalling speed, both effects can be important. Neglecting thermal effects corresponds to considering a flow in which thermal velocities are considerably smaller than the converging bulk velocity, which seems to be a good assumption for low-luminosity X-ray pulsars like X Persei and GX 304-1 [18, 19], but fails to describe the spectra of bright X-ray pulsars. Bulk Comptonization alone leads to a steep power law in the hard X-rays, and therefore the down-scattering of high energy photons due to thermal Comptonization is needed to explain the low spectral index observed in the 1-20 keV range and the quasi-exponential cut off observed at about 20-30 keV in bright X-ray pulsars. In B&W07 both thermal and bulk effects are included.

The inclusion of thermal Comptonization, described mathematically by the Kompaneets equations [113], makes the analytic treatment of the transport equations more difficult. For this reason, the authors in B&W07 use an approximate velocity profile instead of using the exact one employed in their 2005 paper. The upstream flow above the column is composed of fully ionized hydrogen moving at supersonic speed, reaching about half the speed of light. Inside the radiation dominated column, electrons slow down as they transfer energy to the radiation field and stop at the stellar surface. Instead of using the exact solution for the velocity

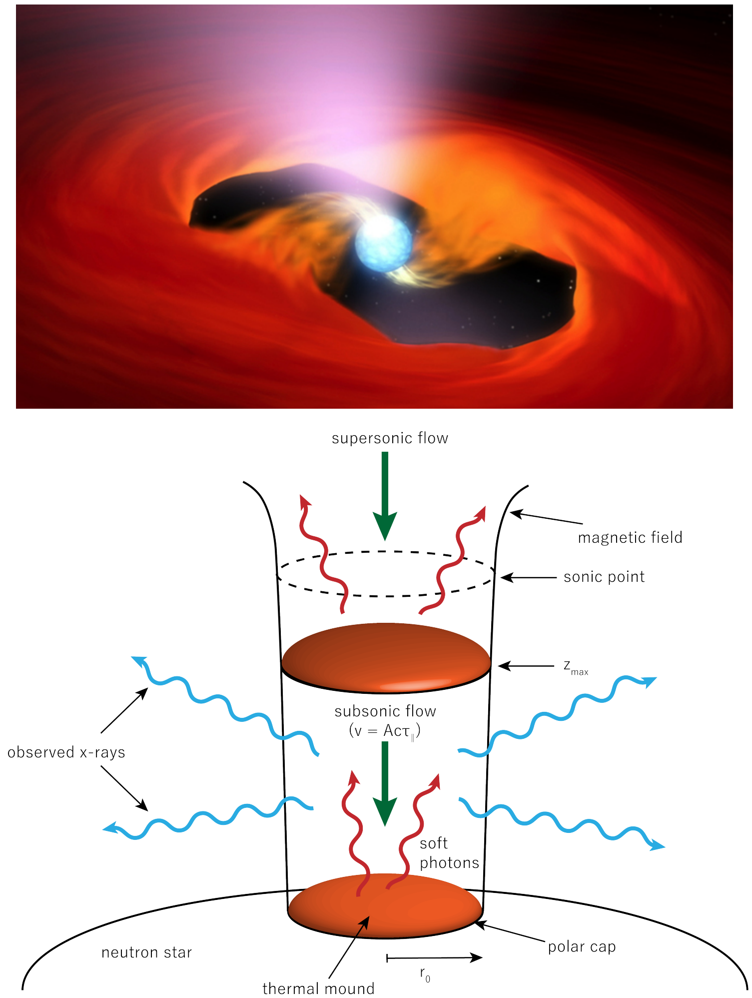

Figure 7.3: Up: artist rendition of an accreting X-ray pulsar; the accretion disk is disrupted at the magnetospheric radius and the ionized gas funneled to the magnetic poles. Credits: NASA/NuSTAR. Down: the accretion column in Becker and Wolff model (adapted from B&W07).

profile derived by Becker [17], the authors in B&W07 use a particular form for the velocity profile that approximates the exact solution and also makes the transport equation separable in energy and space:

$$v(\tau) = -A\tau_{||} \tag{7.1}$$

where A is a constant and $\tau_\parallel$ is the optical depth in the direction parallel to the magnetic field (and the column vertical axis). $\tau_\parallel$ increases vertically, and is equal to zero at the stellar surface. A is calibrated by equating the velocity at the sonic point to the exact velocity, which yields

$$A = 0.20 \left(\frac{M_*}{M_\odot} \right) \left(\frac{R_*}{10\,\mathrm{km}} \right)^{-1} \xi, \quad \xi = \frac{\pi r_0 m_p c}{\dot{M} (\sigma_\parallel \sigma_\perp)^{1/2}} \tag{7.2}$$

where M_* and R_* are the mass and radius of the neutron star, r_0 is the radius of the column, m_p is the mass of the proton, c is the speed of light, $\dot{M}$ is the accretion rate, and $\sigma_\parallel$ and $\sigma_\perp$ are the cross sections for photons travelling parallel and perpendicular to the magnetic field. These quantities are the means of those introduced in Chapter 3 averaged over photon energy and polarization state.

Another approximation in the B&W07 model is given by the treatment of the scattering cross sections. Since radiation pressure is dominant in the column, the dynamical structure of the flow is closely tied to the spatial and energetic distribution of the radiation, making the coupled radiation-hydrodynamic problem extremely complex. For this reason, in B&W07 the directional dependence of the electron scattering is treated in terms of the constant, energy- and mode-averaged cross sections $\sigma_\parallel$ and $\sigma_\perp$. In particular, $\sigma_\perp$ is set $\approx \sigma_T$, the Thomson cross section, while $\sigma_\parallel$ is expressed in terms of the accretion rate $\dot{M}$, of the radius of the accretion column r_0, and of the dimensionless parameter ξ, which determines the importance of the escape of photons from the accretion column in the radiation transfer equation. Both r_0 and ξ are free parameters, recovered by fitting the model to the spectrum. The expression used is given in eq. 83 of B&W07:

$$\sigma_\parallel = \left(\frac{\pi r_0 m_p c}{\dot{M} \xi} \right)^2 \frac{1}{\sigma_\perp} \tag{7.3}$$

I will not use these averaged cross sections in my calculation of the polarization parameters, as I will calculate angle- and energy-dependent cross sections for the different modes in § 7.2.2.

I will base my calculations on the accretion model of B&W07, and use the fitted parameters for the model obtained for Her X-1 in [244]; specifically:

- the radius of the accretion column $r_0 = 107$ m;
- the strength of the magnetic field $B = 4.25 \times 10^{12}$ G;
- the dimensionless parameter $\xi = \pi r_0 m_p c / [\dot{M}(\sigma_{\|}\sigma_{\perp})^{1/2}] = 1.36$;
- the dimensionless constant $A = 0.38$, defined in eq. 7.1;
- the height of the accretion column $z_{\max} = 6.6$ km (see Fig. 7.3), see also next section.

What is the height of the column?

The height of the accretion column in B&W07 is found by equating the approximate velocity at the top of the column to the local free-fall velocity

$$\left(\frac{2GM_*}{R_* + z_{\max}}\right)^{1/2} = cA\tau_{\max} \quad \text{where} \quad \tau_{\max} = \left(\frac{\sigma_{\|}}{\sigma_{\perp}}\right)^{1/4}\left(\frac{2\mathrm{z_{max}}}{\mathrm{A}\xi \mathrm{r_0}}\right)^{1/2} \tag{7.4}$$

Then

$$z_{\max} = \frac{R_*}{2}[(1 + C_1)^{1/2} - 1] \quad \text{where} \quad \mathrm{C_1} = \frac{4\mathrm{GM_*r_0}\xi}{\mathrm{Ac^2R_*^2}}\left(\frac{\sigma_{\perp}}{\sigma_{\|}}\right)^{1/2} \tag{7.5}$$

which gives, for the fitted parameters in [244], $z_{\max} \sim 6.6$ km.

Imposing the free-fall velocity at the top of the column corresponds to assuming that the radiative shock extends to the entire column, where the electron velocity smoothly changes from free-fall to zero. Another possibility would be assuming a strong, adiabatic shock in a thin layer at the top of the column and then a radiative flow in the rest of the column. In an adiabatic, radiation-dominated shock, the jump in velocity is never less then $1/7$ [17], and therefore in this case I would impose the velocity at the top of the column to be $1/7$ (or less) of the local free-fall velocity instead of being equal:

$$\frac{1}{7}\left(\frac{2GM_*}{R_* + z_{\max}}\right)^{1/2} \gtrsim cA\tau_{\max} \tag{7.6}$$

which yields $z_{\max} \lesssim 1.4$ km. The two assumptions give different results for the polarization parameters, as I will show in § 7.2.3.

7.2.2 Polarization at the source

Inside the accretion column, the seed photons for Comptonization are a mixture of bremsstrahlung, cyclotron and blackbody photons. Blackbody photons are emitted in the thermal mound at the bottom of the column, while bremsstrahlung and cyclotron photons are emitted throughout the entire column. The main contribution to the seed photons come from bremsstrahlung [20, 244]. Following the formalism introduced in § 2.2.1, I can take the average polarization of bremsstrahlung photons inside the column as my incident polarization, with Stokes parameters (I, Q, V), and then apply the matrix in eq. 2.46 to calculate the final polarization. But first of all, I need to know the average number of scatterings that a photon undergoes in the column as a function of energy.

Polarization inside the column

From B&W07, I can calculate the optical depth for photons moving horizontally outward of the column, called $\tau_\perp$ in the paper. First, I need to calculate the density profile from the accretion rate $\dot{M}$, kept as a constant fixed parameter of the model. From eq. 19 of B&W07:

$$\dot{M} = \pi r_0^2 \rho |v| = \pi r_0^2 \rho A \tau_{||} c \tag{7.7}$$

where ρ is the density of the gas and where I used eq. 7.1 to express the electrons velocity v. I can therefore calculate the perpendicular optical depth, knowing that the opacity is dominated by electron scattering:

$$\tau_\perp = \frac{r_0 \rho \sigma_\perp}{m_p} \sim \frac{r_0 \rho \sigma_T}{m_p} = \frac{\dot{M} \sigma_T}{m_p \pi r_0 A \tau_{||} c} \tag{7.8}$$

where I have employed the fact that the scattering cross section of photons moving perpendicular to the magnetic field is close to the Thomson cross section σ_T at all energies except very close to the cyclotron energy, where it is even higher (see Figure 7.5). $\tau_{||}$ increases in the vertical direction and is of the order 1 at the top of the column. Employing the fitted parameters from [244] I find that $\tau_\perp \sim 500$ at the top of the column, and therefore greater than 500 throughout the column. This yields an average number of scatterings per photon

$$N_{\rm sc} \sim \tau_\perp^2 \gtrsim 250,000 \tag{7.9}$$

For Compton scattering, the energy transfer for a single scattering is given by [195]

$$\Delta\varepsilon/\varepsilon \sim (\gamma^2 - 1) \lesssim 0.15 \tag{7.10}$$

where $\gamma = 1/\sqrt{1-\beta^2}$ is the Lorentz factor of the scattering center, the electron, and I have used $\beta = 0.5$, which is the velocity of the electrons at the top of the column.

From the estimates in eq.s 7.9 and 7.10, it is clear that an average photon has to undergo many scatterings before it can escape the column and that in the final tens of scatterings, the energy of the photon is very close to its final energy, i.e. its energy when it finally manages to escape from the column. Thus, during the final tens of scatterings of each photon, the elements of the scattering matrix in eq. 2.46 will remain approximately unchanged.

Multiplying a vector by the same matrix many times brings the vector close to the matrix's eigenstate with the largest eigenvalue, unless the vector itself is in an orthogonal eigenstate. Depending on the magnitude of the ratio between the largest eigenvalue and the rest, this process takes relatively few interactions. It is easy to see that, except for energies very close to the cyclotron line, the largest eigenvalue of the scattering matrix is orders of magnitude higher than the other eigenvalues. For this reason, I can safely assume that, independently of the initial polarization state of the photon, its Stokes vector will be in the matrix's predominant eigenstate just after a few scatterings.

Therefore, the predominant eigenstate of the scattering matrix in eq. 2.46 represents the polarization state of radiation inside the column, in the rest frame of the electrons. In the left panels of Figure 7.4 the Stokes parameters for the Comptonized radiation inside the column are shown a as a function of energy and angle θ, which is the angle with respect to the magnetic axis, $\hat{z}$. The results are shown for $\theta < \pi/2$ and are specular for $\theta > \pi/2$. As expected, except for very small

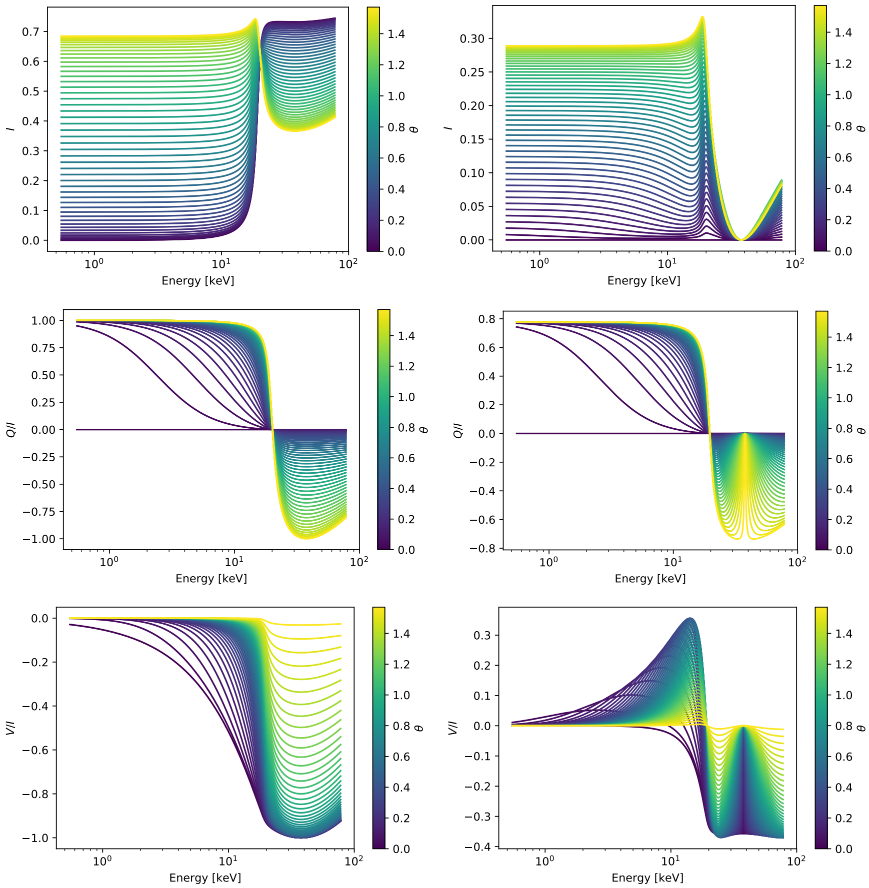

Figure 7.4: Average Stokes parameters. The left panels depict the polarization parameters of radiation inside the column, while panels on the right represent the polarization after the photons have gone through the region of last scattering and left. The calculation does not include beaming effects. From top to bottom: intensity I (arbitrary units), linear polarization fraction Q/I and circular polarization fraction V/I against the energy of the photons. The color code represents the angle with respect to the magnetic field θ.

angles, photons are always nearly linearly polarized in the ordinary mode (positive Q) for energies lower than the cyclotron line (~ 37 keV), while photons around the cyclotron line present a mixture of extraordinary and circular polarization. At the cyclotron line, photons propagating along the magnetic field (at small θ) have no linear polarization (the two linear polarization modes are equally perpendicular to the magnetic field), and have a strong circular polarization due to resonant cyclotron scattering (electrons can be excited to the second Landau level). Photons propagating at $\theta \sim \pi/2$, on the other hand, can resonantly scatter only if in the X-mode, and therefore Q/I is equal to -1.

This picture represents the polarization state of photons propagating inside the column, but in order to find the average polarization parameters of photons leaving the column, I have to take into account the difference in the cross sections for the different polarization modes, and therefore the difference in the volume of the optically thin region close to the column's walls. Since the cross section is much smaller, I expect the volume of the region of last scattering for extraordinary photons to be much larger than for ordinary photons, reducing the extent of linear polarization at all energies.

Region of last scattering

In order to find the polarization of light escaping from the accretion column, I have to consider the difference in volume of the region of last scattering between the different polarization modes. The volume of the optically thin region close to the external wall of the column is proportional to the square of the sine of the incident angle divided by the total cross section of the polarization mode at hand, which will also depend on the incident angle α.

I first calculate the cross sections for the different modes by applying the matrix to a polarization vector completely polarized in the mode under consideration and with a certain distribution in incoming angle α and then by averaging over the outgoing angle θ

$$\sigma = [...] \int_{1}^{-1} I'(\alpha, \theta) d(\cos\theta) \,. \tag{7.11}$$

In this way, I obtain the angle and energy dependent cross sections $\sigma_{\parallel}$ for the ordinary mode (1,1,0), $\sigma_{\perp}$ for the extraordinary mode (1,-1,0), and σ_{+} and σ_{-} for the two circular polarization modes (1,0,1) and (1,0,-1) respectively (see also [85])

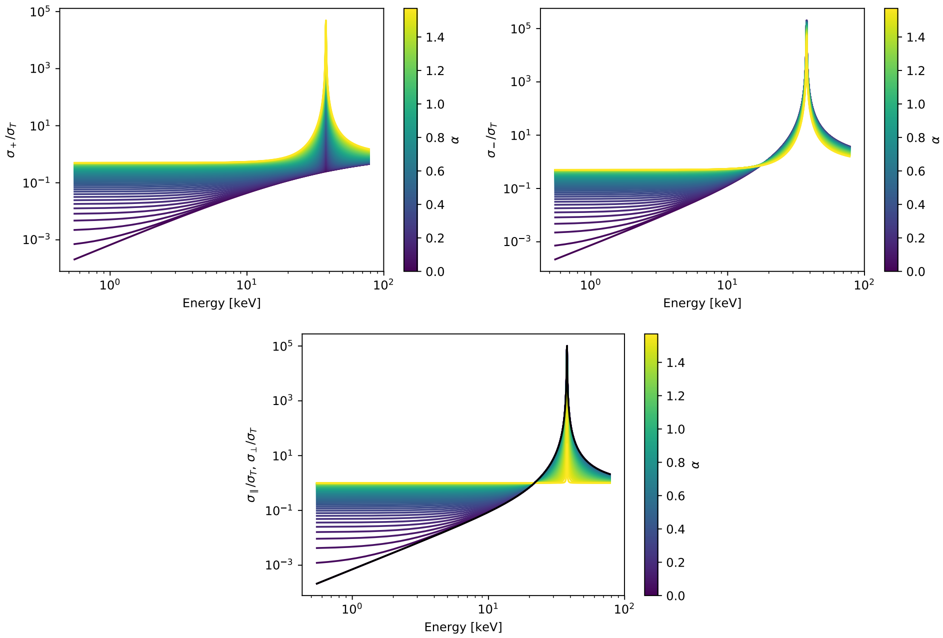

Figure 7.5: These plots show the dependence of the cross sections on the incident angle α and on the energy of the photons. Top left: σ_+/σ_T. Top right: σ_-/σ_T. Bottom: in this plot both $\sigma_\parallel/\sigma_T$ and $\sigma_\perp/\sigma_T$ are shown. $\sigma_\perp$ does not depend on angle and it is shown as the solid black line, while $\sigma_\parallel$ is color-coded with respect to the angle. When $\alpha = 0$, $\sigma_\parallel = \sigma_\perp$.

$$\sigma_\parallel = \sigma_T \left[\sin^2\alpha + \cos^2\alpha \frac{x^2+1}{(x^2-1)^2}\right] \tag{7.12a}$$

$$\sigma_\perp = \sigma_T \frac{x^2+1}{(x^2-1)^2} \tag{7.12b}$$

$$\sigma_+ = \frac{1}{2}\sigma_T \left[\sin^2\alpha + \frac{(x^2+1)(1+\cos^2\alpha) - 4x\cos\alpha}{(x^2-1)^2}\right] \tag{7.12c}$$

$$\sigma_- = \frac{1}{2}\sigma_T \left[\sin^2\alpha + \frac{(x^2+1)(1+\cos^2\alpha) + 4x\cos\alpha}{(x^2-1)^2}\right] \tag{7.12d}$$

where σ_T is the Thomson cross section. The different cross sections are shown in Figure 7.5. They all seem to diverge at the cyclotron line; however, for x very close to 1, the energy transfer from photons heats up the electrons and damping effects become important [148]. The lower panel depicts both $\sigma_\perp$ (black solid line) and $\sigma_\parallel$ (color coded with α) and we can see that they become equal when $\alpha = 0$, i.e. when photons propagate along the magnetic field, as expected.

If I now indicate with (I,Q,V) the average polarization state inside the column and with (I',Q',V') the polarization of the outgoing radiation I can write

$$Q = O - X \tag{7.13}$$

where O and X are the intensities of the ordinary and the extraordinary modes inside the column. The outgoing intensities will be

$$O' = \frac{1}{2}(Q+I)V_\parallel \tag{7.14}$$

$$X' = \frac{1}{2}(I-Q)V_\perp \tag{7.15}$$

where $V_i \propto \sin\theta/\sigma_i$. I can therefore write the Stokes parameters of the radiation coming out of the column as

$$I' = \frac{1}{2}(Q+I)V_\parallel + \frac{1}{2}(I-Q)V_\perp \tag{7.16}$$

$$Q' = \frac{1}{2}(Q+I)V_\parallel - \frac{1}{2}(I-Q)V_\perp \tag{7.17}$$

$$V' = \frac{1}{2}(V+I)V_+ - \frac{1}{2}(I-V)V_- \tag{7.18}$$

The right panels of Figure 7.4 show the average Stokes parameters after the radiation has gone through the region of last scattering. Comparing to the left panels, we can see that the linear polarization is reduced at low energy even for high angles because the low value of $\sigma_\perp$ favour the emission of extraordinary photons. Intensity is drastically lowered at high energies because all the scattering cross sections become divergent close to the cyclotron line. For the same reason, radiation at the cyclotron line is completely unpolarized.

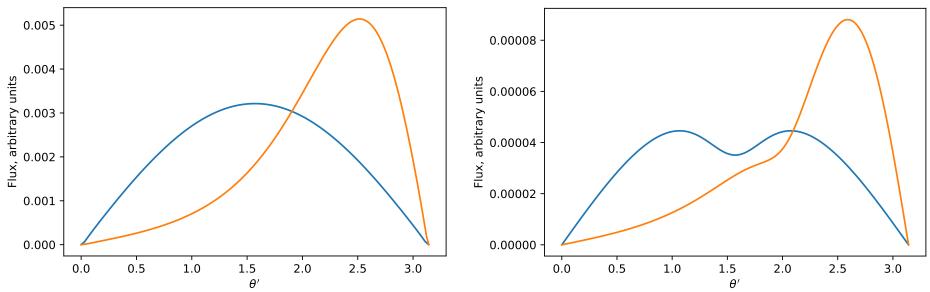

Figure 7.6: The effect of beaming on flux for $\beta = 0.4$ and different photon energies. Solid blue line: flux, without beaming; solid orange line: flux, with beaming. Left panel: photon energy 1 keV; right panel: photon energy 29 keV.

Relativistic beaming

The previous calculations were performed in the instantaneous rest frame of the electrons. Electrons are flowing down the column with a velocity that goes from about 0.5 c at the top to zero at the bottom. For this reason, the emission from the column, especially from the top, where most of the radiation is coming from, will be beamed. If I indicate with a prime the quantities after beaming, I get

$$\theta' = \cos^{-1}\left(\frac{\cos\theta - \beta}{1 - \beta\cos\theta}\right) \tag{7.19}$$

$$E'_p = \frac{E_p}{\gamma(1 + \beta\cos\theta)} \tag{7.20}$$

$$I' = I\left(\frac{E'_p}{E_p}\right)^3 \tag{7.21}$$

where E_p is the energy of the photons and $\beta = A\tau_{\parallel}$ is the speed of the electrons divided by c.

Figure 7.6 shows the effect of beaming on flux for $\beta = 0.4$ and for two photon energies, 1 keV and 29 keV: radiation is strongly beamed toward the surface of the star (high θ'). Figure 7.7 shows the average Stokes parameters after beaming, always for $\beta = 0.4$. Please notice that the angle θ' in the colour bar now does not go from 0 to $\pi/2$, as in the previous plots, but from 0 to the angle where the intensity peaks, at about 2.7 radians (see also Figure 7.6). The main effect

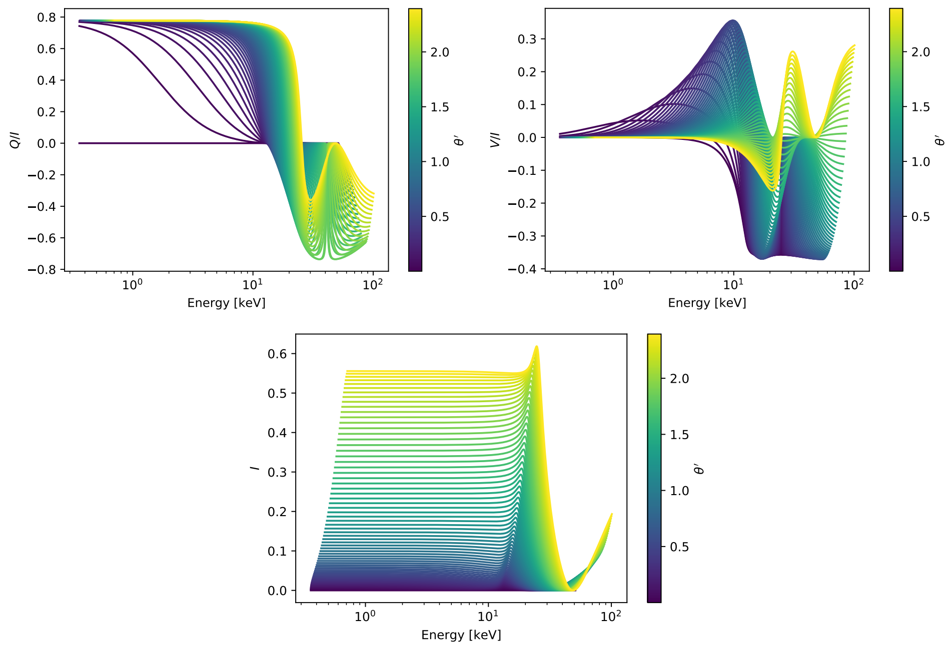

Figure 7.7: Average Stokes parameters after beaming, for $\beta = 0.4$. Top left: linear polarization fraction Q'/I'; top right: circular polarization fraction V'/I'; bottom: intensity I' (arbitrary units). The color code represents the angle with respect to the magnetic field after beaming θ'. Please notice that the angle θ' goes from 0 to the angle where the intensity peaks, at about 2.7 radians (see also Figure 7.6).

of beaming is shifting the angle where intensity peaks toward higher angles (and therefore toward the surface of the star) and to move the cyclotron line to higher energies at higher angles.

Emission from an orthogonal rotator

I can finally sum the contribution of the entire column and find the polarization parameters at emission. In the B&W07 model, most of the flux is coming from the top of the column, where $\tau_\perp$ is smaller. Throughout the column, the relation between flux, $\tau_{\parallel}$ and z (vertical direction coordinate along the column) is the following

$$\frac{L(z)}{L_{\mathrm{tot}}} = \left(\frac{z}{z_{\mathrm{max}}}\right)^{3/2} = \left(\frac{\tau}{\tau_{\mathrm{max}}}\right)^{3} \tag{7.22}$$

In order to integrate the emission from the column, I divide the column in fractions of equal flux, where I calculate the beaming, and sum all the contributions.

I consider the presence of two columns at the two magnetic poles of the neutron star. We expect to see two columns if the magnetic field has a bipolar structure, except if the field is stronger at one pole, in which case the stronger pole would swipe the gas from the accretion disk at a radius outside of the reach of the weaker pole. In this section, I assume an orthogonal rotator, with the magnetic field always lying in the same plane with the line of sight. From the orthogonal rotator, the results for any other rotational geometry can be inferred.

I am still calculating the polarization parameters at emission, so I do not include any light bending, and therefore I can use θ as the angle between the line of sight and the magnetic field and also as the phase (I will now abandon the prime). There is always an entire column visible and the other one is partially covered by the star. If z_{max} is the height of the column, for each θ the part of the back column that we see is given by

$$z_{\mathrm{max}} - R_* \left(\frac{1}{\sin\theta} - 1\right) .$$

One column is at θ and one column is at $\pi - \theta$. The radiation pattern with rotation phase is shown in the upper plots of Figure 7.8 for two photon energies, 1 keV and 29 keV. The sudden rise in intensity at about $\pi/5$ is due to the fact the back column starts to be visible and, since the emission from a column is highly beamed toward the surface of the star, the back column is the one dominating the emission. The same effect can be seen on the average Stokes parameters in Figure 7.9.

7.2.3 Polarization at the observer

Now that I have calculated the emission pattern and polarization at the source, the next step is to analyze how polarization changes as photons propagate to the observer. Specifically, I have two additional effects to take into account: gravitational

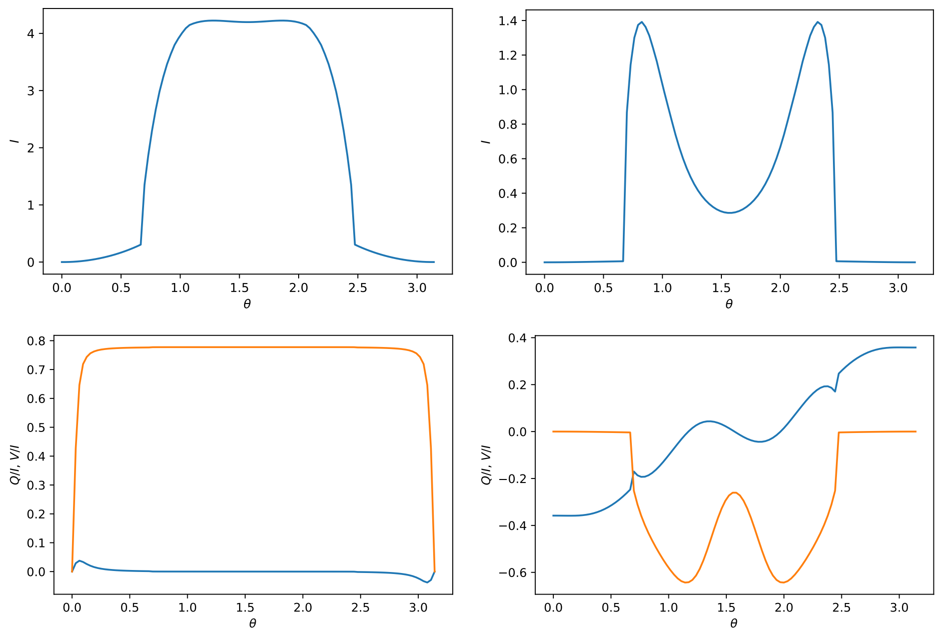

Figure 7.8: Phase pattern for intensity and polarization fractions for 2 columns without light bending. Upper panels: intensity I (arbitrary units). Lower panels: linear polarization fraction Q/I solid orange line, circular polarization fraction V/I solid orange line. Left panels: photon energy 1 keV; right panels: photon energy 29 keV.

lensing and the effect of vacuum birefringence (see also Chapter 4).

Gravitational lensing

Because neutron stars are very compact, their strong gravitational field affects the propagation of light around them, and general relativity needs to be included when calculating the photons' path. In general relativity, the path of light is bent by gravity, and therefore the image of the star results distorted at the observer. Because of light bending, the angle between the magnetic field and the photon momentum at emission, which I call θ, is now different from the phase, that from now on I will call ϕ, and from the angle between the vertical direction of the column ($\hat{z}$) and the line of sight, that I will call ψ (see Fig. 7.10). The relation between θ and ψ in

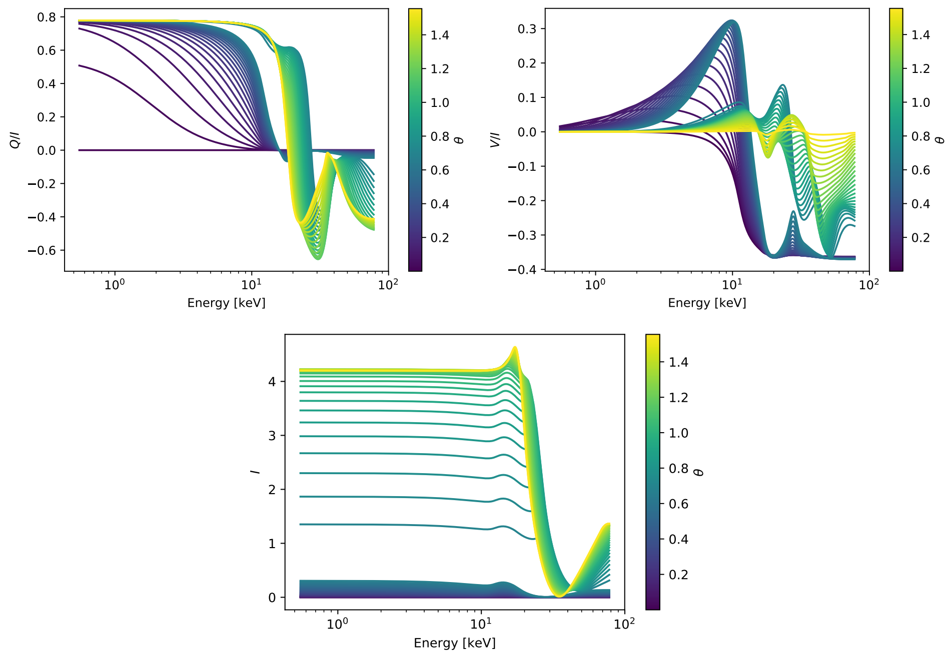

Figure 7.9: Average Stokes parameters from summing up the two column with energy and phase. Top left: linear polarization fraction Q/I; top right: circular polarization fraction V/I; bottom: intensity I. The color code represents the phase angle θ.

general relativity is given by [23]

$$\sin\theta = \frac{b}{R}\sqrt{1-\frac{R_g}{R}} \tag{7.23}$$

$$\psi = \int_R^\infty \frac{-u^\psi}{u^r}dr = \int_R^\infty \frac{dr}{r^2}\left[\frac{1}{b^2}-\frac{1}{r^2}\left(1-\frac{R_g}{r}\right)\right]^{-1/2} \tag{7.24}$$

where $R_g = 2GM_*/c^2$ is the gravitational radius of the neutron star, b is the impact parameter and R is the distance of the emission region from the center of the star. In [23], R is the radius of the star, while, in the case of emission from a column, R is the radius of the star plus z, the height along the column under consideration. For the column in the front of the star, I have to integrate between $R = R_* + z$ and infinity to get ψ. For the column in the back, I have to be more careful. For

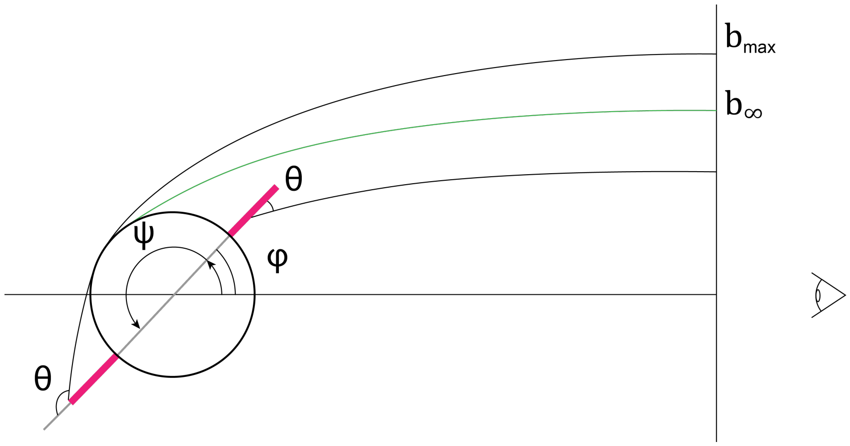

Figure 7.10: Lensing in the neutron star gravitational field. θ is the angle between the vertical direction of the column ($\hat{z}$) and the photon momentum at emission, ψ is the angle between $\hat{z}$ and the line of sight , and ϕ is the rotation phase of the star.

each light ray, labelled by the impact parameter b, I have to calculate the minimum distance from the center of the star of the light path, defined by eq.7.23 when $\sin\theta = 1$, and integrate from $R = R_* + z$ to the minimum distance and then from the minimum distance to infinity.

Depending on the compactness of the star, it is possible to see both sides of one column, from the front and from the back, because of light bending. Thus, for each phase ϕ, I have to sum the contribution from the front column at $\psi = \phi$ and at $\psi = 2\pi - \phi$ and from the back column at $\psi = \pi - \phi$ and at $\psi = \pi + \phi$, making sure of which part of the two columns is not blocked by the neutron star itself.

Furthermore, light bending magnifies the back column, and this effect, together with relativistic beaming, means that most of the emission comes from the back column. The huge magnification that we can see in Figures 7.11 and 7.12 at $\phi \sim 0$ and at $\phi \sim \pi$ hinges on the very particular geometry that I am considering: it requires the column to be pointing essentially directly away from us, creating an Einstein ring around the star. The result of this effect is that any pulsed fraction can be achieved by this model, just by varying the geometry of the star. In this particular geometry, the back column is magnified at $\phi \sim 0$, and the linear polarization fraction at low angles is still high for low energies because it is dominated by the

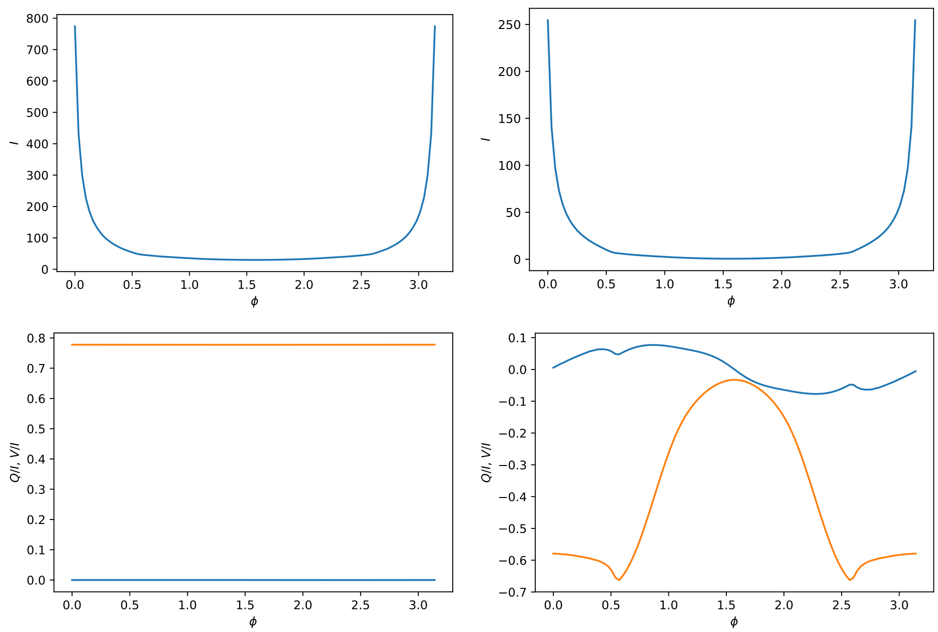

Figure 7.11: Phase pattern for intensity and polarization fractions for 2 accretion columns with light bending. Upper panels: intensity I. Lower panels: linear polarization fraction Q/I solid orange line, circular polarization fraction V/I solid orange line. Left panels: photon energy 1 keV; right panels: photon energy 29 keV.

beamed emission from the back column, for which θ is high.

Before I move on to address the effects of QED, I would like to stop and analyze the effect of lowering the height of the accretion column (see § 7.2.1). In particular, I will consider $z_{\mathrm{max}} = 6.6$ km and $z_{\mathrm{max}} = 1.4$ km. In order to better see the effect, it is simpler to show the case with only one column instead of two.

From Figure 7.13 we can immediately see that the pulse fraction is different in the two cases: in the case with $z_{\mathrm{max}} = 1.4$ km, the back column is blocked by the star at $\phi = \pi$ and therefore there is no huge magnification as in the $z_{\mathrm{max}} = 6.6$ km case, for which the back column is always in sight. The same effect can be seen in the upper panels of Figure 7.14. Also from Figure 7.14, we can see that there is little effect on the polarization fraction; the main effect is due to a shift in the cyclotron depolarization feature with angle, which is more pronounced in the case

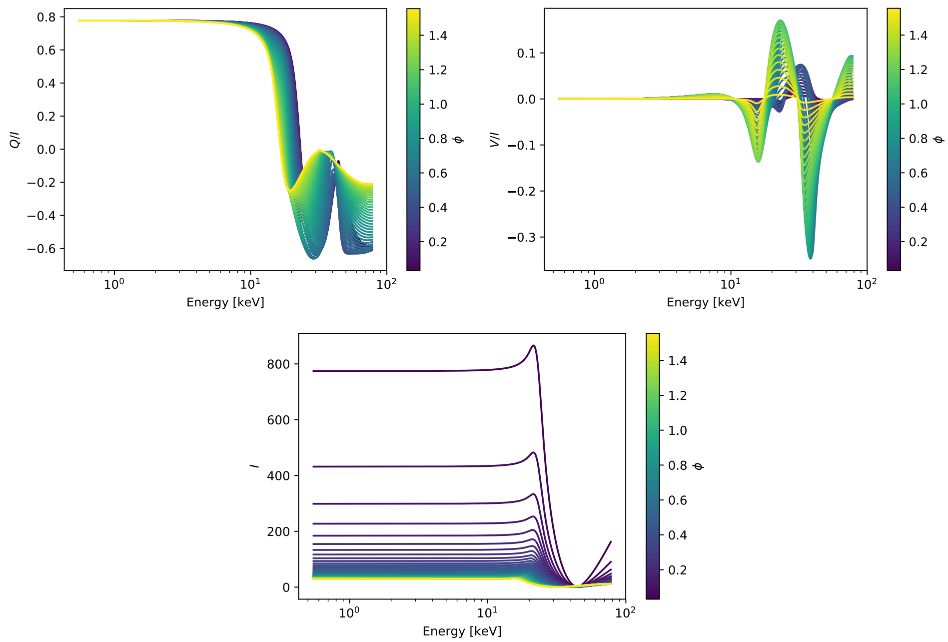

Figure 7.12: Average Stokes parameters for 2 columns with light bending. Top left: linear polarization fraction Q/I; top right: circular polarization fraction V/I; bottom: intensity I. The color code represents the phase angle ϕ, which goes from 0 to $\pi/2$.

of a highest column because of the stronger beaming from the fast electrons at the top of the column.

QED: the quasi-tangential effect

In Chapter 5, I introduced how the effect of vacuum birefringence can affect the polarization of X-ray radiation from neutron stars. For the geometry that I am considering in this chapter, the magnetic field is always in the same plane as the emission column and of the line of sight, and therefore the effect of vacuum birefringence cannot affect the direction of polarization. However, it can still destroy some of the linear and circular polarization due to the so-called *quasi-tangential* (QT) effect. In § 5.1.1 I introduced the QT effect on the emission coming from a polar cap, which is similar to the case in this chapter, with the difference that in

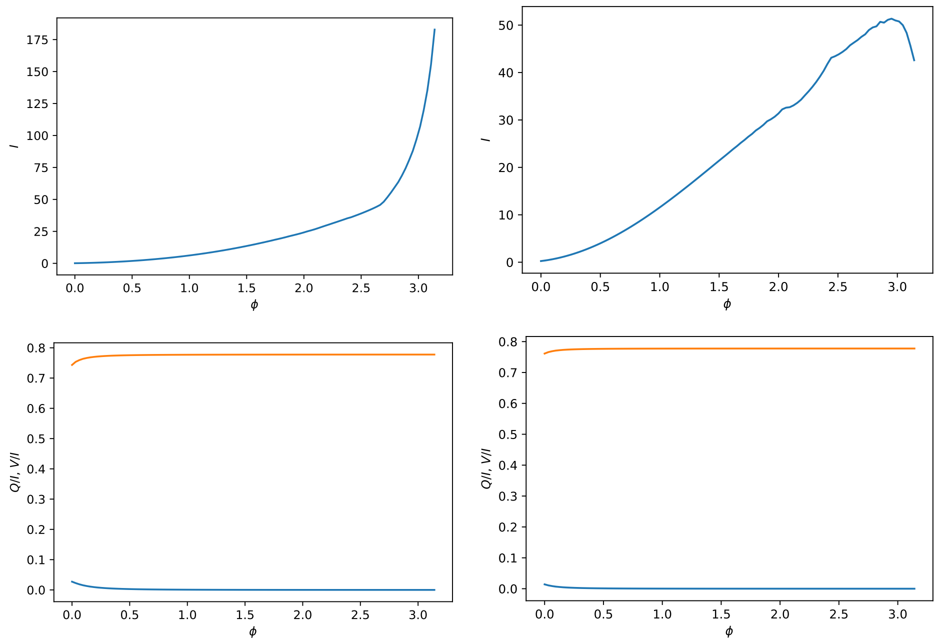

Figure 7.13: Phase pattern for intensity and polarization fractions for 1 accretion column with different heights and photon energy at 1 keV. Upper panels: intensity I. Lower panels: linear polarization fraction Q/I solid orange line, circular polarization fraction V/I solid orange line. Left panels: $z_{\rm max} = 6.6$ km; right panels: $z_{\rm max} = 1.4$ km

this case the radiation is coming from the walls of the column, and therefore I have to consider only the border of the polar cap instead of the full area.

Following the approach in § 5.1.1, I can calculate the QT effect from the ratio $W_t/W_{\rm em}$ for the radiation coming from the columns, where W_t is the width of the region in which the QT effect is important, given by eq. 5.5 and $W_{\rm em}$ is the width of the emission region. The strength of the effect depends on how far from the star the light ray crosses the QT region, as the magnetic field scales as the distance from the star to the power of -3. For this reason, $W_t/W_{\rm em}$ depends on both the z coordinate along the column of the emitting region and on the position of the column with respect to the line of sight (which for 1 column is simply indicated by ϕ). Additionally, $W_t/W_{\rm em}$ decreases with energy to the power of $1/3$ (eq. 5.5). These dependencies are shown in Figure 7.15. On both panels, the x axis represents

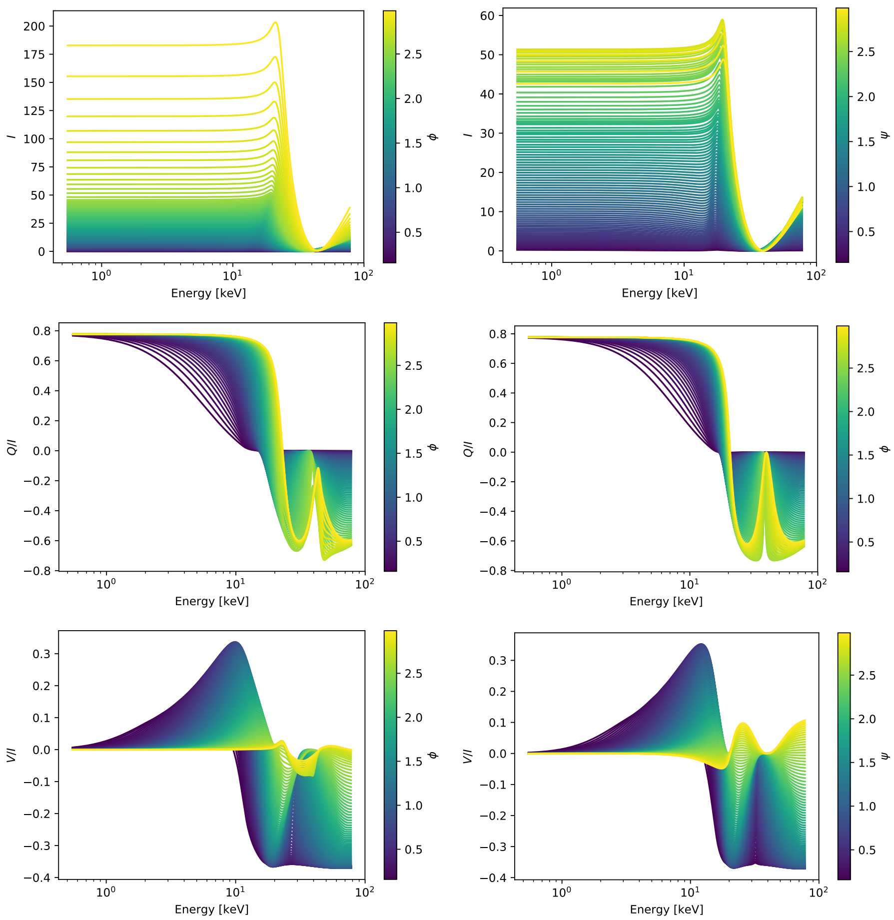

Figure 7.14: Average Stokes parameters for 1 column and different heights. The left panels depict the polarization parameters of radiation from 1 column with $z_{\mathrm{max}} = 6.6$ km, while panels on the right represent a column with $z_{\mathrm{max}} = 1.4$ km. From top to bottom: intensity I, linear polarization fraction Q/I and circular polarization fraction V/I against the energy of the photons. The color code represents the pulsar phase ϕ, and it goes from 0 to π.

the phase ϕ and the y axis is W_t/W_{em}. The horizontal lines are the same as the vertical lines in Figure 5.4: the beige lines delimit the region where the QT effect is important and the red line indicates the value at which it is the strongest. In the left panel, radiation is coming from a region of the column at $z = 0.4\, z_{\mathrm{max}}$ and the

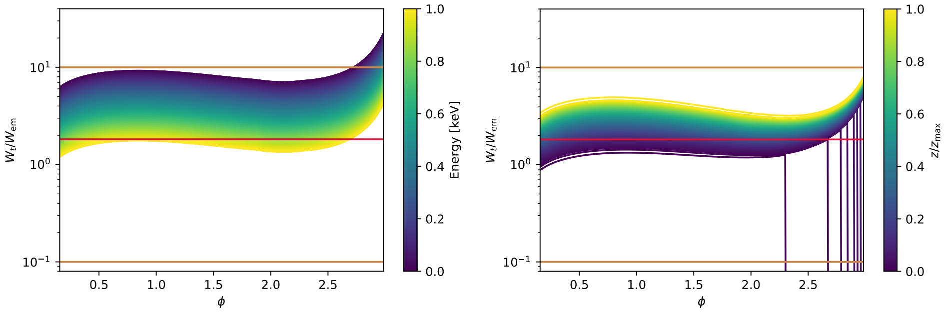

Figure 7.15: Both panels show $W_t/W_{\rm em}$ versus ϕ. The horizontal lines are the same as the vertical lines in Figure 5.4: the beige lines delimit the region where the QT effect is strong and the red line indicates the value at which it is the strongest. Left panel: photons are coming from $z = 0.4z_{\rm max} = 2.6$ km above the stellar surface; the different colors represent different photon energies. Right panel: the photon energy is 30 keV; the different colors represent different position in the column, z, of the emitting region.

different colors depict photons of different energies; we can see the dependence on energy, with higher energies being more affected by the QT propagation effect. On the right panel, photons have the same energy, 30 keV, but come from different altitudes along the column, with yellow lines representing photons coming from the top of the column, and blue lines coming from the bottom. The lower parts of the column are more affected by the QT effect, but are blocked by the star at high ϕ (in the plot, it is shown by $W_t/W_{\rm em}$ dropping abruptly to zero).

I now can finally calculate the effect of QED on the total polarization from the star. The intensity is not affected by the QT crossing, while the linear and circular polarization are. In particular, the circular polarization of each photon receives a random rotation, completely destroying the average circular polarization. The effect on linear polarization can be obtained from the calculations above and the results are shown in Figure 7.16 for a 6.6 km column, for both the 1 column and the 2 columns case.

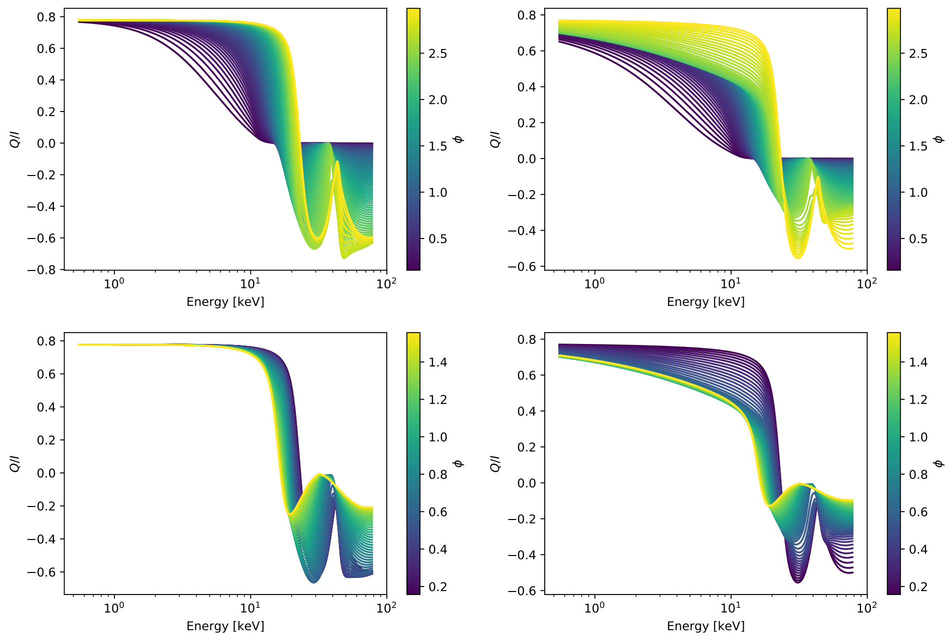

Figure 7.16: Average linear polarization fraction for $z_{\max} = 6.6$ km without and with QED. The upper panels depict the 1 column case and the lower panels the 2 column case. The left panels depict the linear polarization fraction without QED (same as in Figures 7.14 and 7.12), while the right panels show the effect of QT crossing. The color code represents the pulsar phase ϕ, and it goes from 0 to π for the 1 column case and from 0 to $\pi/2$ for the 2 columns case.

7.2.4 Results

In this section, I have calculated the polarization pattern for the radiation of a bright X-ray pulsar as Her X-1, in the context of the Becker and Wolff [20] model. In the model, accretion occurs via a column (or two columns) at the magnetic pole (poles) of the neutron star. In the accretion column, the opacity is dominated by electron scattering and the photosphere for free-free absorption resides at the bottom of the column, at the top of the so-called thermal mound. The production of polarized radiation in the column is dominated by the strong magnetic field, but other effects have to be taken into account to calculate the observed polarization: relativistic beaming, gravitational lensing and QED.

The very high average number of scatterings per photon ($\sim 250,000$) that is predicted by the B&W model leads to an average polarization state inside the column that is determined uniquely by the energy of the photon and by the strength of the magnetic field, and that is independent of the initial polarization of the photon (Fig. 7.4, left panels). At low energies (far from the cyclotron line) the average photon is nearly 100% polarized in the ordinary mode, except for photons propagating in a direction almost parallel to the magnetic field ($\theta = 0$). In the direction parallel to the magnetic field (and to the column axis) there is almost no flux, as the intensity peaks in the direction perpendicular to the column walls ($\theta = \pi/2$). Close to the cyclotron line, there is an inversion in the polarization direction (so that the linear polarization fraction goes through a zero), and at the cyclotron line photons are mostly polarized in the extraordinary mode. At low angles, close to the cyclotron line, circular polarization is predominant, as photons traveling parallel to the magnetic field can resonantly scatter off electrons, that receive enough energy to jump to the second Landau level. The circular polarization fraction decreases with θ.

As photons escape the column, the difference in scattering cross section between photons polarized in the different modes changes the picture (Fig. 7.4, right panels). At low energies, the scattering cross sections for light polarized in the O or in the X mode differ by several orders of magnitude (except for photons propagating parallel to the magnetic field, for which they are equal, see Fig. 7.5). For this reason, photons in the extraordinary mode can escape freely, while photons in the ordinary mode are trapped. This difference causes the linear polarization degree to drop to 80% at low energies. Because all the cross sections diverge in a similar way at the cyclotron energy, photons at the cyclotron energy are completely unpolarized. The increase of all the cross sections close to the cyclotron line also reduces the emission at high energy (the intensity drops sharply above 20 keV).

The right plots of Fig. 7.4 show the polarization parameters of photons coming out of the column in the frame of the accreting gas. In order to calculate the parameters in the frame of the observer, the effect of relativistic aberration and beaming is important, especially at the top of the accretion column, because the electrons in the gas have a bulk downward speed that is as high as half the speed of light at the top of the column and decreases as the gas approaches the stellar surface. The radiation scattered by relativistic electrons is strongly beamed downward (Fig. 7.6) and the features described in the previous paragraph are shifted in energy by an amount that increase with the emission angle, (see Fig. 7.7 for an electron velocity of $\sim 0.4\ c$).

The amount of relativistic beaming depends on the velocity of the electrons and therefore changes along the column. Moreover, if two columns are present at the two magnetic poles, there is always one column that is completely visible and a column that is partially blocked by the neutron star. In this chapter, I have considered an orthogonal rotator, with the columns always in the same plane with the line of sight. Fig. 7.8 shows the intensity and the polarization pattern for the two columns, without light bending for now, at the different rotation phases. When only the front column is visible ($\theta \sim 0, \pi$), the emission is low because the relativistic beaming in the column is collimating the emission toward the neutron star surface. For the same reason, as soon as the back column starts to be visible (at about $\theta \sim \pi/5$), the intensity jumps and the emission is completely dominated by the back column. The same effect can be seen in Fig. 7.9.

Fig. 7.9 shows the Stokes parameters as seen by the observer if there were no gravitational lensing. Gravitational lensing bends the path of light and distorts the image of the star. An important consequence is that part of the back of the star's surface becomes visible, and, in the case of the two columns, the back column is visible even close to $\phi \sim 0,\ \pi$. If the height of the column is ~ 7 km, as predicted by the B&W07 model, the back column is seen at all phases, and when it is exactly in the opposite direction with respect to the line of sight ($\phi = 0,\ \pi$), gravitational lensing generates a huge magnification, as it projects the column in an Einstein ring around the star (see Fig. 7.11). Of course, if the back column is not perfectly aligned with the line of sight, the effect is reduced, and therefore, depending on the geometry of the system, very large pulse fractions can be achieved.

In § 7.2.1, I showed how a different assumption on the velocity profile inside the column predicts a shorter column: $z_{\rm max} = 1.4$ km instead of $z_{\rm max} = 6.6$ km. The effect of having a smaller column is principally seen in the pulse fraction, as a smaller column cannot be seen at $\phi = \pi$ and therefore the huge magnification of the back column does not occur (see Fig. 7.13). However, the effect on the polarization fraction is subtle, and it mainly consists of a reduction of the energy shift due to relativistic beaming (see Fig. 7.14).

The final effect to be considered is the effect of QED, and specifically the so-called quasi-tangential effect. Due to the birefringence of the vacuum, when a photon crosses a region where its momentum is nearly aligned with the local magnetic field (the QT region), the polarization direction of the photon can rotate. The overall effect is a reduction of the linear polarization fraction and a complete destruction of the circular polarization. The final linear polarization fraction for the 1 and 2 columns possibilities is shown in Fig. 7.16.

Chapter 8

Polarization of Magnetars Soft Emission

Magnetars are isolated neutron stars that are powered by their magnetic field. As seen in § 1.1.3, magnetars were discovered because of their strong bursting activity; however, many magnetars are seen in a quiescent state as persistent X-ray sources, and their spectra are interpreted as a mixture of thermal and magnetospheric emission. In this chapter, I derive the polarization in the soft X-rays (0.5–10 keV) of persistent magnetars in quiescence, as for example 4U 0142+61, in the context of different physical models.

As mentioned in § 1.1.3, between outbursts, magnetars display persistent or slowly decaying X-ray emission, with luminosities $L \sim 10^{34} - 10^{35}$ erg s^{-1}. The X-ray spectrum is characterized by two peaks, with similar luminosities. The soft spectrum peaks at about 1 keV and is usually interpreted as thermal emission from the neutron star surface. The thermal emission is thought to be reprocessed in the atmosphere and/or in the magnetosphere, because the soft emission can be well fitted with an absorbed blackbody with an excess above the peak (between 1 and 10 keV). The excess can be described by a steep power law with photon index $\sim 2 - 4$, or by a second, hotter blackbody component, usually associated with emission from a hot-spot. The second, higher peak is above 100 keV. The emission between 10 and 100 keV has a positive small spectral index, of about 1-1.5, and is very pulsed. Fig. 8.1 shows the spectrum of the magnetar 4U 0142+61, with data

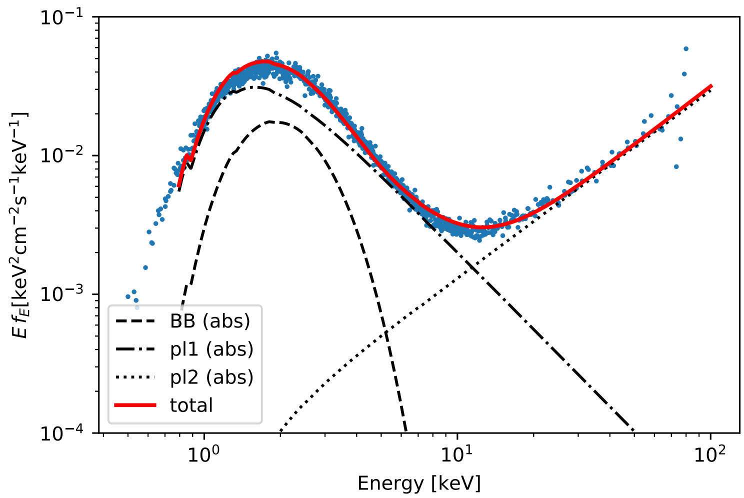

Figure 8.1: The figure shows the spectrum of the magnetar 4U 0142+61. The spectral data was acquired by Tendulkar et al. [221] with *Swift* and *NuSTAR*. A phenomenological fit is shown, as the sum of an absorbed blackbody and two absorbed powerlaws.

from *Swift* and *NuSTAR* [221]. 4U 0142+61 presents clearly in its spectrum the three main features of a magnetar spectrum, which are shown as phenomenological fits.

8.1 Thermal emission: Lloyd's atmospheres

The soft X-ray emission is interpreted as thermal emission coming from the hot neutron star surface, heated by the magnetic field decay inside the neutron star [92, 227]. The thermal peak, at about 0.5 keV, is usually fitted by a blackbody. However, many studies have shown that the emission from a real atmosphere can be quite different from a blackbody, and that the temperature of the atmosphere is usually overestimated by blackbody-fitting [132]. In this chapter, I will use the models by Lloyd [95, 96, 131] to simulate the spectrum and polarization of the thermal emission.

Lloyd's method is very efficient at computing light-element (hydrogen and/or helium), plane-parallel atmospheres in radiative equilibrium in the limit of complete ionization, and is extensible to partial ionization. Also, in the code, the direction of the magnetic field is allowed to vary from the vertical direction, and the effects of vacuum and plasma birefringence are included self-consistently.

In the models, the atmosphere is assumed to be in hydrostatic equilibrium (any bulk motion is neglected). The pressure at any depth is the sum of ideal gas pressure, radiation pressure and non-ideal effects rising from Coulomb interactions in the ionized plasma. The ideal gas pressure includes the contribution from the degenerate pressure of electrons. In a strongly magnetized plasma though, electrons are forced into Landau levels, and the phase space volume occupied by the electron distribution is small; therefore, the onset of degeneracy occurs at higher densities compared to a weakly-magnetized plasma and the degeneracy pressure contributes for less than $\sim 4\%$ even in the deepest layer.

The principal opacity sources in the ionized plasma are Thomson scattering and free-free absorption. The presence of a strong magnetic field creates a preferred orientation to scattering and absorption processes, modifying the cross sections in the two modes and generating a finite polarization in the propagating radiation, as described in § 3.2.1. Cyclotron resonances are treated by the self-consistent inclusion of ions and vacuum in the plasma dielectric.

The X-ray spectrum and polarization are found by iteratively solving the radiative transfer equations over a mesh in energy, polar angles and depth. The code assumes a plane-parallel atmosphere, which is a very good approximation since the atmosphere is incredibly thin compared to the radius of the star (centimeters compared to kilometers). However, the magnetic field varies in magnitude and direction across the surface of the neutron star, and therefore the surface of the star is divided in small patches in which the direction and strength of the magnetic field can be considered constant. In order to get the total spectrum and polarization, one needs to sum over all the different patches.

8.1.1 Thermal structure and the angular dependence of the effective temperature

The difference between the patches is not only given by the direction and strength of the magnetic field, but also by a difference in effective temperature. The thermal structure of neutron stars is affected by the presence of the strong magnetic field and this results in an angular dependence of the effective temperature across the surface. As I have mentioned before, in the strong magnetic field, the energy of the electrons is quantized, and their thermal energy is typically lower than their Landau energy ($\hbar\omega_c$). This quantization determines the structure of the electron phase-space and must be taken into account in calculating the thermodynamics of the electron gas. Heyl and Hernquist [91] calculated the thermal conduction in the thin region, the envelope, which insulates the bulk of the neutron star, for the low-temperature, strong-field regime (when only one Landau level is filled). They found that the flux from the surface depends on the angle between the local direction of the magnetic field and the normal to the surface (ψ) with a $\cos^2\psi$ dependence, and on the strength of the local magnetic field as $\sim B^{0.4}$.

In order to calculate the thermal emission from the surface, I therefore create several atmosphere patches, using Lloyd's code, to simulate the emission from different regions on the neutron star surface. Specifically, for a patch at colatitude θ, the local magnetic field strength is given by (dipolar field)

$$B = B_p \sqrt{\frac{3\cos^2\theta + 1}{4}}\,, \tag{8.1}$$

where B_p is the magnetic field at the pole; the angle between the local vertical and the magnetic field is given by

$$\cos^2\psi = \frac{4\cos^2\theta}{3\cos^2\theta + 1}\,; \tag{8.2}$$

while the flux is given by

$$F = F_p \left(\frac{B}{B_p}\right)^{0.4} \cos^2\psi = F_p \left[\sqrt{\frac{3\cos^2\theta + 1}{4}}\right]^{0.4} \frac{4\cos^2\theta}{3\cos^2\theta + 1}\,, \tag{8.3}$$

where F_p is the flux at the pole. The effective temperature of the patch is therefore given by

$$T_{\rm eff} = T_{{\rm eff}p} \left[\left(\frac{3\cos^2\theta + 1}{4}\right)^{0.2}\right]^{1/4} \left(\frac{4\cos^2\theta}{3\cos^2\theta + 1}\right)^{1/4}\,, \tag{8.4}$$

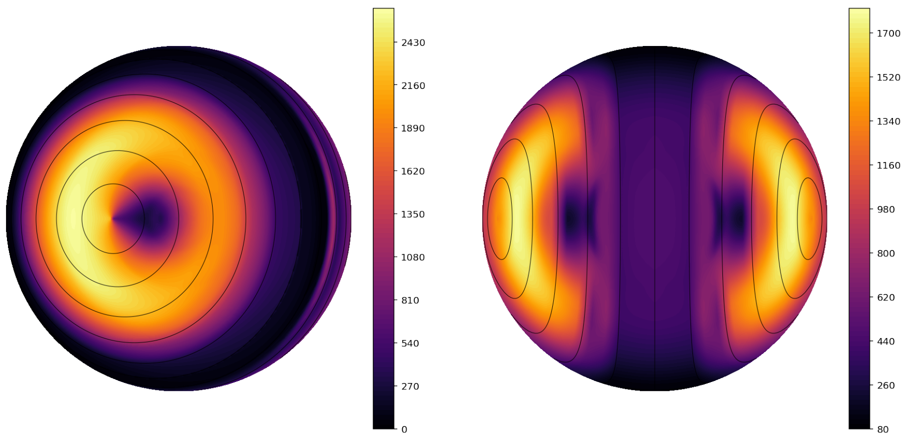

Figure 8.2: Intensity map for the thermal emission of a magnetar with $T_{\mathrm{eff}p} = 3.0 \times 10^6$ K and $B_p = 1.3 \times 10^{14}$ G, including light bending. Left: viewing angle 30°; right: viewing angle 90°. Black circles indicate contours of equal colatitude, The colormap shows the intensity of the emission for 2 keV photons.

where $T_{\mathrm{eff}p}$ is the effective temperature at the pole.

Fig. 8.2 shows the intensity map for the thermal emission at 2 keV from a magnetar with the magnetic pole at 30° (left) and at 90° (right) from the line of sight. The black circles are drawn at constant colatitude. Gravitational light bending is included in the calculation, and that is why both magnetic poles are visible in the 90° case. To calculate the intensity, I divided the surface in colatitude in 18 patches (from one pole to the other), and for each patch I calculated the atmosphere emission using Lloyd's code. The effective temperature and magnetic field at the pole are taken to be $T_{\mathrm{eff}p} = 3.0 \times 10^6$ K and $B_p = 1.3 \times 10^{14}$ G, and the temperature and magnetic field for each patch are calculated using Eqs. 8.1 and 8.4. The $\cos^2$ dependence can be seen in the map. The dark region close to the pole in the left image and the two dark regions at mirrored positions with respect to the center in the right image correspond to the regions where the local magnetic field is pointing in the direction of the line of sight. This seems counter-intuitive, as photons can escape more easily when streaming along the magnetic field line; however, I cannot resolve the very small region in angle around the magnetic field direction where the intensity peaks, and the region around the peak is depleted of photons because they can easily get scattered in the magnetic field direction. This behavior can be seen in Fig. 3.4, where the intensity as a function of angle is shown for photons at 0.32 keV, but the peak is much finer (and harder to resolve) at 2 keV.

8.2 Non-thermal emission: a twisted magnetosphere

The non-thermal emission is thought to be fueled by the energy stored in the magnetosphere of the neutron star. Similar to the Sun, magnetars are believed to possess twisted magnetospheres. Inside the star, magnetic fields can reach values close to $\sim 10^{17}$ G and the poloidal and toroidal components are expected to be roughly in equipartition [225, 226]. The internal toroidal field creates strong stresses on the surface layers, causing occasional starquakes or slow plastic flowing of the crust [227]. The magnetosphere is anchored to the crust and, similar to the Sun's corona, gets twisted by the motions of the crust [228]. As a result, the magnetosphere becomes non-potential ($\nabla \times \boldsymbol{B} \neq 0$) and is threaded by force-free electric currents, that flow along the magnetic field lines ($\boldsymbol{j} \times \boldsymbol{B} = 0$) [28]. Twisted, force-free magnetospheres in axial symmetry can be described by the Grad-Schlüter-Shafrenov (GSS) equation, and numerical solutions have been found for a self-similar twisted dipole [245] and self-similar multipoles [176]. Realistic, non-self-similar solutions were only explored for the case of weak twists [24, 25].

The first solution for an axisymmetrical, force-free and self-similar magnetar magnetosphere was proposed by Thompson et al. [228]. They express the flux of the poloidal component of the field with the function $\mathscr{P} = \mathscr{P}(r,\theta)$, independent of the azimuth ϕ because of the symmetry. The magnetic field can be therefore expressed as a sum of the poloidal and the toroidal component:

$$\boldsymbol{B} = \frac{\nabla \mathscr{P}(r,\theta) \times \hat{\boldsymbol{e}}_\phi}{r \sin\theta} + B_\phi(r,\theta)\hat{\boldsymbol{e}}_\phi \tag{8.5}$$

where $\hat{\boldsymbol{e}}_\phi$ is the unit vector in the ϕ direction. The force-free condition imposes B_ϕ to be a function of $\mathscr{P}$, and therefore, by writing $B_\phi = F(\mathscr{P})/(r\sin\theta)$, one can obtain the GSS equation

$$\frac{\partial^2 \mathscr{P}}{\partial r^2} + \frac{\sin^2\theta}{r^2}\frac{\partial^2 \mathscr{P}}{\partial \cos^2\theta} + F(\mathscr{P})\frac{\mathrm{d}F}{\mathrm{d}\mathscr{P}} = 0 \tag{8.6}$$

Thompson et al. [228] assume a self-similar solution, that makes eq. 8.6 separable:

$$\mathscr{P} = \mathscr{P}_0 \left(\frac{r}{R_*}\right)^{-p} f(\cos\theta) \tag{8.7}$$

where R_* is the radius of the neutron star and the constant is set to $\mathscr{P}_0 = B_p R_*^2/2$ in order to find the right value of the magnetic field at the pole (B_p). In this way, the GSS equation becomes a second order eigenvalue differential equation for $f(\cos\theta)$, that can be solved for $0 \leq p \leq 1$. If the boundary conditions are chosen for a dipolar field, one finds the polar components of the magnetic field to be

$$B_r = -\frac{B_p}{2}\left(\frac{r}{R_*}\right)^{-2-p} \frac{\mathrm{d}f}{\mathrm{d}\cos\theta} \tag{8.8}$$

$$B_\theta = \frac{B_p}{2}\left(\frac{r}{R_*}\right)^{-2-p} \frac{pf}{\sin\theta} \tag{8.9}$$

$$B_\phi = \frac{B_p}{2}\left(\frac{r}{R_*}\right)^{-2-p} \sqrt{\frac{Cp}{p+1}}\frac{f^{1+1/p}}{\sin\theta} \tag{8.10}$$

where C is an eigenvalue that depends only on p. The parameter p controls the radial decrease of the magnetic field, but also the net amount of twist. The twist angle, defined as the displacement between the north and south footprints of the magnetic field lines, is found as

$$\Delta\phi_{\mathrm{N-S}} = \int_{\text{fieldline}} \frac{B_\phi}{B_\theta}\frac{\mathrm{d}\cos\theta}{\sin^2\theta} = 2\sqrt{\frac{C}{p(p+1)}} \lim_{\theta_0 \to 0} \int_{\theta_0}^{\pi/2} \frac{f^{1/p}}{\sin\theta}\mathrm{d}\theta \tag{8.11}$$

From the magnetic structure, one can find the current density induced along the twisted field lines

$$\boldsymbol{j} = \sum_i Z_i e n_i \boldsymbol{\beta}_i c = \frac{(p+1)c}{4\pi r}\frac{B_\phi}{B_\theta}\boldsymbol{B} \tag{8.12}$$

where $Z_i e$ is the electric charge of the particles species i carrying the current, n_i is the particle density, and $\boldsymbol{\beta}_i$ is the particle velocity in units of c in the direction of the local magnetic field.

The twisted magnetosphere stores energy in the currents, and tends to dissipate it over time and to "untwist". The plasma that fills the magnetosphere converts this energy into radiation, generating the non-thermal emission. Beloborodov [24] studied the electrodynamics of untwisting, and found that whenever the crustal motion that causes the twist stops or slows down, the electric currents flowing on magnetic field lines close to the neutron star surface (with apex radii $R_{\max} \lesssim 2R_*$, where R_* is the radius of the neutron star) are quickly removed and absorbed by the crust. The lifetimes of the currents on field lines with $R_{\max} \gg R_*$ are much longer, and therefore the persistent emission has to be created by the plasma on the extended field lines, which form what he calls a "j-bundle". The plasma that fills the j-bundle is responsible for carrying the electric currents $\boldsymbol{j} = c/4\pi\nabla \times \boldsymbol{B}$ and is continually created by electron-positron pairs ($e^{\pm}$) discharge near the surface. Because the discharge has a threshold voltage of about 10^9 V [28], the boundary between the depleted region where $j = 0$ and the j-bundle is sharp, and it moves toward the magnetic dipole axis with time.

8.2.1 Non-thermal models: the 5-10 keV range

The twisted magnetosphere around the neutron star is bound to affect the thermal emission from the surface, and to cause the observed non-thermal power laws. Several models have been proposed to explain the power law or excess emission observed above the thermal peak in the 2-10 keV range. I will briefly introduce some of the models here that I will employ later to calculate the spectral shape and polarization.

The hot-spot model

The impact of the particles carrying the current on the neutron star surface could be a source of heating, as a fraction of the kinetic energy could be deposited in the surface layer of the neutron star, and could create a hot-spot at the magnetic poles. In particular, the transient X-ray emission from the magnetar XTE J1810-197 is best fitted with a double blackbody (one for the surface emission and one for the hot-spot). The luminosity of the hot-spot was observed to decrease [96], implying a shrinking of the surface area, which is in agreement with the picture of a shrinking j-bundle. In § 8.3.1, I will analyze the spectrum and polarization in this context by modeling the thermal emission and the excess above the peak with an hydrogen atmosphere model for the entire surface and coupled with a hotter model for the hot spot.

The resonant Compton scattering model

In the twisted magnetosphere picture, an electric current $\boldsymbol{j} = c/4\pi\nabla \times \boldsymbol{B}$ must flow along the magnetic field lines and has to be provided by the $e^{\pm}$ pairs generated from the discharge in the magnetosphere, or, alternatively, by a flow of electrons and ions ripped from the neutron star surface. In the model first introduced by Thompson et al. [228], the positive and negative charges are counter-streaming along the magnetic field lines and possess similar number densities $n_{+} \sim n_{-}$; in this way, the coronal plasma is nearly neutral and the required current is provided: $j = e(v_{+}n_{+} - v_{-}n_{-})$, where $v_{+}v_{-} < 0$.

In the Thompson et al. [228] model, the thermal ($\sim$ 1 keV) photons emitted from the stellar surface are resonantly Compton scattered by the coronal plasma at large radii ($\sim$ 100 R_{*}), where the dipolar magnetic field has a strength $B \sim 10^{11} - 10^{12}$ G. In order to be able to resonantly scatter photons in this region, the flowing charges have to be mildly relativistic (see § 3.2.3). In the Thompson et al. [228] model, the velocities of the charges v_{+} and v_{-} are considered free parameters, which may be adjusted so that the scattering of the thermal photons can reproduce the observed spectrum.

Fernández and Thompson [62] have performed Monte Carlo simulations to determine the basic types of non-thermal spectra and pulse profile that can be obtained by varying the free parameters of this model, namely the twist angle $\Delta\phi_{\mathrm{N-S}}$ (eq. 8.12), the spectral distribution of seed photons (they assume a blackbody distribution), the polarization of the seed photons (they assume either 100% X or 100% O), the angular distribution of the seed photons and the momentum distribution of the charge carriers. They obtain a variety of spectral shapes, some of which resemble the magnetar soft X-ray emission, although they never fit them to observed X-ray spectra. When they employ a broad, relativistic distribution of charge momenta, they obtain a spectrum that dips above the thermal peak and then rises again as a power law to a maximum frequency that increases with the maximum Lorentz factor of their distribution. This would suggest that RCS could be at the origin of the hard power law (20–100 keV) as well. A similar model was employed by Nobili et al. [165], and in [250] they successful fit the obtained spectra to several magnetars, with a few exceptions.

The RCS model is very successful at fitting the soft spectrum of magnetars [250]; however, Beloborodov [27] points out that the RCS picture for the soft spectrum, in which two mildly relativistic fluids of opposite charges scatter photons far away from the star, presents a problem. In the region where the magnetic field is about $B \sim 10^{11} - 10^{12}$ G, the radiation pressure pushes the plasma away from the star and a strong electric field parallel to the magnetic field line needs to be present to counteract the radiative drag and bring the particles back toward the star. The same electric field, however, will push the particles with opposite sign away, increasing the effect of the drag, and bringing the particle velocity to be highly, and not mildly, relativistic.

In § 8.3.3 I will present a heuristic model to calculate the number of scatterings needed to reproduce the spectrum in case of a partial Comptonization due to mildly relativistic electrons, and I calculate the polarization expected in this case.

Saturated Comptonization model

An alternative explanation for the excess above the thermal peak, that has not been proposed before, is a saturated Comptonization of the thermal photons by a non-relativistic population of electrons close to the stellar surface. This is the most conservative model, as it does not require relativistic or ultra-relativistic electrons, or a specific distance from the star. However, because the majority of thermal photons are being emitted in the X-mode, and the scattering cross section for X-mode photons is very small, resonant scattering has been invoked in order to build enough optical depth to explain the power law excess with Compton scattering of X-mode photons. This is not necessary though in the case in which at least a small fraction of thermal photons are emitted in the O-mode; from Lloyd's atmosphere models, the amount of photons emitted in the O-mode is of the order of 2%.

The difference in scattering cross section between the two modes at these energies is several orders of magnitude (the O-mode cross section is simply the Thom-

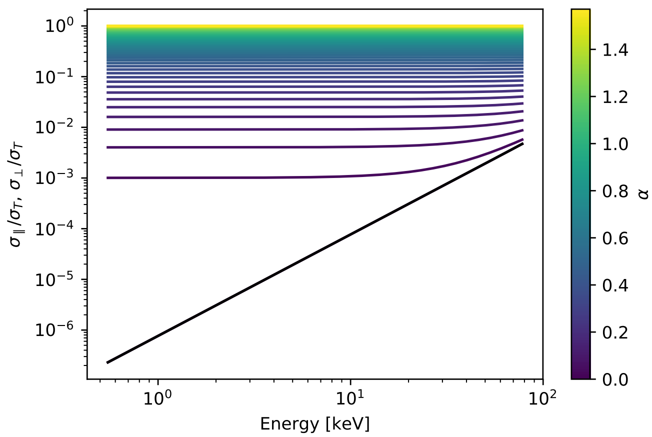

Figure 8.3: O-mode ($\sigma_{\parallel}$) and X-mode ($\sigma_{\perp}$) cross section in the X-rays for a magnetar magnetic field. The different colors show the O-mode cross section for different angles α (in radians) between the incident photon direction and the magnetic field, while the black solid line shows the X-mode cross section, which is equal to the O-mode cross section for $\alpha = 0$. Except for photons propagating along the magnetic field direction, the X-mode cross section is several order of magnitudes smaller than the O-mode cross section. Same as Fig. 7.5 but for $B = 1.3 \times 10^{14}$ G instead of $B = 4.3 \times 10^{12}$ G.

son cross section, see Fig. 8.3), and therefore, for O-mode photons, it is much easier to build enough optical depth to fully Comptonize the population. Moreover, whenever an X-mode photon happens to scatter, it is immediately converted into an O-mode photon, because we are considering energies far below the electron cyclotron line, and afterwards, its scattering cross section is hugely increased.

The evolution of the spectrum in the presence of repeated scatterings off non-relativistic or mildly relativistic electrons can be calculated with the Kompaneets equation [113] (see § 8.3.2) and in case of saturated scattering, the equation leads to an approximated Wien law. This is because, when photons undergo many scatterings, they reach a thermal equilibrium with the electrons, and get "scattered up" into a Bose-Einstein distribution [195]. Even if only 2% photons are in the O-mode, this is enough to explain the observed excess above the thermal peak if the scattering plasma has a temperature of ~ 2 keV.

8.2.2 Non-thermal models: the 20-100 keV range

Resonant Compton scattering has been also invoked to explain the high-energy tail observed in several magnetars. A similar model to the one introduced in § 8.2.1, with thermal photons from the surface scattering off a counter-streaming flow of opposite charges in the magnetosphere at about 100 km from the surface, was employed by Fernández and Thompson [62] and by Wadiasingh et al. [236] to try and fit the high-energy tail. The high-energy emission is explained in this model by assuming a broader, highly-relativistic ($\gamma > 20$) distribution of scattering centers in the magnetosphere, compared to the mildly relativistic flow assumed in the soft-emission model.

An alternative model was proposed by Beloborodov [26, 27], who also invokes RCS, but off a different plasma flow in the magnetar corona: instead of having two counter-streaming flows of opposite charge, in Beloborodov's model the required current for the twist is provided by $e^{\pm}$ flowing in the same direction away from the star but with a small difference in velocity. The density of the plasma is much higher than the density required by the current j/ec, and the current is sustained in the outflow by a moderate electric field parallel to the magnetic field lines. The flow of $e^{\pm}$ is the same from the two magnetic poles and the particles accumulate at the equatorial plane, where they annihilate.

In this picture, $e^{\pm}$ are created at the footprints of the magnetic field lines and accelerated to high Lorentz factor, until they can resonantly scatter in the strong magnetic field, at about $\gamma \sim 10^3$. The upscattered photons immediately produce more $e^{\pm}$. Some of the $e^{\pm}$ flow out along the magnetic field lines; as they move to larger radii, the strength of the magnetic field decreases, and the charges can scatter photons of lower energy, which are more abundant. In the region between the surface of the star and where $B \lesssim B_{\rm QED}$, all the scattered photons convert to $e^{\pm}$ and the pair density goes up by a factor of ~ 100. In this region, the particles slow down but cannot radiate away their energy, and the total kinetic energy is conserved but shared by more particles. Near the region where $B \sim 10^{13}$ G, pair creation ends, and outside this surface the resonantly scattered photons can escape. The outflow decelerates and annihilates at the top of the magnetic loop, in the equatorial plane; here it becomes very opaque to the thermal keV photons flowing from the star.

Photons reflected from this region have the best chance of being upscattered by the relativistic outflow in the high magnetic field region, because of their incident angles, and control its deceleration.

Since both models employ RCS to explain the high-energy emission, a similar polarization signal is expected, which is about 33% in the X-mode (see below). Other models have been proposed that predict a different polarization signal. For example, Thompson and Beloborodov [224] suggest the origin of the high-energy tail to be thermal bremsstrahlung in the surface layers of the star, heated by the returning charges flowing in the twisted magnetosphere. In their model, the energy is deposited in a shallow layer on the surface, and therefore they assume that photons emerging from the atmosphere, mainly in the X-mode, cannot scatter and cool down the layer, which has to cool by emitting O-mode photons.

8.3 Modeling the spectrum and polarization of 4U 0142+61

The spectrum of magnetar 4U 0142+61 presents clearly the three main features observed in magnetar spectra: the thermal emission peaking at ~ 1 keV, the hard excess above the thermal peak and below 10 keV, and the hard tail above 10 keV. I will therefore use its spectrum, observed by NuSTAR and Swift [221], as a reference for modeling the spectrum and polarization of magnetars X-ray emission. In this section, I will always use Lloyd's hydrogen atmospheres to model the thermal emission, but with different effective temperatures as required by the different models.

For the hard-energy tail, I will not derive the spectral shape from a theoretical physical model, and I will simply employ a power law with $\Gamma \sim 1.3$. If one assumes a RCS model (either the counter-streaming or the Beloborodov model), the polarization is determined by the number of scatterings in the magnetosphere (see the discussion in § 3.2.3): the probability of a photon to resonantly scatter into a X-photon or into a O-photon is given by the ratio of the resonant cross sections and is, respectively, 3/4 and 1/4, and an X-photon is three times more likely to scatter. Therefore, if the incident photons are all in X, the polarization after one scattering is about 50% in X and it is subsequently reduced for further scatterings. The analysis of Fernández and Davis [61] shows that the average number of scatterings at energies above ~ 10 keV converges to about 2, and the polarization degree consequently converges to $\sim 33\%$ in X.

In the following sections, I will focus on the soft emission and I will derive the spectral shape and polarization in the context of the different models proposed. In order to compare the calculated spectrum with the observed one, I model the absorption in the X-ray from the interstellar medium using the model developed by Wilms et al. [243] for a neutral hydrogen column density $N_H \sim 10^{22}$ cm^{-2} (this is included in `XSPEC` as the `tbabs` model).

8.3.1 The hot spot

The spectrum of magnetar 4U 0142+61 can be fitted with a double black body, which hints to the possibility of the excess above the thermal peak to be caused by a hot spot. In [221], the two black bodies used to fit the spectrum have temperatures $kT_{\rm eff} = 0.422 \pm 0.004$ keV for the whole surface and $kT_{\rm eff} = 0.93 \pm 0.02$ keV for the hot spot. However, Lloyd et al. [132] have shown that using a blackbody function leads to an overestimation of the surface temperature, and that detailed atmosphere calculations are needed to obtain a proper fit of the spectral shape of neutron stars. I now use the equations introduced in § 8.1.1 to calculate the emission from the whole surface using Lloyd's hydrogen atmospheres, assuming a temperature at the pole $kT_{\rm eff}{}_p = 0.26$ keV and a magnetic field $B_p = 1.3 \times 10^{14}$ G. For the patches within $\theta = 2°$ from the magnetic pole, I use a different temperature $kT_{\rm eff}{}_p = 1.33$ keV. In this way, I obtain a hot-spot at the magnetic pole, and a spectral shape that compares well with the observed spectrum. The intensity map obtained is shown in Fig. 8.6 for photons with energy 5 keV; since the small hot spot is much hotter than the rest of the star, the logarithm of the intensity is shown (a linear map would only show the hot spot).

The upper panel of Fig. 8.4 shows the observed spectral data from [221], together with the calculated emission. The black lines show the contribution from the hydrogen atmosphere (dashes), which includes the hot spot, and from the high-energy power-law (dots). The red line shows the sum of the contributions as observed at infinity with an inclination angle of 30°, including the effects of light

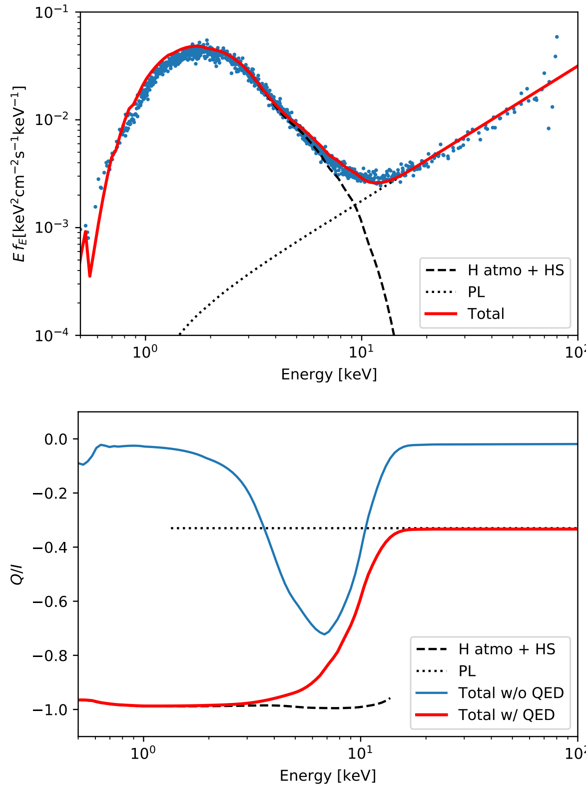

Figure 8.4: Spectral shape and polarization for the hot spot model. Upper panel: the figure shows the spectral data of 4U 0142+61 [221]; on top, the different components are shown in black: the absorbed hydrogen atmosphere and the hot spot (dashed) and the high-energy power-law, with spectral index $\Gamma = 1.4$ (dotted). The red line shows the sum of the 2 components and it is plotted on top of the spectral data for comparison. Lower panel: linear polarization fraction; the components in black are the same as for the upper panel. The total polarization fraction is shown with (red solid line) and without (blue solid line) taking into account QED.

bending and gravitational redshift. I did not attempt spectral fitting, which is left as a task for future work; however, Fig. 8.4 shows that the emission from the surface and the hot spot can describe well the spectral shape observed below 10 keV.

The lower panel of Fig. 8.4 shows the linear polarization degree as function of

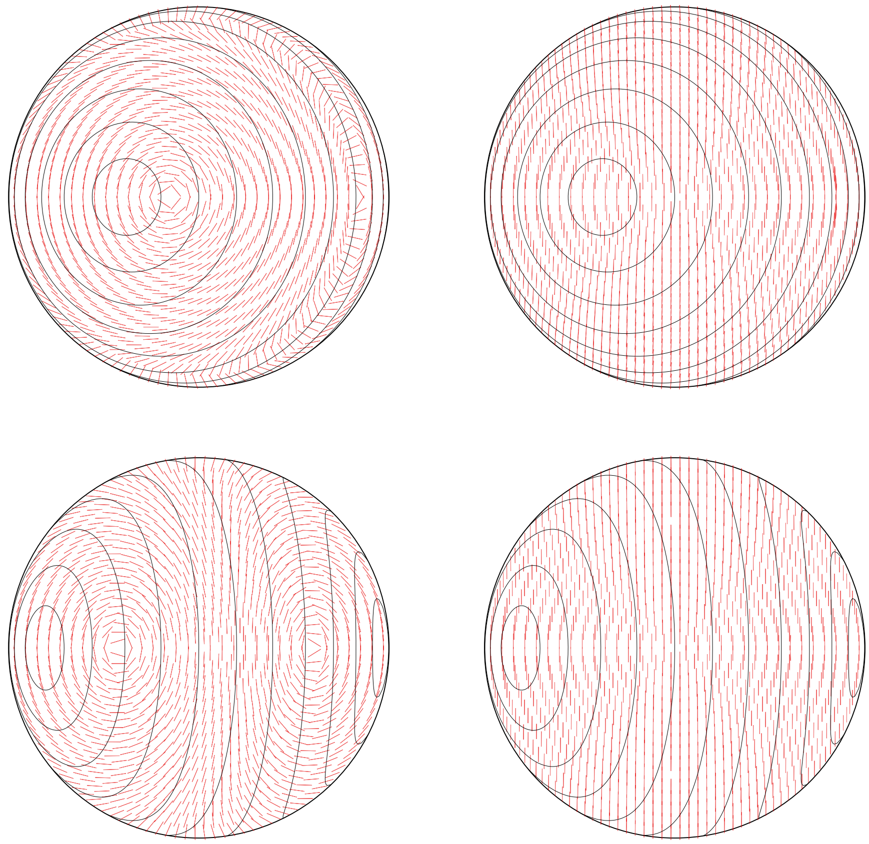

Figure 8.5: Polarization map for a magnetar with and without QED. Black circles indicate contours of equal colatitude, while red lines indicate the direction of polarization. Upper images: viewing angle 30°; lower images: viewing angle 75°. Left images: polarization map at surface assuming 100% X-mode photons, $B_p = 1.3 \times 10^{14}$ G and no QED. Right images: polarization map at the polarization-limiting radius (and therefore at the observer) assuming 100% X-mode photons, $B_p = 1.3 \times 10^{14}$ G, and including QED.

the photon energy, where a positive Q/I corresponds to O-mode polarization and a negative Q/I corresponds to X-mode polarization. The viewing angle is again 30°. The components in black are the same as for the upper panel: the multi-temperature atmosphere as dashes and the power-law as dots, and they were both calculated including QED. The total is shown including the QED effect of vacuum birefringence in red and without including QED in blue. If QED is not included, the degree of polarization at the observer is dramatically reduced. This is because, even if the polarization degree at surface is more than 90% in the X-mode for the thermal emission, when the contributions from different parts of the surface are summed over, the total polarization degree is reduced because the magnetic field points in all different directions. The left images of Fig. 8.5 show the polarization map for the emission at surface, assuming it is all polarized perpendicularly to the local field lines, in the X-mode, and taking into account gravitational lensing. The upper images show the surface map of the star for an inclination angle of 30°, while the lower images for an inclination angle of 75°. The black circles indicate contours of equal colatitude, while the red lines indicate the direction of polarization locally. If QED is not included, the polarization observed at infinity is the sum of the contribution from the whole surface of the left images, where the magnetic field is pointed in many different directions and so is the polarization. Even if the surface emission is 100% polarized, the total observed polarization is very low, as can be seen from the blue line in Fig. 8.4 at low energies. The blue line starts getting more polarized around 4 keV because at this point the emission from the hot spot becomes predominant. The reason can be seen in Fig. 8.6: if we restrict to the emission from the hot spot (yellow dot), where the magnetic field is quite uniform in direction, the polarization is aligned in also in the left image.

The effect of QED in presence of a high magnetic field, as shown in Chapter 5, is to preserve the polarization degree at emission. This effect is shown in the right images of Fig. 8.5: if one includes QED, the polarization direction is not frozen to the value at the surface (shown in the left images), but keeps changing following the local magnetic field to the polarization-limiting radius, tens of stellar radii away from the surface in the case of magnetars, where the magnetic field through which the radiation passes is uniform. If a photon is emitted in the X-mode, its polarization will rotate so that it keeps being perpendicular to the local magnetic field (the photons keeps staying in the X-mode) and the same for an O-mode photon. In the right images of Fig. 8.5 the polarization at the r_{pl} is almost completely aligned in the map, and therefore by summing over the entire map one re-obtain the polarization at emission. The treatment for the high-energy power law is similar. It is

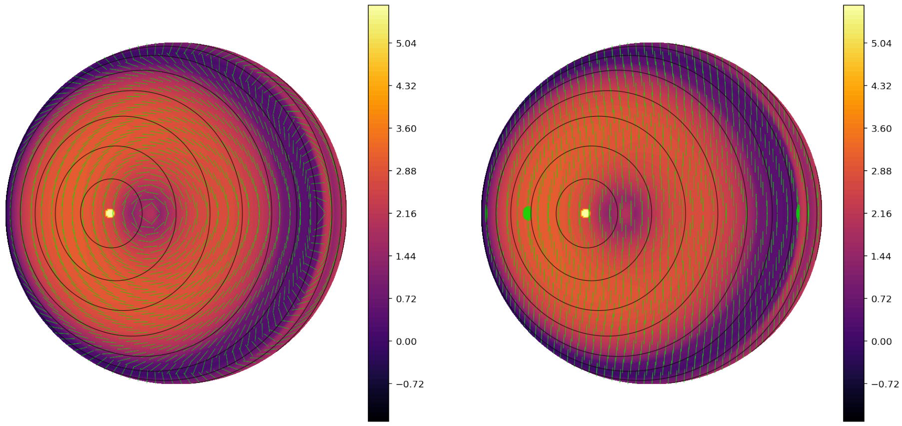

Figure 8.6: Polarization and intensity map for the hot spot model. Same as the upper images of Fig. 8.5: viewing angle 30°, without QED (left) and with QED (right). The yellow dot is the hot spot, and the green ellipses are regions where circular polarization is generated through the quasi-tagential effect (§ 5.1.1). Black circles indicate contours of equal colatitude, while green lines indicate the direction of polarization. The colormap shows the logarithm of the intensity for 5 keV photons.

emitted in the magnetosphere with a 33% polarization degree in X, from a sphere of about 100 km in radius, where the magnetic field is pointed in many directions. Therefore, without QED, the observed polarization is almost zero. Since 100 km is well within the polarization-limiting radius for a magnetar, QED has the same effect of preserving the polarization, and the observed polarization is the same as at emission, about 33%.

The red line of Fig. 8.4 shows the polarization at the observer for a viewing angle of 30°. At low energy, the contribution from the atmosphere (and the hot spot) is predominant, and the emission is highly polarized in the X-mode. As the high-energy power law becomes more important, around 6 keV, the polarization degree diminishes and reaches the 33% of the power law around 10 keV.

8.3.2 The saturated Comptonization

In this section, I will assume that the excess above the thermal peak is caused by inverse Compton scattering off a population of hot electrons in a plasma above the atmosphere. The evolution of the photon phase space density, $n(\omega)$, due to scattering off electrons is described by the Boltzmann equation [195]

$$\frac{\partial n(\omega)}{\partial t} = c\int \mathrm{d}^3 p \int \frac{\mathrm{d}\sigma}{\mathrm{d}\Omega}\mathrm{d}\Omega[f_e(\boldsymbol{p}_1)n(\omega_1)(1+n(\omega)) - f_e(\boldsymbol{p})n(\omega)(1+n(\omega_1))] \tag{8.13}$$

where $f_e(\boldsymbol{p})$ is the phase density of electrons of momentum $\boldsymbol{p}$. The first term of the sum represent photons scattering into the frequency ω and the second term represents photons scattering out of the frequency ω, in the scattering events generically described as

$$p+\omega \leftrightarrow p_1+\omega_1 \tag{8.14}$$

This is the standard Boltzmann equation, with the addition of the quantum corrections $(1+n(\omega))$ for stimulated emission. In the case of a non-relativistic thermal distribution of electrons ($f_e(\boldsymbol{p}) = n_e(2\pi m_e kT_e)^{-3/2}e^{-p^2/2m_e kT_e}$), and a small energy transfer per scattering ($\hbar(\omega_1-\omega)/kT_e \ll 1$), eq. 8.13 can be approximated by the Kompaneets equation

$$\frac{\partial n}{\partial t_c} = \left(\frac{kT}{m_e c^2}\right)\frac{1}{x^2}\frac{\partial}{\partial x}[x^4(n'+n+n^2)] \tag{8.15}$$

where $x = \hbar\omega/kT_e$, $n' = \partial n/\partial x$ and where

$$t_c \equiv (n_e \sigma_T c)t \tag{8.16}$$

is the time measured in units of mean time between scatterings. When photons are scattered many times, the spectrum reaches a steady state solution, which is, the photons tend to be in equilibrium with the electrons and assume a Bose-Einstein distribution with a chemical potential, because photons cannot be created or destroyed by scattering

$$n(x) = (e^{\frac{\mu}{kT_e}+x}-1)^{-1}\,. \tag{8.17}$$

In order to calculate the emission spectrum from the magnetar in the case of full Comptonization, I will therefore take the thermal emission from the surface and divide the photons in X-mode and O-mode photons. The X-mode photons escape freely and preserve the original distribution, while for the O-mode photons I

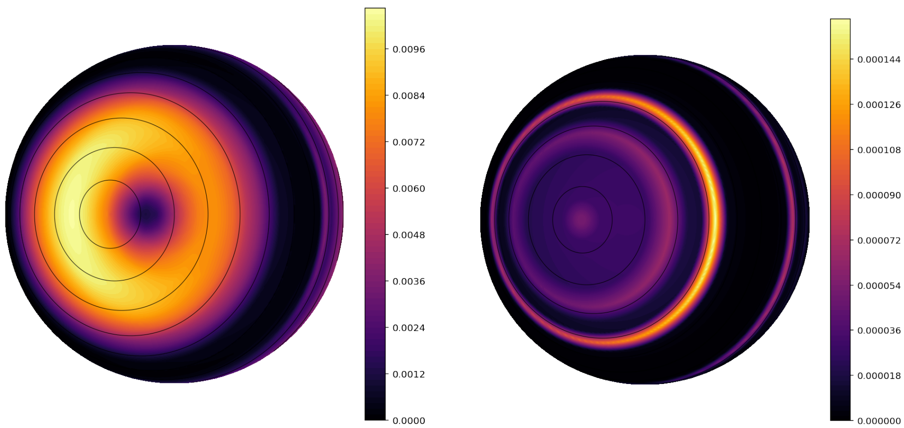

Figure 8.7: Intensity map for the saturated Comptonization model, for a viewing angle 30°. The left image shows the intensity for the X-mode photons, while the right image is intensity of the O-mode photons, both at 5 keV. The total intensity looks like the image to the left for energies below 6-7 keV; for higher energies, the O-mode photons begin to dominate and the total intensity starts looking like the right image.

calculate the Comptonized spectrum assuming they reach a Bose-Einstein distribution.

For the thermal emission, I now assume a pole temperature of $kT_{\mathrm{eff}p} = 0.32$ keV and a magnetic field at the pole $B_p = 1.3 \times 10^{14}$ G, to calculate the atmosphere models at the surface, following the equations in § 8.1.1. For each patch, the amount of O-mode radiation (which is about 2%) gets scattered up by an electron-dominated plasma at a temperature of $kT_e = 2.1$ keV, and reaches a Bose-Einstein distribution with a chemical potential $\mu/kT_e \sim 10$. I calculate the chemical potential by making sure that the total number of O-photons remain the same before and after scattering. Fig. 8.7 shows the intensity map for the X-mode and the O-mode on the surface of the neutron star for a viewing angle of 30°. The left panel shows the intensity map for the X-mode photons at 2 keV, which escape directly from the atmosphere without scattering. As most of the atmosphere photons are in the X-mode, the intensity shown in the left panel is very similar to the total thermal emission shown in Fig. 8.2. The right panel shows the intensity map for the O-mode photons, which scatter many times in a hot corona right above the neutron

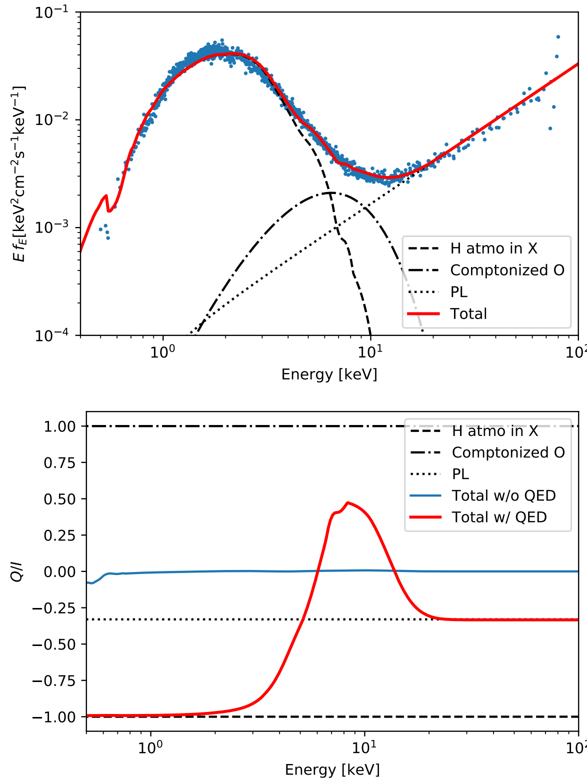

Figure 8.8: Spectral shape and polarization for the saturated Comptonization model. Upper panel: the figure shows the spectral data of 4U 0142+61 [221]; the different components are shown in black: the absorbed hydrogen atmosphere subtracted of the O-mode photons (dashed), the Comptonized O-mode photons (dots and dashes) and the high-energy powerl-law, with spectral index $\Gamma = 1.4$ (dotted). The red line shows the sum of the 3 components and it is plotted on top of the spectral data for comparison.Lower panel: linear polarization fraction; the components in black are the same as for the upper panel. The total polarization fraction is shown with and without taking into account QED.

star surface. Because of the inclination of the magnetic field with respect to the surface, the atmosphere patch at 45° produces a higher fraction of O-mode photons, and a bright ring is shown at about 45° in the right panel.

The total emission as function of energy is shown in Figure 8.8: the X-mode photons of the hydrogen atmosphere in black dashes, the Comptonized O-mode photons in black dashes and dots, and the power law in black dots. The red solid line is the sum of the three components, and it is plotted on top of the spectral data of 4U 0142+61 [221] for comparison. The comparison is aimed to show that this model produces a spectral shape that can explain the observed spectrum; however, no fitting attempt was made, and proper fitting has been left as a task for future work.

The lower panel of Fig. 8.8 shows the polarization at the observer, with and without QED. The effect of QED, as discussed in the previous section, is to conserve the polarization degree of radiation at emission, while without QED, the sum of the contributions over the entire surface brings the polarization degree to less than a few percent. The polarization at low energies is dominated by the thermal emission and the polarization is almost 100% X. At intermediate energies, the O-photons in the Wien spectrum make the polarization swing to positive values, until the power-law starts to dominate and brings the polarization degree down to the -33% assumed for the high-energy tail.

8.3.3 The resonant Compton scattering

In order to simulate the RCS model, I have developed a simple estimate of the effect of RCS on the thermal polarization coming from the neutron star surface. In the previous section, I have considered a case in which the Comptonized spectrum saturates to the Wien spectrum for most photons. In the RCS model, the Compton process is not saturated and I have to analyze partial Comptonization. A steady-state form of the Kompaneets equations (eq. 8.15) in presence of a photon source $Q(x)$ is given by [195]

$$0 = \left(\frac{kT}{m_e c^2}\right)\frac{1}{x^2}\frac{\partial}{\partial x}[x^4(n'+n)] + Q(x) - \frac{n}{\mathrm{Max}(\tau_{es},\tau_{es}^2)} \tag{8.18}$$

where the small n^2 term of eq. 8.15 has been dropped. Since the medium in consideration is finite, both incoming ($Q(x)$) and escaping photons have to be taken into account. The probability for a photon to escape is proportional to the inverse of the maximum value between τ_{es} and τ_{es}^2, where τ_{es} is the scattering optical depth, and therefore the term $n/\mathrm{Max}(\tau_{es}, \tau_{es}^2)$ is included to consider the escaping photons.

In the RCS model for the soft emission, the electrons are mildly relativistic. I therefore assume a Maxwellian distribution with $kT_e = 150$ keV, which means a typical Lorentz factor of $\gamma \sim 1.2$. In the soft region, with $\hbar\omega < 10$ keV, x is small and thus I can neglect the n term in eq. 8.18. A power-law solution to eq. 8.18 can then be found for $Q(x) = 0$:

$$n(x) \propto x^m \tag{8.19a}$$

$$m(m+3) = \frac{4}{y} \tag{8.19b}$$

$$m_{\pm} = -\frac{3}{2} \pm \sqrt{\frac{9}{4} + \frac{4}{y}} \tag{8.19c}$$

where

$$y = \frac{4kT_e}{m_e c^2} \mathrm{Max}(\tau_{es}, \tau_{es}^2) \tag{8.20}$$

is the Compton y parameter, which is given by the product of the average energy gained per scattering ($4kT_e/m_e c^2$) times the average number of scatterings, and gives an estimate of the total average energy gain per photon: $\varepsilon_f = \varepsilon_i e^y$. From these two power-law solutions, a kernel can be built to solve eq. 8.18 including the photon source function. If I define the function

$$f'(x) = \begin{cases} x^{m_+} & \text{for } x < 1 \\ x^{m_-} & \text{for } x > 1 \end{cases} \tag{8.21}$$

then the normalized function

$$f(x) = \frac{f'(x)}{\int_{-\infty}^{\infty} f'(x')\mathrm{d}x'} \tag{8.22}$$

acts as the Green's function for eq. 8.18 if the initial energy is equal to 1, with the right boundary conditions.

A solution of the steady state Kompaneets equation (eq. 8.18) that includes the source function $Q(x)$ can therefore be found through the integral

$$n(x) = \int_{-\infty}^{\infty} f\left(\frac{x}{x'}\right) Q(x')\mathrm{d}x' \,. \tag{8.23}$$

The Kompaneets equation redistribute the same number of photons to a new scattered distribution in energy, where the average energy gain per photon is regulated by the y parameter. In our case, we are redistributing the photons in energy through resonant Compton scattering, which means that the angular distribution of the scattering cross section is different (in order for a photon to be scattered, it needs to be beamed toward the electron); the redistribution formalism, however, is still valid. Since I do not know the optical depth of the electron population, I choose the right y parameter by picking the value that reproduces the soft spectrum power law and I find that the best value is $y \sim 0.15$. This sets the optical depth of the plasma. However, I can change both the temperature of the electrons and the optical depth of the plasma keeping y fixed and I will obtain the same spectral shape.

As described in § 3.2.3, the linear polarization degree of the resonantly scattered radiation depends on the average number of scatterings per photon, and it decreases by 50% for each scattering. Therefore, I need to find how many times on average a photon of a certain final energy has scattered to reach that energy. The mean relative energy gained by a photon of final energy x can be obtained as

$$\left\langle \left| \ln\left(\frac{x}{x_i}\right) \right| \right\rangle = \frac{1}{n(x)} \int_{-\infty}^{\infty} f\left(\frac{x}{x'}\right) Q(x') \left| \ln \frac{x}{x'} \right| \mathrm{d}x' \tag{8.24}$$

where $x_i = \hbar\omega_i / kT_e$ is the initial energy of the photon divided by kT_e. If ε_i is the energy of a photon before scattering, the ratio of its energy after scattering ε_f and the initial energy is on average

$$\left\langle \frac{\varepsilon_f}{\varepsilon_i} \right\rangle = 1 - \frac{\varepsilon_i}{m_e c^2} + \frac{4kT_e}{m_e c^2} \sim 1 + \frac{4kT_e}{m_e c^2} \tag{8.25}$$

The average number of scatterings of a photon with final energy x can be therefore found as the ratio between the average total energy gain per photon with final energy x divided by the average gain per scattering

$$n_{\mathrm{sc}}(x) = \frac{\left\langle \left| \ln\left(\frac{x}{x_i}\right) \right| \right\rangle}{\ln \left\langle \frac{\varepsilon_f}{\varepsilon_i} \right\rangle} = \frac{\left\langle \left| \ln\left(\frac{x}{x_i}\right) \right| \right\rangle}{\ln\left(1 + \frac{4kT_e}{m_e c^2}\right)}; \tag{8.26}$$

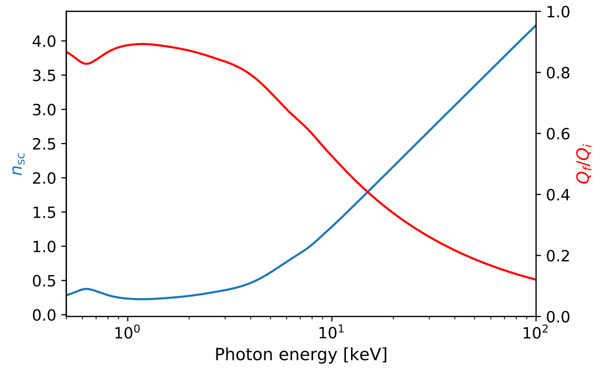

Figure 8.9: Mean number of scattering in the RCS model as function of energy (left axis, blue line) and resulting depolarization (right axis, red line).

the amount of depolarization can be found directly from the average number of scatterings.

I now take the seed photons $Q(x)$ to be thermal photons coming from the surface, with $kT_{\mathrm{eff}p} = 0.26$ keV and $B_p = 1.3 \times 10^{14}$ G. The complete treatment for this model would imply assuming a geometry for the magnetospheric plasma and determining the angular dependence of the scattering between the radiation coming from the surface and the plasma at 100 km from the neutron star. This is beyond the scope of this work and it is left for future work. For illustration, I take the emission from a surface patch at colatitude 49°, and I calculate the effect of the partial Comptonization on the final polarization.

Fig. 8.9 shows the average number of scatterings n_{sc} as function of the final photon energy ($\hbar\omega = xkT_e$) in the frame of the star (left y-axis, in blue), and the depolarization effect as Q_f/Q_i (right y-axis, in red). At low energies, the average number of scattering per photon is low, as expected, and the polarization fraction is lowered only by a few percent. In order for a thermal photon (~ 1 keV) to reach a high final energy greater than 7 keV or more, it has to undergo more scatterings on average, and therefore its final polarization decreases with energy.

The upper panel of Fig. 8.10 shows the spectral shape of the Comptonized atmosphere obtained with eq. 8.23, in the frame of the observer (after gravitational redshift, black dashes and dots). The red line shows the sum of the contributions

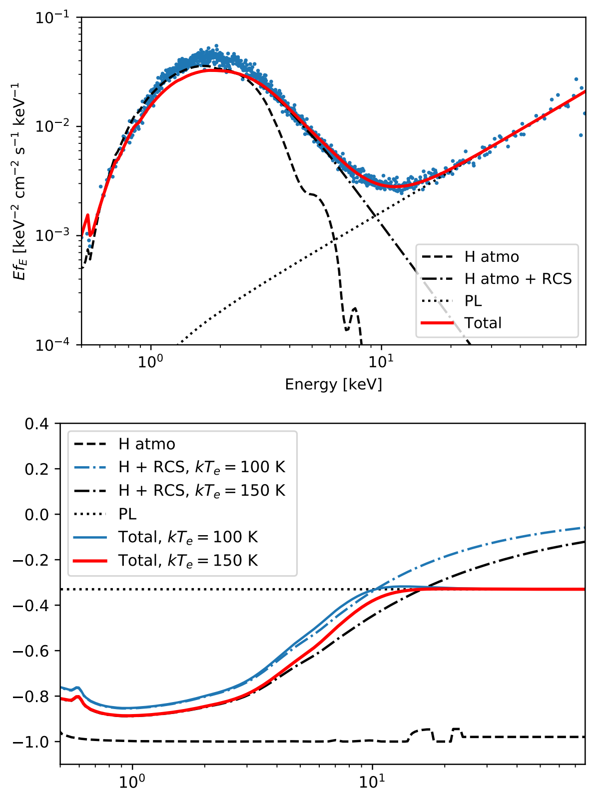

Figure 8.10: Spectral shape and polarization for the RCS model. Upper panel: the figure shows the spectral data of 4U 0142+61 [221]; the different components are shown in black: the absorbed hydrogen atmosphere (dashed), the Comptonized atmosphere (dots and dashes) and the high-energy power-law, with spectral index $\Gamma = 1.3$ (dotted). The red line shows the sum of the 3 components and it is plotted on top of the spectral data for comparison. Lower panel: linear polarization fraction; the components in black and red are the same as for the upper panel. In blue: Comptonized atmosphere (dashes and dots) and total (solid line) for an electron temperature $kT_e = 100$ K

for the Comptonized atmosphere and the power law at high energy. The spectral data of 4U 0142+61 is plotted in blue for comparison. Again, no spectral fitting was attempted, and the comparison is only to show that this model can reproduce the observed spectral shape as well. The polarization signal is shown in the lower panel of Fig. 8.10 for the hydrogen atmosphere (black dashes), the Comptonized atmosphere (black dashes and dots), for the power law (black dots) and for the total (red solid line). The Comptonized atmosphere is dominant at low energy and it is less polarized than the thermal emission because of the scatterings. As the energy increases the Comptonized atmosphere becomes less and less polarized because of the increase in the number of scatterings, but at about 10 keV the power law becomes dominant and brings Q/I to $-1/3$.

The polarization degree is also shown in blue for a different electron temperature, $kT_e = 100$ K. Since the Compton y parameter is kept the same, $y = 0.15$, the spectral shape for this choice of electron temperature is identical, but the optical depth for scattering is higher. This results in an higher number of scatterings at all energies, and can be seen in Fig. 8.10 as a bigger depolarization.

Chapter 9

Conclusions and Future Perspectives

Neutron stars and black holes emit a good fraction of their energy in the X-rays; for accreting or highly-magnetized objects such fraction is dominant, and the development of X-ray astronomy in the second half of last century has brought many discoveries and a deeper understanding of compact objects. The detection of X-ray polarization from compact objects will provide two additional observables, the polarization degree and angle, which carry information on the geometry of the sources and on the strong magnetic and gravitational fields.

9.1 The developement of X-ray polarimetry

X-ray polarimetry is an "old" field of astronomy, as the first evidence of polarization in the X-rays from a celestial source was obtained by the rocket experiment on-board of *Aerobee* 350, in 1971, which detected the polarized emission from the Crab nebula [167, 239]. However, performing polarimetry in the X-rays with enough sensitivity is a hard task, and until recently, the Crab was the only celestial source for which a positive measurement was taken, by the polarimeter on board of the *OSO*-8 satellite in 1978 [240].

The classical X-ray polarimeters were mainly based on two physical processes: Bragg diffraction and Thomson scattering. For the latter, a Thomson polarimeter exploits the fact that the majority of photons that are scattered at about 90° degree from the initial direction of propagation end up preferentially in a direction perpendicular to the electric field of the incident photon, and therefore a Thomson polatimeter measures the angular distribution of photons scattered at 90° from the incoming beam. Bragg diffraction, on the other hand, occurs when radiation with a similar wavelength to the atomic spacing of a crystal gets reflected by the different lattice points in the crystal with a positive interference. In X-ray polarimetry, the crystal is oriented at 45° with respect to the incoming beam, and only light with a polarisation vector normal to the incidence plane, that is the plane containing the incoming direction and the normal to the crystal plane, gets reflected; the radiation with the opposite polarisation is, instead, absorbed or passes through the crystal.

Achieving good sensitivity and addressing all the systematics and calibration problems with the classical techniques is difficult; moreover, these past 50 years have shown that X-ray polarimetry cannot be done as a by-product of a different core science mission, because the instrument has to be optimized for polarimetry to reach a reasonable sensitivity. For this reason, it has been hard for the community to have a polarimetry mission accepted by a space agency. Recent developments of new techniques have given a new push to the field, in particular the development of Gas Pixel Detectors, based on the photoelectric effect, in the early 2000s [47, 209, 210]. The photoelectric effect consists of a material emitting electrons, called photoelectrons, when shone on by light. In the case of X-rays, the photons are energetic enough to strip the most bound electron, or K-shell electron, from the nucleus. The direction of emission of a K-shell photoelectron for 100% linearly polarized incident radiation, is modulated around the polarization direction with a $\cos^2$ function of the azimuth angle. For this reason, the photoelectric effect is an ideal tracer of polarization. However, the path length of the photoelectron is short, of the order of a few hundreds of microns even for a light gas, and the reconstruction of its direction of emission is very hard. In the Gas Pixel Detectors, this problem is solved by using a finely pixelized collecting anode, which allows a detailed imaging of the photoelectron track in a gas chamber, and of a Gas Electron Multiplier (GEM) to amplify the electron current.

Several observatories with an X-ray polarimeter on board are now at different stages of development: in the 1–10 keV range, the NASA SMEX mission *IXPE*

[241] and the Chinese–European *eXTP* [253]; in the hard-X-ray range, 15–150 keV, the balloon-borne *X-Calibur* [22] and *PoGO+* [43]; and, in the sub-keV range, the narrow band (250 eV) *LAMP* [208] and the broad band (0.2–0.8 keV) rocket-based *REDSox* [64]. A broadband polarimeter has also been proposed as a second generation after *IXPE* in the 0.2–60 keV band: *XPP* [104]. Of these observatories, *IXPE* and *eXTP* are currently at the most advanced stage of development, and they both employ Gas Pixel Detectors to perform imaging polarimetry in the 1–10 keV range. *IXPE* will be the first mission entirely devoted to X-ray polarimetry, and is planned for launch in April 2021. The scientific payload of *eXTP* consists of four instruments: the Spectroscopic Focusing Array (SFA), the Large Area Detector (LAD), the Polarimetric Focusing Array (PFA) and the Wide Field Monitor (WFM), of which the PFA is composed of 4 identical telescopes for sensitive X-ray imaging and polarimetry. The extended phase A was completed for *eXTP* at the end of 2018 and the planned launch date is around 2025.

9.2 Neutron stars and black holes polarization studies with the *IXPE* and *eXTP*

X-ray spectral and timing analysis in the past few decades has broadened our understanding of neutron stars and black holes, but several open questions remain which can be answered by observing their polarization in the X-rays. Specifically, in this work I have shown that the polarization signal is sensitive to the physics and geometry of accretion onto black holes and X-ray pulsars, and on the shape and strength of the magnetic field threading black-hole accretion disks and magnetar magnetospheres. In the following sections, I will focus on the 1–10 keV energy range of the upcoming polarimeters *IXPE* and *eXTP*, and I will show some simulations performed using the code XIMPOL[1] [10] for these two instruments.

9.2.1 Black holes

A core science case of both *IXPE* and *eXTP* is to study the polarized radiation from accreting black holes. The effect of vacuum birefringence, that is dramatic for highly magnetized objects like magnetars, is more subtle for accreting black holes,

[1] https://github.com/lucabaldini/ximpol

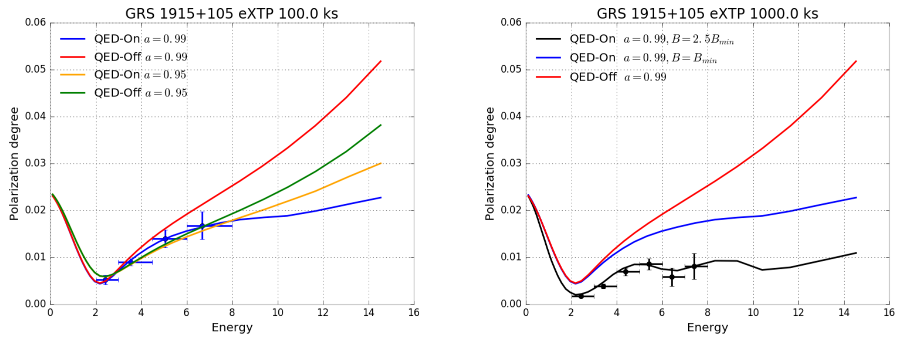

Figure 9.1: Simulated polarization degree for the black-hole binary GRS 1915+105. **Left panel**: Model with $a_\star = 0.99$ with QED (blue line) and without QED (red line); model with $a_\star = 0.95$ with QED (yellow line) and without QED (green line). Blue dots are a simulated 100 ks observation with *eXTP* (approximately 300 ks with *IXPE*) for the blue line model. **Right panel**: Model with $a_\star = 0.99$ with QED and the minimum magnetic field (blue line) and without QED (red line); model with $a_\star = 0.99$ with QED and 2.5 times the minimum magnetic field (black line). Black dots are a simulated 1 Ms observation with *eXTP* for the black line model.

where magnetic fields are expected to be several orders of magnitudes below the critical QED field $B_{\rm QED} = 4.4 \times 10^{13}$ G. In Chapter 6, however, I have shown that QED affects the propagation of polarized light in the black hole magnetosphere, so that the observed polarization becomes sensitive to the strength and shape of the magnetic field threading the accretion disk.

Fig 9.1 shows a simulated 100 ks observation with *eXTP* of the black-hole binary GRS 1915+105, which would correspond to an observation of approximately 300 ks with *IXPE*. The simulated data (blue and black dots) is plotted on top of the models shown in Fig. 6.4 of Chapter 6. As I already stressed in § 6.4.4, these figures show preliminary calculations, and further work is required to model the expected polarization degree, including the contribution of photons coming from more distant regions than the ISCO and a more realistic structure for the magnetic field. However, Fig 9.1 shows the importance of including QED in modeling the expected polarization: the left panel shows the polarization degree for a black hole rotating at 99% the critical velocity (blue solid line and blue dots); if QED was not included in the calculation, the signal would be mistaken for a black hole rotating at $a_\star = 0.95$.

Another important effect of QED is to make the polarization signal sensitive to the strength of the magnetic field. The magnetic field in the accretion disk is not strong enough to modify the scattering cross sections, and polarization of light at emission derives from regular Thomson scattering, following the Chandrasekhar result shown in § 3.1, and doesn't carry information on the local magnetic field. The depolarization effect of vacuum birefringence, on the other hand, depends strongly on the strength of the magnetic field and the right panel of Fig 9.1 shows the how the polarization signal changes with the strength of the magnetic field. The difference between the two models would be easily detected in a 1000 ks observation with *eXTP*.

These results present both a challenge and a promise for the upcoming polarimeters. Including the effect of QED in the modeling of the polarization signal is hard, because it is important to keep track of the polarization direction and how it changes due to the local magnetic field while calculating light tracing in the Kerr metric. An additional complication rises when one considers photons coming out of the plane of the disk: the structure of the magnetic field is here expected to be ordered on a large scale, and therefore a magnetic field structure needs to be assumed and included in the calculation. Nonetheless, if properly modeled including QED, the polarization signal from accreting black holes can provide a measure of the black hole spin, independent of other techniques as spectral fitting or reverberation, and of the magnetic field close to the ISCO.

9.2.2 X-ray pulsars

The geometry of accretion and the physics abehind the X-ray spectra in accreting X-ray pulsars is still debated. The upcoming polarimeters will provide new observables that can help constrain the different models. In Chapter 7, I have calculated the polarization signal, including general relativity and QED, for the existing models by Mészáros and Nagel [150] and by Kii [111], and I presented a new model for polarization based on the accretion model by Becker and Wolff [20].

Fig. 9.2 shows the predicted polarization signal in the two models in the band

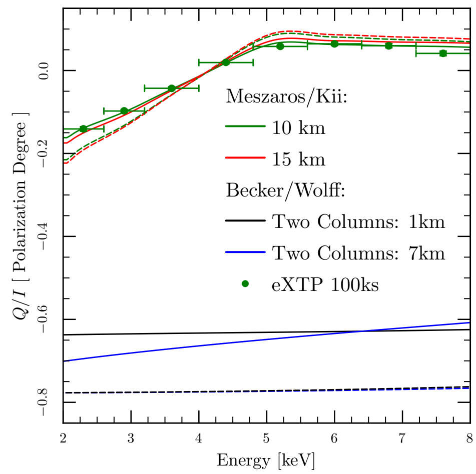

Figure 9.2: Simulated polarization degree for Her X-1. Positive Q/I here indicates X-mode polarization. Solid lines: models calculated including QED; dashed lines: without QED. The green and orange lines are for Mészaros and Nagel and Kii models with a stellar radius of 10 km (green) and 15 km (orange). Green dots are a simulated 100 ks observation with *eXTP* (approximately 300 ks with *IXPE*) for the green line model. Blue and black models are for a two-accretion-column model, with $z_{\rm max} = 6.6$ km (blue) and $z_{\rm max} = 1.4$ km (black).

of the upcoming polarimeters, together with a simulation for a 100 ks (300 ks) observation with *eXTP* (*IXPE*). The predicted polarization signal is very different in the two models, as a short observation would easily detect: the old slab model predicts a small polarization degree, which goes through a zero in the band, while the new column model is very polarized in the O-mode. Also, the effect of QED would be easily detected in both models.

9.2.3 Magnetars

Magnetars are amongst the prime targets for the upcoming polarimeters because they are bright in the X-rays and because they can provide the first test of the QED effect of vacuum birefringence. Indeed, in Chapter 8 I have shown that the difference in polarization signal is huge between the models calculated with QED and the models without QED. Apart from testing QED, the polarization signal

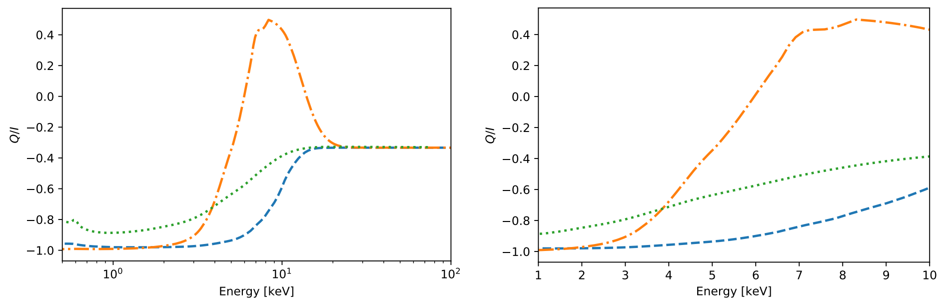

Figure 9.3: The polarization fraction for the three models. The left panel shows the full energy range, and the right panel depicts the energy range of *IXPE* and *eXTP*. The blue dashed curve depicts the hotspot model, the orange dot-dashed curve depicts the full Comptonization of the ordinary polarization model and the green dotted curve depicts the resonant Comptonization model for the emission at about 5 keV against non-relativistic electrons. In all cases, the highest energy emission is generated through resonant Comptonization against relativistic electrons. The typical measurement uncertainty in Q/I for a 100 ks *eXTP* observation for 4U 0142+61 is five percent with twenty energy bins between 2 and 8 keV.

can provide insights on the nature of the non-thermal processes happening in the magnetosphere of the stars. In Chapter 8, I have calculated the polarization of the thermal emission from persistent magnetars employing a realistic model for the hydrogen atmosphere, previously developed by Lloyd [95, 96, 131]. For the non-thermal emission, I have analyzed different proposed emission models (the hot-spot and the RCS models) together with a new model (the saturated Comptonization model), and calculated the polarization signal for each one of them.

Fig. 9.3 shows the polarization fraction for the three models: at low energy the polarization fraction is high in the X-mode (negative Q/I) and at high energies it is dictated by the polarization fraction of the high-energy power law (that here is assumed to be 1/3 in X). The energy range of the upcoming polarimeters, between 1 and 10 keV, is where the models are mostly different (right panel). Magnetars are very bright in this range, and both *IXPE* and *eXTP* will be able to resolve the difference between the models with short exposure times. The typical uncertainty in Q/I is five percent with twenty energy bins.

9.3 Future work

Some of the calculations shown in this work are still preliminary, and further analysis is needed to make robust predictions for what the upcoming polarimeters are going to detect.

For the black hole case, my analysis is restricted to edge-on photons, traveling close to the disk plane, where the magnetic field is expected to be partially organized on small scales. Further studies are needed to calculate the effect of QED for photons coming out of the disk plane, where the magnetic field is expected to be organized on large scales. In this case, the effect of QED could be the opposite of what happens for edge-on photons: the organized magnetic field could align the polarization of photons traveling through the magnetosphere, resulting in a larger net observed polarization. This analysis will be crucial to predict the polarization signal for system that are observed at high inclination angles. Additionally, the calculations shown in Fig. 9.1 only consider photons coming from a region close to the ISCO, which is a good approximation only for high energy photons, whose contribution is mainly due to the region very close to the ISCO. The next step would be to add the contribution from photons coming from more distant regions.

The spectral formation model by Becker and Wolff [20] is very promising because it is based on a robust theoretical model and it fits well the observed spectra of accreting X-ray pulsars. The polarization signal prediction that I obtained in the context of the B&W model is also robust, and it is worth further analysis. In particular, it will be important to create a full suite of models with predictions on the polarization degree and angle as a function of energy and phase for different possible viewing angles and rotation geometries.

Similarly, a full suite of predictions for the different emission models will be needed for the polarization degree and angle of magnetars. Also, the predicted spectral shapes should be fitted to the observed spectra. In order to make realistic predictions on the polarization signal in the context of the RCS model, a correct geometry for the magnetospheric plasma has to be taken into account. Regarding the high-energy power law, several models have been proposed for its origin of but in Chapter 8 I have not calculated the spectral emission and polarization for the different models. Since the power-law component becomes important at energies below 10 keV, it will be necessary to calculate the expected polarization in the context of the different models.

Bibliography

[1] *Astrophysics and gravitation. Proceedings of the sixteenth Solvay Conference on Physics at the University of Brussels, September 1973.*, Jan 1974. → page 5

[2] *Neutron Stars 1 : Equation of State and Structure*, volume 326, Jan 2007. → page 3

[3] B. P. Abbott, et al., and the LIGO Scientific Collaboration, and the Virgo Collaboration. Observation of Gravitational Waves from a Binary Black Hole Merger. *Physical Review Letters*, 116(6):061102, Feb 2016. doi:10.1103/PhysRevLett.116.061102. → page 12

[4] S. L. Adler. Photon splitting and photon dispersion in a strong magnetic field. *Ann. Phys.*, 67:599, 1971. → page 70

[5] P. R. Amnuél' and O. K. Guseinov. Accretion of matter by a neutron star in a binary system. I. *Astrophysics*, 6(3):214–217, Jul 1970. doi:10.1007/BF01002657. → page 112

[6] J. Antoniadis, P. C. C. Freire, N. Wex, T. M. Tauris, R. S. Lynch, M. H. van Kerkwijk, M. Kramer, C. Bassa, V. S. Dhillon, T. Driebe, J. W. T. Hessels, V. M. Kaspi, V. I. Kondratiev, N. Langer, T. R. Marsh, M. A. McLaughlin, T. T. Pennucci, S. M. Ransom, I. H. Stairs, J. van Leeuwen, J. P. W. Verbiest, and D. G. Whelan. A Massive Pulsar in a Compact Relativistic Binary. *Science*, 340(6131):448, Apr 2013. doi:10.1126/science.1233232. → page 4

[7] W. Baade and F. Zwicky. On Super-novae. *Proceedings of the National Academy of Science*, 20(5):254–259, May 1934. doi:10.1073/pnas.20.5.254. → page 5

[8] S. A. Balbus and J. F. Hawley. A powerful local shear instability in weakly magnetized disks. I - Linear analysis. II - Nonlinear evolution. *The Astrophysical Journal*, 376:214–233, July 1991. doi:10.1086/170270. → pages 18, 92, 94

[9] S. A. Balbus and J. F. Hawley. Instability, turbulence, and enhanced transport in accretion disks. *Reviews of Modern Physics*, 70(1):1–53, Jan 1998. doi:10.1103/RevModPhys.70.1. → page 18

[10] L. Baldini, F. Muleri, P. Soffitta, N. Omodei, M. Pesce-Rollins, C. Sgro, L. Latronico, F. Spada, A. Manfreda, and N. Di Lalla. Ximpol: a new X-ray polarimetry observation-simulation and analysis framework. In *41st COSPAR Scientific Assembly*, volume 41 of *COSPAR Meeting*, July 2016. → page 173

[11] C. Bambi. Astrophysical Black Holes: A Compact Pedagogical Review. *Annalen der Physik*, 530(6):1700430, Jun 2018. doi:10.1002/andp.201700430. → page 12

[12] M. G. Baring and A. K. Harding. Resonant Compton upscattering in anomalous X-ray pulsars. *Astrophysics and Space Science*, 308:109–118, Apr. 2007. doi:10.1007/s10509-007-9326-x. → page 53

[13] M. G. Baring, P. L. Gonthier, and A. K. Harding. Spin-dependent Cyclotron Decay Rates in Strong Magnetic Fields. *The Astrophysical Journal*, 630(1):430–440, Sep 2005. doi:10.1086/431895. → page 11

[14] M. G. Baring, Z. Wadiasingh, P. L. Gonthier, and A. K. Harding. Hard X-ray quiescent emission in magnetars via resonant Compton upscattering. In *Journal of Physics Conference Series*, volume 932 of *Journal of Physics Conference Series*, page 012021, Dec. 2017. doi:10.1088/1742-6596/932/1/012021. → page 53

[15] M. M. Basko and R. A. Sunyaev. Radiative transfer in a strong magnetic field and accreting X-ray pulsars. *Astronomy & Astrophysics*, 42(3):311–321, Sep 1975. → pages 8, 112

[16] M. M. Basko and R. A. Sunyaev. The limiting luminosity of accreting neutron stars with magnetic fields. *Monthly Notices of the Royal Astronomical Society*, 175:395–417, May 1976. doi:10.1093/mnras/175.2.395. → pages 8, 112

[17] P. A. Becker. Dynamical Structure of Radiation-dominated Pulsar Accretion Shocks. *The Astrophysical Journal*, 498(2):790–801, May 1998. doi:10.1086/305568. → pages 120, 122

[18] P. A. Becker and M. T. Wolff. Spectral Formation in X-Ray Pulsar Accretion Columns. *The Astrophysical Journal Letters*, 621(1):L45–L48, Mar 2005. doi:10.1086/428927. → pages 9, 119

[19] P. A. Becker and M. T. Wolff. Spectral Formation in X-Ray Pulsars: Bulk Comptonization in the Accretion Shock. *The Astrophysical Journal*, 630(1): 465–488, Sep 2005. doi:10.1086/431720. → page 119

[20] P. A. Becker and M. T. Wolff. Thermal and Bulk Comptonization in Accretion-powered X-Ray Pulsars. *The Astrophysical Journal*, 654(1):435–457, Jan 2007. doi:10.1086/509108. → pages 8, 9, 56, 112, 114, 118, 123, 140, 175, 178

[21] P. A. Becker, D. Klochkov, G. Schönherr, O. Nishimura, C. Ferrigno, I. Caballero, P. Kretschmar, M. T. Wolff, J. Wilms, and R. Staubert. Spectral formation in accreting X-ray pulsars: bimodal variation of the cyclotron energy with luminosity. *Astronomy & Astrophysics*, 544:A123, Aug 2012. doi:10.1051/0004-6361/201219065. → page 8

[22] M. Beilicke, F. Kislat, A. Zajczyk, Q. Guo, R. Endsley, M. Stork, R. Cowsik, P. Dowkontt, S. Barthelmy, T. Hams, T. Okajima, M. Sasaki, B. Zeiger, G. de Geronimo, M. G. Baring, and H. Krawczynski. Design and Performance of the X-ray Polarimeter X-Calibur. *Journal of Astronomical Instru-*

mentation, 3:1440008, 2014. doi:10.1142/S225117171440008X. → pages 2, 173

[23] A. M. Beloborodov. Gravitational Bending of Light Near Compact Objects. *The Astrophysical Journal Letters*, 566(2):L85–L88, Feb 2002. doi:10.1086/339511. → page 133

[24] A. M. Beloborodov. Untwisting Magnetospheres of Neutron Stars. *The Astrophysical Journal*, 703(1):1044–1060, Sep 2009. doi:10.1088/0004-637X/703/1/1044. → pages 149, 151

[25] A. M. Beloborodov. Activated Magnetospheres of Magnetars. *Astrophysics and Space Science Proceedings*, 21:299, Jan 2011. doi:10.1007/978-3-642-17251-9_24. → page 149

[26] A. M. Beloborodov. On the Mechanism of Hard X-Ray Emission from Magnetars. *The Astrophysical Journal*, 762:13, Jan. 2013. doi:10.1088/0004-637X/762/1/13. → pages 53, 155

[27] A. M. Beloborodov. Electron-Positron Flows around Magnetars. *The Astrophysical Journal*, 777:114, Nov. 2013. doi:10.1088/0004-637X/777/2/114. → pages 153, 155

[28] A. M. Beloborodov and C. Thompson. Corona of Magnetars. *The Astrophysical Journal*, 657:967–993, Mar. 2007. doi:10.1086/508917. → pages 53, 149, 151

[29] V. B. Berestetskii, E. M. Lifshitz, and L. P. Pitaevskii. *Quantum Electrodynamics*. Pergamon, Oxford, second edition, 1982. → pages 59, 70

[30] R. D. Blandford and D. G. Payne. Hydromagnetic flows from accretion disks and the production of radio jets. *Monthly Notices of the Royal Astronomical Society*, 199:883–903, Jun 1982. doi:10.1093/mnras/199.4.883. → page 18

[31] R. D. Blandford and R. L. Znajek. Electromagnetic extraction of energy from Kerr black holes. *Monthly Notices of the Royal Astronomical Society*, 179:433–456, May 1977. doi:10.1093/mnras/179.3.433. → page 92

[32] C. T. Bolton. Identification of Cygnus X-1 with HDE 226868. *Nature*, 235 (5336):271–273, Feb 1972. doi:10.1038/235271b0. → page 12

[33] W. Brinkmann. Thermal radiation from highly magnetized neutron stars. *Astronomy & Astrophysics*, 82:352–361, Feb. 1980. → page 49

[34] D. J. Burnard, J. Arons, and R. I. Klein. Accretion powered pulsars - Continuum spectra and light curves of settling accretion mounds. *The Astrophysical Journal*, 367:575–592, Feb. 1991. doi:10.1086/169653. → pages 8, 112

[35] V. Burwitz, F. Haberl, R. Neuhäuser, P. Predehl, J. Trümper, and V. E. Zavlin. The thermal radiation of the isolated neutron star RX J1856.5-3754 observed with Chandra and XMM-Newton. *Astronomy & Astrophysics*, 399: 1109–1114, Mar. 2003. doi:10.1051/0004-6361:20021747. → pages 49, 53

[36] A. Cadez and M. Javornik. Free-Free Opacity in Strong Magnetic Fields. *Astrophysics and Space Science*, 77:299–318, Jul 1981. doi:10.1007/BF00649461. → page 46

[37] I. Caiazzo and J. Heyl. Probing Black Hole Magnetic Fields with QED. *Galaxies*, 6:57, May 2018. doi:10.3390/galaxies6020057. → pages v, vi, 78

[38] I. Caiazzo and J. Heyl. Vacuum birefringence and the x-ray polarization from black-hole accretion disks. *Physical Review D*, 97(8):083001, Apr. 2018. doi:10.1103/PhysRevD.97.083001. → pages v, vi, 78

[39] I. Caiazzo, J. Heyl, A. R. Ingram, T. Belloni, E. Cackett, A. De Rosa, M. Feroci, D. S. Swetz, A. Damascelli, P. Dosanjh, S. Gallagher, L. Gallo, D. Haggard, C. Heinke, K. Hoffman, D. Kirmizibayrak, S. Morsink, W. Rau, P. Ripoche, S. Safi-Harb, G. R. Sivakoff, I. Stairs, L. Stella, and J. N. Ullom. Testing general relativity with accretion onto compact objects. In *Bulletin of the American Astronomical Society*, volume 51 of *Bullettin of the AAS*, page 516, May 2019. → page v

[40] I. Caiazzo, J. Heyl, and R. Turolla. *Polarimetry of Magnetars and Isolated*

Neutron Stars, chapter 12, pages 301–336. Springer, Berlin, 2019. → page v

[41] V. Canuto, J. Lodenquai, and M. Ruderman. Thomson scattering in a strong magnetic field. *Physical Review D*, 3:2303–2308, May 1971. doi:10.1103/PhysRevD.3.2303. URL https://link.aps.org/doi/10.1103/PhysRevD.3.2303. → pages 44, 45

[42] S. Chandrasekhar. *Radiative transfer*. 1960. → pages 21, 23, 39, 40, 41

[43] M. Chauvin, H.-G. Florén, M. Friis, M. Jackson, T. Kamae, J. Kataoka, T. Kawano, M. Kiss, V. Mikhalev, T. Mizuno, H. Tajima, H. Takahashi, N. Uchida, and M. Pearce. The PoGO+ view on Crab off-pulse hard X-ray polarisation. *Monthly Notices of the Royal Astronomical Society*, Feb. 2018. doi:10.1093/mnrasl/sly027. → pages 2, 173

[44] C. K. Chou. Stokes Parameters for Thomson Scattering in a Strong Magnetic Field. *Astrophysics and Space Science*, 121(2):333–344, Apr 1986. doi:10.1007/BF00653705. → pages 28, 30

[45] T. L. Cline, U. D. Desai, B. J. Teegarden, W. D. Evans, R. W. Klebesadel, J. G. Laros, C. Barat, K. Hurley, M. Niel, G. Bedrenne, I. V. Estulin, V. G. Kurt, G. A. Mersov, V. M. Zenchenko, M. C. Weisskopf, and J. Grindlay. Precise source location of the anomalous 1979 March 5 gamma-ray transient. *The Astrophysical Journal*, 255:L45–L48, Apr 1982. doi:10.1086/183766. → page 9

[46] W. Coburn, W. A. Heindl, R. E. Rothschild, D. E. Gruber, I. Kreykenbohm, J. Wilms, P. Kretschmar, and R. Staubert. Magnetic Fields of Accreting X-Ray Pulsars with the Rossi X-Ray Timing Explorer. *The Astrophysical Journal*, 580(1):394–412, Nov 2002. doi:10.1086/343033. → page 7

[47] E. Costa, P. Soffitta, R. Bellazzini, A. Brez, N. Lumb, and G. Spandre. An efficient photoelectric X-ray polarimeter for the study of black holes and neutron stars. *Nature*, 411(6838):662–665, Jun 2001. → page 172

[48] H. T. Cromartie, E. Fonseca, S. M. Ransom, P. B. Demorest, Z. Arzoumanian, H. Blumer, P. R. Brook, M. E. DeCesar, T. Dolch, J. A. Ellis, R. D. Ferdman, E. C. Ferrara, N. Garver-Daniels, P. A. Gentile, M. L. Jones, M. T. Lam, D. R. Lorimer, R. S. Lynch, M. A. McLaughlin, C. Ng, D. J. Nice, T. T. Pennucci, R. Spiewak, I. H. Stairs, K. Stovall, J. K. Swiggum, and W. W. Zhu. Relativistic Shapiro delay measurements of an extremely massive millisecond pulsar. *Nature Astronomy*, page 439, Sep 2019. doi:10.1038/s41550-019-0880-2. → page 4

[49] T. Daishido. Anisotropic Thomson scattering for pulse formation in X-ray pulsars. *Astronomical Society of Japan, Publications*, 27:181–189, Jan 1975. → page 112

[50] J. K. Daugherty and J. Ventura. Absorption of radiation by electrons in intense magnetic fields. *Physical Review D*, 18:1053–1067, Aug 1978. doi:10.1103/PhysRevD.18.1053. → page 46

[51] K. Davidson and J. P. Ostriker. Neutron-Star Accretion in a Stellar Wind: Model for a Pulsed X-Ray Source. *The Astrophysical Journal*, 179:585–598, Jan 1973. doi:10.1086/151897. → pages 112, 113

[52] S. W. Davis, O. M. Blaes, S. Hirose, and J. H. Krolik. The Effects of Magnetic Fields and Inhomogeneities on Accretion Disk Spectra and Polarization. *The Astrophysical Journal*, 703:569–584, Sept. 2009. doi:10.1088/0004-637X/703/1/569. → pages 93, 100

[53] P. B. Demorest, T. Pennucci, S. M. Ransom, M. S. E. Roberts, and J. W. T. Hessels. A two-solar-mass neutron star measured using Shapiro delay. *Nature*, 467(7319):1081–1083, Oct 2010. doi:10.1038/nature09466. → page 4

[54] W. Dittrich and H. Gies. *Probing the Quantum Vacuum*. Springer-Verlag, Berlin, 2000. → page 59

[55] W. Dittrich and M. Reuter. *Effective Lagrangians in quantum electrodynamics*. Springer-Verlag, Berlin, 1985. → page 59

[56] R. C. Duncan and C. Thompson. Formation of Very Strongly Magnetized Neutron Stars: Implications for Gamma-Ray Bursts. *The Astrophysical Journal*, 392:L9, Jun 1992. doi:10.1086/186413. → page 9

[57] A. Einstein. Die Grundlage der allgemeinen Relativitätstheorie. *Annalen der Physik*, 354(7):769–822, Jan 1916. doi:10.1002/andp.19163540702. → page 12

[58] G. G. Fahlman and P. C. Gregory. An X-ray pulsar in SNR G109.1-1.0. *Nature*, 293(5829):202–204, Sep 1981. doi:10.1038/293202a0. → page 10

[59] R. Farinelli, C. Ferrigno, E. Bozzo, and P. A. Becker. A new model for the X-ray continuum of the magnetized accreting pulsars. *Astronomy & Astrophysics*, 591:A29, Jun 2016. doi:10.1051/0004-6361/201527257. → page 113

[60] R. P. Fender, S. T. Garrington, D. J. McKay, T. W. B. Muxlow, G. G. Pooley, R. E. Spencer, A. M. Stirling, and E. B. Waltman. MERLIN observations of relativistic ejections from GRS 1915+105. *Monthly Notices of the Royal Astronomical Society*, 304:865–876, Apr. 1999. doi:10.1046/j.1365-8711.1999.02364.x. → page 108

[61] R. Fernández and S. W. Davis. The X-ray Polarization Signature of Quiescent Magnetars: Effect of Magnetospheric Scattering and Vacuum Polarization. *The Astrophysical Journal*, 730:131, Apr. 2011. doi:10.1088/0004-637X/730/2/131. → page 157

[62] R. Fernández and C. Thompson. Resonant Cyclotron Scattering in Three Dimensions and the Quiescent Nonthermal X-ray Emission of Magnetars. *The Astrophysical Journal*, 660:615–640, May 2007. doi:10.1086/511810. → pages 53, 54, 152, 155

[63] D. Finkelstein. Past-Future Asymmetry of the Gravitational Field of a Point Particle. *Physical Review*, 110(4):965–967, May 1958. doi:10.1103/PhysRev.110.965. → page 12

[64] H. M. Gaenther, M. Egan, R. K. Heilmann, S. N. T. Heine, T. Hellickson, H. L. Frost, J.and Marshall, N. S. Schulz, and A. Theriault-Shay. REDSoX: Monte-Carlo ray-tracing for a soft x-ray spectroscopy polarimeter. volume 10399, pages 10399 – 10399 – 13, Aug. 2017. doi:10.1117/12.2273772. URL http://dx.doi.org/10.1117/12.2273772. → pages 2, 78, 173

[65] J. García, T. Dauser, C. S. Reynolds, T. R. Kallman, J. E. McClintock, J. Wilms, and W. Eikmann. X-Ray Reflected Spectra from Accretion Disk Models. III. A Complete Grid of Ionized Reflection Calculations. *The Astrophysical Journal*, 768:146, May 2013. doi:10.1088/0004-637X/768/2/146. → page 17

[66] F. P. Gavriil, V. M. Kaspi, and P. M. Woods. Magnetar-like X-ray bursts from an anomalous X-ray pulsar. *Nature*, 419(6903):142–144, Sep 2002. doi:10.1038/nature01011. → page 10

[67] F. P. Gavriil, R. Dib, and V. M. Kaspi. Activity From Magnetar Candidate 4U 0142+61: Bursts and Emission Lines. In C. Bassa, Z. Wang, A. Cumming, and V. M. Kaspi, editors, *40 Years of Pulsars: Millisecond Pulsars, Magnetars and More*, volume 983 of *American Institute of Physics Conference Series*, pages 234–238, Feb 2008. doi:10.1063/1.2900150. → page 10

[68] R. Giacconi, H. Gursky, F. R. Paolini, and B. B. Rossi. Evidence for x Rays From Sources Outside the Solar System. *Physical Review Letters*, 9(11): 439–443, Dec 1962. doi:10.1103/PhysRevLett.9.439. → page 6

[69] R. Giacconi, H. Gursky, E. Kellogg, E. Schreier, and H. Tananbaum. Discovery of Periodic X-Ray Pulsations in Centaurus X-3 from UHURU. *The Astrophysical Journal*, 167:L67, Jul 1971. doi:10.1086/180762. → page 6

[70] H. Gies and K. Langfeld. Loops and Loop Clouds - A Numerical Approach to the Worldline Formalism in QED. *International Journal of Modern Physics A*, 17:966–976, 2002. doi:10.1142/S0217751X02010388. → page 67

[71] Y. N. Gnedin and R. A. Sunyaev. The Beaming of Radiation from an Accreting Magnetic Neutron Star and the X-ray Pulsars. *Astronomy & Astrophysics*, 25:233, Jan 1973. → page 112

[72] T. Gold. Rotating Neutron Stars as the Origin of the Pulsating Radio Sources. *Nature*, 218(5143):731–732, May 1968. doi:10.1038/218731a0. → page 6

[73] P. Goldreich and W. H. Julian. Pulsar Electrodynamics. *The Astrophysical Journal*, 157:869, Aug. 1969. doi:10.1086/150119. → pages 83, 86

[74] D. Goldstein. *Polarized light*. 2003. → page 34

[75] D. González Caniulef, S. Zane, R. Taverna, R. Turolla, and K. Wu. Polarized thermal emission from X-ray dim isolated neutron stars: the case of RX J1856.5-3754. *Monthly Notices of the Royal Astronomical Society*, 459: 3585–3595, July 2016. doi:10.1093/mnras/stw804. → page 49

[76] D. González-Caniulef, S. Zane, R. Turolla, and K. Wu. Atmosphere of strongly magnetized neutron stars heated by particle bombardment. *Monthly Notices of the Royal Astronomical Society*, 483:599–613, Feb. 2019. doi: 10.1093/mnras/sty3159. → pages 49, 91

[77] D. Götz, S. Mereghetti, A. Tiengo, and P. Esposito. Magnetars as persistent hard X-ray sources: INTEGRAL discovery of a hard tail in SGR 1900+14. *Astronomy & Astrophysics*, 449:L31–L34, Apr. 2006. doi: 10.1051/0004-6361:20064870. → page 53

[78] P. C. Gregory and G. G. Fahlman. An extraordinary new celestial X-ray source. *Nature*, 287(5785):805–806, Oct 1980. doi:10.1038/287805a0. → page 10

[79] J. P. Halpern and E. V. Gotthelf. The Fading of Transient Anomalous X-Ray Pulsar XTE J1810-197. *The Astrophysical Journal*, 618:874–882, Jan. 2005. doi:10.1086/426130. → page 11

[80] T. Hamada. Theory of Thomson Scattering in a Strong Magnetic Field. II. *Astronomical Society of Japan, Publications*, 27:275–286, Jan 1975. → page 45

[81] T. Hamada. Theory of Thomson Scattering in a Strong Magnetic Field - Part Four -. *Astronomical Society of Japan, Publications*, 32:117, Jan 1980.

[82] T. Hamada and S. Kanno. Theory of Thomson Scattering in a Strong Magnetic Field, I. *Astronomical Society of Japan, Publications*, 26:421, Jan 1974. → page 45

[83] J. F. Hawley, C. F. Gammie, and S. A. Balbus. Local Three-dimensional Magnetohydrodynamic Simulations of Accretion Disks. *The Astrophysical Journal*, 440:742, Feb 1995. doi:10.1086/175311. → page 18

[84] D. J. Helfand, R. H. Becker, G. Hawkins, and R. L. White. The Nature of the Compact X-Ray Source in the Supernova Remnant G27.4+0.0. *The Astrophysical Journal*, 434:627, Oct 1994. doi:10.1086/174764. → page 10

[85] H. Herold. Compton and Thomson scattering in strong magnetic fields. *Physical Review D*, 19:2868–2875, May 1979. doi:10.1103/PhysRevD.19.2868. → pages 45, 54, 126

[86] A. Hewish, S. J. Bell, J. D. H. Pilkington, P. F. Scott, and R. A. Collins. Observation of a Rapidly Pulsating Radio Source. *Nature*, 217(5130):709–713, Feb 1968. doi:10.1038/217709a0. → page 5

[87] J. Heyl and I. Caiazzo. Strongly Magnetized Sources: QED and X-ray Polarization. *Galaxies*, 6:76, July 2018. doi:10.3390/galaxies6030076. → pages v, vi

[88] J. Heyl, I. Caiazzo, S. Safi-Harb, C. Heinke, S. Morsink, E. Cackett, A. De Rosa, M. Feroci, D. S. Swetz, A. Damascelli, P. Dosanjh, S. Gallagher, L. Gallo, D. Haggard, K. Hoffman, A. R. Ingram, D. Kirmizibayrak, H. Marshall, W. Rau, P. Ripoche, G. R. Sivakoff, I. Stairs, L. Stella, and J. N. Ullom. Exploring the physics of neutron stars with high-resolution, high-throughput

X-ray spectroscopy. In *Bulletin of the American Astronomical Society*, volume 51 of *Bullettin of the AAS*, page 491, May 2019. → page v

[89] J. S. Heyl and L. Hernquist. Birefringence and dichroism of the QED vacuum. *Journal of Physics A Mathematical General*, 30(18):6485–6492, Sep 1997. doi:10.1088/0305-4470/30/18/022. → pages 70, 71

[90] J. S. Heyl and L. Hernquist. Analytic form for the effective Lagrangian of QED and its application to pair production and photon splitting. *Physical Review D*, 55(4):2449–2454, Feb 1997. doi:10.1103/PhysRevD.55.2449. → page 71

[91] J. S. Heyl and L. Hernquist. Almost analytic models of ultramagnetized neutron star envelopes. *Monthly Notices of the Royal Astronomical Society*, 300 (2):599–615, Oct 1998. doi:10.1046/j.1365-8711.1998.01885.x. → pages 76, 147

[92] J. S. Heyl and S. R. Kulkarni. How Common Are Magnetars? The Consequences of Magnetic Field Decay. *The Astrophysical Journal Letters*, 506 (1):L61–L64, Oct 1998. doi:10.1086/311628. → pages 10, 145

[93] J. S. Heyl and N. J. Shaviv. Polarization evolution in strong magnetic fields. *Monthly Notices of the Royal Astronomical Society*, 311:555–564, Jan. 2000. doi:10.1046/j.1365-8711.2000.03076.x. → page 37

[94] J. S. Heyl and N. J. Shaviv. Qed and the high polarization of the thermal radiation from neutron stars. *Physical Review D*, 66:023002 (4 pages), 2002. → page 116

[95] J. S. Heyl, N. J. Shaviv, and D. Lloyd. The high-energy polarization-limiting radius of neutron star magnetospheres: I. slowly rotating neutron stars. *Monthly Notices of the Royal Astronomical Society*, 342:134–144, 2003. → pages 145, 177

[96] J. S. Heyl, D. Lloyd, and N. J. Shaviv. The High-Energy Polarization-Limiting Radius of Neutron Star Magnetospheres II – Magnetized Hy-

drogen Atmospheres. *ArXiv Astrophysics e-prints*, Feb. 2005. → pages 145, 151, 177

[97] S. Hirose, J. H. Krolik, and O. Blaes. Radiation-Dominated Disks are Thermally Stable. *The Astrophysical Journal*, 691:16–31, Jan. 2009. doi:10.1088/0004-637X/691/1/16. → page 97

[98] W. C. G. Ho and D. Lai. Atmospheres and spectra of strongly magnetized neutron stars - II. The effect of vacuum polarization. *Monthly Notices of the Royal Astronomical Society*, 338:233–252, Jan. 2003. doi:10.1046/j.1365-8711.2003.06047.x. → pages 87, 88, 91, 116, 118

[99] W. C. G. Ho, D. Lai, A. Y. Potekhin, and G. Chabrier. Atmospheres and Spectra of Strongly Magnetized Neutron Stars. III. Partially Ionized Hydrogen Models. *The Astrophysical Journal*, 599:1293–1301, Dec. 2003. doi:10.1086/379507. → page 49

[100] A. I. Ibrahim, S. Safi-Harb, J. H. Swank, W. Parke, S. Zane, and R. Turolla. Discovery of Cyclotron Resonance Features in the Soft Gamma Repeater SGR 1806-20. *The Astrophysical Journal*, 574:L51–L55, Jul 2002. doi:10.1086/342366. → page 10

[101] G. L. Israel, S. Mereghetti, and L. Stella. The Discovery of 8.7 Second Pulsations from the Ultrasoft X-Ray Source 4U 0142+61. *The Astrophysical Journal*, 433:L25, Sep 1994. doi:10.1086/187539. → page 10

[102] C. Itzykson and J.-B. Zuber. *Quantum Field Theory*. McGraw-Hill, New York, 1980. → pages 59, 66

[103] J. D. Jackson and R. F. Fox. Classical Electrodynamics, 3rd ed. *American Journal of Physics*, 67(9):841–842, Sep 1999. doi:10.1119/1.19136. → page 28

[104] K. Jahoda, H. Krawczynski, F. Kislat, H. Marshall, T. Okajima, I. Agudo, L. Angelini, M. Bachetti, L. Baldini, M. Baring, W. Baumgartner, R. Bellazzini, S. Bianchi, N. Bucciantini, I. Caiazzo, F. Capitanio, P. Coppi, E. Costa, A. De Rosa, E. Del Monte, J. Dexter, L. Di Gesu, N. Di Lalla,

V. Doroshenko, M. Dovciak, R. Ferrazzoli, F. Fuerst, A. Garner, P. Ghosh, D. Gonzalez-Caniulef, V. Grinberg, S. Gunji, D. Hartman, K. Hayashida, J. Heyl, J. Hill, A. Ingram, W. Buz Iwakiri, S. Jorstad, P. Kaaret, T. Kallman, V. Karas, I. Khabibullin, T. Kitaguchi, J. Kolodziejczak, C. Kouveliotou, Y. Liodakis, T. Maccarone, A. Manfreda, F. Marin, A. Marinucci, C. Markwardt, A. Marscher, G. Matt, M. McConnell, J. Miller, I. Mitsubishi, T. Mizuno, A. Mushtukov, S. Ng, M. Nowak, S. O'Dell, A. Papitto, D. Pasham, M. Pearce, L. Peirson, M. Perri, M. Pesce Rollins, V. Petrosian, P.-O. Petrucci, M. Pilia, A. Possenti, J. Poutanen, C. Prescod-Weinstein, S. Puccetti, T. Salmi, K. Shi, P. Soffita, G. Spandre, J. Steiner, T. Strohmayer, V. Suleimanov, J. Svoboda, J. Swank, T. Tamagawa, H. Takahashi, R. Taverna, J. Tomsick, A. Trois, S. Tsygankov, R. Turolla, J. Vink, J. Wilms, K. Wu, F. Xie, G. Younes, A. Zaino, A. Zajczyk, S. Zane, A. Zdziarski, H. Zhang, W. Zhang, and P. Zhou. The X-ray Polarization Probe mission concept. *arXiv e-prints*, art. arXiv:1907.10190, Jul 2019. → page 173

[105] M. D. Johnson, et al., and the Event Horizon Telescope collaboration. Resolved magnetic-field structure and variability near the event horizon of Sagittarius A*. *Science*, 350:1242–1245, Dec. 2015. doi:10.1126/science.aac7087. → pages 18, 92, 101

[106] S. Kanno and T. Hamada. Theory of Thomson scattering in a strong magnetic field. III. *Astronomical Society of Japan, Publications*, 27:545–552, Jan 1975. → page 45

[107] V. M. Kaspi and A. M. Beloborodov. Magnetars. *Annual Review of Astronomy and Astrophysics*, 55(1):261–301, Aug 2017. doi:10.1146/annurev-astro-081915-023329. → page 10

[108] V. M. Kaspi and K. Boydstun. On the X-Ray Spectra of Anomalous X-Ray Pulsars and Soft Gamma Repeaters. *The Astrophysical Journal*, 710:L115–L120, Feb. 2010. doi:10.1088/2041-8205/710/2/L115. → page 53

[109] V. M. Kaspi, F. P. Gavriil, P. M. Woods, J. B. Jensen, M. S. E. Roberts, and D. Chakrabarty. A Major Soft Gamma Repeater-like Outburst and Rotation

Glitch in the No-longer-so-anomalous X-Ray Pulsar 1E 2259+586. *The Astrophysical Journal*, 588(2):L93–L96, May 2003. doi:10.1086/375683. → page 10

[110] R. P. Kerr. Gravitational Field of a Spinning Mass as an Example of Algebraically Special Metrics. *Physical Review Letters*, 11(5):237–238, Sep 1963. doi:10.1103/PhysRevLett.11.237. → page 13

[111] T. Kii. X-ray polarizations from accreting strongly magnetized neutron stars - Case studies for the X-ray pulsars 4U 1626-67 and Hercules X-1. *Astronomical Society of Japan, Publications*, 39:781–800, 1987. → pages xiii, 55, 113, 114, 115, 116, 117, 175

[112] R. I. Klein, J. Arons, G. Jernigan, and J. J. L. Hsu. Photon Bubble Oscillations in Accretion-powered Pulsars. *The Astrophysical Journal*, 457:L85, Feb 1996. doi:10.1086/309897. → pages 8, 113

[113] D. A. Kompaneets. Oscillations in films of superfluid solutions. *Soviet Journal of Experimental and Theoretical Physics*, 40:208, Jul 1975. → pages 119, 154

[114] J. Kormendy and D. Richstone. Inward Bound—The Search For Supermassive Black Holes In Galactic Nuclei. *Annual Review of Astronomy & Astrophysics*, 33:581, Jan 1995. doi:10.1146/annurev.aa.33.090195.003053. → page 12

[115] A. Kostenko and C. Thompson. QED Phenomena in an Ultrastrong Magnetic Field. I. ElectronPhoton Scattering, Pair Creation, and Annihilation. *The Astrophysical Journal*, 869:44, Dec 2018. doi:10.3847/1538-4357/aae0ef. → page 45

[116] C. Kouveliotou, J. P. Norris, T. L. Cline, B. R. Dennis, U. D. Desai, L. E. Orwig, E. E. Fenimore, R. W. Klebesadel, J. G. Laros, J. L. Atteia, M. Boer, K. Hurley, M. Neil, G. Vedrenne, A. V. Kuznetsov, R. A. Sunyaev, and O. V. Terekhov. SMM Hard X-Ray Observations of the Soft Gamma-Ray Repeater 1806-20. *The Astrophysical Journal*, 322:L21, Nov 1987. doi:10.1086/185029. → page 9

[117] C. Kouveliotou, S. Dieters, T. Strohmayer, J. van Paradijs, G. J. Fishman, C. A. Meegan, K. Hurley, J. Kommers, I. Smith, D. Frail, and T. Murakami. An X-ray pulsar with a superstrong magnetic field in the soft γ-ray repeater SGR1806 - 20. *Nature*, 393(6682):235–237, May 1998. doi:10.1038/30410. → page 10

[118] C. Kouveliotou, T. Strohmayer, K. Hurley, J. van Paradijs, M. H. Finger, S. Dieters, P. Woods, C. Thompson, and R. C. Duncan. Discovery of a Magnetar Associated with the Soft Gamma Repeater SGR 1900+14. *The Astrophysical Journal*, 510(2):L115–L118, Jan 1999. doi:10.1086/311813. → page 10

[119] H. Kubo and R. Nagata. Vector representation of behavior of polarized light in a weakly inhomogeneous medium with birefringence and dichroism. *Journal of the Optical Society of America (1917-1983)*, 73:1719, Dec. 1983. → page 33

[120] H. Kubo and R. Nagata. Vector representation of behavior of polarized light in a weakly inhomogeneous medium with birefringence and dichroism. *J. Opt. Soc. Am.*, 73(12):1719–1724, Dec 1983. doi:10.1364/JOSA.73.001719. URL http://www.osapublishing.org/abstract.cfm?URI=josa-73-12-1719. → page 84

[121] L. Kuiper, W. Hermsen, and M. Mendez. Discovery of Hard Nonthermal Pulsed X-Ray Emission from the Anomalous X-Ray Pulsar 1E 1841-045. *The Astrophysical Journal*, 613:1173–1178, Oct. 2004. doi:10.1086/423129. → page 53

[122] D. Lai. Matter in strong magnetic fields. *Reviews of Modern Physics*, 73:629, July 2001. doi:10.1103/RevModPhys.73.629. → page 49

[123] D. Lai and W. C. G. Ho. Resonant conversion of photon modes due to vacuum polarization in a magnetized plasma: Implications for x-ray emission from magnetars. *The Astrophysical Journal*, 566(1):373, 2002. URL http://stacks.iop.org/0004-637X/566/i=1/a=373. → pages 87, 88, 91

[124] D. Lai and E. E. Salpeter. Hydrogen Phases on the Surfaces of a Strongly Magnetized Neutron Star. *The Astrophysical Journal*, 491:270–285, Dec. 1997. doi:10.1086/304937. → page 49

[125] F. K. Lamb, C. J. Pethick, and D. Pines. A Model for Compact X-Ray Sources: Accretion by Rotating Magnetic Stars. *The Astrophysical Journal*, 184:271–290, Aug. 1973. doi:10.1086/152325. → page 7

[126] L. D. Landau. To the Stars theory. *Phys. Zs. Sowjet*, 1:285, Dec 1932. → page 5

[127] M. I. Large, A. E. Vaughan, and B. Y. Mills. A Pulsar Supernova Association? *Nature*, 220(5165):340–341, Oct 1968. doi:10.1038/220340a0. → page 6

[128] J. G. Laros, E. E. Fenimore, R. W. Klebesadel, J. L. Atteia, M. Boer, K. Hurley, M. Niel, G. Vedrenne, S. R. Kane, C. Kouveliotou, T. L. Cline, B. R. Dennis, U. D. Desai, L. E. Orwig, A. V. Kuznetsov, R. A. Sunyaev, and O. V. Terekhov. A New Type of Repetitive Behavior in a High-Energy Transient. *The Astrophysical Journal*, 320:L111, Sep 1987. doi:10.1086/184985. → page 9

[129] R. Lieu. Electron bremsstrahlung cross-section in the high magnetic field of pulsars. *Monthly Notices of the Royal Astronomical Society*, 205:973–981, Dec 1983. doi:10.1093/mnras/205.4.973. → page 46

[130] D. A. Lloyd. Model atmospheres and thermal spectra of magnetized neutron stars. *ArXiv Astrophysics e-prints*, Mar. 2003. → pages 46, 47, 48, 49, 50, 90

[131] D. A. Lloyd. *Model atmospheres and spectra of cooling neutron stars*. PhD thesis, HARVARD UNIVERSITY, 2003. → pages 145, 177

[132] D. A. Lloyd, L. Hernquist, and J. S. Heyl. Temperature Discrepancies From Fits to Thermal Spectra of Neutron Stars. In P. O. Slane and B. M. Gaensler, editors, *Neutron Stars in Supernova Remnants*, volume 271 of *Astronomical Society of the Pacific Conference Series*, page 323, Jan 2002. → pages 145, 157

[133] A. G. Lyne and F. Graham-Smith. *Pulsar astronomy*. 1998. → page 6

[134] M. Lyutikov and F. P. Gavriil. Resonant cyclotron scattering and Comptonization in neutron star magnetospheres. *Monthly Notices of the Royal Astronomical Society*, 368:690–706, May 2006. doi:10.1111/j.1365-2966.2006.10140.x. → page 53

[135] F. Mandl and G. Shaw. *Quantum Field Theory*. John Wiley & Sons, Chichester, revised edition, 1993. → page 59

[136] D. Marsden and N. E. White. Correlations between Spectral Properties and Spin-down Rate in Soft Gamma-Ray Repeaters and Anomalous X-Ray Pulsars. *The Astrophysical Journal*, 551:L155–L158, Apr. 2001. doi:10.1086/320025. → page 53

[137] E. P. Mazets, S. V. Golenetskii, V. N. Ilinskii, V. N. Panov, R. L. Aptekar, I. A. Gurian, I. A. Sokolov, Z. I. Sokolova, and T. V. Kharitonova. Venera 11 and 12 observations of gamma-ray bursts - The Cone experiment. *Soviet Astronomy Letters*, 5:163–167, Jan 1979. → page 9

[138] E. P. Mazets, S. V. Golentskii, V. N. Ilinskii, R. L. Aptekar, and I. A. Guryan. Observations of a flaring X-ray pulsar in Dorado. *Nature*, 282(5739):587–589, Dec 1979. doi:10.1038/282587a0. → page 9

[139] E. P. Mazets, S. V. Golenetskii, I. A. Gurian, and V. N. Ilinskii. The 5 March 1979 event and the distinct class of short gamma bursts Are they of the same origin. *Astrophysics and Space Science*, 84:173–189, May 1982. doi:10.1007/BF00713635. → page 9

[140] D. Mazur and J. S. Heyl. Casimir interactions between magnetic flux tubes in a dense lattice. *Physical Review D*, 91(6):065019, Mar. 2015. doi:10.1103/PhysRevD.91.065019. → page 67

[141] J. E. McClintock and R. A. Remillard. *Black hole binaries*, volume 39, pages 157–213. 2006. → pages 12, 18

[142] J. E. McClintock, R. Shafee, R. Narayan, R. A. Remillard, S. W. Davis, and L.-X. Li. The Spin of the Near-Extreme Kerr Black Hole GRS 1915+105. *The Astrophysical Journal*, 652:518–539, Nov. 2006. doi:10.1086/508457. → page 108

[143] Z. Medin and D. Lai. Density-functional-theory calculations of matter in strong magnetic fields. II. Infinite chains and condensed matter. *PRA*, 74: 062508, Dec. 2006. doi:10.1103/PhysRevA.74.062508. → page 49

[144] Z. Medin and D. Lai. Condensed surfaces of magnetic neutron stars, thermal surface emission, and particle acceleration above pulsar polar caps. *Monthly Notices of the Royal Astronomical Society*, 382:1833–1852, Dec. 2007. doi:10.1111/j.1365-2966.2007.12492.x. → page 49

[145] Z. Medin, D. Lai, and A. Y. Potekhin. Radiative transitions of the helium atom in highly magnetized neutron star atmospheres. *Monthly Notices of the Royal Astronomical Society*, 383:161–172, Jan. 2008. doi:10.1111/j.1365-2966.2007.12518.x. → page 44

[146] S. Mereghetti and L. Stella. The Very Low Mass X-Ray Binary Pulsars: A New Class of Sources? *The Astrophysical Journal*, 442:L17, Mar 1995. doi:10.1086/187805. → page 10

[147] S. Mereghetti, D. Götz, I. F. Mirabel, and K. Hurley. INTEGRAL discovery of persistent hard X-ray emission from the Soft Gamma-ray Repeater SGR 1806-20. *Astronomy & Astrophysics*, 433:L9–L12, Apr. 2005. doi:10.1051/0004-6361:200500088. → page 53

[148] P. Mészáros. *High-energy radiation from magnetized neutron stars.* U. Chicago Press, 1992. → pages 44, 45, 84, 91, 128

[149] P. Mészáros and W. Nagel. X-ray pulsar models. I - Angle-dependent cyclotron line formation and comptonization. *The Astrophysical Journal*, 298: 147–160, Nov. 1985. doi:10.1086/163594. → pages 8, 55, 93, 100, 113

[150] P. Mészáros and W. Nagel. X-ray pulsar models. II. Comptonized spectra

and pulse shapes. *The Astrophysical Journal*, 299:138–153, Dec 1985. doi:10.1086/163687. → pages xiii, 8, 113, 114, 115, 116, 117, 175

[151] P. Meszaros, R. Novick, A. Szentgyorgyi, G. A. Chanan, and M. C. Weisskopf. Astrophysical implications and observational prospects of X-ray polarimetry. *The Astrophysical Journal*, 324:1056–1067, Jan. 1988. doi:10.1086/165962. → pages 55, 115, 118

[152] R. P. Mignani, V. Testa, D. González Caniulef, R. Taverna, R. Turolla, S. Zane, and K. Wu. Evidence for vacuum birefringence from the first optical-polarimetry measurement of the isolated neutron star RX J1856.5-3754. *Monthly Notices of the Royal Astronomical Society*, 465:492–500, Feb. 2017. doi:10.1093/mnras/stw2798. → page 93

[153] D. Mihalas. *Stellar atmospheres*. 1978. → pages 55, 115

[154] J. M. Miller, J. Raymond, A. Fabian, D. Steeghs, J. Homan, C. Reynolds, M. van der Klis, and R. Wijnands. The magnetic nature of disk accretion onto black holes. *Nature*, 441:953–955, June 2006. doi:10.1038/nature04912. → pages 18, 92

[155] J. M. Miller, J. Raymond, C. S. Reynolds, A. C. Fabian, T. R. Kallman, and J. Homan. The Accretion Disk Wind in the Black Hole GRO J1655-40. *The Astrophysical Journal*, 680:1359-1377, June 2008. doi:10.1086/588521. → pages 18, 92

[156] J. M. Miller, M. L. Parker, F. Fuerst, M. Bachetti, F. A. Harrison, D. Barret, S. E. Boggs, D. Chakrabarty, F. E. Christensen, W. W. Craig, A. C. Fabian, B. W. Grefenstette, C. J. Hailey, A. L. King, D. K. Stern, J. A. Tomsick, D. J. Walton, and W. W. Zhang. NuSTAR Spectroscopy of GRS 1915+105: Disk Reflection, Spin, and Connections to Jets. *The Astrophysical Journal Letters*, 775:L45, Oct. 2013. doi:10.1088/2041-8205/775/2/L45. → page 108

[157] J. M. Miller, J. Raymond, A. C. Fabian, E. Gallo, J. Kaastra, T. Kallman, A. L. King, D. Proga, C. S. Reynolds, and A. Zoghbi. The Accretion Disk

Wind in the Black Hole GRS 1915+105. *The Astrophysical Journal Letters*, 821:L9, Apr. 2016. doi:10.3847/2041-8205/821/1/L9. → pages 18, 92, 97

[158] I. F. Mirabel and L. F. Rodríguez. A superluminal source in the Galaxy. *Nature*, 371:46–48, Sept. 1994. doi:10.1038/371046a0. → page 108

[159] C. W. Misner, K. S. Thorne, and J. A. Wheeler. *Gravitation*. 1973. → page 13

[160] K. Mori and W. C. G. Ho. Modelling mid-Z element atmospheres for strongly magnetized neutron stars. *Monthly Notices of the Royal Astronomical Society*, 377:905–919, May 2007. doi:10.1111/j.1365-2966.2007.11663.x. → page 44

[161] A. A. Mushtukov, V. F. Suleimanov, S. S. Tsygankov, and J. Poutanen. The critical accretion luminosity for magnetized neutron stars. *Monthly Notices of the Royal Astronomical Society*, 447:1847–1856, Feb. 2015. doi:10.1093/mnras/stu2484. → page 8

[162] W. Nagel. Radiative transfer in a strongly magnetized plasma. I - Effects of anisotropy. II - Effects of Comptonization. *The Astrophysical Journal*, 251:278–296, Dec 1981. doi:10.1086/159463. → pages 8, 113

[163] W. Nagel and J. Ventura. Coulomb bremsstrahlung and cyclotron emissivity in hot magnetized plasmas. *Astronomy & Astrophysics*, 118:66–74, Feb 1983. → page 46

[164] A. H. Nitz, C. Capano, A. B. Nielsen, S. Reyes, R. White, D. A. Brown, and B. Krishnan. 1-OGC: The First Open Gravitational-wave Catalog of Binary Mergers from Analysis of Public Advanced LIGO Data. *The Astrophysical Journal*, 872(2):195, Feb 2019. doi:10.3847/1538-4357/ab0108. → page 12

[165] L. Nobili, R. Turolla, and S. Zane. X-ray spectra from magnetar candidates - I. Monte Carlo simulations in the non-relativistic regime. *Monthly Notices of the Royal Astronomical Society*, 386:1527–1542, May 2008. doi:10.1111/j.1365-2966.2008.13125.x. → pages 53, 153

[166] L. Nobili, R. Turolla, and S. Zane. X-ray spectra from magnetar candidates - II. Resonant cross-sections for electron-photon scattering in the relativistic regime. *Monthly Notices of the Royal Astronomical Society*, 389:989–1000, Sep 2008. doi:10.1111/j.1365-2966.2008.13627.x. → pages 53, 54

[167] R. Novick, M. C. Weisskopf, R. Berthelsdorf, R. Linke, and R. S. Wolff. Detection of X-Ray Polarization of the Crab Nebula. *The Astrophysical Journal Letters*, 174:L1, May 1972. doi:10.1086/180938. → page 171

[168] I. D. Novikov and K. S. Thorne. Astrophysics of black holes. In C. Dewitt and B. S. Dewitt, editors, *Black Holes (Les Astres Occlus)*, pages 343–450, 1973. → pages 16, 17, 18, 38, 94, 95

[169] S. A. Olausen and V. M. Kaspi. The McGill Magnetar Catalog. *The Astrophysical Journal Supplement*, 212(1):6, May 2014. doi:10.1088/0067-0049/212/1/6. → page 11

[170] J. R. Oppenheimer and H. Snyder. On Continued Gravitational Contraction. *Physical Review*, 56(5):455–459, Sep 1939. doi:10.1103/PhysRev.56.455. → page 12

[171] J. R. Oppenheimer and G. M. Volkoff. On Massive Neutron Cores. *Physical Review*, 55(4):374–381, Feb 1939. doi:10.1103/PhysRev.55.374. → page 5

[172] M. Orlandini. Broad-band spectral properties of accreting X-ray binary pulsars. *Advances in Space Research*, 38(12):2742–2746, Jan 2006. doi:10.1016/j.asr.2006.04.026. → page 113

[173] B. Paczynski. GB 790305 as a Very Strongly Magnetized Neutron Star. *Acta Astronomica*, 42:145–153, Jul 1992. → page 9

[174] K. Parfrey, D. Giannios, and A. M. Beloborodov. Black hole jets without large-scale net magnetic flux. *Monthly Notices of the Royal Astronomical Society*, 446:L61–L65, Jan. 2015. doi:10.1093/mnrasl/slu162. → page 102

[175] B. Paul, M. R. Gopala Krishna, and R. Puthiya Veetil. POLIX: A Thomson X-ray polarimeter for a small satellite mission. In *41st COSPAR Scientific Assembly*, volume 41, pages E1.15–8–16, Jul 2016. → page 2

[176] L. Pavan, R. Turolla, S. Zane, and L. Nobili. Topology of magnetars external field - I. Axially symmetric fields. *Monthly Notices of the Royal Astronomical Society*, 395(2):753–763, May 2009. doi:10.1111/j.1365-2966.2009.14600.x. → page 149

[177] G. G. Pavlov and A. D. Kaminker. Free-free absorption of photons in a strong magnetic field. *Soviet Astronomy Letters*, 1:181–183, Oct. 1975. → page 46

[178] G. G. Pavlov and I. A. Shibanov. Influence of vacuum polarization by a magnetic field on the propagation of electromagnetic waves in plasmas. *Zhurnal Eksperimentalnoi i Teoreticheskoi Fiziki*, 76:1457–1473, May 1979. → page 91

[179] G. G. Pavlov, Y. A. Shibanov, J. Ventura, and V. E. Zavlin. Model atmospheres and radiation of magnetic neutron stars: Anisotropic thermal emission. *Astronomy & Astrophysics*, 289:837–845, Sept. 1994. → page 49

[180] M. E. Peskin and D. V. Schroeder. *Introduction to Quantum Field Theory*. Addison-Wesley, Reading, Massachusetts, 1995. → pages 59, 60

[181] A. Y. Potekhin. Atmospheres and radiating surfaces of neutron stars. *Physics Uspekhi*, 57:735-770, Aug. 2014. doi:10.3367/UFNe.0184.201408a.0793. → pages 46, 49

[182] A. Y. Potekhin and D. Lai. Statistical equilibrium and ion cyclotron absorption/emission in strongly magnetized plasmas. *Monthly Notices of the Royal Astronomical Society*, 376:793–808, Apr 2007. doi:10.1111/j.1365-2966.2007.11474.x. → page 46

[183] A. Y. Potekhin, V. F. Suleimanov, M. van Adelsberg, and K. Werner. Radiative properties of magnetic neutron stars with metallic surfaces and thin atmospheres. *Astronomy & Astrophysics*, 546:A121, Oct. 2012. doi:10.1051/0004-6361/201219747. → pages 51, 52

[184] J. E. Pringle. Accretion discs in astrophysics. *Annual Review of Astronomy*

& *Astrophysics*, 19:137–162, 1981. doi:10.1146/annurev.aa.19.090181.001033. → pages 18, 93

[185] J. E. Pringle and M. J. Rees. Accretion Disc Models for Compact X-Ray Sources. *Astronomy & Astrophysics*, 21:1, Oct. 1972. → pages 7, 112

[186] M. Rajagopal, R. W. Romani, and M. C. Miller. Magnetized Iron Atmospheres for Neutron Stars. *The Astrophysical Journal*, 479:347–356, Apr. 1997. doi:10.1086/303865. → page 44

[187] N. Rea, G. L. Israel, and L. Stella. First evidence of a cyclotron feature in an anomalous X-ray pulsar. *Nuclear Physics B Proceedings Supplements*, 132:554–559, Jun 2004. doi:10.1016/j.nuclphysbps.2004.04.093. → page 10

[188] N. Rea, R. Turolla, S. Zane, A. Tramacere, L. Stella, G. L. Israel, and R. Campana. Spectral Modeling of the High-Energy Emission of the Magnetar 4U 0142+614. *The Astrophysical Journal*, 661:L65–L68, May 2007. doi:10.1086/518434. → page 53

[189] N. Rea, S. Zane, R. Turolla, M. Lyutikov, and D. Götz. Resonant Cyclotron Scattering in Magnetars' Emission. *The Astrophysical Journal*, 686:1245–1260, Oct. 2008. doi:10.1086/591264. → page 53

[190] R. A. Remillard and J. E. McClintock. X-Ray Properties of Black-Hole Binaries. *Annual Review of Astronomy & Astrophysics*, 44(1):49–92, Sep 2006. doi:10.1146/annurev.astro.44.051905.092532. → pages 12, 18

[191] H. Riffert and H. Herold. Relativistic Accretion Disk Structure Revisited. *The Astrophysical Journal*, 450:508, Sept. 1995. doi:10.1086/176161. → pages 94, 95

[192] G. Risaliti, F. A. Harrison, K. K. Madsen, D. J. Walton, S. E. Boggs, F. E. Christensen, W. W. Craig, B. W. Grefenstette, C. J. Hailey, E. Nardini, D. Stern, and W. W. Zhang. A rapidly spinning supermassive black hole at the centre of NGC 1365. *Nature*, 494:449–451, Feb. 2013. doi:10.1038/nature11938. → page 106

[193] R. R. Ross and A. C. Fabian. A comprehensive range of X-ray ionized-reflection models. *Monthly Notices of the Royal Astronomical Society*, 358: 211–216, Mar. 2005. doi:10.1111/j.1365-2966.2005.08797.x. → page 17

[194] M. Ruderman. Matter in Superstrong Magnetic Fields: The Surface of a Neutron Star. *PRL*, 27:1306–1308, Nov. 1971. doi:10.1103/PhysRevLett.27.1306. → pages 44, 49

[195] G. B. Rybicki and A. P. Lightman. *Radiative Processes in Astrophysics*. 1986. → pages 21, 26, 124, 154, 162, 165

[196] E. E. Salpeter. Accretion of Interstellar Matter by Massive Objects. *The Astrophysical Journal*, 140:796–800, Aug 1964. doi:10.1086/147973. → page 12

[197] N. Sartore, A. Tiengo, S. Mereghetti, A. De Luca, R. Turolla, and F. Haberl. Spectral monitoring of RX J1856.5-3754 with XMM-Newton. Analysis of EPIC-pn data. *Astronomy & Astrophysics*, 541:A66, May 2012. doi:10.1051/0004-6361/201118489. → page 53

[198] J. D. Schnittman and J. H. Krolik. X-ray Polarization from Accreting Black Holes: The Thermal State. *The Astrophysical Journal*, 701:1175–1187, Aug. 2009. doi:10.1088/0004-637X/701/2/1175. → pages 42, 108

[199] J. D. Schnittman and J. H. Krolik. X-ray Polarization from Accreting Black Holes: Coronal Emission. *The Astrophysical Journal*, 712:908–924, Apr. 2010. doi:10.1088/0004-637X/712/2/908. → page 38

[200] J. D. Schnittman, J. H. Krolik, and S. C. Noble. X-Ray Spectra from Magnetohydrodynamic Simulations of Accreting Black Holes. *The Astrophysical Journal*, 769:156, June 2013. doi:10.1088/0004-637X/769/2/156. → page 97

[201] K. Schwarzschild. Über das Gravitationsfeld eines Massenpunktes nach der Einsteinschen Theorie. *Sitzungsberichte der Königlich Preußischen Akademie der Wissenschaften (Berlin*, pages 189–196, Jan 1916. → page 12

[202] J. Schwinger. On gauge invariance and vacuum polarization. *Phys. Rev.*, 82:664–679, Jun 1951. doi:10.1103/PhysRev.82.664. URL https://link.aps.org/doi/10.1103/PhysRev.82.664. → pages 67, 69

[203] J. Schwinger. On gauge invariance and vacuum polarization. *Physical Review*, 82:664, 1951. → page 66

[204] F. D. Seward, P. A. Charles, and A. P. Smale. A 6 Second Periodic X-Ray Source in Carina. *The Astrophysical Journal*, 305:814, Jun 1986. doi:10.1086/164294. → page 10

[205] N. I. Shakura and R. A. Sunyaev. Black holes in binary systems. Observational appearance. *Astronomy & Astrophysics*, 24:337–355, 1973. → pages 16, 17, 18, 38, 92, 93, 94

[206] S. L. Shapiro and S. A. Teukolsky. *Black holes, white dwarfs, and neutron stars : the physics of compact objects*. 1983. → page 15

[207] N. J. Shaviv, J. S. Heyl, and Y. Lithwick. Magnetic lensing near ultramagnetized neutron stars. *Monthly Notices of the Royal Astronomical Society*, 306:333–347, 1999. → page 75

[208] R. She, H. Feng, F. Muleri, P. Soffitta, R. Xu, H. Li, R. Bellazzini, Z. Wang, D. Spiga, M. Minuti, A. Brez, G. Spandre, M. Pinchera, C. Sgrò, L. Baldini, M. Wen, Z. Shen, G. Pareschi, G. Tagliaferri, K. Tayabaly, B. Salmaso, and Y. Zhan. LAMP: a micro-satellite based soft x-ray polarimeter for astrophysics. In *UV, X-Ray, and Gamma-Ray Space Instrumentation for Astronomy XIX*, volume 9601 of *Proc. SPIE*, page 96010I, Aug. 2015. doi:10.1117/12.2186133. → pages 2, 173

[209] P. Soffitta, E. Costa, E. Morelli, R. Bellazzini, A. Brez, and R. Raffo. Sensitivity to x-ray polarization of a microgap gas proportional counter. In S. Fineschi, editor, *Proc. SPIE*, volume 2517 of *Society of Photo-Optical Instrumentation Engineers (SPIE) Conference Series*, pages 156–163, Oct 1995. doi:10.1117/12.224922. → page 172

[210] P. Soffitta, E. Costa, G. di Persio, E. Morelli, A. Rubini, R. Bellazzini, A. Brez, R. Raffo, G. Spandre, and D. Joy. Astronomical X-ray polarimetry based on photoelectric effect with microgap detectors. *Nuclear Instruments and Methods in Physics Research A*, 469(2):164–184, Aug 2001. doi:10.1016/S0168-9002(01)00772-0. → page 172

[211] D. H. Staelin and I. Reifenstein, Edward C. Pulsating Radio Sources near the Crab Nebula. *Science*, 162(3861):1481–1483, Dec 1968. doi:10.1126/science.162.3861.1481. → page 6

[212] A. W. Steiner, J. M. Lattimer, and E. F. Brown. The Neutron Star Mass-Radius Relation and the Equation of State of Dense Matter. *The Astrophysical Journal Letters*, 765:L5, Mar. 2013. doi:10.1088/2041-8205/765/1/L5. → page 4

[213] R. J. Stoneham. Vacuum polarization effects on Thomson scattering in a strong magnetic field. *Optica Acta*, 27:545–548, Jan 1980. → page 45

[214] V. Suleimanov, A. Y. Potekhin, and K. Werner. Models of magnetized neutron star atmospheres: thin atmospheres and partially ionized hydrogen atmospheres with vacuum polarization. *Astronomy & Astrophysics*, 500:891–899, June 2009. doi:10.1051/0004-6361/200912121. → pages 44, 49

[215] V. F. Suleimanov, G. G. Pavlov, and K. Werner. Magnetized Neutron Star Atmospheres: Beyond the Cold Plasma Approximation. *The Astrophysical Journal*, 751:15, May 2012. doi:10.1088/0004-637X/751/1/15. → page 49

[216] V. F. Suleimanov, D. Klochkov, G. G. Pavlov, and K. Werner. Carbon Neutron Star Atmospheres. *The Astrophysical Journal Supplement Series*, 210:13, Jan. 2014. doi:10.1088/0067-0049/210/1/13. → page 44

[217] R. A. Sunyaev and J. Truemper. Hard X-ray spectrum of CYG X-1. *Nature*, 279:506–508, June 1979. doi:10.1038/279506a0. → page 17

[218] H. Tananbaum, H. Gursky, E. M. Kellogg, R. Levinson, E. Schreier, and R. Giacconi. Discovery of a Periodic Pulsating Binary X-Ray Source in

Hercules from UHURU. *The Astrophysical Journal*, 174:L143, Jun 1972. doi:10.1086/180968. → page 6

[219] R. Taverna, F. Muleri, R. Turolla, P. Soffitta, S. Fabiani, and L. Nobili. Probing magnetar magnetosphere through X-ray polarization measurements. *Monthly Notices of the Royal Astronomical Society*, 438:1686–1697, Feb. 2014. doi:10.1093/mnras/stt2310. → pages 54, 78

[220] A. Tchekhovskoy, R. Narayan, and J. C. McKinney. Efficient generation of jets from magnetically arrested accretion on a rapidly spinning black hole. *Monthly Notices of the Royal Astronomical Society*, 418:L79–L83, Nov. 2011. doi:10.1111/j.1745-3933.2011.01147.x. → page 92

[221] S. P. Tendulkar, R. Hascöet, C. Yang, V. M. Kaspi, A. M. Beloborodov, H. An, M. Bachetti, S. E. Boggs, F. E. Christensen, W. W. Craig, S. Guillot, C. A. Hailey, F. A. Harrison, D. Stern, and W. Zhang. Phase-resolved NuSTAR and Swift-XRT Observations of Magnetar 4U 0142+61. *The Astrophysical Journal*, 808:32, July 2015. doi:10.1088/0004-637X/808/1/32. → pages 145, 156, 157, 158, 164, 165, 169

[222] The LIGO Scientific Collaboration, the Virgo Collaboration, B. P. Abbott, and al. GWTC-1: A Gravitational-Wave Transient Catalog of Compact Binary Mergers Observed by LIGO and Virgo during the First and Second Observing Runs. *arXiv e-prints*, art. arXiv:1811.12907, Nov 2018. → page 12

[223] A. Thirumalai and J. S. Heyl. Energy Levels of Light Atoms in Strong Magnetic Fields. *Advances in Atomic Molecular and Optical Physics*, 63: 323, 2014. doi:10.1016/B978-0-12-800129-5.00005-5. → page 44

[224] C. Thompson and A. M. Beloborodov. High-Energy Emission from Magnetars. *The Astrophysical Journal*, 634:565–569, Nov. 2005. doi:10.1086/432245. → pages 11, 156

[225] C. Thompson and R. C. Duncan. Neutron Star Dynamos and the Origins of Pulsar Magnetism. *The Astrophysical Journal*, 408:194, May 1993. doi:10.1086/172580. → page 149

[226] C. Thompson and R. C. Duncan. The soft gamma repeaters as very strongly magnetized neutron stars - I. Radiative mechanism for outbursts. *Monthly Notices of the Royal Astronomical Society*, 275(2):255–300, Jul 1995. doi:10.1093/mnras/275.2.255. → pages 9, 149

[227] C. Thompson and R. C. Duncan. The Soft Gamma Repeaters as Very Strongly Magnetized Neutron Stars. II. Quiescent Neutrino, X-Ray, and Alfven Wave Emission. *The Astrophysical Journal*, 473:322, Dec 1996. doi:10.1086/178147. → pages 9, 10, 145, 149

[228] C. Thompson, M. Lyutikov, and S. R. Kulkarni. Electrodynamics of Magnetars: Implications for the Persistent X-Ray Emission and Spin-down of the Soft Gamma Repeaters and Anomalous X-Ray Pulsars. *The Astrophysical Journal*, 574:332–355, July 2002. doi:10.1086/340586. → pages 53, 83, 149, 150, 152

[229] K. S. Thorne and R. H. Price. Cygnus X-1 - an interpretation of the spectrum and its variability. *The Astrophysical Journal Letters*, 195:L101–L105, Feb. 1975. doi:10.1086/181720. → page 17

[230] R. C. Tolman. Static Solutions of Einstein's Field Equations for Spheres of Fluid. *Physical Review*, 55(4):364–373, Feb 1939. doi:10.1103/PhysRev.55.364. → page 5

[231] R. Turolla, S. Zane, and J. J. Drake. Bare Quark Stars or Naked Neutron Stars? The Case of RX J1856.5-3754. *The Astrophysical Journal*, 603:265–282, Mar. 2004. doi:10.1086/379113. → page 49

[232] R. Turolla, S. Zane, and A. L. Watts. Magnetars: the physics behind observations. A review. *Reports on Progress in Physics*, 78(11):116901, Nov 2015. doi:10.1088/0034-4885/78/11/116901. → page 10

[233] M. van Adelsberg, D. Lai, A. Y. Potekhin, and P. Arras. Radiation from Condensed Surface of Magnetic Neutron Stars. *The Astrophysical Journal*, 628:902–913, Aug. 2005. doi:10.1086/430871. → pages 49, 53

[234] J. van Paradijs, R. E. Taam, and E. P. J. van den Heuvel. On the nature of the 'anomalous' 6-s X-ray pulsars. *Astronomy & Astrophysics*, 299:L41, July 1995. → page 10

[235] R. P. Veetil, B. Paul, M. R. G. Krishna, R. Duraichelvan, C. M. Ateequlla, C. Maitra, G. Rajagopala, H. N. Nagaraja, M. S. Ezhilarasi, P. Sandhya, T. S. Mamatha, J. Devasia, and M. James. Thomson X-ray polarimeter for a small satellite mission. In *Astronomical Society of India Conference Series*, volume 3, page 165, Jan 2011. → page 2

[236] Z. Wadiasingh, M. G. Baring, P. L. Gonthier, and A. K. Harding. Resonant Inverse Compton Scattering Spectra from Highly Magnetized Neutron Stars. *The Astrophysical Journal*, 854:98, Feb. 2018. doi:10.3847/1538-4357/aaa460. → pages 53, 155

[237] C. Wang and D. Lai. Polarization evolution in a strongly magnetized vacuum: QED effect and polarized X-ray emission from magnetized neutron stars. *Monthly Notices of the Royal Astronomical Society*, 398:515–527, Sept. 2009. doi:10.1111/j.1365-2966.2009.14895.x. → pages xii, 79, 80, 81, 82, 83, 116

[238] B. L. Webster and P. Murdin. Cygnus X-1-a Spectroscopic Binary with a Heavy Companion ? *Nature*, 235(5332):37–38, Jan 1972. doi:10.1038/235037a0. → page 12

[239] M. C. Weisskopf, R. Berthelsdorf, G. Epstein, R. Linke, D. Mitchell, R. Novick, and R. S. Wolff. A graphite crystal polarimeter for stellar X-ray astronomy. *Review of Scientific Instruments*, 43:967–976, Jan 1972. doi:10.1063/1.1685840. → page 171

[240] M. C. Weisskopf, E. H. Silver, H. L. Kestenbaum, K. S. Long, and R. Novick. A precision measurement of the X-ray polarization of the Crab Nebula without pulsar contamination. *The Astrophysical Journal*, 220:L117–L121, Mar. 1978. doi:10.1086/182648. → page 171

[241] M. C. Weisskopf et al. The Imaging X-ray Polarimetry Explorer (IXPE). In *Space Telescopes and Instrumentation 2016: Ultraviolet to Gamma Ray*,

volume 9905 of *Proc. SPIE*, page 990517, July 2016. doi:10.1117/12.2235240. → pages 2, 173

[242] N. E. White, J. H. Swank, and S. S. Holt. Accretion powered X-ray pulsars. *The Astrophysical Journal*, 270:711–734, Jul 1983. doi:10.1086/161162. → page 7

[243] J. Wilms, A. Allen, and R. McCray. On the Absorption of X-Rays in the Interstellar Medium. *The Astrophysical Journal*, 542:914–924, Oct. 2000. doi:10.1086/317016. → page 157

[244] M. T. Wolff, P. A. Becker, A. M. Gottlieb, F. Fürst, P. B. Hemphill, D. M. Marcu-Cheatham, K. Pottschmidt, F.-W. Schwarm, J. Wilms, and K. S. Wood. The NuSTAR X-Ray Spectrum of Hercules X-1: A Radiation-dominated Radiative Shock. *The Astrophysical Journal*, 831(2):194, Nov 2016. doi:10.3847/0004-637X/831/2/194. → pages 9, 55, 115, 121, 122, 123, 124

[245] R. Wolfson. Shear-induced Opening of the Coronal Magnetic Field. *The Astrophysical Journal*, 443:810, Apr 1995. doi:10.1086/175571. → page 149

[246] R. Z. Yahel. X-ray spectra from accreting, magnetized neutron stars - Inclusion of the optically thick region. *The Astrophysical Journal*, 236:911–920, Mar 1980. doi:10.1086/157818. → pages 8, 113

[247] D. G. Yakovlev, P. Haensel, G. Baym, and C. Pethick. Lev Landau and the concept of neutron stars. *Physics Uspekhi*, 56(3):289-295, Mar 2013. doi:10.3367/UFNe.0183.201303f.0307. → page 5

[248] S. Zane and R. Turolla. Unveiling the thermal and magnetic map of neutron star surfaces though their X-ray emission: method and light-curve analysis. *Monthly Notices of the Royal Astronomical Society*, 366:727–738, Mar. 2006. doi:10.1111/j.1365-2966.2005.09784.x. → page 49

[249] S. Zane, R. Turolla, L. Stella, and A. Treves. Proton Cyclotron Features

in Thermal Spectra of Ultramagnetized Neutron Stars. *The Astrophysical Journal*, 560:384–389, Oct. 2001. doi:10.1086/322360. → page 91

[250] S. Zane, N. Rea, R. Turolla, and L. Nobili. X-ray spectra from magnetar candidates - III. Fitting SGR/AXP soft X-ray emission with non-relativistic Monte Carlo models. *Monthly Notices of the Royal Astronomical Society*, 398:1403–1413, Sep 2009. doi:10.1111/j.1365-2966.2009.15190.x. → pages 53, 153

[251] S. Zane, R. Turolla, L. Nobili, and N. a. Rea. Modeling the broadband persistent emission of magnetars. *Advances in Space Research*, 47:1298–1304, Apr 2011. doi:10.1016/j.asr.2010.08.003. → page 53

[252] Y. B. Zel'dovich. The Fate of a Star and the Evolution of Gravitational Energy Upon Accretion. *Soviet Physics Doklady*, 9:195, Sep 1964. → page 12

[253] S. N. Zhang et al. eXTP: Enhanced X-ray Timing and Polarization mission. In *Space Telescopes and Instrumentation 2016: Ultraviolet to Gamma Ray*, volume 9905 of *Proc. SPIE*, page 99051Q, July 2016. doi:10.1117/12.2232034. → pages 2, 173